Compliant Torsional Micromirrors with Electrostatic Actuation

Jianliang You

A Thesis

In the Department of

Mechanical and Industrial Engineering

Presented in Partial Fulfillment of the Requirements

For the Degree of

Doctor of Philosophy (Mechanical Engineering) at

Concordia University

Montreal, Quebec, Canada

December, 2011

© Jianliang You, 2011

CONCORDIA UNIVERSITY
SCHOOL OF GRADUATE STUDIES

This is to certify that the thesis prepared

By: Jianliang You

Entitled: Compliant Torsional Micromirrors with Electrostatic Actuation

and submitted in partial fulfillment of the requirements for the degree of

complies with the regulations of the University and meets the accepted standards with respect to originality and quality.

Signed by the final examining committee:

Dr. Ahmed K. Elhakeem	Chair
Dr. Yuu Ono	External Examiner
Dr. Mojtaba Kahrizi	External to Program
Dr. Abulk K.W. Ahmed	Examiner
Dr. Narayanswamy Sivakumar	Examiner
Dr. Muthukumaran Packirisamy & Dr. Ion Stiharu	Thesis Supervisor

Approved by

Chair of Department or Graduate Program Director

Dean of Faculty

Abstract

Compliant Torsional Micromirrors with Electrostatic Actuation

Jianliang You, PhD

Concordia University, 2011

Due to the existence of fabrication tolerance, property drift and structural stiction in MEMS (Micro Electro Mechanical Systems), characterization of their performances through modeling, simulation and testing is essential in research and development. Due to the microscale dimensions, MEMS are more susceptible and sensitive to even minor external or internal variations. Moreover, due to the current limited capability in micro-assembly, most MEMS devices are fabricated as a single integrated micro-mechanical structure composed of two essential parts, namely, mass and spring, even if it may consist of more than one relatively movable part. And in such a scale of dimensions, low resonant micro-structures or compliant MEMS structures are hard to achieve and difficult to survive. Another problem arises from the limited visibility and accessibility necessary for characterization. Both of these issues are thus attempted in this research work.

An investigation on micromirrors with various actuations and suspensions is carried out, with more attention on the micromirrors with compliant suspensions, electrostatic actuation and capable of torsional out-of-plane motion due to their distinct advantages such as the low resonance and the low drive voltage. This investigation presents many feasible modeling methods for prediction and analysis, aiming to avoid the costly microfabrication. Furthermore, both linear and nonlinear methods for structure and electrostatics are all included. Thus, static and dynamic performances of the proposed

models are formularized and compared with those from FEA (Finite Element Analysis) simulation. The nonlinear modeling methods included in the thesis are Pseudo Rigid Body Model (PRBM) and hybrid PRBM methods for complex framed microstructures consisting of compliant beam members.

The micromachining technologies available for the desired micromirrors are reviewed and an SOI wafer based micromachining process is selected for their fabrication. Though the fabrication was executed outside of the institution at that time, the layout designs of the micro-chips for manufacture have included all related rules or factors, and the results have also demonstrated the successful fabrication.

Then investigation on non-contact test methods is presented. Laser Doppler Vibrometer (LDV) is utilized for the measurement of dynamic performances of proposed micromirrors. Two kinds of photo-sensing devices (PSDs), namely, the digitized PSD formed by CCD arrays and the analog PSD composed of a monolithic photosensing cell, are used for static test set-ups. An interferometric method using Mirau objective along with microscope is also employed to perform static tests of the selected micromirrors. Comparison of the tested results and their related theoretical results are presented and discussed, leading to a conclusion that the proposed hybrid PRBM model are appropriate for prediction or analysis of compliantly suspended micromirrors including issues arising from fabrication tolerance, structural or other parametric variations.

ACKNOWLEDGEMENT

I would like to thank my supervisors Dr. Ion Stiharu and Dr. Muthukumaran Packirisamy for their persistent encouragement and support throughout the work of the thesis. I am grateful to Dr. Stiharu who has opened up the door and led me all the way to the success of the research. I am also very grateful to Dr. Packirisamy who has provided great help and shared his confidence and persistence.

I would like to thank Drs. Rama B. Bhat and Narayanswamy Sivakumar for their valuable suggestions or lab supports. And I would like to take this chance to thank all of my colleagues in MEMS group. They are Dr. Gino Rinaldi, Dr. Luis Flores, Dr. Xing Li, and Dan Juras, Yunqiang Li, Avinash, Ashin, Arvind, Kiran, Roku, Murali, Alfin, Alvin, Alberto Fang, in which a special thank is expressed to both Gino and Dan for their wholehearted help in the experimental set-ups. I am in debt to my family since without their sacrifice I would not be able to present the thesis.

Table of Contents

List of Figures……………………………………………………………..…….xi

List of Tables …………………………………………………………………..xxi

Nomenclature………………………………………………………………….xxii

Chapter 1: Introduction…………………………………………………………1

1.1 MEMS and Optical MEMS……………………………………………..…...1

1.2 Optical Micromechanisms……………………………………..……......3

1.3 Optical MEMS actuation………………………………………………….....5

1.4 SOI Based Microfabrication…………………………………………….....8

1.4.1 Silicon Micromachining………………………………………….....8

1.4.2 Silicon-on-Insulator (SOI) Wafers…………………………...…10

1.4.3 SOI-Based MEMS Fabrication……………………………….....12

1.5 Micromirrors…………………………………………………………….......14

1.5.1 Classification of Micromirrors………………………….………15

1.5.2 Actuation of Movable Micromirrors…………………………....15

1.5.3 Out-of-Plane Deformable and Translation Tunable Micromirrors……………………………………………………....17

1.5.4 Out-of-Plane Piston Bistable Micromirrors……………………18

1.5.5 Out-of-Plane Torsional Bistable Micromirrors ………………...19

1.5.6 Out-of-Plane Torsional Micromirrors…………………………..21

1.6 Structure and Compliant Suspension of Micromirrors…………………..23

1.7 Characterization of Torsional Micromirrors ……………………………26

1.7.1 Modeling Methodologies………………………………….........27

1.7.2 Testing Methodologies……………………………...……..29

1.8 Rationale and Objectives ……………………………………….......30

1.9 Summary ……………………………………………………………...34

1.10Thesis Layout…………………………………………………………35

1.11Contributions…………………………………………………………37

Chapter 2: Modeling Methodologies for Planar Micro Mechanisms……………….40

2.1 Planar Micromechanisms…………………………………….………...40

2.2 Analysis of a Bridged Torsional Micromirror……………………………42

2.2.1 Strain Energy and Mechanical Deformation…………………….....43

2.2.2 Electrostatic Energy ………………………………….……………47

2.2.3 Static Equations of Motion……………………...………………49

2.2.4 Static Analysis of a Torsional Micromirror…………………......51

2.2.5 Pull-in Characteristics…………………………………………..52

2.2.6 Introduction of Dynamic Modeling Using Energy Method……….58

2.2.7 Structural Effects on Compliant Beams…………………….…..64

2.2.7.1 Large Deflections…………………………………………..65

2.2.7.2 Effect of Shear Strain………………………………………66

2.2.7.3 Stiffening or Loosening Effect by Axial or Shear Force…..67

2.3 Linear Matrix Method for Framed Micro-Mechanisms………..………70

2.3.1 Planar Framed Microstructures……………………………………..71

2.3.2 Matrix Method Origination………………………………………73

2.3.3 Flexibility Matrix Method……………………………………….………75

2.3.4 Stiffness Matrix Method…………………………………………………77

2.4 Pseudo Rigid Body Model Method…………………………………..…...79

2.4.1 Pseudo Rigid Body Model……………………………………….....80

2.4.2 Comparison of PRBM and FEM……………………………………88

2.4.3 Analysis of Torsional Micromirror Using PRBM Method…………95

2.5 Summary……………………………………………………………….....98

Chapter 3: Torsional Micromirrors with Serpentine Springs……………..…….100

3.1 Introduction…………………………………………………………...100

3.2 Planar Serpentine Springs……………………………………………….102

3.3 Modeling by the Energy Method…………………………………..…104

3.3.1 Formulation of Stiffness for Rotational Serpentine Springs………105

3.3.2 Static Analysis of Torsional Micromirrors……………………. …110

3.4 Modeling by Structural Matrix Method ………………………………...111

3.4.1 The Static Equation for a Rotational Serpentine Element……...…113

3.4.2 Static Matrix Equations for Initial and Final Parts ……………….122

3.4.3 Static Matrix Equation of Motion for a Side Spring………………128

3.5 Modeling by Matrix Method with PRBM Models ………………..……131

3.5.1 Structural Member Stiffness Matrices…………………………….132

3.5.2 Global Stiffness Matrix and the Equations of Motion……………137

3.6 Numerical Simulation, Analysis and Comparison…………………….....142

3.6.1 Numerical Simulation……………………………………………..142

3.6.2 Analysis and Comparison……………………………………......145

3.7 Summary……………………………………………………………..……..148

Chapter 4: Micromachining of Torsional Micromirrors……………………….….151

4.1 Introduction………………………………………………………..151

4.2 MUMPs Process ……………………………………………………...152

4.3 SOI Wafers and SOI MEMS Fabrication ………………………………155

4.4 MicraGEM Process…………………………………………………...156

4.5 Layout Design, Wire Bonding, and Packaging……………………..…..163

4.6 Discussion on Limitations………………………………………………167

4.7 Fabricated Results………………………………………………………168

4.8 Summary………………………………………………………………...177

Chapter 5: Experimental Set-up and Characterization……………….……………178

5.1 Introduction……………………………………………………….……..178

5.2 LDV for Dynamic Testing………………………………………………180

5.2.1 Doppler Effect LDV for Dynamic Test…………………………...180

5.2.2 Dynamic Test Set-up……………………………………………...182

5.2.3 Excitation Mechanisms…………………………………..……183

5.3 PSD for Static Test…………………………………………………...187

5.3.1 Test Set-up Details………………………………………………...187

5.3.2 PSD Sensor and Data Conversion…………………………..…….189

5.3.3 Position Sensing Detection……………………………………..…195

5.4 Optical Interferometry Technique for Static Test……………………….200

5.4.1 Optical Interference……………………………………………….201

5.4.2 Mirau Interferometry ……………………………………………..203

5.4.3 Static Test Set-up with Mirau Objective…………………………......206

5.4.4 Fringe Pattern Processing……………………………………………208

5.5 Verification and Discussion…………………………………………..211

5.5.1 Micromirror #1…………………………………………………….212

5.5.2 Micromirror #2……………………………………………………215

5.5.3 Micromirror #3……………………………………………………217

5.5.4 Measurement of Eigen-Frequency………………………………...219

5.6 Summary…………………………………………………………………...223

Chapter 6: Conclusions and Extensions……………………………………..224

6.1 Conclusions…………………………………………………………...224

6.2 Extensions……………………………………………………………228

References……………………………………………………………………..229

List of Figures

Figure 1.1 The cross-section of a stacked structure of an SOI wafer with removal of the silicon handle layer……………………………………………………………………14

Figure 1.2 A typical process for SOI-MEMS fabrication: (*a*) the process starts with an SOI wafer that is composed of layers of silicon-silicon dioxide and silicon substrate; (*b*) the photo-resist layer is deposited and patterned; (*c*) the SCS layer is deeply etched using DRIE process; (*d*) the microstructures are released by removal of the sacrifice layer; (*e*) the top surfaces of microstructures and the exposed surfaces on the bottom substrate are coated with metal for better electrical conduction and optical reflectivity……………..16

Figure 1.3 The schematic view of a deformable micromirror for applications in the field of adaptive optics (Adapted from [71])………………………………………………….21

Figure 1.4 The schematic views of DMD^{TM} matrix: (a) a view of two DMD pixels in opposite tilting states; (b) the SEM pictures of the DMD arrays in -10° (the upper) and +10° (the lower) positions……………………….……………………………………23

Figure 1.5 SEM picture of an individual micromirror in an OXC array ……………….24

Figure 1.6 The SEM picture of a symmetric micromirror with two very thin torsion beams in between the two half mirrors…………………….…………………….……25

Figure 2.1 Schematic diagrams of a torsional micromirror in 3-D coordinates: (*a*) The top view shows isometric view of the structure; (*b*) The bottom diagram shows the cross-

section of electrostatic force applied on the structure; and (*c*) The side view shows its equalized fixed-to-fixed beam with a lumped mass in the midpoint……………………..…42

Figure 2.2 Three models of beams and their applied loads used for modeling of torsional micromirrors: (*a*) a cantilever; (*b*) a guided end cantilever; (*c*) a fixed-fixed beam……46

Figure 2.3 Electrostatic curves for the vertical deflection versus the applied voltage of a micromirror (*L*=300μm, *W*=200μm) symmetrically suspended by two guided-end beams and two cantilever beams, respectively…………………………………………………53

Figure 2.4 Pull-in characteristics versus variation of width of the cross-section or length of each side beam from their original dimensions (*w*=7μm or l_p=200μm)..……………..58

Figure 2.5 An equivalent graph of the 2-DOF system for the given torsional micromirror used in the dynamics analysis…………………………………………….…………..62

Figure 2.6 The force diagram representing for the stiffening effect incurred by the axial loads in a beam……………………………………………………………………...68

Figure 2.7 Various planar framed microstructures made of beams and mass plates……73

Figure 2.8 Free body diagrams of the flexibility matrix terms for a beam member in an in-plane rectangle grid…………………………………………………………………..76

Figure 2.9 Indications of the related terms in a stiffness matrix for a planar frame beam member……………………………………………………………………………………..79

Figure 2.10 (*a*) A compliant cantilever beam with loads at free end; (*b*) The diagram of the applied external loads; (*c*) The equivalent PRBM model when *M* is void (two rigid links and a rotational spring); (*d*) The equivalent PRBM model when *M* exists (three rigid links and two rotational springs)…………………………………………………………84

Figure 2.11 Deflection diagrams of a cantilever subjected to three kinds of loads at the free end: (*a*) a vertical force; (*b*) a vertical force along with a synclastic moment; and (*c*) a vertical force along with a moment in opposite direction…………………………….....87

Figure 2.12 The load-deflection curves of a cantilever beam at the free end subjected to a vertical force, obtained by using linear beam theory, linear PRBM, nonlinear PRBM and FEA simulation …………………………..…………………………..…………91

Figure 2.13 Different load-deflection curves of a cantilever at free end are simulated using linear beam theory, PRBM and FEM software: the curves in (*a*) are resulted from a range of moment with a fixed force; and the curves in (*b*) are resulted from a range of force with a fixed moment……………………………………………………………….93

Figure 2.14 Vertical deflections at free end of a cantilever resulted from a varied force or moment along with the conversely applied and fixed moment or force using linear bem theory, PRBM, and FEA simulation…………………………………………………….97

Figure 2.15 The approximated PRBM models for the two cantilever beams in the given torsional micromirror……………………………………………………………………98

Figure 3.1 Suspensions for micro-platforms: (*a*) a bridge by two cantilevers; (*b*) L-type folded beams; (*c*) U-type folded beams; (d) Sagittal springs; (*e*) Classical serpentine springs; (*f*) Double L-type folded beams…………………………………………….....101

Figure 3.2 Several types of planar serpentine springs: (*a*) one with multiple loops of rotational serpentine; (*b*) one with multiple loops of classical serpentine; (*c*) one zigzag classical serpentine; (*d*) one with rounded classical serpentine; (*e*) a rotational serpentine spring with one serpentine loop……………………………………………………...103

Figure 3.3 Schematic views of a torsional micromirror suspended by two rotational serpentine springs and their main dimensions. (a) the top view; (b) the side view…….105

Figure 3.4 Schematic diagrams for a rotational serpentine spring. (*a*) the free body diagram of a rotational serpentine spring with applied loads and geometry notations; (*b*) the joint and segment numbering of the spring; (*c*) the internal loads on a segment…..107

Figure 3.5 Schematic of micromirrors suspended by framed suspensions: (*a*) the ideally fabricated microstructure with numbering of nodes and beam segments; (*b*) the possible deviation of the fabricated microstructure…………………………………………...112

Figure 3.6 The schematic diagrams for (*a*) a serpentine spring with multiple loops of rotational serpentine; (*b*) the initial part attached to the substrate; (*c*) one rotational serpentine loop and (*d*) the final part attached with the mirror plate……………….…..113

Figure 3.7 A basic serpentine element with four segments and five nodes ……..……114

Figure 3.8 A stiffness matrix for a planar beam segment. The terms in the columns and rows of the matrix are arranged in the same order as the numbering of joints and are set to conform to the order of load and displacement vectors………………………………..115

Figure 3.9 The global stiffness matrix for a complete rotational serpentine spring that is assembled from all member stiffness matrices in the global coordinates………………118

Figure 3.10 The schematic diagrams for (*a*) the initial part and (*b*) the final part of a rotational serpentine spring……………………………………………………………..121

Figure 3.11 A schematic diagram to assemble for the global static equation of motion for a serpentine spring from sub-equations of the three portions…………………………..128

Figure 3.12 The free diagrams for a rotational serpentine spring with a single serpentine loop, where (*c*) is the equivalent structure after PRBM approximation for the three long segments…………………………………………………………………………...132

Figure 3.13 A stiffness matrix for a PRBM equivalent beam. The columns and rows of the matrix are arranged in the order of local coordinates and the numbering for joints..134

Figure 3.14 The simulated torsional micromirror and the deformation before pull-in: (*a*) the top view of the torsional micromirror meshed using SOLID95 element (1378 elements in total); (*b*) the side view of the deflected micromirror before pull-in………143

Figure 3.15 FEM simulated results: (*a*) the top view of the stress distribution on the SOLID95 meshed micromirror; (*b)* the simulated maximum stress locations on rotational serpentine springs of the micromirror before pull-in…………………………………. 146

Figure 3.16 Comparison between electrostatic curves obtained using linear energy method and FEM simulation with SOLID95 element…………………………………146

Figure 4.1 Cross-section view of PolyMUMPs micromachining process (Adapted from MUMPs Process [175])…………………………………………………………………152

Figure 4.2 A PolyMUMPs design layout showing two compliant micro-platforms, each of which is suspended by four symmetric classical serpentine springs and has four bottom electrodes underneath the platform……………………………………………154

Figure 4.3 A typical process flow for MicraGEM SOI MEMS fabrication, which briefly shows a few main steps of operation, that is, Pyrex glass etching, metal deposition, device layer etching, handle layer etching, and wafer bonding………………………………..158

Figure 4.4 SEM photos of the fabricated torsional micromirror with rotational serpentine springs: (*a*) view of the whole mirror; (*b*) view of a side spring; (*c*) view of the mirror plate……………………………………………………………………………………..160

Figure 4.5 SEM pictures of another fabricated micromirror: (a) top view; (b) view of a side spring; (c) view of the uniform gap………………………………………………161

Figure 4.6 Design layout for a variety of torsional micromirrors with the size of the mirror plate at 600μm × 500μm on a standard chip of MicraGEM…………………....164

Figure 4.7 Design layouts for a variety of torsional micromirrors with the size of the mirror plate at 300μm×240μm on a standard chip of MicraGEM……………………..164

Figure 4.8 The wire bonding machine WEST BOND 7400E and the diagrams of an 84 PGA die with pin number used for packaging of the diced MicraGEM chips…………165

Figure 4.9 AFM pictures of micro-platforms supported by "a cantilever". This cantilever can be a real cantilever or made of serially connected multiple serpentine beams……167

Figure 4.10 AFM pictures of a torsional micromirror in size of 300μm×240μm suspended symmetrically by two identical rotational serpentine springs. The lower picture shows one of the side springs…………………………………………………..168

Figure 4.11 AFM pictures of a torsional micromirror with the mirror plate at size of 300μm×240μm symmetrically suspended by two side springs, each of which is made of two rotational serpentine loops. The lower photo shows a side spring………………..169

Figure 4.12 AFM pictures of a torsional micromirror with the mirror plate size of 500μm×400μm suspended by two pairs of classical serpentine springs perpendicular to each other for strengthening……………………………………………………………….170

Figure 4.13 AFM pictures of torsional micromirrors with the mirror plate at size of 300μm×240μm symmetrically suspended by two straight beams. The top photo shows the two side beams are lined up with the central line of the mirror plate; the bottom photo shows the torsional axis formed by the two side beams has some eccentric distance to the central line of the mirror plate……………………………………………………….171

Figure 4.14 AFM pictures of torsional micromirrors with the mirror plate at size of 300μm×240μm symmetrically suspended by two side springs. The top photo shows a single rotational serpentine spring for a side spring; the bottom picture shows each side spring is made of two rotational serpentine springs…………………………….……172

Figure 4.15 AFM pictures of torsional micromirrors at size of 300μm×240μm that are suspended symmetrically by two pairs of rotational serpentine springs (*a*) or two pairs of straight beams (*b*). ………………………………………………………………..173

Figure 4.16 AFM pictures of torsional micromirrors at size of 300μm×240μm with their compliant suspensions and the multiple electrodes underneath the micromirrors: (*a*) eight electrodes as shown; (*b*) six equally distributed electrodes; and (*c*) three electrodes….174

Figure 5.1 The schematic of working principle of a Laser Doppler Vibrometer from B & K using Michelson interferometer……………………………… …………………..179

Figure 5.2 An experimental set-up for dynamic tests of torsional micromirrors. The diced MEMS chip with the micromirrors and other microstructures is bonded onto an acoustic speaker (see in the top picture); the bottom picture shows the detail fixtures for alignment of the laser beam. Similar set-up can be found in [205]……………………………..…182

Figure 5.3 Piezo-stack and the drive circuit. (a) a large amplitude (>80μm) of stroke or displacement is obtainable for this stack; (b) the flat top of the stack is suitable for bonding of MEMS chips; (c) a sample of drive circuits for the stacks [208]…………184

Figure 5.4 The schematic diagram of the test set-up for static performance using PSD sensor……………………………………………………………………………...186

Figure 5.5 (a) The sensing head of the SpotOn CCD sensor; (b) The image in the computer for the laser spot on the PSD sensing area that is reflected by the test micromirror…………………………………………………………………………..188

Figure 5.6 The schematic geometries for the optical paths when PSD sensing system is involved in a static test: (*a*) for measurement of vertical bending deflections; (*b*) for measurement of torsional deflections…………………………………………………..191

Figure 5.7 Schematic diagrams of PSD based open-loop static test set-up and the signal processing circuit for the PSD as well as a photo of the set-up………………………..195

Figure 5.8 Photos of the PSD based static test set up: the bottom left is the mounted micro-chip and the reflecting torsional micromirror; the bottom right is the hosting computer with algorithms for the static tests…………………………………..……196

Figure 5.9 (*a*) The schematic diagram for the 2-D PSD and its equivalent circuit and electrodes. (*b*) A sample of the tested results. The *x*-axis represents the time duration with a unit of 100μs and the *y*-axis is the output voltage proportional to the spotlight position on the PSD sensing surface……………………………………………………….…...197

Figure 5.10 Multiple beam reflections and interferometry. (*a*) multiple beams generated due to the high reflectivity of the surfaces; (*b*) the breadth of the fringes depends on the

reflectivity levels; (c) the comparison of two beam fringes with the multiple beam fringes or the synthetic light waves by two beams and multiple beams………………………..200

Figure 5.11 The schematic diagrams and views of the two beam interferometric static test set up involving Mirau objective. (*a*) the schematic of the set up; (*b*) the schematic of the Mirau objective; (*c*) view of the set up; (*d*) the micro-stage used for positioning tuning…………………………………………………………………………...202

Figure 5.12 (*a*): The interference fringe images captured from the interferometric microscope that has Mirau objective. The voltages are shown for individual images. The last image herein is captured when the micromirror is in perpendicular to the incident light beam (in horizontal level)…………………………………………………………204

Figure 5.12 (*b*): The interference fringe images captured from the interferometric microscope that has Mirau objective. The voltages are shown for individual images. The first image is captured when the micromirror is in perpendicular to the incident light beam and the last image shows the fringe pattern before pull-in…………………...…205

Figure 5.13 (*a*) The interference fringe image captured from Mirau interferometric microscope; (*b*) The processed (wrapped) fringe pattern; (*c*) The 3-D unwrapped phase map showing the bending slope along the micromirror……………………………...208

Figure 5.14 A photo of the PSD sensor (Spot-On CCD) based experimantal set-up for static performance test of a torsional micromirror……………………………………...211

Figure 5.15 Electrostatic curves obtained from the analytical model using linear energy method (Matlab), FEA simulation using SOLID95 element (Ansys) and static test…..212

Figure 5.16 The electrostatic curves obtained from using FEM simulation, linear energy method, PRBM with linear matrix method (Hybrid PRBM) and the PSD detector based experimental results for the torsional micromirror #2……………………………….214

Figure 5.17 The electrostatic curves obtained from using FEM simulation, linear energy method, Pseudo Rigid Body Model with linear matrix method (Hybrid PRBM) and PSD sensor based experimental results for the torsional micromirror #3………………...….215

Figure 5.18 The simulated Eigen frequency spectrums for the two torsional micromirrors with the single-loop and the double-loop rotational serpentine springs………………..217

Figure 5.19 The two frequency responses of a torsional micromirror subjected a DC voltage along with a small magnitude of AC sinusoidal voltage………………………218

Figure 5.20 The different frequency responses of a torsional micromirror subjected to direct excitation (the bottom) and indirect excitation (the top)………………………...219

List of Tables

Table 2.1 Strain energy, displacement and stiffness for three kinds of beams ………...43

Table 2.2 Structural dimensions and material properties of a torsional micromirror…...49

Table 2.3 Pull-in performance of a torsional micromirror using two models of beams...52

Table 2.4 Coefficients γ , κθ, cθ with different end forces……………………………...78

Table 3.1 Internal moments and torques for individual segments……………………..105

Table 3.2 Comparison of static performance and pull-in voltage by different methods.166

Table 4.1 Layer or material names and individual thicknesses of PolyMUMPs…...….151

Table 5.1 The related specifications of the SpotOn sensor…………………..…. …….187

Table 5.2 The related physical parameters of S1880 type 2-D PSD…………………..192

Table 5.3 The designed dimensions for the torsional micromirror #1………..………..210

Table 5.4 PSD read-out and converted deflection…………………….……………….211

Table 5.5 The designed dimensions for the torsional micromirror #2…………………212

Table 5.6 Comparison of pull-in parameters using different methods………………...213

Table 5.7 The designed dimensions for Micromirror #3………………………………214

Table 5.8 The designed dimensions and structures for two micromirrors……………..215

Nomenclature

U - Strain energy or potential energy;

U_{elec} - Electrostatic potential energy;

W_{ext} - Work done by external loads;

T - Torque;

T_e - Torque induced by electrostatic load and applied on a micromirror;

F_e - Force induced by electrostatic load and applied on a micromirror;

M - Moment;

E - Young's modulus of elasticity of a material;

G - Shear modulus of elasticity of a material;

I - Cross-sectional moment of inertia;

J_p - Polar mass moment of inertia of a mirror plate;

I_p - Polar moment of inertia;

M - Mass of a micromirror;

W - Width of a micromirror;

L - Length of a micromirror;

w - Width of a beam;

t - Thickness;

g_0 - The initial gap

z - The vertical displacement of a micromirror

α - The torsion angle of a micromirror

C - The electrical capacitance between a micromirror plate and its substrate electrode;

V - Electrical voltage;

ε - Dielectric coefficient;

K_b - Bending stiffness of a micromirror structure;

K_t - Torsional stiffness of a micromirror structure;

k_b - Bending stiffness constant of a side spring or a cantilever;

k_t - Torsinal stiffness constant of a side spring or a cantilever;

Z - Normalized vertical deformation of a micromirror;

α' - Normalized torsional angle of a micromirror;

U_d - Energy dissipated by air squeeze film damping;

U_m - Mechanical strain energy;

ω - Resonant frequency of a structure;

ω^2 - Rayleigh's quotient;

[C] - Flexibility matrix of a framed structure;

[S] - Stiffness matrix of a framed structure;

{D} - Displacement array in a framed structure;

{P} - Load array in a framed structure;

K_{mi} - Stiffness matrix of the ith member in a framed structure;

K_{ff} - Stiffness submatrix for all free nodes or joints due to loads applied on all free nodes or joints in a frame structure;

K_{fr} - Stiffness submatrix for all free nodes or joints due to loads applied on all restraints in a frame structure;

K_{rf} - Stiffness submatrix for all restraints due to loads applied on all free joints in a frame structure;

K_{rr} - Stiffness submatrix for all restraints due to loads applied on all restraints in a frame structure;

D_f - Displacement array at all free joints or nodes;

D_r - Displacement array at all restraint joints or nodes;

F_f - Force array applied on all free joints or nodes;

F_r - Force array applied on all restraint joints or nodes;

γ - Characteristic radius factor for a pseudo-rigid-body model;

Θ - Pseudo-rigid-body-model angle;

κ_θ - Rotational spring factor for a pseudo-rigid-body model;

l_p - Length of the long parallel beam segment in a rotational serpentine spring;

l_o - Length of the short orthogonal beam segment in a rotational serpentine spring;

l_i - Length of the initial beam segment of a rotational serpentine spring at the side anchored to the substrate;

l_f - Length of the final beam segment of a rotational serpentine spring at the side attached to the micromirror;

d_i - The distance between two neighbor short segments in a rotational serpentine spring;

K_{msi} - A member stiffness matrix in the global Cartesian or structural member stiffness;

R - Structural rotation matrix;

K_{ms}^{f} - A member stiffness matrix in the global Cartesian or structural member stiffness matrix for a beam segment in the final part of a rotational serpentine spring;

K_{ms}^{i} - A member stiffness matrix in the global Cartesian or structural member stiffness matrix for a beam segment in the initial part of a rotational serpentine spring.

CHAPTER 1: INTRODUCTION

1.1 MEMS and Optical MEMS

It is well known that MEMS (Micro-Electro-Mechanical Systems) are derived from the advances in micromachining processes achieved for fabrication of silicon based microelectronic integrated circuits (IC) that is growing all the way from the low scale IC (a few components on a chip) to presently the ultra-large-scale IC (ULSI) that has more than 10,000 electronic components per chip. Historically, the first IC chip was fabricated in the late 1950s [1], and the first MEMS, the silicon based piezo-resistive diaphragm for pressure sensing, was reported only a few years later in 1960s by researchers from Honeywell [2]. The first movable MEMS is an electrostatic micro-motor developed in the 1980s [3], which demonstrated the great progress in micromachining of complex MEMS. Then the digital micromirror device (DMD) applied for projection displays and the first micro-accelerometer for the automobile air bag system were carried out successfully by Texas Instruments and Analog Devices, respectively, in the 1990s [4, 5]. Then since the past decade, MEMS technology has experienced very rapid growth due to the great demand of miniaturization from optical fiber telecommunication and other optics related industries.

The miniaturization trend of MEMS is reported approaching toward the nano scale due to the advancement in research on sub-micrometer fabrication [6] and in NEMS (Nano-electro-Mechanical Systems). On the other hand, the miniaturization capability has

enabled a MEMS chip to be integrated with conditioning or preprocessing circuits on the same substrate, chip or wafer, which results in a further compactness in dimensions. The conventional MEMS chips with size of a few square millimeters can thus be upgraded to a higher functionality level such as the Lab-on-a-Chip or Micro Total Analysis Systems (μTAS) [7, 8]. Such devices behave as independent systems and execute the expected perception or actuation on its own. In other words, due to miniaturization, the new generation MEMS can be regarded as an integration of microelectronic circuits with various sensing or actuation mechanisms.

Unlike IC chips that only consist of a lot of electronic devices and circuits in micro-scale, MEMS are originally constructed by both mechanical components and the electrical leads for external connection. These mechanical components can be beams, bridges, plates, gears, tubes, diaphragms, springs and etc, all in micro-scale [9]. These mechanical components work with electrical actuations or other sensing and actuation mechanisms such as optical, fluidic, thermal, magnetic, piezoelectric and piezoresistive to fulfill expected functions [10]. Thus MEMS devices are actually machines or systems in micro scale, which is one of the reasons it is called Microsystems in Europe and Micro-machines in Japan, respectively [11].

Though a variety of mechanisms have been applied in MEMS research and development, the majority of commercially successful MEMS in recent years are optical MEMS or MOEMS (Micro-Opto-Electro Mechanical Systems). These include various optical switches, cross-connects, projection displays and other MEMS devices involved with

optical sensing, actuation and imaging. If classified by the dominant working principle of transduction, MEMS can be such defined as it uses electrical transduction technique, and MOEMS is then defined similarly as it utilizes not only electrical transducing but also optical transduction techniques [12]. Moreover, other MEMS devices such as the inertial sensors for accelerometer [13], gyroscope [14], hydro-phone [15] and geophone [16] have also involved with optical transducing techniques, which can also be classified into the category of optical MEMS. Further, there have appeared recently the optical MEMS devices that combine electronics with microfluidics, fluorescence, photonics and other disciplinary principles for biological, medical and space applications. Examples of such research or developments can be found in the recent literatures [17-23]. No matter how many disciplines are involved in MOEMS devices, the two basic components or functions, perception or actuation and microfabrication, are the skeleton to construct the MEMS technology.

1.2 Optical Micromechanisms

As mentioned, optical MEMS refer to MEMS that utilize at least a kind of optical transducing principles or MEMS that can be applied in optical fiber telecom or optical network datacom. The typical features of MEMS, given to micro size of the devices, can be listed apparently as invisible to our naked eyes, the fragility by mechanical contacts or manual operations, and the susceptibility in performance variation by ambient conditions. These have lended the popularity to optical non-contact tests for MEMS characterization and thus also to optical MEMS.

Taking advantages of non-contact sensing or actuation, optical micromechanisms are exploited and combined with other micromechanisms in most MEMS devices recently. A list of optical non-contact sensing mechanisms for MEMS [24] includes but does not limit to 1) reflection such as the micromirrors for projection displays [25-27]; 2) diffraction such as the grating light valves for high resolution display [28]; 3) refraction such as the waveguides in the integrated optics for light propagation between dielectric microstructures and light sources [29]; 4) interference used for phase modulation and interferometry [30, 31]. In general, optical micromechanisms can be based on light intensity, wavelength and phase for sensing, and photothermal or photomechanical actuations [12]. Photothermal actuation is realized by converting optical energy into heat through light absorption by an optical media and the heat is then conducted to expand or deform an active component in the structure. Instead, photomechanical actuation is a type of direct actuation using photo-generated charges to induce stress variation along the surface or the bulk body of a silicon component in MEMS. As size goes down to nano scale, optical actuation has more advantages in applications such as nanotubes, which is beyond scope of discussion [32].

Light intensity based sensing technique works based on light energy that is detected or received by a photodetector. Light intensity can be easily affected by the reflecting surface, air space, and optical conducting media between light source and photodetector to propagate the light signals. The received light intensity and its variation can indicate the mechanical movement of the target. An array or a matrix of photodetectors or photo-transistors can thus perform realtime measurements of acceleration or mechanical

movement when it is integrated with MEMS chips [33, 34]. Based on the previous classification, both reflection from an optical reflecting surface and refraction through an optical media except air belong to light intensity based sensing techniques. Meanwhile, diffraction through grating and fluorescence is a kind of wavelength based method. However, interference or interferometry is a kind of optical phase based techniques. This method is often utilized to detect or measure nano-scale displacements or profiles in high precision and can be applied in a high temperature environment (up to 700°C) [12].

Due to the relatively large size of MEMS, direct optical actuation can not provide enough energy to fulfill a desired actuation. This is the reason that optical based sensing techniques are more popular in MEMS applications for perception instead of actuation. Actuation of MEMS is mostly realized through non-optical mechanisms. Optical MEMS is actually the micro device that utilizes optical sensing with or without non-optical actuation. This will be introduced in the following section.

1.3 Optical MEMS Actuation

As mentioned, MEMS encompass a wide variety of micro-devices including MOEMS. However, there is another more specified classification based on applications. For example, RF MEMS is MEMS working in radio high frequency [35]; Bio-MEMS is intended for biological applications; Inertial-MEMS are capable of sensing inertial forces or their actuations are performed by inertial forces; and optical MEMS is the MEMS used in optical engineering. Due to MEMS interdisciplinary feature, this classification does

not specify clearly any sensing or actuation mechanisms. Optical MEMS involves optical physics for sensing and also other domains of actuation [36-38]. Sensing and actuation are sometimes related each other in MEMS to fulfill an operation. In order for effective sensing, non-active actuation is needed for transduction. And there is no difference in actuation of MEMS and MOEMS.

Movable MEMS have parts in structures that are designed such that they are able to be actuated and perform mechanical movement. In other words, the movable MEMS can be actuated by a physical domain for in-plane or out-of-plane motions, though ranges of motions are very limited due to the confined spaces and micro-sized structures. In most cases, sensing function of a MEMS device containing movable parts is realized by reading the signals converted or transduced from the movement or actuation of movable parts in MEMS. The main kind of actuations is strictly a mechanical movement to execute a final task such as grasping and rotation. Therefore there exist two kinds of actuation, that is, the actuation for perception and the actuation for mechanical operation. There are a lot of examples for the second kind of actuation in optical MEMS, such as micro-switches, micro-scanners, optical-cross-connects, and etc. There are also a few examples of actuation for perception, such as micro-accelerometers, the inertial micro-sensors. And in recent years a few types of MEMS that can execute complex tasks like micro-robots which can move in a limited space without tethers [39, 40] were reported.

Due to mechanical fragility, behavior of MEMS is detected by using a non-mechanical contact principle, such as optical, piezoelectric, piezo-resistive or pyroelectric physics.

Similarly, actuation of MEMS or optical MEMS can be fulfilled by electrostatic, piezoelectric, electro-thermal, photo-thermal, photo-mechanical methods, of which electrostatic actuation is the most popular. It is widely employed in those movable MEMS that consist of parallel plates where the relative movement between a pair of conductive electrodes can be performed due to an attraction induced by the electrical bias applied on the pair of plates. The attractive or pulling force thus generated is proportional to the square of the electrical bias but is inversely proportional to the square of the distance between the two plates, resulting in high nonlinearity of the attraction force. Electrostatic characteristics and corresponding phenomena can be found in [41-43]. The main advantages using electrostatic actuation for optical MEMS include easy fabrication, fast response, capability of out-of-plane motion, less energy consumption, easy control, and beam reflection tunability. Examples of MEMS electrostatic actuation can be found in micro-resonators, optical switches, bistable micro-relays, torsional micromirrors, combdrive micromirrors, micro-valves, micro-accelerometers, micro-geophones, micro-gyros, and micro-seisomometers, just to name a few [13-16, 44,45].

As mentioned in previous section, both photothermal and photomechanical actuations have not received much attention because of their reduced capability in MEMS actuation. In the other hand, although piezoelectric materials have been widely applied in conventional instruments, piezoelectric actuation to fulfil a required motion in MEMS was not recognized in the past century. Moreover the material is sensitive to the ambient temperature and it may malfunction or errors may be performed. If such a principle is used as a piezo-sensing element, a complex conditioning circuit is needed to match the

high output impedance in order to process the signals. However, this situation has been recently reconsidered given the achievements in microfabrication especially the SOI (silicon-on-insulator) based micromachining. A large displacement range of actuation can be performed by using piezoelectric material and framed microstructures in MEMS with low drive voltage [46-48]. Similarly, given the availability of surface micromachining, electro-thermal micro-structures for a desirable actuation could be created in which they usually take the form of stacked or laminated structures. Heat is generated when an electrical current passes thorugh a resistor layer, and deforms the other laminated structure at this location. A typical advantage of using electro-thermal actuation is that it needs very low voltage to drive, as compared with either piezoelectric or electrostatic actuation [49-51].

1.4 SOI-Based Microfabrication

Realizing the aforementioned optical MEMS mechanisms for perception or actuation at the micro scale relies on the achieved microfabrication techniques. Thus in the following sub-sections, silicon micromachining is first introduced and then the main features and advantages of SOI wafers for optical MEMS fabrication will also be reviewed.

1.4.1 Silicon Micromachining

Silicon based bulk micromachining was first reported in the fabrication of micromechanical parts in the 1970s [52]. Then both additive processes that refer to

surface micromachining techniques and subtractive processes that mainly refer to bulk micromachining processes have been widely employed since 1980s. Some new techniques and tools such as anodic bonding, high-aspect-ratio lithography, electro-chemical-plating, ion beam, electron beam, laser beam, etc, have also added more capabilities to this planar micromachining technology [53-55].

Summarily speaking, chemical vapor deposition process (CVD), sputtering, evaporation, spin-on application, plasma spraying and plating are some of the individual processes in surface micromachining. Instead, plasma etching, reactive-ion-enhanced (RIE) etching, deep reactive ion etching (DRIE), wet chemical etching and electrochemical etching are mainly intended for bulk micromachining. Etch-stop is used to control the depth of etching, which can be realized by doping, i.e., through thermal diffusions including pre-deposition and drive-in and ion implantation by bombardment of the dopant ions [56].

Surface micromachining processes produce thin layers (for example ~2μm thick) for MEMS structures. It is difficult for surface micromachining techniques to yield relatively large micro-plates with satisfactory uniformity of thickness and acceptable flat surface. Unfortunately these two features are indispensable for efficient optical reflection. However, it can be accepted for fabrication of small body micro-devices and various approaches have been employed to improve their performance. Combinations of different techniques for fabrication of complex MEMS have become a necessity [57]. Though it has very limited capabilities, MUMPs (Mult-User MEMS Processes) is the first multi-

user commercial process in surface micromachining. There are a few typical complex MEMS devices that were made by MUMPs [58].

For large size MEMS fabrication, bulk micromachining processes are involved. Etch holes on structural layers are usually required in order for fast removal of sacrifice layers, which may affect optical performance. In order to overcome this defect, however, the aforementioned etch-stop techniques are employed during production of silicon wafers. The uniformity of layer thickness and material composition as well as flatness of large reflective surfaces can be acquired by epitaxial growing of single crystal silicon on substrates or during wafer production. The structural layer thickness and the sacrificial layer thickness for cavities are controlled either by grinding, etching with etch-stops, or by anodic bonding or flip-chip bonding. This kind of fabrication processes is called SOI based MEMS fabrication technology, which starts from wafer preparation.

1.4.2 Silicon-on-Insulator (SOI) Wafers

The silicon-on-insulator (SOI) wafer refers to a stacked structure that is made of a thin layer of single-crystal-silicon (SCS, also called structural layer or device layer), a layer of electrical insulator, and a silicon substrate. SOI wafers can be classified into thick and thin-film types depending on different thicknesses of structural layer. The thin-film SOI wafer refers to thickness of the device layer less than 1.5μm [59]. Originally they were used for IC production in order to reduce parasitic capacitance in IC [60]. Other advantages include the improved isolation, higher circuit speed, lower power

consumption, compactness and compatibility with the existing IC fabrication processes [61-63]. Thereafter, SOI wafers with thick structural layers have also received a lot of attention and gained very successful applications in optical MEMS fabrication.

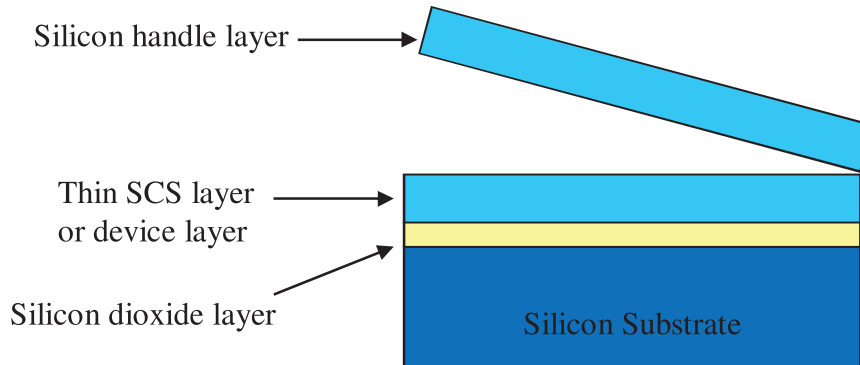

Figure 1.1 The cross-section of a stacked SOI wafer with removal of the silicon handle layer

As mentioned in [64], SOI wafers can be made using either wafer bonding or epitaxial SCS growing. The manufacture involving wafer bonding is a more popular method. Figure 1.1 shows a cross-section of this kind of SOI wafers. The handle silicon layer (the temporary silicon layer or the second substrate) at the topmost can be conveniently bonded with the first oxidized silicon substrate. A thin SCS layer with a desired thickness is formed by cutting and fine grinding of the handle silicon layer. After removal of the handle layer, the device layer is exposed to become the topmost layer of the stacked structure, whereas the insulator layer directly underneath it provides electrical isolation between the top device layer and the bottom. The insulator layer can be made of silicon dioxide (oxidization by doping or implanting), glass or other insulation materials such as sapphire and zirconia [65]. According to wafer flats and dopants, SOI wafers can be of *P*-type or *N*-type with <100> or <111> crystal orientations. SOI wafers with *N*-type and

<100> orientation of single crystal silicon have identical chemical and physical properties including Young's modulus on all lattice planes.

1.4.3 SOI-Based MEMS Fabrication

The thick-film SOI wafers, due to uniformity, thickness, flatness and low roughness for device layers, greatly enhance both optical and mechanical performances, suitable for optical MEMS fabrication. As comparison, these bonded SOI wafers have demonstrated their advantages over bulk silicon wafers [66, 67]. Except the above mentioned advantages, other benefits include the superior silicon structure, low internal stress, good reproducibility and feasibility in both sizes and structures, and fewer masks needed in micromachining. SOI MEMS have also advantages over surface micromachining in that higher aspect ratio microstructures, better mechanical properties, pure SCS composition, while a wider range of thickness for silicon device layers are achievable.

Deep reactive ion etching (DRIE) is the critical step in SOI based MEMS fabrication. A typical process of SOI wafer based MEMS fabrication is illustrated in Figure 1.2. The first step is the deposition and photolithography patterning of the photoresist layer. The patterned photoresist layer thus becomes a mask for dry-etching of the underneath silicon device layer using deep reactive ion etching process (DRIE). The silicon dioxide layer herein also serves as an etch stop for the DRIE process. The sacrificial layers, i.e., the photo-resist and the silicon dioxide layer can be removed by oxygen plasma etching and hydrofluoric acid (49% concentration of HF), respectively. Metallization of the surfaces

on both the device layer and the bottom trenches is performed as the final step of the SOI MEMS fabrication process, which is in a purpose to increase the conductivity and reflectivity of the MEMS devices.

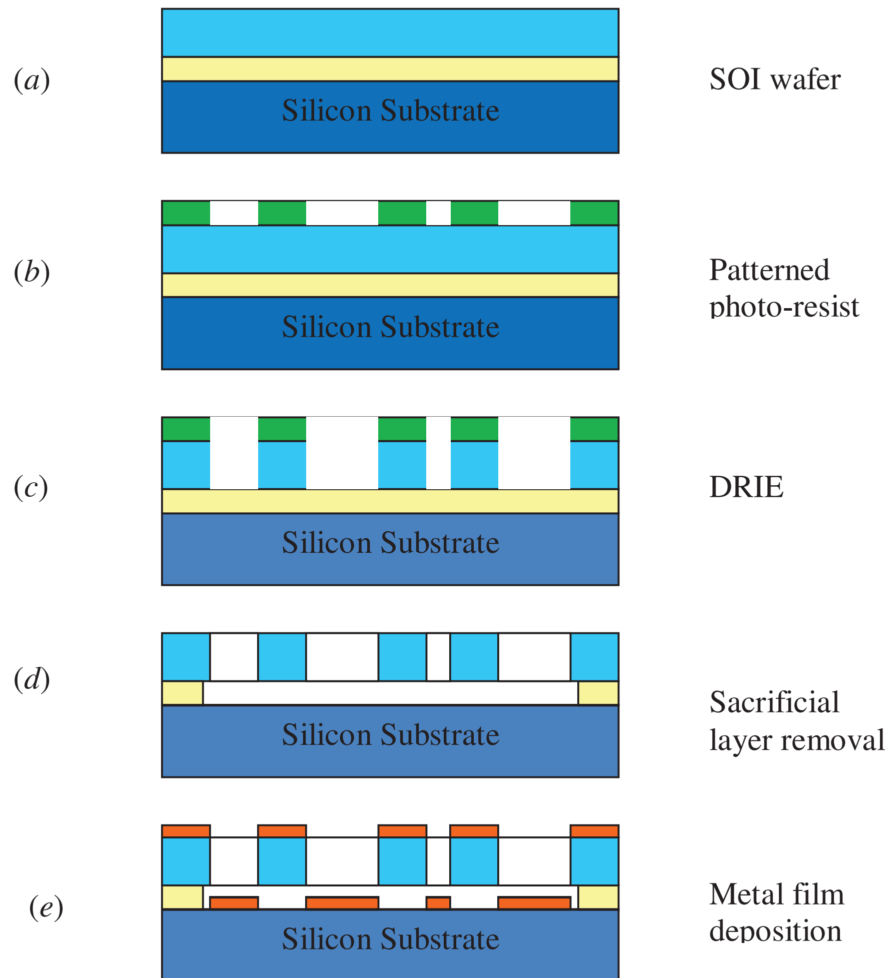

Figure 1.2 A typical process for SOI-MEMS fabrication: (*a*) The process starts with an SOI wafer that is made of layers of silicon, silicon dioxide and silicon substrate; (*b*) The photo-resist layer is deposited and patterned; (*c*) The SCS layer is deeply etched using DRIE process; (*d*) The removal of the sacrifice layer; (*e*) The top surfaces of microstructures and the exposed surfaces on the bottom substrate are coated with metal for better electrical conductivity and optical reflectivity.

The versatility in thickness for both silicon dioxide layers and device layers can provide more solid structures and much thicker free space for movable components. Among these movements, out-of-plane motion is often desired for light reflecting in MOEMS devices, such as optical cross connects (OXC), optical scanners, micro-accelerometers, and etc. Although there are quite a few bottle-necks to produce fully movable 3D MEMS, MEMS capable of out-of-plane motion for light reflecting is one of the hot topics of research in optical MEMS. There is a popular word - micromirror- to name after all of these devices which will be given a review in the next section.

1.5 Micromirrors

A mirror usually reflects an incident light according to a schedule towards a target or a surface through manipulation of the reflecting surface. Research on micromirrors started in the late 1970s and early 1980s [68]. Like the mirrors in macro optical systems, micromirrors in MEMS are also used for position measurement, imaging or switching via sensing of light route, phase, intensity and wavelength. With advances in IC and MEMS fabrication techniques achieved in the past decades, SOI (thin or thick silicon film) based optical MEMS especially micromirrors have gained great success in various applications such as optical fiber telecom and biomedical endoscopy [69-72]. Micromirrors are hence considered the leading technology for optical MEMS.

1.5.1 Classification of Micromirrors

A lot of micromirror configurations have been developed in the past decade. Though light reflecting surfaces can be made on non-movable components, most micromirrors in literature refer to movable micromirrors. For better understanding, these micromirrors can be classified into two groups, that is, micromirrors capable of in-plane motions (two lateral Cartesian coordinates) and micromirrors capable of out-of-plane motions. Since out-of-plane motions are the most interest, out-of-plane micromirrors can further be divided into three types: out-of-plane augular torsion, vertical translation and their combination. Another classification was reported in [73] in which these out-of-plane motion micromirrors are classified as deformable micromirrors, movable micromirrors, piston micromirrors and torsional micromirrors. Deformable micromirrors deform reflecting surfaces like a membrane [68], whereas movable micromirrors can move or deform in three dimensions (3D), that is, out-of-plane and in-plane motions [74]. The piston micromirrors are actuated to move up and down vertically and have two stable positions, and are also called bistable micromirrors [75].

1.5.2 Actuation of Movable Micromirrors

All movable micromirrors must be integrated with some actuation mechanism capable of either in-plane or out-of-plane motions. Usually two mechanical routines are adopted for the movements, that is, either through elastic deformation of structural components or the relative kinematic movements of structural components around pivots, latches, or along slots or sliders. The MEMS devices capable of out-of-plane kinematic movement are more

complicated to fabricate and may involve micro assembly processes [76, 77]. Abrasion and contact fatigue accumulated on contact surfaces due to repetitive operation will damage these microstructures by themselves [78-79]. The use of the integral capabilities of the mechanical structures to fulfill the desired kinematic motions is more complex. Other non-mechanical examples for out-of-plane motion of micromirrors can be found in [80-82] where mercury drops or liquid-metal pivots in micro size are employed to realize the out-of-plane motion of the attached micromirrors based on surface tension or electrowetting effect.

However the microstructures with minimal or without manual assembly are more popular and easier to fabricate even though they have to include a large number of beams and plates in the structures to achieve the targeted deformation, actuation or structural resonance. The micromirrors actuated through internal elastic deformation are well compatible to the micromachining processes based on SOI wafers. The whole device is one single part in most cases. No or very unchallenging assembly work is required. Given the elastic restoring force or torque, no extra mechanism to recover to its original position after release of actuation is required. As previously mentioned, actuation of these micromirrors can be performed by comb-drives or parallel plate electrostatic [83, 84], piezoelectric [18, 46-48, 70], electro-thermal bimorph [51, 74] and electromagnetic [85]. No matter what kind of actuations involved in such elastically movable micromirrors, their structural counteracting or restoring mechanical properties such as stiffness can be defined by their geometries and specific physical parameters [86]. Given the vast diversity of micromirrors built so far, only some typical examples that are fabricated using bulky SOI wafers and contain light reflecting micromirrors are introduced in the following section. Special attention will be given to

those having electrostatic actuation and performing out-of-plane motion, which is the dominant approach in recent years in optical MEMS [87-93]. A more detailed classification of out-of-plane motion micromirrors and the corresponding examples are given below.

1.5.3 Out-of-Plane Deformable and Translation Tunable Micromirrors

The first two micromirror devices using deformable micromirror arrays for projection display and light modulation were described in 1980 and 1983, respectively [68, 94] where mirror arrays are formed by a sheet of thinly metalized polymer stretched over a supporting grid structure. The static deflection or actuation for the arrays is realized by electrical bias applied between the sheet and the bottom electrodes. With deformations at individual mirror arrays under diferent electrical voltages, an incident light is modulated. Another typical example of deformable micromirrors used for adaptive optics is shown in Figure 1.3 [95], in which SU-8 photoresist [96] with gold coating is used as reflecting mirrors. The significant advantage of using polymer as a structural layer for mirrors is its low Young modulus which requires low voltages to be driven electrostatically. This deformable membrane is also called an optical cross connect (OXC) fabric. After deformed, the total membrane has some curve across the surface. There is another kind of out-of-plane micromirrors with uniform vertical displacement for the whole mirror plate. The mirror can be held at a position under an applied voltage, which means it is tunable in translational bending. An example of these micromirrors can be found in [97].

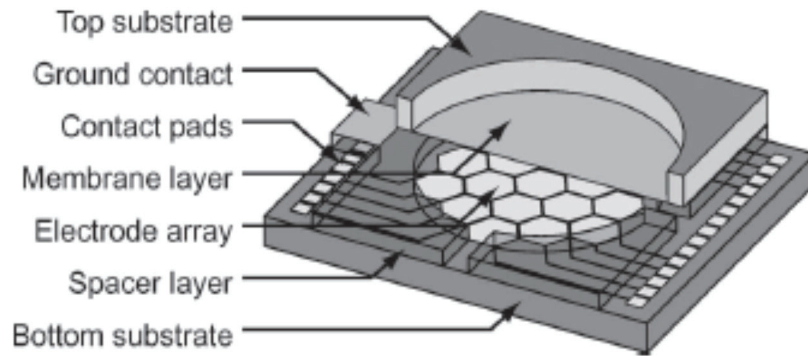

Figure 1.3 The schematic view of a deformable micromirror for applications in the field of adaptive optics (Adapted from [95]).

1.5.4 Out-of-plane Piston Bistable Micromirrors

The piston motion of a micromirror as recently reported is realized by electrowetting effect of a liquid-metal drop (LMD) with a low voltage applied [98]. The reflecting micromirror is diced and placed on the top of a mercury droplet. A voltage as low as 2V is applied between the micromirror at the top of the droplet and the electrode on the bottom substrate, in which it deforms the height of the droplet, thus realizes the translational piston motion of the micromirror. The characterization of the LMD-pivot micromirrors were performed in [99], in which the snap-down voltage (pull-in voltage), frequency response, laser beam steering, light signal switching, survival of mechanical shake and operation cycle life are discussed. Resonant frequency of this kind of micromirrors drops in a range from 0.01Hz to 3.0kHz, with piston amplitudes from about 10 μm to the maximum 60μm for a micromirror at the size of 1mm×1mm×20μm for mirror plate and the diameter of 500μm for the mercury drop [100, 101]. However, it is the first development in which piston motion of the micromirrors is realized through electrostatic comb-drive where a group of movable

comb fingers attached with a micromirror pair with the determined quantity of fixed comb fingers to perform electrostatic actuation [102]. The composite beams having various electrothermal bimorph structures have also been employed in micromirrors to drive for piston motion [103, 104].

1.5.5 Out-of-Plane Torsional Bistable Micromirrors

In 1990s an electrostatic controlled, MEMS based 800×600 micromirror matrix was successfully incorporated into commercial projection display products [105~106]. Though this type of devices is actually composed of rigid bistable micromirror arrrays for optical cross connect (OXC) applications, it is also called Digital Micromirror Device™ (DMD) by the developer. Figure 1.4 illustrates the schematic structure for a pair of individual micromirrors and SEM pictures for a portion of the micromirrors at "on" or "off" positions (+10° or -10°) [105, 107]. Each mircromirror works independently as a bistable on-off switch for optical beam transmission. The structural layer for switching operation is located under the reflective micromirror where it is driven by the electrical bias applied between one of the two symmetric side plates on this layer and its opposite electrode on substrate. The whole structure is symmetrically supported by the torsion hinge along the symmetry axis.

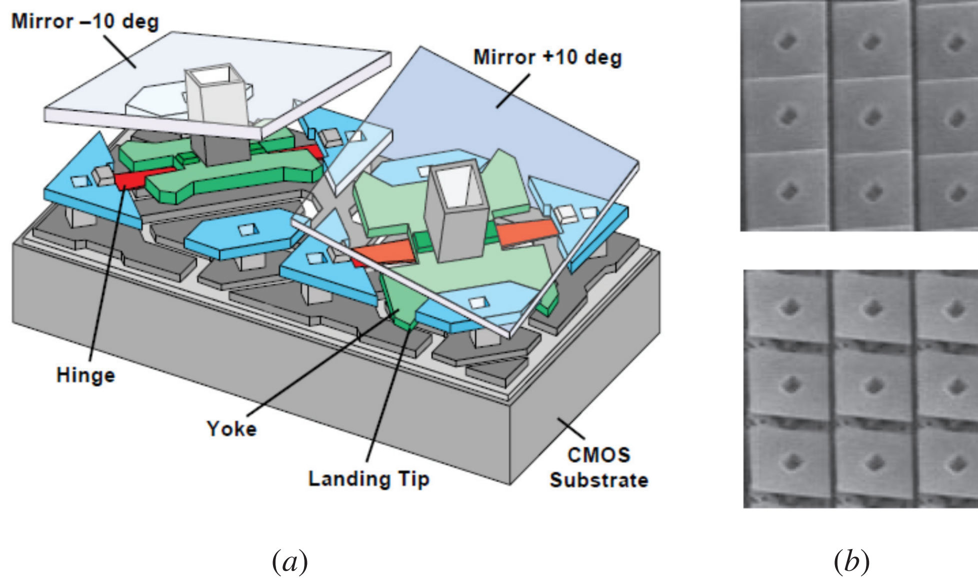

Figure 1.4 The schematic views of DMD™ matrix: (a) a view of two DMD pixels in opposite tilting states; (b) the SEM pictures of the DMD arrays in -10° (the upper) and +10° (the lower) positions (Adapted from [105, 107]).

Another type of torsional bistable micromirrors for OXC was reported in [108, 109]. They are composed of torsional micromirrors capable of 90° torsional rotation along the torsion axis. Dimensions for an individual micromirror in one of these two reports are $500\times250\times20\mu m^3$ (length×width×thickness) with a pair of 6µm–wide torsion beams at a length of 350µm and a thickness of 0.4µm. An SEM picture for the micromirror is shown in Figure 1.5. Supporting for the suspended micromirror is a pair of slim beams attached to the micromirror and the substrate at their ends. The micromirror is pulled down by the electrostatic actuation and rotated to some angle along its torsion axis. The operation switches the mirror to its “on” status and a light beam is then reflected by the mirror. Due to the large gap, a rather high drive voltage is needed for the 90° angle switching operation. Though a low resonant frequency may be obtainable, actuation may cause

nonnegligible vertical bending due to the long and slim beams. An extra trench and a vertical electrode are added to the parallel plate micromirrors in order to reduce the drive voltage (around 50% less) and to stop the micromirror at exact 90° vertically after it is electrostatically actuated [109].

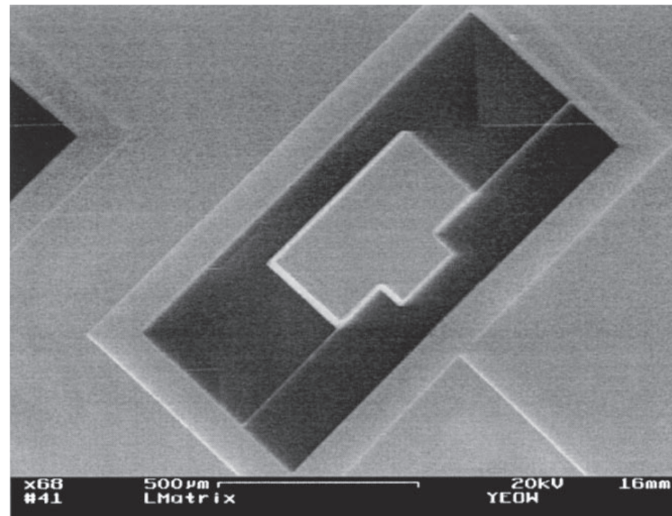

Figure 1.5 SEM picture of an individual micromirror in an OXC array (Adapted from [108]).

1.5.6 Out-of-Plane Torsional Micromirrors

A few torsional micromirrors actuated by parallel electrostatic field and capable of angular tuning before they are snapped to the opposite electrode by a relatively large voltage are reported. Figure 1.6 illustrates an SEM picture of a symmetric torsional micromirror, in which bending deflection due to the thin torsion beam can not been neglected [110]. The micromirror fabricated using three-layer-polysilicon surface micromachining process yields a 100μm×100μm mirror surface and is suspended by a short bridge attached to the substrate through two torsion beams of 65μm×1.55μm. The snap-down voltage of the micromirror in a gap of 2.75μm is tested to be around 17.4V.

The etched holes on the micromirror and thin structural layers confined by this micromachining process limit its optical performance and the applications. However, the robust torsional micromirrors with large gap (>10μm) and dimensions (hundreds to a thousand microns) have been reported in the past decades yielded through SOI based microfabrication [111-114]. The out-of-plane movable micromirrors can be held at a desired angle before it is snapped down. Applications of these tunable torsional micromirrors include but not limit to beam steering, scaning operation, tunable reflectors, optical switch ports. Their performance largely depends on the range of torsion motion and the magnitude of drive voltage. According to statistics from recently published literature, out-of-plane torsional micromirrors have received the most attention and continue to constitute the main stream of research in optical MEMS. In this consideration, structural features for a few recently reported micromirrors will be briefly analyzed in the next section.

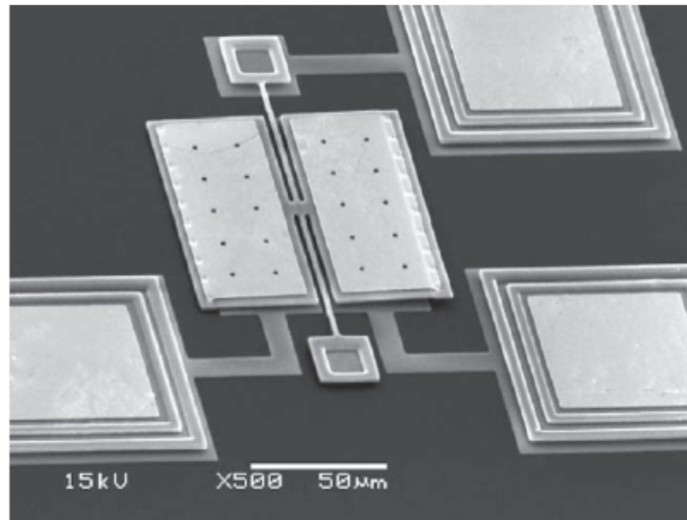

Figure 1.6 The SEM picture of a symmetric micromirror with two very thin torsion beams in between the two half mirrors (Adapted from [110]).

1.6 Structure and Compliant Suspension of Micromirrors

As above mentioned, most micromirrors are movable with out-of-plane motion. This represents for the main type of micromirror designs. They all contain a suspension to support the movable mass or the mirror plate. Although it can be made of mechanical or liquid [98], the suspension for an out-of-plane torsional motion micromirror is usually realized mechanically. The stuctural design of micromirrors relies heavily on the availability in 3-D micromachining. Since there is no much room to improve or modify the micromirror plate, most research focus on the suspension design and approach for improvement. An ideal suspension design for a torsional micromirror is the one that can rotate and stay still at any desireable rotation angle with low power consumption, low drive voltage and fast response. This has remained a huge challenge for the researchers because of the limitations in the present 3-D micromachining. However, a few approaches on new structure of torsional micromirrors have been performed based on the present level of microfabrication. Their structural characteristics are briefly reviewed as below.

Laterally actuated torsional micromirrors using SOI/SOI wafer-bonding process was reported in [115]. Here, a lateral mechanical transfer mechanism combined with electrostatic comb drive in structural design and SOI plus SOI bonding process in fabrication concept are used to build a robust micromirror capable of steering or scanning operation within a range at a potential of about 70V. Another typical torsional micromirror was reported in [116], where the torsional actuation of the micromirror is

realized by the symmetric lateral comb-drives. Buckling problem for the micromirrors is solved by the localized plastic deformation of silicon torsion beam that is resulted from passing an electrical current through the selected portion in the structure. The prototyped micromirror is able to rotate up to an angle of 50.9° under a driving voltage of 30V DC plus 14V AC and has proved a very long life expectancy.

An in-plane thermal actuator under an applied DC voltage of around 13V performs torsion of 5.2°~6.5° for the rounded micromirrors at a size of a few hundred microns as reported in [117]. Another typical torsional micromirror design has been also reported from the same research group, in which both electrothermal and electromagnetic actuators are utilized for actuation of the discussed torsional micromirrors [118].

A novel approach for a tilting micromirror was implemented in the form of a circular micromirror suspended by four helical beams and rested on the peak of a micro-pyramid located underneath the central point of micromirror. The micromirror can be electrostatically pulled to tilt along the peak at around ±30°. The micromachining process of the pyramid is simply based on the anisotropic etching nature of the silicon wafer and the etchant [119]. Diameter of the fabricated micromirror is 75µm, 2µm thick, and width of each helical beam is 8µm while the gap of the micromirror with the bottom electrodes is 30µm. The drive voltage for this micromirror is around 200V.

Aiming to increase out-of-plane motion of the micromirrors, the report in [120] presents a pre-bent mirror plate before removal of the sacrificial layer, leading to a non-flat mirror

plate. A very different electrostatic actuation mechanism is reported in [121], in which a pair of electrodes is attached on a U-shape suspension beam for the micromirror. This pair of electrodes can attract each other under an electrical bias thus to rotate the micromirror by a certain angle, while a large angle of torsion of the micromirror may be resulted if multiple pairs of electrodes are involved in the structure. There are many other typical stuctures and materials for the torsional micromirrors together with various actuation mechanisms for various applications while many more are under development.

From the aforementioned examples, suspension compliance for a torsional micromirror largely depends on design and fabrication of its compliant micro-mechanism. This refers to an elastic and continuous mechanical structure in micro-scale having flexible flexures for suspension and lumped masses of mirror plates to transfer the desired motion by actuation. Compared to a pivotal micro-structure that contains two or more continuous solid members in it, the main advantages of compliant micromirrors include easier to fabricate, no micro-assembly, no internal wear and friction and uniformly distributed compliance, which is associated with less power consumed, lower drive voltage and large out-of-plane motion.

Compliantly suspended micromirrors have applications in low frequency domains and inertial MEMS such as micro-accelerometers, geophones, micro-relays, and microrobots. Due to their delicate structures owing to availability of SOI based micromachining in recent years, MEMS with compliant suspensions have started to receive more attentions [122-124]. Typical examples include compliant bistable micromechanisms [125, 126]

and microactuators with lengthy beams for suspensions of their proof mass microplates [127, 128]. Other examples of compliant MEMS can be found in [129-131]. Although in the above-mentioned examples the suspension designs are not compliant enough, they are suitable in solving or alleviating problems of wear, friction, backlash or hysteresis, and thus offer greater versatility.

Since the movable micromirrors are mainly mass-spring structures, the suspension mechanism for a mass component dominantly determines its mechanical performance such as the stiffness thus the resonance of the structure. However, neither the size of micromirrors or proof mass plates can be increased unlimitedly nor the flexibility or compliance of a mechanical suspension can be greatly enhanced. There exists a limit in compliance of suspension structures due to fabrication limitations. Modeling and characterizing of such kind of complex compliant microstructures may be quite challenging. Therefore in the next section, characterization methodolgies for torsional micromirrors having suspension mechanisms and electrostatic actuation are briefly reviewed and discussed.

1.7 Characterization of Torsional Micromirrors

The sophisticated micromachining technologies available at the present time mainly produce the planar microstructures consisting of two essential parts, that is, the planar beams and the planar mass plates, though they can be conceived of multiple layers by means of bonding or deposition. The rigid micromirrors are usually suspended by short

hinges or directly clamped to substrates at their edges. In comparison, the relatively compliant suspension is obtained through adding either longer beams or more mass to the mirror or mass plates, thus resulting in a frame-type suspension for the masses. Performance charactization and prediction of these micro-frames will become difficult if more compliant members are involved in the microstructure. Thus among the two stages of MEMS research, modeling is more accepted and more economical due to the expensive individual fabrication owing to the micro-scale dimensions whereas testing is utilized to verify or validate modeling or prediction. However modeling is tricky as it requires modeling both the MEMS stucture and the corresponding fabrication process. If anything in the fabrication process is changed, the entire model needs to be modified accordingly. And the tested results obtained during characterization tests help improving the model design and the fabrication process design. A lot of methodologies used in modeling and testing of the beam or frame-suspended micromirrors have been performed in the past decades. A brief introduction to these characterization methodologies is hereafter provided.

1.7.1 Modeling Methodologies

There are two major approaches in modeling methodologies for framed MEMS. These are the End-Effect approach based on computerized topology and optimal design for the desired frames [131] and Flexure-Synthesis approach based on the assumed structures and parameters that target directly to a specific application. From user-defined inputs or force-deflection requirements, the former approach generates topological structures that

are hard to fabricate in reality or it may lead to a deadlock without any practical result though its output is clearly defined. Moreover this trial-and-error method is also time consuming [122, 131-134]. Instead, the second approach is based on the established knowledge and experience and natural phenomena of various microstructures and the already-well-demonstrated micromachining proceses along with specific materials [135-138] thus is more acceptable.

Comparatively the Flexure-Synthesis modeling or design approach of compliant MEMS mostly deals with familiar and regular micro-structures, such as the rectangular or the circular micro-plates and micro-beams. The designed models are easy to understand, more predictable and implementable. As is reviewed in [44], this series of characterizing methodologies includes conceptual, mathematical, numerical (finite element analysis) modeling methods and thereafter various experimental procedures. This methodology has gained success in MEMS research in the past years. The essential mechanism in modeling the elastic micro-mechanical structures is the energy conservation principle. All individual modeling methods such as classic energy methods, stiffness matrix methods and finite element methods are based on this mechanism and work with different orders of structural discretization to perform analysis or prediction for MEMS with framed mechanisms.

1.7.2 Testing Methodologies

Due to the micro scale, the currently available test methods can mainly be classified in two groups: the non-destruction methods and the destructive methods [139-141]. The latter group is normally used for material test or the tests to verify if any performance changes on MEMS after they are exposed to harsh condition during post-processing, packaging, testing or actual operation. This kind of tests usually involves some mechanical disturbers to deflect or touch the test objects. And the detection is based on non-contact optical or electrical instruments to sense or pick up the feedback, deflection or profile of a microstructure. The disturbers can be a microprobe, a nanoindenter or a loading mass [142-146]. These disturbers cannot be used in characterization tests of movable micromirrors with compliant suspension due to their micro-size and fragility.

Instead, the non-destructive or non-mechanical-contact test methods employ non-mechanical disturbers such as electrical bias or current to pull or deflect the test objects and non-contact detections to pick up the deflections or changes [147]. Optical transducing technology is derived from light transmission and propagation laws such as light reflection, refraction or diffraction and thus leads to the testing methods based on direct light reflection, interferometry [148-151] and Laser Doppler velocimetry methods (LDV) [152-154]. The integrated photo-sensing devices such as CCDs (charge-coupled devices) or embedded monolithic photo-sensing cells (or photo-sensing detector-PSD) are used to measure position variation of the reflected or refracted light beams. Laser Doppler velocimetry is used as a vibrometer to detect resonance properties and vibration

spectrum for MEMS devices. These testing methods are also used for surface profiling of microstructures and for the measurement of mechanical performances of MEMS. Therefore optical non-contact sensing methods together with various electrical or electrothermal actuations have become the main stream for MEMS characterization.

1.8 Rationale and Objectives

Based on the above analysis, the main aspects discussed in this thesis are related to modeling, design, fabrication and characterization of the micromirrors made of SOI wafers, which perform out-of-plane motions and which are electrostatically actuated while supported by compliant framed suspensions. The rationale in support of this proposition is herein summarized below and then the specific objectives of the research are listed thereafter in this section.

Batch fabrication of MEMS greatly cuts down the cost of individual MEMS devices. However, modeling, prototyping and experimental characterization are three indispensable steps before one can move to a commercial product. Besides the three stages, the precise, repeatable and flexible dimension control of micromachining is the key to a successful design. The thick device layer SOI wafers not only feature in the precise dimensions and uniform material composition along the cross-section but also the robust planar structure and flat surface on the device layer according to the introduction on SOI wafer production [69-70]. Moreover, the insulator layer in a SOI wafer can be easily removed by etching without etching holes. This forms a free space for out-of-plane

motion of mass components with their suspension. Very large free space for movable components can be created using the flip-chip bonding techniques [155]. The flexibility in thickness of the device layer and its free space with the bottom substrate enables the SOI-based MEMS in large variety of geometries. The capability thus represents an attractive reasoning towards the study of optical MEMS, specifically out-of-plane micromirrors in SOI technology.

As a substrate material for IC production, silicon micro-chips including SOI wafers are also suitable for building mechanical micro-components given the excellent mechanical performance and adaptivity to micromachining. Suspensions made of one or more very slim micro-beams are able to support relatively large mass microplates because of material strength and the available micromachining techniques. Microbeams of several microns or below that are achievable and reliable according to previous investigations [156]. However, there is a limit in how far the miniaturization can go given the limits in microfabrication and the requirements for effective optical transmission. To avoid or alleviate such shortages, approaches on various structures made of planar beams and plates are needed, in which structural modeling represents the essential work and critical for applicable designs.

A compliant suspension needs elaborate modeling and design. Though various suspensions in macro size can be utilized for micro mechanical designs, most of them are not feasible based on the current capabilities of micromachining. Thus fabricable models have to go through the complete process of modeling and characterization. Moreover, a

flat and highly reflective surface can be acquired using a relatively thick microplate at one hand, meaning a relatively large micro mass plate. Then out-of-plane motion of thick microplates will require stronger suspensions. On the other hand, this requires either a relatively large drive voltage or a large size of thin plate to be electrostatically actuated. Though this actuation has a lot of advantages over other actuation methods (see Section 1.3), compliant suspensions are necessary for the movable micromirrors. Modeling of these micromirrors with compliant suspension is thus focused on reducing electrostatic drive voltage and avoiding issues arising from the fabrication such as sticktion and structural sinking.

Structural stiffness is therefore one of the main parameters in modeling and characterization of suspended micromirrors. Most of out-of-plane movable micromirrors are supported by short hinges or beams with higher value of stiffness according to the literature [88-93]. However, the serpentine springs consisting of multiple folds of straight beam setions are reported [157, 158]. Modeling for practical applications of these springs for out-of-plane torsional micromirrors still needs lots of work. Very important aspect in this effort is to set up mathematical or analytical models aiming to predict or analyze their performances. These models can be numerically solved and virtually tested using the commercial FEA (Finite Element Analysis) software. An important aspect of characterization in MEMS research is the set up of a proper test-bench for validation of the fabricated prototypes. As above introduced, there are a few non-contact optical test methods for movable micromirrors such as CCDs or monolithic silicon photodetectors, interferometry, and Laser Doppler Velocimetry. The design of the appropriate test bench

is usually related to the design and the function of the optical MEMS. However, the proper selection of the test procedures and limits is one of the challenges that create the rationale of the present investigation.

In consideration of batch fabrication, the commercially available micromachining processes are applied for the prototype manufacture. These processes use thick SOI film wafers as the base material for the micromirrors in this research. Proper selection of one of these processes and proper design of the micromirrors compatible to its fabrication rules are essential to the success of a design, and this also represents one of the main contents of the research.

In consideration of the above rationale, the research focuses on the study of torsional micromirrors with compliant suspensions that are driven by parallel electrostatic actuation. Analytical models are etablished and used for prediction of the behavior of the torsional micromirrors, and the feasible models are selected and fabricated for experimental validation. The test instruments are selected and set up for both static and dynamic tests, then results obtained from analytical modeling, numerical simulations and the tests are compared. The main objective of the research is to contribute to the knowledge about the out-of-plane movable micromirrors with compliant suspensions and parallel field electrostatic actuation.

The mirror plate suspended by one or more springs or hinges will rotate or be pulled toward its opposite electrode plate in some angle when it is applied by an external non-

contact mechanical force (such as gravity or an acceleration) or an electrical bias. This angular deformation or other displacement is detectable in real-time by means of non-contact optical sensing techniques. The approach targets those applications that require low stiffness such as the angular tuning positioners, scanners, on-off switches or multiple optical port switches, projection displays, and the low resonant micro-accelerometers in inertial MEMS. The particular objectives are listed as follows:

- Analysis of parallel electrostatic fields
- Analysis of framed suspensions for out-of-plane micromirrors
- Modeling of torsional motions via compliant suspensions
- Linearization of mathematical models
- Design and fabrication of compliant torsional micromirrors
- Experimental set-up for performance measurement using various non-contact optical sensing techniques

1.9 Summary

This chapter gives an introduction to MEMS and optical MEMS, optical micro-mechanisms and optical MEMS actuation mechanisms. Further, it introduceds in details the main purpose and the fundamens of the investigation as well as the technical routines used to accomplish the research topic. Electrostatic actuation is emphasized to be very suitable for MEMS actuation in comparison to other actuations such as piezoelectric, piezoresistive, electro-thermal, magenetic, etc. MEMS made of SOI wafers for optical applications are the primary focus of the research, thus a brief review of SOI wafers and

the main SOI based MEMS process are given thereafter. Robust micromirrors fabricated using SOI wafers are the main components in Optical MEMS. Classification and typical structures and functions of these micromirrors are given. In order to arrive at such a research goal, a review of the literature related to the topic is given. The review indicated there is interest but less work has been carried out so far on the compliant torsional micromirrors due to the limits in micromachining, though the low resonance inertial MEMS are highly demanded. A brief introduction to the methods based on Flexure-Synthesis algorithm, modeling methods which include the conventional energy method, matrix method for framed microstructures and numerical methods are briefly introduced. Test methods used for MEMS characterization are also reviewed and non-contact test methods using light reflection, interference and Doppler effects are mentioned and will be further used in our research.

1.10 Thesis Layout

This thesis is written following the stream of modeling methods, case modeling, case micromachining, and characterization. As shown above, the first chapter provides the literature review of all related sub-topics such as MEMS fundament, MEMS actuation, micromirrors, micromachining for micromirrors, compliant micromirrors and modeling and testing methods for MEMS, as well as the rationale and objectives of the research for compliant torsional micromirrors with eelectrostatic actuation.

The following chapter, Chapter 2, provides in more detail the mathematical methods for MEMS structural modeling, especially for the compliantly framed MEMS. This includes the conventional energy method and matrix methods used for linear micro-structures and Finite Element Methods such as chain algorithm, Pseudo Rigid Body Model and combination of linear and nonlinear methods for large deformation or non-linearity of framed microstructures.

Chapter 3 gives detail modeling and formulates the process using the four theorectical methods for the analysis of the torsional micromirrors with compliant serpentine springs and electrostatic actuation. Comparisons between different modeling methods and results of the numerical simulation are presented.

In Chapter 4, the detailed micromachining process using SOI wafers suitable for fabrication of the proposed micromirrors is presented after a brief review of micromachining technologies based on surface deposition and SOI wafers. The layout design rules and limits for the micromachining process of the micro-chips that contain the proposed micromirrors are introduced and presented. Some fabrication problems are also reviewed and finally the final fabricated micromirrors are presented.

Chapter 5 gives an overview of non-contact test methods for MEMS. Further, a detailed presentation of every individual test set up using LDV, PSD and interferometry, and the results of the tests are presented. Comparisons of data retrieved from the different test methods and the results of the numerical or analytical predictions are presented.

Chapter 6 gives a general view on the conclusions of the research and lists the achievements or contributions of the work. The future work and recommendations for the further approach to the proposed topic are also discussed.

1.11 Contributions

The main contributions of this research are listed as follows:

- Detail analysis on electrostatic actuated torsional micromirrors was fulfilled;
- Effects arising from large deflections and shear strain were discussed;
- Structural matrix method was extended to analyze the framed micro-mechanisms;
- PRBM method was extended to analyze out-of-plane motions of compliant beams;
- The general formula of stiffness matrix for the planar rotational or classical serpentine springs was derived;
- Structural matrix method was combined with PRBM method to solve framed micro-mechanisms that have compliant beams;
- Three kinds of test benches for static performance were established;
- Data acquisition and post-processing after tests were developed;
- FEM modeling of compliant hinges was developed and verified.

A list of publications is given below:

1. **Jianliang You**, M. Packirisamy, I. Stiharu,"Study of an eletrostatically actuated torsional micromirror with compliant planar springs" , Journal of Microsystems Technologies, Issue 14, No. 1, pp. 7-16, 2007;

2. **Jianliang You,** Avinash K. Bhaskar, Muthukumaran Packirisamy and Rama Bhat, “Static and dynamic evaluation of SOI based scanning micromirrors”, International Journal of Intelligent Systems Technologies and Applications, Vol. 5, No. 1/2, pp. 185-200, 2008;
3. A. Chandrasekaran, Shanmugasundaram, P., **J. You,** A. Acharya, M. Packirisamy, D. Maxwell’ “Bio-resistive identification of Heat Shock Protein 90”, Journal of BioMicrofluidics, Accepted, June 28 2008. *Biomicrofluidics* vol.2(3) 2008, pp 034102:1-10. Also published Virtual Journal of Biological Physics Research, July 15, 2008;
4. **Jianliang You,** Luis Flores, Muthukumaran Packirisamy and Ion Stiharu, ‘Modeling the Effect of Channel Bends on Microfluidic Flow’, IASME Transactions, Issue 1, Vol. 1, Jan. 2005, pp. 144-151;
5. Arvind Chandrasekaran, Ashwin Acharya, **Jian Liang You,** Kim Young Soo, Muthukumaran Packirisamy, Ion Stiharu, Andre Darveau, “Hybrid integrated Silicon microfluidic platform for fluorescence based biodetection” *Sensors* 2007, *7*, 1901-1915;
6. **J. You**, M. Packirisamy, I. Stiharu, ‘Dynamic Analysis of a Cantilevered Electrostatic Actuator’, CDIC’06 Conference, Queretaro, Mexico, August 2006;
7. **J. You**, M. Packirisamy, I. Stiharu, ‘Static Modeling and Pull-in Analysis of a Cantilevered Electrostatic Actuator’, IEEE-ISIE2006 Conference, July 9-13, Montreal, Canada

8. **Jianliang You**, Muthukumaran Packirisamy and Ion Stiharu, 'Modelling of Torsional Micromirrors with Springs made of Multiple Rotational Serpentine Elements', NSTI Nanotech2006, Boston, May7-11 2006. Vol. 3, pp. 590-593;
9. **J. You**, M. Packirisamy, I. Stiharu, 'Study on Symmetrically Supported Electrostatic Actuated Micro-Platform', SPIE Photonics North conference, June 5-8, 2006, Quebec City;
10. **J. You**, M. Packirisamy, I. Stiharu, 'Modelling of Torsional Micromirrors with Springs made of Multiple Rotational Serpentine Elements', Conf. on Modeling and Simulation of Microsystems, Nanotech 2006, Boston, Massachusetts, May 7-11, 2006 (Accepted for Poster);
11. **J. You**, M. Packirisamy, I. Stiharu, 'Analysis, Simulation and Testing of a Micromirror with Rotational Serpentine Springs', Third International Conference on Intelligent Sensing and Information Processing, 14-17 December 2005, Bangalore, India. **(Received the IEEE Best Paper Award);**
12. **J. You**, M. Packirisamy, I. Stiharu, 'Analysis, Simulation and Testing of a Compliant Planar Spring for Micromirrors', Poster Session, 4th Canadian Workshop on MEMS, Opportunities and Challenges on the Road to Microsystems Integration, August 19, 2005.

CHAPTER 2: MODELING METHODOLOGIES FOR PLANAR MICROMECHANISMS

As introduced in Section 1.7.1, Flexure-Synthesis approach of modeling is a more intuitive method. It starts from modeling of the essential structural members such as beams and plates in conjunction with the electrostatic or the electrothermal actuation for optical MEMS. This chapter will first give a review of the features of the planar micro-mechanisms capable of out-of-plane motion based on the currently available micromachining processes. This will be followed by the example of a full analysis for a micromirror nonsymmetrically supported by torsion beams and actuated by uniform electrostatic field using the conventional energy method. The linear matrix method and pseudo-rigid-body model method that are individually applied in the analysis of a planar and framed microstructure are presented.

2.1 Planar Micromechanisms

The planar micro-mechanisms refer to microstructures that are composed of planar beams and plates in micro scale of dimensions. Suface micromachining has been very capable so far in creating planar microstructures consisting of beams and plates [159]. An expected compliance or structural resonance of a micro-structure can be realized without exception by adjusting the ratio of proof mass and stiffness of the suspension. As introduced, this ratio is limited by both material strength and microfabrication capability. The flat surface necessary for light reflecting requires a non-compliant mirror plate. On another hand it is

difficult to reduce endlessly the stiffness of suspension while the proof mass stays rigid. Such requirement is even more difficult to achieve for the planar micromechanisms. In macro fabrication, suspension by vertical springs for a mass can be very soft thus enabling a reduced ratio of suspension stiffness versus the structure mass. However it is difficult within the current micromachining capabilities to make their counterparts in 3-D spatial structure [159]. Moreover, the 3-D movable MEMS have been demonstrated to be hard and costly when obtained from assembly of a few separated micro-components [160,161]. Instead, the planar springs made of integrated planar beams and plates are thus adopted for compliant suspensions in micro world.

Moreover, for the movable micro mechanisms, compliance or the total elasticity is exploited to convert the available energy into a useful movement of the mechanism. More displacement or deformation can be achieved by the same amount of energy input in a compliant microstructure. Similarly, an integrated MEMS device made by planar micromachining may be granted the desired compliance by involving lengthy beams in its framed microstructure. The sophisticated 2-D micromachining technology for planar microstructures represents topic of high interest in MEMS area. The concept of planar micro-mechanisms thus not only deals with applicable micromachining, but also requires analysis and modeling of planar framed microstructures. As the main focus of this chapter, investigation on modeling methodologies for the micro-frames is performed through a typical example of out-of-plane torsional micromirrors with electrostatic actuation. This device is assumed to be a rectangle mirror plate supported by two identical torsion beams at both sides and anchored to the substrate at the other ends of the

beams. The electrostatic field between the mirror and the substrate under the mirror is generated by electrical bias and used for actuation (see Figure 2.1).

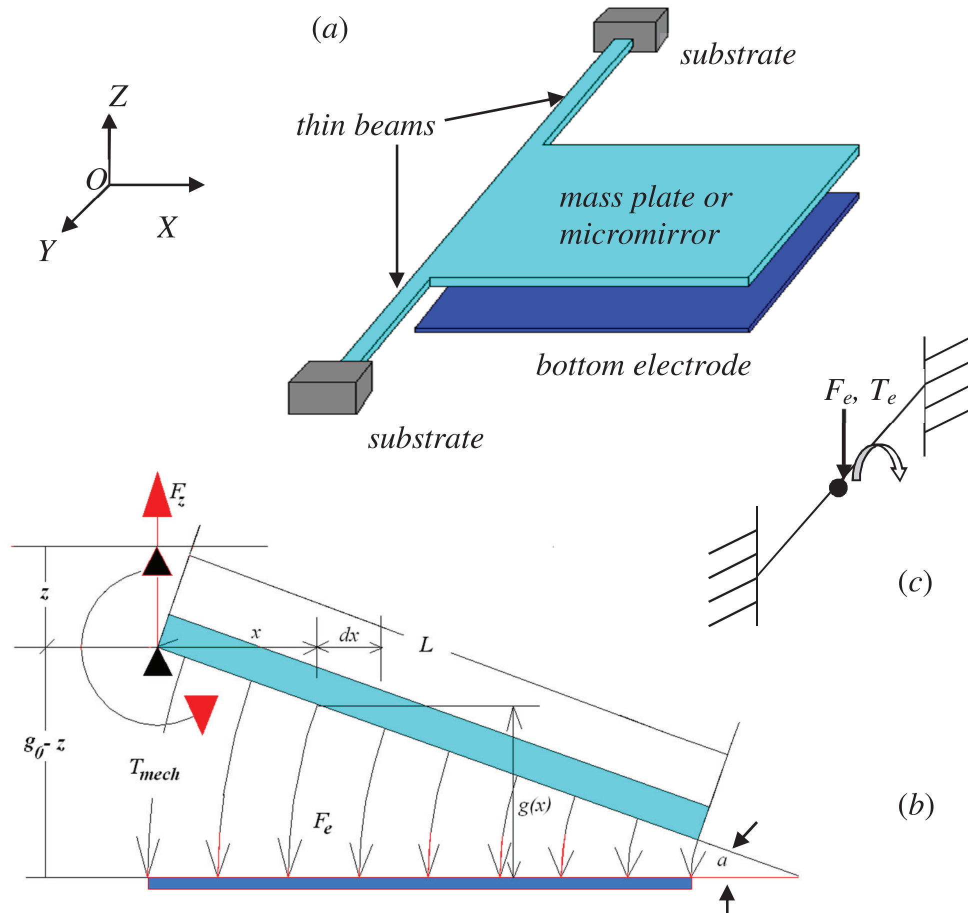

Figure 2.1 Schematic diagrams of a torsional micromirror in 3-D coordinates: (*a*) The top view shows isometric view of the structure; (*b*) The bottom diagram shows the cross-section of electrostatic force applied on the structure; and (*c*) The side view shows its equalized fixed-to-fixed beam with a lumped mass in the midpoint.

2.2 Analysis of a Bridged Torsional Micromirror

Energy methods are widely used in the analysis of applied mechanics. This method involves concept of work (such as virtual work) and energy to solve for linear and nonlinear mechanical problems. The essential of this method is the energy conservative

principle for any isolated mechanical system. Thus this section provides mathematical derivatives of the mechanical strain energy, the electrostatic potential energy, and nonlinear characteristic analysis of a torsional micromirror suspended by a bridge as well as its corresponding static and dynamic equations of motion.

2.2.1 Strain Energy and Mechanical Deformation

Strain energy is generated and stored in a beam or other elastic members whenever it is bent by an external force. If it is released the beam tends to recover to its original status [167]. In other words, strain energy refers to the energies that are absorbed by the elastic structure during external loading process. Theoretically this strain energy U_{int} is equal to the work W_{ext} done by the external loads, provided no other energy is added into the system or no energy in the system is transferred in the form of heat. Thus,

$$U_{int}=W_{ext} \tag{2.1}$$

Under the assumption of structural linearity or small deflection of elastic structures that follows Hooke's law, the expressions of strain energy for a beam subjected to axial forces, torqes, and bending moments, respectively, can be written [162]:

$$U_{axi}=\int_0^L \frac{P^2(x)dx}{2EA}=\frac{1}{2}\frac{EA}{L}\delta^2=\tfrac{1}{2}k_{axi}\delta^2 \tag{2.2}$$

$$U_t=\int_0^L \frac{T^2(x)dx}{2GI_p}=\frac{1}{2}\frac{GI_p}{L}\varphi^2=\frac{1}{2}k_t\varphi^2 \tag{2.3}$$

$$U_b=\int_0^L \frac{M^2(x)dx}{2EI}=\frac{1}{2}\frac{EI}{L}\theta^2=\frac{1}{2}k_b\theta^2 \tag{2.4}$$

where L is the length of the beam; E is Young's modulus of elasticity of the material; A is the cross-section area of the beam; $P(x)$, $T(x)$, and $M(x)$ are the locally applied axial pulling or pushing load, torsional torque, and bending moment or force couple applied on the beam respectively; k_{axi} is the spring stiffness; δ is the axial strain deformation of the beam; G is the shear modulus of elasticity of the material; I_p is the polar moment of inertia of the beam; φ is the twist angle of the beam; k_t is the torsional spring stiffness; I is the cross-sectional moment of inertia of the beam; θ is the rotational angle of the beam and finally k_b is the bending stiffness of the beam.

In general terms, if an elastic structure is subjected to n loads P_1, P_2, P_3, …, P_i, …, P_n and has n correspondent displacements δ_1, δ_2, δ_3, …, δ_i, …, δ_n, Castigliano's first theorem states that the partial derivative of strain energy of the structure with respect to any displacement δ_i is equal to the corresponding force P_i [162]:

$$P_i = \frac{\partial U}{\partial \delta_i} \tag{2.5}$$

Strain energy can be expressed either as a function of displacement or as a function of loads. Castigliano's second theorem states that the partial derivative of the strain energy with respect to any load P_i is equal to the corresponding displacement δ_i:

$$\delta_i = \frac{\partial U}{\partial P_i} \tag{2.6}$$

There is another derivative for a displacement of a beam based on energy method, which is called the unit-load method for linear elastic structures. The method is based on the work principle that the internal virtual work done by the internal stresses equals the external virtual work done by the external loads applied on the structure during a virtual

displacement. The external work is assumed to be fully absorbed by the beam and stored in as strain energy and the displacement is then found by assumption of a unit-load applied on the beam [163, 164]:

$$\Delta = \int \frac{N_U N_L dx}{EA} + \int \frac{M_U M_L dx}{EI} + \int \frac{f_s V_U V_L dx}{GA} + \int \frac{T_U T_L dx}{GI_p} \tag{2.7}$$

where Δ represents the displacement in solving. N_U, M_U, V_U and T_U represent stress components along the beam due to the axial forces, moments, shears and torques converted from the unit load. This virtual load is assumed to apply on the location of displacement. Instead, N_L, M_L, V_L and T_L are the corresponding stress components resulted from the actual loads on the beam.

As a typical example of torsional micromirrors shown in Figure 2.1, their suspensions are usually formed by a bridge or two cantilever beams. Depending on different boundary conditions, three types of beams can be classified for their mechanical strain energies, displacements and spring constants (listed in Table 2.1) under application of point loads (bending and torsion) on either the free end of cantilever beams or the middle point of the fix-fix bridge. Figure 2.2 shows these three types of beams useful for the torsional micromirrors where F and T indicate the equivalent bending force and torsional torques respectively on the location of displacment. It is noted that in the table the shear and axial deformations due to the applied loads are neglected since they are small when compared to other deformations in the linear structure. The prismatic cross-sections for these three types of beams in discussion are the same with each other in dimensions of width w and thickness t. Table 2.1 indicates the cantilever beam as the most flexible and the fixed-fixed beam is the least flexible in bending. No matter what boundary conditions are

subjected to, all beams have the same torsional performance for the same cross section due to the same length.

Table 2.1 Strain energy, displacement and stiffness for three kinds of beams

	Cantilever	Guided-end cantilever	Fixed-fixed beam
Strain energy	$\frac{F^2L^3}{6EI}+\frac{T^2L}{2GI_p}$	$\frac{F^2L^3}{24EI}+\frac{T^2L}{2GI_p}$	$\frac{F^2L^3}{48EI}+\frac{T^2L}{4GI_p}$
Bending deflection	$\delta=\frac{FL^3}{3EI}$	$\delta=\frac{FL^3}{12EI}$	$\delta=\frac{FL^3}{24EI}$
Torsion angle	$\varphi=\frac{TL}{GI_p}$	$\varphi=\frac{TL}{GI_p}$	$\varphi=\frac{TL}{2GI_p}$
Bending stiffness	$k_b=\frac{3EI}{L^3}$	$k_b=\frac{12EI}{L^3}$	$k_b=\frac{24EI}{L^3}$
Torsion stiffness	$k_t=\frac{GI_p}{L}$	$k_t=\frac{GI_p}{L}$	$k_t=\frac{2GI_p}{L}$

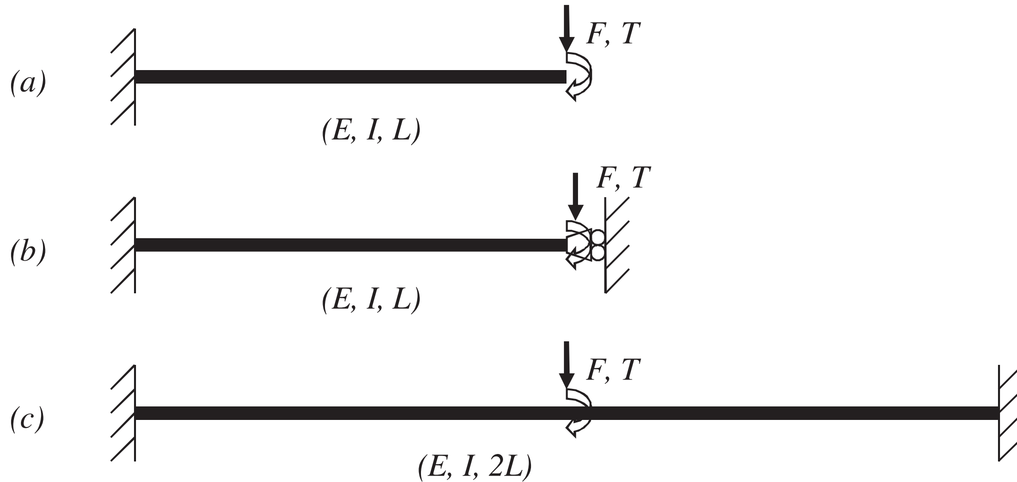

Figure 2.2 Three models of beams and their applied loads used for modeling of torsional micromirrors: (*a*) a cantilever; (*b*) a guided end cantilever; (*c*) a fixed-fixed beam.

As shown in Figure 2.1, the torsional micromirror has two long but thin beams of uniform rectangular cross-section ($l\times w\times t$, where l is the length of one of the two beams) at both sides of the micromirror. These two beams are attached to the micromirror to

form a rotational (torsion) axis for out-of-plane motion of the mirror plate. The other ends of the beams are anchored to substrate. Thus out-of-plan motion of the micromirror is actuated by electrostatic force underneath. At the same time the beam is also subjected to a resistant force or torque due to the twisted angle of the two beams resulted from electrostatic actuation. The external energy is thus balanced by the internal strain energy of the beams. We denote g_0 as an initial gap between the bottom electrode and the top micromirror; z, α as vertical displacement and torsion angle of the micromirror at location of the torsion axis, which means a mechanical system with two degrees of freedom (2-DOF); k_b and k_t as the corresponding bending and torsional spring constants; J_p and I_p as the polar mass moment of inertia of the mirror plate and the polar moment of inertia of the beams; respectively. Thus strain energy of the torsional micromirror is found as it follows,

$$U_{mech} = 2\int_0^l \left(\frac{M^2(x)}{2EI} + \frac{T^2(x)}{2GI_p} \right) d\xi + \frac{1}{2} J_p \alpha^2 \tag{2.8}$$

where moment $M(x)$ and torque $T(x)$ are the internal moment and torque at cross-section x of the beams, respectively. A fixed-to-fixed beam (length of $2l$) for the side beams is further considered.

2.2.2 Electrostatic Energy

The electrostatic or potential energy U_{elec} from the electrostatic actuation (see Figure 2.1) can be written as [165]

$$U_{elec} = \frac{1}{2} C \cdot V^2 \tag{2.9}$$

The rectangular mirror plate has dimensions of $L \times W \times t$ (the same thickness as of the beams). Thus the capacitance C between the mirror plate and bottom substrate and the potential energy are

$$C = \int_0^L dC = \int_0^L \frac{\varepsilon W dx}{g(x)} = \int_0^L \frac{\varepsilon W dx}{g_0 - z - x \sin\alpha} \\ = \frac{\varepsilon W}{\sin\alpha} \ln\left(\frac{g_0 - z}{g_0 - z - L\sin\alpha}\right) \quad (2.10)$$

$$U_{elec} = \frac{\varepsilon W V^2}{2\sin\alpha} \ln\left(\frac{g_0 - z}{g_0 - z - L\sin\alpha}\right) \quad (2.11)$$

where V is the applied electrical bias; ε is dielectric constant of the material in the space between two plates, usually air. The capacitance is derived from integration of the differential capacitance along the length, i.e., from the torsional axis (the origin) to the free end of the micromirror *(0, L)*. Some assumptions are taken into consideration, for example, the bottom electrode and the top micromirror are assumed to be overlapped exactly, and no stray loss of energy is assumed in this parallel plate electrical field.

A small torsion angle can be obtained by electrostatic actuation due to the large mirror plate and the relatively small gap of the micromirror. Thus tangential or sine of angle α is approximated as the angle itself. Thus the two formulas can be rewritten.

$$C = \frac{\varepsilon W}{\alpha} \ln\left(\frac{g_0 - z}{g_0 - z - L\alpha}\right) \quad (2.12)$$

$$U_{elec} = \frac{\varepsilon W V^2}{2\alpha} \ln\left(\frac{g_0 - z}{g_0 - z - L\alpha}\right) \quad (2.13)$$

The vertical electrostatic force F_e and the electrostatic torque T_e as shown in Figure 2.1 can then be derived from partial differentiation of the potential energy U_{elec} with respect

to displacement z according to Castigliano's first theorem and by integral of infinitesimal torque ($dT=x\times dF_e$) along the length of the micromirror, respectively. These are written as follows:

$$dF_e = \frac{1}{2}\frac{\partial(dC)}{\partial z}\cdot V^2$$

$$F_e = \frac{1}{2}\frac{dC}{dz}\cdot V^2 \tag{2.14}$$

$$F_e = \frac{\varepsilon W V^2}{2\sin\alpha}\left(\frac{1}{g_0 - z - L\sin\alpha} - \frac{1}{g_0 - z}\right) \tag{2.15}$$

$$T_e = \int_0^L dF_e.x = \frac{\varepsilon W V^2}{2\sin^2\alpha}\left(\frac{L\sin\alpha}{g_0 - z - L\sin\alpha} - \ln\frac{g_0 - z - L\sin\alpha}{g_0 - z}\right) \tag{2.16}$$

When taking into account of small torsion angle or small deformation, they can be simplified as:

$$F_e = \frac{\varepsilon W V^2}{2\alpha}\left(\frac{1}{g_0 - z - L\alpha} - \frac{1}{g_0 - z}\right) \tag{2.17}$$

$$T_e = \frac{\varepsilon W V^2}{2\alpha^2}\left(\frac{L\alpha}{g_0 - z - L\alpha} + \ln\frac{g_0 - z}{g_0 - z - L\alpha}\right) \tag{2.18}$$

2.2.3 Static Equations of Motion

The static equilibrium in a 2-D mechanical system can be expressed by static equations of motion. The static equations of the torsional micromirror in Figure 2.1 can be derived by equaling the vertical electrostatic force F_e to the vertical restoring force and equating the electrostatic torque to the mechanical resistant torque from the torsion beam, respectively:

$$K_b z = F_e, \quad K_t \alpha = T_e \tag{2.19}$$

where K_b and K_t can either be derived from partial differential of the mechanical strain energy U_{mech} in equation (2.8) with respect to corresponding deformations according to Castigliano's second theorem or from the unit-load Equation (2.7) according to Hook's law. Rigid anchorage is assumed for the fix-to-fix torsion beams in consideration of SOI based micromachining. A rigid mirror plate is considered suspended by two torsion beams at both sides. For the mirror plate itself, neither torsional deformation nor bending deformation is assumed due to the thick SCS device layer. According to Table 2.1, the static equations can be rewritten as:

$$\frac{24EI}{l^3}z = \frac{\varepsilon WV^2}{2\alpha}\left(\frac{1}{g_0 - z - L\alpha} - \frac{1}{g_0 - z}\right) \tag{2.20}$$

$$\frac{2GI_p}{l}\alpha = \frac{\varepsilon WV^2}{2\alpha^2}\left(\frac{L\alpha}{g_0 - z - L\alpha} + \ln\frac{g_0 - z}{g_0 - z - L\alpha}\right) \tag{2.21}$$

where l is the length of a side beam, L is the length of the mirror plate. The bending moment of inertia I and torsional moment of inertia I_p for a rectangular cross-section beam are provided as [166]:

$$I = \frac{wt^3}{12}, \quad I_p = \frac{wt^3}{16}\left[\frac{16}{3} - 3.36\frac{t}{w}\left(1 - \frac{t^4}{12w^4}\right)\right] \tag{2.22}$$

where width of the beam w is assumed larger than thickness t in the formula. They need to be replaced each other if thickness is larger than width. The static performance of the electrostatic actuated torsional micromirror can thus be predicted by solving the static equilibrium equations. Due to electrostatic nonlinearity, Newton-Raphson method is used to solve for these implicit nonlinear equations. The equations can be normalized by using nondimensional parameters of $Z=z/g_0$, $\acute{\alpha}=\alpha/\alpha_{cr}$ and $\alpha_{cr}=g_0/L$ as

$$\kappa_b Z = \frac{V^2}{\alpha'}\left(\frac{1}{1-Z-\alpha'} - \frac{1}{1-Z}\right) \tag{2.23}$$

$$\kappa_t \alpha' = \frac{V^2}{\alpha'^2}\left(\frac{\alpha'}{1-Z-\alpha'} + \ln\frac{1-Z}{1-Z-\alpha'}\right) \tag{2.24}$$

where $\kappa_b = \frac{2g_0^3 K_b}{\varepsilon WL}$, $\kappa_t = \frac{2g_0^3 K_t}{\varepsilon WL^3}$, $K_b = 2\times\frac{12EI}{l^3}$ *and* $K_t = 2\times\frac{GI_p}{l}$ for the two guided-end side beams. Torsion angle and vertical displacement at torsion axis under a given voltage can be solved from these two equations.

2.2.4 Static Analysis of a Torsional Micromirror

As an example, Table 2.2 provides the related material properties of silicon [167,168] and the dimensions of a torsional micromirror. Solving the derived static equations with the provided parameters yields electrostatic curves of displacement versus applied voltage as illustrated in Figure 2.3. As illustrated in Figures 2.2, the micromirror is assumed to be supported by either two identical cantilever beams or two equivalent guided-end beams. From Figure 2.3, the pull-in voltage for the cantilever supported micromirror is around $51V$ as compared to the pull-in voltage of $54V$ for the guided-end-beam supported micromirror. Due to the dominant torsional motion of the micromirror, the resultant vertical displacement at front edge of the micromirror (see Figure 2.3 (*c*)) does not show much difference before pull-in voltage. The approximate linear electrostatic phenomenon (torsion versus applied voltage) can be observed from the analytical results. In the comparison shown in Table 2.3, the guided-end beam supported micromirror has a more stiff bending or less vertical bending deflection at the torsion axis than the cantilever

supported micromirror, which results in a more linear domain of the electrostatics, as illustrated in Figure 2.3. Moreover, more bending stiffness arising from the two guided-end beams enables a more reliable micromirror. As a result, the more rigid anchorage for both side beams of the torsional micromirrors will yield more reliable suspension and this does not deteriorate the torsional flexibility. This is one of significant required features of torsional micromirrors for optical switching applications.

Table 2.2 Structural dimensions and material properties of a torsional micromirror

Micromirror $L\times W$ (μm^2)	Beam $l\times w$ (μm^2)	Thickness T, t (μm)	Gap g_0 (μm)	Young modulus E (GPa)	Poisson ratio ν	density ρ (kg/m^3)
300×200	221×10	8	12	129.5	0.21	2320

2.2.5 Pull-in Characteristics

The static equations indicate that every applied voltage corresponds to a position of the micromirror before it reaches a value where the micromirror is pulled down to the bottom electrode. This critical value of voltage is called pull-in voltage. The corresponding performance of the micromirror when it is pulled down is then called pull-in characteristics. Before pull-in, the whole micromirror is kept suspended and its behavior follows the derived static equations. However, these equations are not anymore effective after pull-in. Thus the critical values used to describe pull-in phenomenon is pull-in voltage and mirror position: torsion angle and vertical displacement at the front edge of the plate before pull-in. The prediction of the phenomenon requires a new function which is defined by combining the two static equations for the given 2-DOF system [169-172],

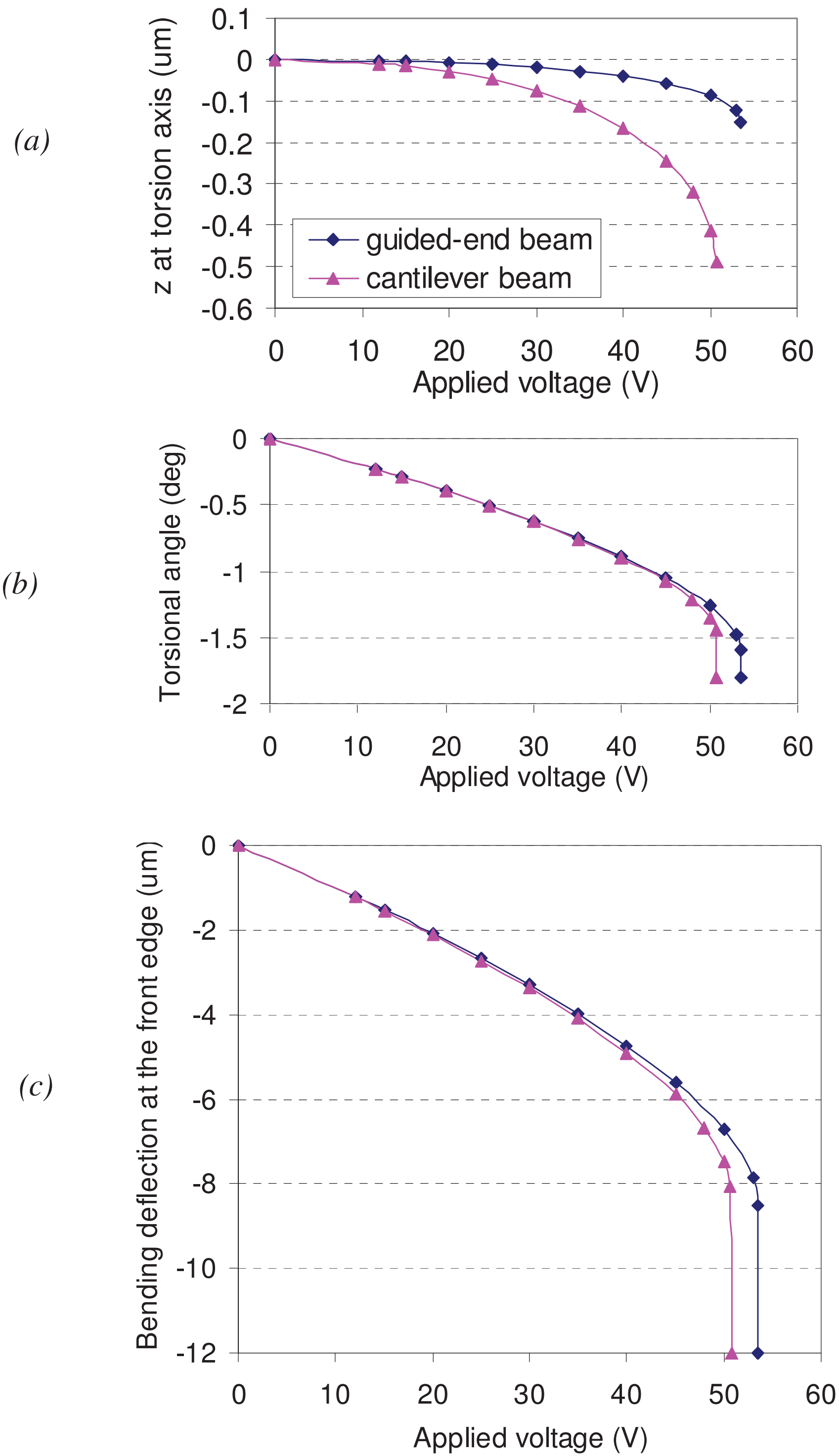

Figure 2.3 Electrostatic curves for vertical deflection versus applied voltage of a micromirror (*L*=300μm, *W*=200μm) symmetrically suspended by two guided-end beams and two cantilever beams, respectively.

$$f(\acute{\alpha}, Z)=V_1+\lambda(V_1-V_2) \qquad (2.25)$$

where λ is an arbitrary number called Lagrange's number, V_1 and V_2 are the applied voltages that are found from both equations (2.23) and (2.24), respectively,

$$V_1 = \left(\frac{\kappa_b Z\alpha'}{1/(1-Z-\alpha') - 1/(1-Z)} \right)^{1/2} \qquad (2.26)$$

$$V_2 = \left(\frac{\kappa_t \alpha'^3}{\alpha'/(1-Z-\alpha') + \ln\left((1-Z)/(1-Z-\alpha')\right)} \right)^{1/2} \qquad (2.27)$$

The pull-in status represents the extremes of the equation (2.25) that can therefore be deduced from solving the following partial differential equations

$$\partial f/\partial\alpha' = 0; \quad \partial f/\partial Z = 0; \quad V_1 = V_2 \qquad (2.28)$$

A further deduction replaces the arbitrary number λ with the differentials and Equations (2.28) such that the differential equations can be reduced to two algebraic equations as follows,

$$\frac{\partial V_1}{\partial Z}\cdot\frac{\partial V_2}{\partial\alpha'} = \frac{\partial V_1}{\partial\alpha'}\cdot\frac{\partial V_2}{\partial Z}, \quad V_1 = V_2 \qquad (2.29)$$

where $\acute{\alpha}$ and Z are the normalized torsional angle of the mirror plate and the bending displacement in the middle of the torsion axis of the micromirror. The normalized values can be obtained by solving these two implicit nonlinear equations. Newton's method that involves Jacobian matrix is employed. The pull-in characteristics can thus be obtained from these solutions. It is noted the pull-in characteristics, i.e., the pull-in voltage and the pull-in position for any given micromirror structure is a kind of build-in attribute, which is not changeable. Table 2.3 shows the resulted pull-in parameters for the torsional micromirror given in the previous section.

Table 2.3 Pull-in performance of a torsional micromirror using two models of beams

Models for beams	Pull-in voltage (V)	Normalized deflection at torsion axis	Normalized angular torsion	Deflection at torsion axis (μm)	Torsion angle (°)	Vertical deflection at front edge (μm)
Cantilever beam	50.785	0.044	0.6492	0.528	1.4879	8.3175
Guided-end beam	53.531	0.0125	0.6964	0.15	1.596	8.506

Pull-in voltage in Table 2.3 is found by substitution of the normalized pull-in deflections (Z, $\acute{\alpha}$) into either Equation (2.26) or Equation (2.27). Similarly, the actual deflections can be converted from $z=g_0\times Z$ and $\alpha= g_0\times\acute{\alpha} /L$. The resultant vertical deflection at front edge of the micromirror is calculated by geometry relation, which is equal to ($z+L\times Sin\alpha$). Different beam models for the same torsional micromirror result in a slight difference in the pull-in characteristics. As shown in Table 2.3, the difference of pull-in voltage from the two beam models for the same micromirror is around 5%. Differences of 2.2% and 6.8% for synthetic bending deflection and angular deflection are found.

The pull-in characteristics for a torsional micromirror vary with structural dimensions. Figure 2.4 shows the pull-in characteristics (mainly the pull-in voltage and the pull-in torsional angle) versus the varied width and length of the side beams (the guided-end beam models are used) for the micromirror with dimensions as it follows: the mirror plate: $L\times W$=300×200µm^2; the two rectangle side beams at length, width and thickness of $l_p\times w\times t$=200µm×10×8µm^3; the gap: g_0=12µm. It is observed from this figure that pull-in torsional angle of the micromirror decreases whereas pull-in voltage increases as the width of the beams increases. The torsional deflection is not as sensitive as pull-in

voltage to a small deviation of dimensions of the beam cross-section, which allows for higher tolerance of the beam width during fabrication. Comparatively, torsional deflection is more sensitive to length variation than to that of width of the beams. It again proves that torsional stiffness and torsional motion of these torsional micromirrors are independent on boundary conditions on the attachment of the beams to the substrate.

The actual vertical displacement of the micromirror resulted from pull-in angle is more than 10 times of the vertical displacement at the torsional axis due to the amplification effect of the mirror length to the torsion angle, although the two normalized pull-in deflections at torsion axis are in the same order [172]. The micromirror will have a dominant torsional motion when the beam width is small and short due to the strong bending stiffness and the negligible bending deflection resulted from short beams; however, bending deflection increases as the length of the beams increases, which may lead to sinking of the micromirror if the length of the straight beams is increased to a specific extent. With a long and straight torsion beam, the vertical bending deflection at torsion axis occupies around 20% of the whole gap, leaving less room for torsional deformation though it may have a low pull-in voltage.

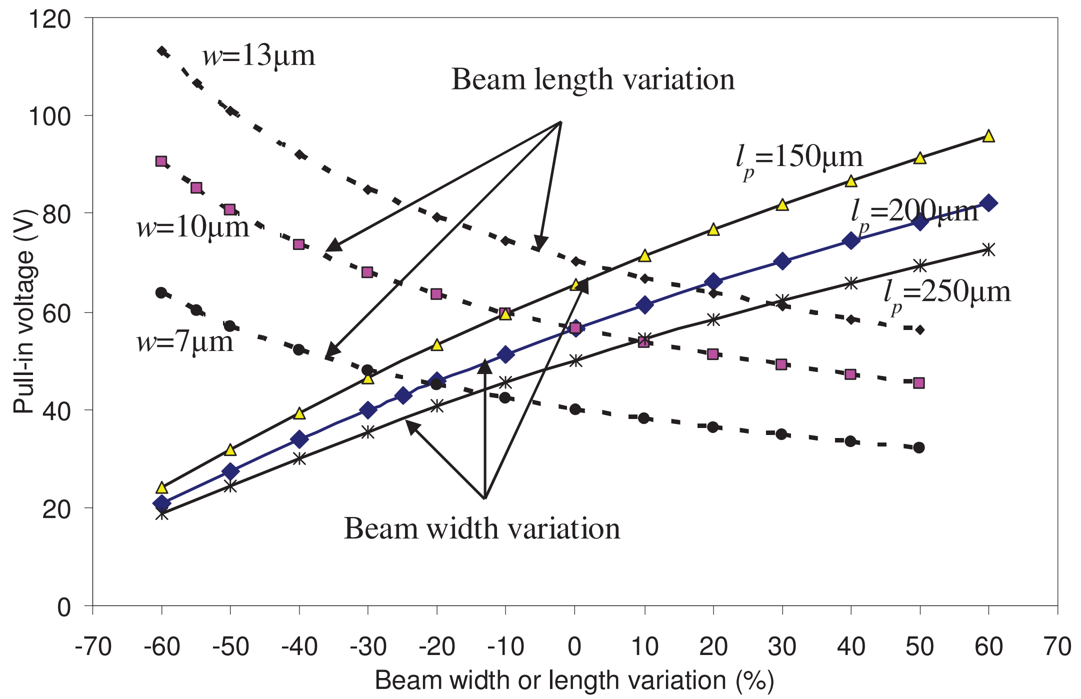

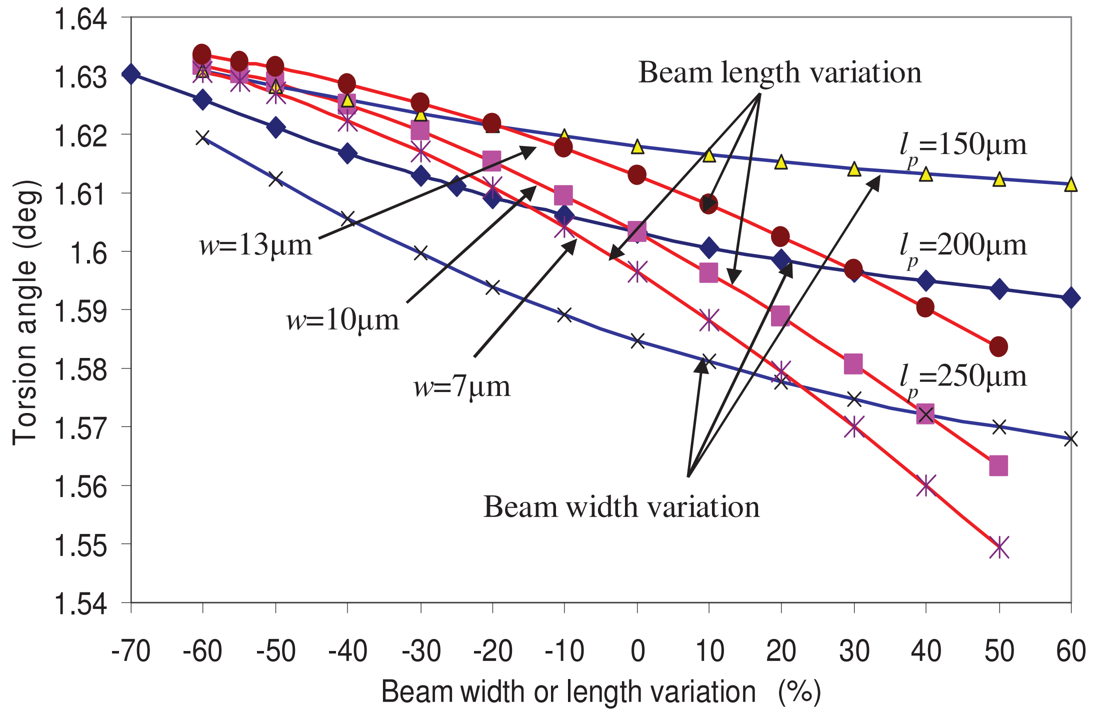

Figure 2.4 Pull-in characteristics versus variation of width of the cross-section or length of each side beam from their original dimensions (w=7µm or l_p=200µm).

2.2.6 Introduction of Dynamic Modeling Using Energy Method

In a mechanical system with n degrees of freedom, kinetic energy (T), potential (strain) energy (U) and energy dissipated (D) can be formulated when lumped-parameter method is used [173]:

$$T = \frac{1}{2}\sum_{i=1}^{n}\sum_{j=1}^{n} m_{ij}\dot{q}_i\dot{q}_j \tag{2.30 a}$$

$$U = \frac{1}{2}\sum_{i=1}^{n}\sum_{j=1}^{n} k_{ij}q_i q_j \tag{2.30 b}$$

$$D = \frac{1}{2}\sum_{i=1}^{n}\sum_{j=1}^{n} C_{ij}\dot{q}_i\dot{q}_j \tag{2.30 c}$$

where m_{ij} is inertia coefficient or generalized mass; k_{ij} is stiffness coefficient or the generalized stiffness, and C_{ij} is the generalized damping coefficient, while q_i and q_j represent the ith and jth coordinates. These generalized coefficients are deduced with respect to their corresponding deflections. For example, the generalized masses m_{ij} in any direction of motion can be expressed by lumped parameter method as

$$m_{ij} = \sum_{p=1}^{N} m_p \phi_i(x_p)\phi_j(x_p) \tag{2.31}$$

or

$$m_{ij} = \int \phi_i(x)\phi_j(x)dm \tag{2.32}$$

where N is the number of the lumped masses (m_p) in a continuous structure. This function gives the effective mass or the equivalently lumped mass for a specified point in the structure. $\emptyset_i$ and $\emptyset_j$ are the assumed i^{th} and j^{th} elastic deformation forms (normal mode shapes) that satisfy the related boundary conditions. Modal analysis is an important work

in dynamic modeling which includes solving for the mode shapes and the corresponding natural frequencies. The mode shape *u(x, t)* or the general displacement at position *x* for any degree of freedom is represented by

$$u(x,t) = \sum_{i=1}^{N} \phi_i(x) q_i(t) \tag{2.33}$$

where *u(x,t)* can be the vertical bending *z(x, t)* or torsion motion *α(x, t)* with time *t*. They can be rewritten correspondingly, such as $z(x,t) = \sum_{i=1}^{N} z_i(x) q_i(t)$ for bending motion and $\alpha(x,t) = \sum_{i=1}^{N} \alpha_i(x) q_i(t)$ for torsion motion for the given example shown in Section 2.2.2 if it is lumped as *N* masses in the system. The natural frequencies of a mechanical system can be solved through application of Rayleigh method, which states that the the maximum kinetic energy equals to the maximum strain or potential energy,

$$T_{\max} = U_{\max} \tag{2.34}$$

Thus the natural frequency for a mode of motion can be derived by this energy conservative rule as

$$\omega^2 = \frac{U_{\max}}{T^*_{\max}} \tag{2.35}$$

where *ω* is the resonant frequency or eigen-frequency of the structure. The expression of ω^2 is also called Rayleigh's quotient.

Stiffness coefficients k_{ij} in Equation (2.30) can be represented with respect to their coordinates of motion as follows.

$$k_{ij} = \int EI z_i''(x) z_j''(x) dx \quad \text{(for bending mode)} \tag{2.36}$$

$$k_{ij} = \int GI_p \alpha_i''(x)\alpha_j''(x)dx \quad \text{(for torsion mode)} \tag{2.37}$$

The generalized damping coefficient C_{ij} has to be considered in dynamic modeling if squeeze damping effect of the air film between the top mirror plate and the bottom electrode is taken into account. For low frequency applications, this air film can be neglected due to the low velocity of vibration on tilting mirror plates. However, for high frequency applications, the squeeze damping effect in the out-of-plane motion micromirrors is not negligible. It dissipates some energy if the mirror plate is large and works in a high frequency of vibration. The air film is squeezed and released at high frequencies of oscillation, thus it behaves as an air spring to the mirror plate. The energy U_d dissipated by air squeeze film damping is represented by

$$U_d = c\int \dot{x}dx \tag{2.38}$$

where c is damping coefficient, $\dot{x}$ is the squeezing velocity at position of x. However in most applications of torsional micromirrors that target low drive voltages with large torsion angles, the dissipative effect from squeeze damping can be neglected [174, 175].

For an n-DOFs (n degrees of freedom) system, Lagrange's equations of motion is shown as follows in terms of kinetic energy, potential energy and work that are associated with generalized coordinates:

$$\frac{d}{dt}\left(\frac{\partial L}{\partial \dot{q}_i}\right) - \frac{\partial L}{\partial q_i} = Q_i \qquad i = 1,2,\cdots,n \tag{2.39}$$

The Lagrange's equations of motion for a system that has only viscous damping can be written as

$$\frac{d}{dt}\left(\frac{\partial L}{\partial \dot{q}_i}\right)-\frac{\partial L}{\partial q_i}+\frac{\partial U_d}{\partial \dot{q}_i}=0 \qquad i=1,2,\cdots,n \tag{2.40}$$

The free vibration for a conservative mechanical system without energy dissipation by damping can be further simplified as

$$\frac{d}{dt}\left(\frac{\partial T}{\partial \dot{q}_i}\right)-\frac{\partial T}{\partial q_i}+\frac{\partial U}{\partial q_i}=0 \qquad i=1,2,\cdots,n \tag{2.41}$$

where $L=T-U$ is the Lagrangian operator; T is the total kinetic energy stored in the masses of the mechanism by virtue of their velocities; U is the potential energy stored in the form of strain energy in the system that arises from conservative forces; U_d is the energy dissipation (which is a kind of potential energy) by viscous damping in the system; and Q_i is the generalized non-conservative force. Various dynamic reponses can thus be solved.

For the typical example shown in Figure 2.1, two degrees of freedom (z and α) are chosen to represent for vertical bending motion and torsion angle with respect to the torsional axis of the micromirror. The axial displacement along the torsion beams is assumed negligible according to the structure. The equivalent graph for dynamic responses can be approximated in Figure 2.5.

By means of lumped-parameter method, the generalized parameter for the continuous torsion beam m_{eff} is lumped to the mid-point of the beam with respect to the coordinate z. And the effective mass of the torsion beam with respect to torsional displacement at the mid-point can be neglected due to its small amount compared to the polar moment of

inertia of the mirror plate. Therefore the kinetic energy and potential energy of the system are written as:

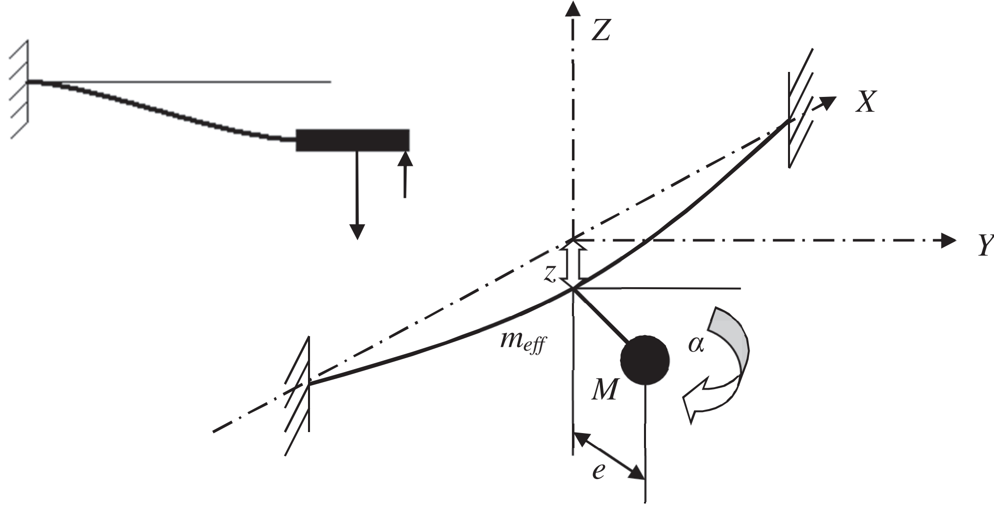

Figure 2.5 An equivalent graph of the 2-DOF system for the given torsional micromirror used in the dynamic analysis

$$T = \frac{1}{2}\sum_{i=1}^{2}\sum_{j=1}^{2} m_{ij}\dot{z}\dot{\alpha} = \frac{1}{2}M(\dot{z} + e\dot{\alpha})^2 + \frac{1}{2}J\dot{\alpha}^2 + \frac{1}{2}m_{eff}\dot{z}^2 \quad (2.42)$$

$$U = \frac{1}{2}K_t\alpha^2 + \frac{1}{2}K_b z^2 \quad (2.43)$$

where m_{ij} is the generalized mass matrix; e is the eccentric distance of c.g of the mass of the mirror plate to the torsion axis; M is the mass of the mirror plate; J is the polar moment of inertia of the mirror plate with respect to its midpoint along the length with an assumption of the uniformly distributed mass; m_{eff} is the equivalent mass of the beams at the mid point; K_t and K_b are the stiffness constants of torsion and bending modes of the torsion beam. The kinetic energy for the rotation of the beams is neglected as the polar moment of inertia of the beams is very small compared to that of the plate.

The equivalent mass of the torsion beam with respect to displacement z is obtained based on an assumption of a fourth order polynomial of the normal mode shape for bending motion of the beam. The boundary conditions for clamped beams in this case can be expressed by:

$$\begin{cases} z(0,t) = z'(0,t) = 0 \\ z(1,t) = z'(1,t) = 0 \\ z(0.5,t) = z_{\max} \\ z'(0.5,t) = 0 \end{cases} \tag{2.44}$$

where $z(\xi,t) = z(\xi)q(t)$, $\xi = x/2l$ and $q(t)$ is a load excitation; the micromirror plate is assumed to be a rigid body lumped to the central point of the mirror plate. The normal mode shape for bending motion of the beam is then deduced as:

$$z(x) = z_{\max}\left(-\frac{4x^2}{l^2} + \frac{8x^3}{l^3} - \frac{3x^4}{l^4}\right) \tag{2.45}$$

Therefore m_{eff} is obtained

$$m_{eff} = \int z^2(x)dm = 2\rho A\int_0^l z^2(x)dx = \frac{22}{105}\rho A l z_{\max}^2 \tag{2.46}$$

Substitution of the above functions into functions (2.42) and (2.43) gives the kinetic and strain energies. The equations for free vibration of the micromirror can then derived by substituting these energy expressions into Equation (2.41):

$$\begin{cases} (M + m_{eff})\ddot{z} + Me\ddot{\alpha} + K_b z = 0 \\ Me\ddot{z} + (J + Me^2)\ddot{\alpha} + K_t\alpha = 0 \end{cases} \tag{2.47}$$

The natural frequencies or the eigen-frequencies of the system can be obtained from the following equation of determinant:

$$|\Delta(\omega)| = \begin{vmatrix} K_b - (M + m_{eff})\omega^2 & -Me\omega^2 \\ -Me\omega^2 & K_t - (J + Me^2)\omega^2 \end{vmatrix} = 0 \tag{2.48}$$

where ω is the natural frequency of the system. For inertial applications such as micro-accelerometers, the excitation is a force caused by multiplication of the proof mass M of the mirror plate and the unknown acceleration a. The amplitude of the forced vibrations can be predicted by

$$[\Delta(\omega)]\begin{Bmatrix} Z \\ \alpha \end{Bmatrix} = \begin{Bmatrix} F_z \\ 0 \end{Bmatrix} \tag{2.49}$$

where $F_z = M.a$. Application of an electrical bias to the micromirror, it can be shifted and works in a desired electrostatic range and the initial position of the micromirror is thus preset at (z_0, α_0). The external excitations disturb it and induce a new balance or vibration to the system. The dynamic transition or harmonic vibration can be obtained through solving the above equations.

2.2.7 Structural Effects on Compliant Beams

Electrostatic nonlinearity has been demonstrated in the electrostatic formulation, whereas the structural linearity is always assumed and other structural effects are neglected in the previous discussions. However structural nonlinearity may arise from either large deflection or compliant members involved in a framed structure and has significant effects on the actual performance of the structure [176]. As a result, assumption of linearity may distort the predictions and cause failure of modeling. The following sub-section discusses the relevant issues associated with structural nonlinearity of beams such as large deflection, deflection due to shear strain, stiffening effect due to axial force and loosening effect due to shear force.

2.2.7.1 Large Deflections

The exact expression for bending displacement of a linearly elastic beam (an Euler-Bernoulli beam) is provided in the equation

$$\frac{y''}{\left(1+y'^2\right)^{3/2}} = -\frac{M}{EI} \tag{2.50}$$

where y is bending deflection of the beam, and y'' $(=d^2y/dx^2)$ is the second-order differential of the deflection with respect to the axial position x; M is the internal moment of bending at cross-section x; EI is the flexural rigidity of the beam. For small displacements, the slope dy/dx is small, thus $(dy/dx)^2$ is negligible. However this term becomes comparable when large deflection occurs. The nonlinear equation (2.50) can be solved approximately using either the conventional elliptic integrals or the numerical programs such as MathCAD or MatLab. Analytical methods in dealing with such nonlinearity due to large deflection have been approached, which include but do not limit to Chain Algorithm (CA), Pseudo-Rigid-Body Model (PRBM), and finite element method (FEM). The essential of these analytical methods is to split compliant beams into a few segments, in which the separation of two or three segments is used in PRBM method and separation of several segments is used in CA method. Each segment can thus be linearized and applied the linear beam theory for analysis. The load-displacement relation is therefore obtained by synthesis of all individual segments.

2.2.7.2 Effect of Shear Strain

Shear strain is usually very small and negligible as compared to other flexural deflections on a beam if its length is long or its cross-section is thin. This kind of beams usually belongs to Euler-Bernouli type of beams. However if the length-to-thickness ratio is less than 3-5 [177, 178], the shear strain incurred by the shear force component is comparable to bending due stress. This kind of beams is called Timoshenko beams [166]. The shear deflection at the free end of a cantilever subjected to a vertical force F at the same location can be written according to Castigliano's theorem as

$$y_s = \frac{f_s\, l}{GA} F \tag{2.51}$$

where f_s is a coefficient concerning the shape of the cross-section. As a comparison, the bending deflection due to the vertical force is

$$y_b = \frac{l^3}{3EI} F \tag{2.52}$$

The ratio of deflections can thus be written as [179]

$$\frac{y_s}{y_b} = \frac{6 f_s\,(1+\mu) I}{A l^2} = \frac{f_s (1+\mu)}{2} \left(\frac{t}{l} \right)^2 \tag{2.53}$$

Therefore an error may be generated if the Euler-Bernouli beam theory is used in the analysis of short beams. If an acceptable range of errors (e) is taken from 1% to 5% (e=y_s/y_b), the ratio of beam length-to-thickness (l/t) can be from 3 to 9. This result tells that if the length of a beam is 9 times or more than its thickness, the effect of shear strain on accuracy of deflections can be ignored.

The accuracy of displacement may be enhanced by including the term of shear if the ratio of length-to-thickness drops between 3 and 9. A full expression of bending deflection of a beam using unit-load method was derived and rewritten as follows [157]

$$\Delta = \int \frac{N_U N_L dx}{EA} + \int \frac{M_U M_L dx}{EI} + \int \frac{f_s V_U V_L dx}{GA} + \int \frac{T_U T_L dx}{GI_p} \tag{2.54}$$

where the cross-section coefficient f_s is derived as

$$f_s = \frac{A}{I^2} \int_A \frac{Q^2}{w^2} dA$$

$$Q = \frac{w}{2} \left(\frac{t^2}{4} - y_1^2 \right)$$

For a rectangular cross-section beam of width and thickness of $w \times t$, the coefficient is

$$f_s = \frac{144}{wt^5} \int_{-t/2}^{t/2} \frac{1}{4} \left(\frac{t^2}{4} - y_1^2 \right)^2 w dy_1 = \frac{6}{5} \tag{2.55}$$

2.2.7.3 Stiffening or Loosening Effect by Axial or Shear Force

Involvement of axial loads along a beam may also affect accuracy of analytical results. Although the axial strain in a straight beam subjected to an axial load may be very small and negligible, the axial or longitudinal stress thus incurred in the beam may stiffen the beam itself, which may result in higher stiffness in other flexural deflections [180]. This can be illustrated as follows and in Figure 2.6. The axial force in a side beam of the structure is derived as

$$P_e = \frac{F_e}{2 \sin \varphi} \approx \frac{F_e}{2} \frac{l}{z} \tag{2.56}$$

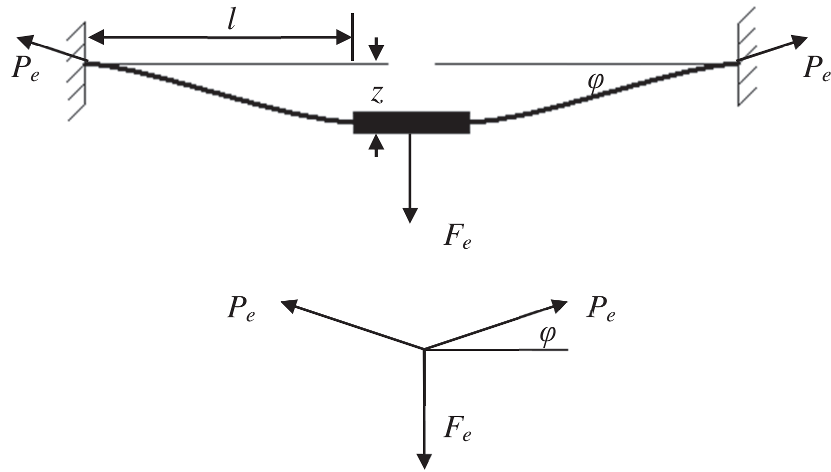

Figure 2.6 The force diagram representing for the stiffening effect incurred by the axial loads in a beam.

Equation (2.56) indicates a larger axial pulling force P_e can be resulted from a smaller vertical deflection in the conjunction of the two symmetric side beams. The differential equations of bending deflection for the two side beams can be written respectively as

$$EI\frac{d^2z}{dx^2} = P_e\cos\varphi \cdot z - P_e\sin\varphi \cdot x \doteq P_e \cdot z - \frac{F_e}{2} \cdot x \tag{2.57 a}$$

$$EI\frac{d^2z}{dx^2} = -P_e\cos\varphi \cdot z + P_e\sin\varphi \cdot (2l - x) \doteq -P_e \cdot z + \frac{F_e}{2} \cdot (2l - x) \tag{2.57 b}$$

The maximum deflection occurs at the central joint for the two side beams and can be derived as:

$$z_{\max} = \frac{F_e l^3}{24EI} \cdot \frac{\tan u - u}{\frac{1}{3}u^3} \tag{2.58}$$

where the coefficient u is proportional to the axial force P_e; z_{max} is the vertical deflection of the central joint. The bending stiffness of the micromirror located at the central joint can be thus deduced as:

$$K_b = \frac{24EI}{L^3} \cdot \frac{\frac{1}{3}u^3}{\tan u - u} \quad (2.59)$$

As compared to the corresponding stiffness in Table 2.1, it can be concluded that there exists a stiffening effect on the bending of the beam due to the axial force in the beam, though this force is actually transferred from the applied lateral loads, such as the electrostatic force applied on the micromirror. However, loosening effect due to a shear force in a short beam can be demonstrated from the following deductions for Tomoshenko beams [180]. The equivalent shear force $V_{i,eq}$ in the ith short beam is deduced from the applied shear force V_i by

$$V_{i,eq} = \frac{V_i}{1 - \alpha_i} \quad (2.60)$$

where the coefficient α_i is defined by

$$\alpha_i = \frac{P_i (2L_i)^2}{E_i I_i \pi^2} \quad (2.61)$$

where P_i is the axial force; $E_i I_i$ is the flexural rigidity and L_i is length of the beam. The bending deflections can thus be approximated by using linear beam theory:

$$\delta_{z,i} = \frac{1}{E_i I_i} \left(\frac{V_{i,eq} L_i^3}{3} + \frac{M_i L_i^2}{2} \right) \quad (2.62)$$

$$\theta_i = \frac{1}{E_i I_i} \left(\frac{V_{i,eq} L_i^2}{2} + M_i L_i \right) \quad (2.63)$$

where $\delta_{z,i}$ is the bending displacement; θ_i is the bending slope and M_i is the bending moment at the calculation point of the beam. The errors in these approximations increase as the axial force P_i increases. The calculated displacements are a bit larger than the results using linear beam theory, leading to the loosening effect of the beam. However,

because of the high strength of silicon beams, this loosening effect is usually negligible in MEMS. Nevertheless, longitudinal stiffening effect has to be considered in modeling and in the estimation of MEMS consisting of compliant beams.

2.3 Linear Matrix Method for Framed Micro-Mechanisms

Matrix method is named such because the basic term used in analysis of mechanics is the mathematical matrix. Matrix method is a compact mathematic expression describing the mechanical performance of every individual member in a framed structure with multiple degrees of freedom (DOF's). Structural linearity is assumed during applications of this method. Flexibility matrix or stiffness matrix is used as the terms in the derived equations. This method is easy to be computerized and thus is powerful in dealing with complicated structural problems. In macro world, a lot of examples involve mechanical frames such as bridges, buildings, etc. However, only in recent years, the planar framed microstructures for suspensions of micromirrors or microplatforms are reported [158, 165 and 179]. The matrix method has just been recently used in analysis of micro-framed structures. Therefore this section will start with an introduction of planar framed microstructures and the origin of matrix method. This will be followed by a review on flexibility matrix and stiffness matrix methods and their applications.

2.3.1 Planar Framed Microstructures

The framed microstructures are made of various beam members. According to the degree of freedom (DOF) for individual beams, they can be divided into a few types: 1) the axial beam, which is also called truss; this type of beams is subjected to axial force and strain only; 2) the in-plane framed beam; each beam has three degrees of freedom, that is, axial, in-plane lateral and in-plane moment; 3) the in-plane grid beam; each has the three DOFs as in the second type plus an axial torsion; and 4) the spatial framed beam; each beam has the complete six DOFs.

Because of the sophisticated surface micromachining technologies, more and more planar framed microstructures are fabricated for various applications. These microstructures are made of beams and plates or of laminated structures. Suspended by a beam or a group of beams as suspension, a proof mass microplate can move up and down by an actuation. A planar grid can thus be formed if many beams are entirely connected with each other in a plane. This is the third case that has been above mentioned. Figure 2.8 shows some examples of micro planar grids. Connection of beams can take the form of a serial chain or the parallel attachment to the mass plate.

A beam segment discussed hereafter is such that it has two nodes at both ends and is substantially longer than the width. A single beam is recognized by the three features: 1) its uniform cross-section; 2) its straightness in length and 3) no intersection along the length. In other words, a curved beam is thus recognized as a formation of multiple beam

segments. Two or more series of beams can join together to form a strengthened frame (see Figure 2.7 (*g*)). The intersection of chains is called *joint* whereas the intersection between two neighbor beams is defined a *node*. The mirror or platform in the frames can be recognized as a joint because of its rigidity compared to its framed suspensions. These rigid joints or nodes distribute and transfer the internal strains and the external loads continuously and throughout the structure.

As mentioned, an in-plane grid is made of in-plane beams and plates and is more inclined to out-of-plane motion. External loads are applied on the structure either along the plane of the grid or along the normal direction to the plane. Such loading direction may lead to in-plane or lateral movement and out-of-plane motion for any beam in the grid. The two in-plane lateral deflections and torsion may be neglected for a beam in a grid composition of beams and joints that are perpendicular to each other, thus it remains only three out-of-plane deflections due to vertical force and bending moment and out-of-plane torque (see Figure 2.8). This planar structure can be called an in-plane rectangle grid, which is a known microstructure for micromirrors or microplatform. Some examples can be found in Figure 2.7 and the coordinates system of the three deflections is shown in Figure 2.8 (*a*). Though these planar framed microstructures can be easily fabricated using SOI based micromachining techniques, modeling or analysis represents a challenge.

2.3.2 Matrix Method Origination

The mathematical matrix method is powerful in analysis of framed structures. Physically it is originated from the energy conservation principle. The strain energy of any framed structure can be expressed in terms of individual displacements or in terms of loads and redundant forces and given by [163],

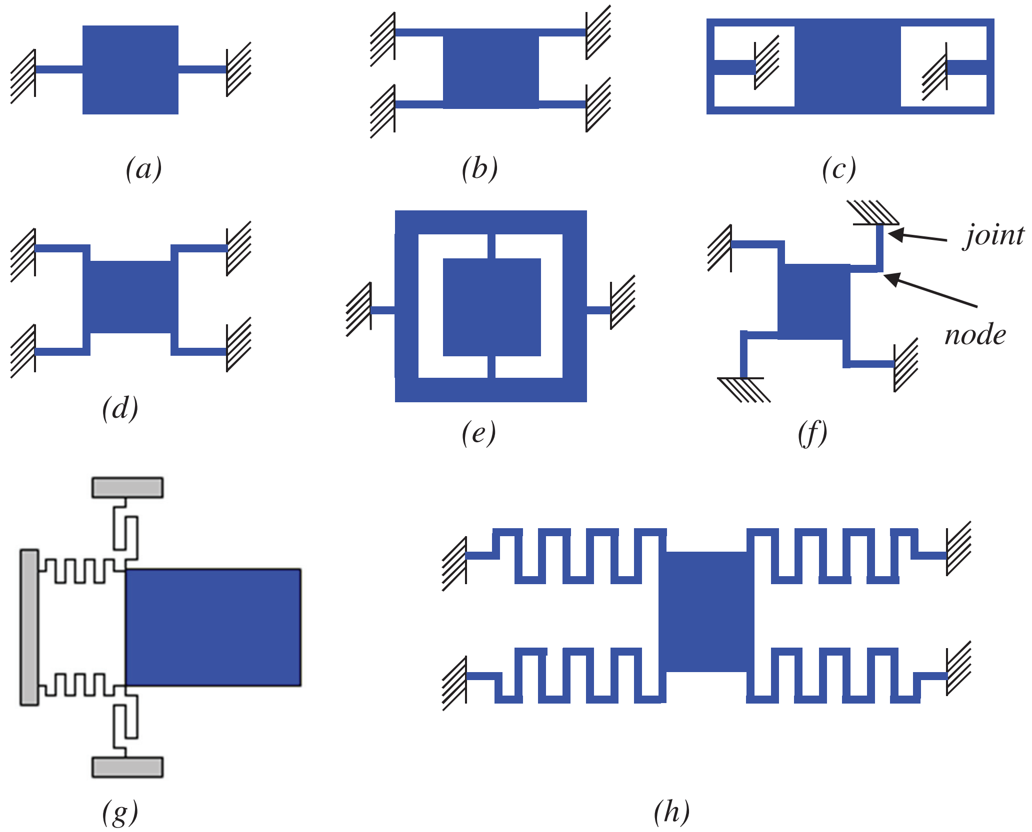

Figure 2.7 Various planar framed microstructures made of beams and plates.

$$U = a_{11}D_1^2 + a_{12}D_1D_2 + \ldots + a_{1n}D_1D_n + a_{21}D_2D_1 + a_{22}D_2^2 + \ldots + a_{2n}D_2D_n + \ldots + a_{n1}D_nD_1 + a_{n2}D_nD_2 + \ldots + a_{nn}D_n^2 \tag{2.64}$$

or

$$U = b_{11}P_1^2 + b_{12}P_1P_2 + \ldots + b_{1n}P_1P_n + b_{21}P_2P_1 + b_{22}P_2^2 + \ldots + b_{2n}P_2P_n$$
$$+ \ldots + b_{n1}P_nP_1 + b_{n2}P_nP_2 + \ldots + b_{nn}P_n^2 \quad (2.65)$$

where the a's and the b's are the geometric dependent constants derived from the configuration of the structure; the D's and the P's are the individual displacements and their corresponding loads or redundant forces on the joints and the nodes of the structure. A general form of matrix equations can be derived by Castigliano's first and second theorems as,

$$\{D\} = [C]\{P\} \quad (2.66)$$

$$\{P\} = [S]\{D\} \quad (2.67)$$

where [C] in the first equation is called flexibility or compatibility matrix and [S] in the second equation is the stiffness matrix with size of $n \times n$, whereas {D} and {P} in the equations are the arrays of displacements and loads with an order of $n \times 1$, respectively. The flexibility matrix [C] and the stiffness matrix [S] relate displacements {D} to the actions (loads and reactions) {P} at joints or nodes. Either of the two matrices is the inverse of the other, provided that the same set of loads, reactions and displacements is employed. Each flexibility member C_{ij} in [C] represents the displacement at joint i that is caused by a unit load or a reaction force P_j applied at joint or node j. Similarly each stiffness member in [S] represents the action or reaction force (loads or reactions) due to a unit displacement. Involving either matrix [C] or matrix [S] in the analysis of frames thus leads to two different matrix methods, that is, the flexibility matrix method and the stiffness matrix method.

2.3.3 Flexibility Matrix Method

The flexibility matrix is determined by material properties and the set of joints and nodes in a frame. The standard form of the flexibility matrix C for a beam member in the previously mentioned in-plane rectangle grid can be given as [164]:

$$C_{mi} = \begin{bmatrix} C_{11} & C_{12} & C_{13} \\ C_{21} & C_{22} & C_{23} \\ C_{31} & C_{32} & C_{33} \end{bmatrix} = \begin{bmatrix} \frac{L}{GJ} & 0 & 0 \\ 0 & \frac{L}{EI} & \frac{L^2}{2EI} \\ 0 & \frac{L^2}{2EI} & \frac{L^3}{3EI} \end{bmatrix} \tag{2.68}$$

where the subscript mi in C_{mi} mean the ith beam member; L is the length of the beam; E and G are the elastic modulus and shear elastic modulus of the material; I represents the cross-sectional moment of inertia with respect to the z-axis. Figure 2.9 shows the corresponding free body diagrams of the action forces and the corresponding displacements for this kind of beam members. Indication for each member in flexibility matrix is shown in Figure 2.9 from *(b)* through *(d)* under a unit load.

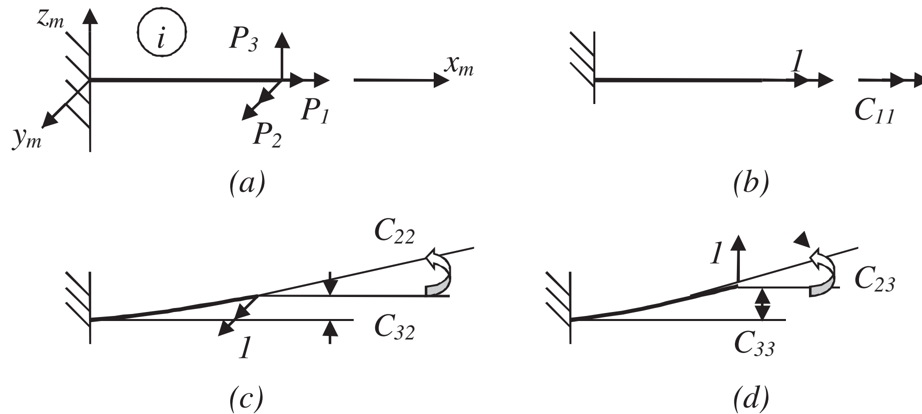

Figure 2.8 Free body diagrams of the flexibility matrix terms for a beam member in an in-plane rectangle grid.

The flexibility matrix for all beam members (n) in the grid can thus be assembled according to the arrangement of joints and nodes. The general static equations of motion can be derived in the following form:

$$\begin{Bmatrix} D_j \\ D_r \end{Bmatrix} = \begin{bmatrix} C_{jj} & C_{jr} \\ C_{rj} & C_{rr} \end{bmatrix} \begin{Bmatrix} P_j \\ P_r \end{Bmatrix} \tag{2.69}$$

where D_j, D_r and P_j, P_r are the displacements and loads at all movable joints and restraint joints in the structure, and C_{jj}, C_{jr}, C_{rj} and C_{rr} are sub-matrices or terms of the general flexibility matrix that show the displacement at joint j or restraint joint r when a unit load (reaction or external load) applied at the joint j or the restraint joint r, respectively. Therefore the deformation at any desired joint or node in the framed structure can be solved. The detail deduction of flexibility matrix method can be found in [163].

For the example given in the previous section (see Figures 2.1 and 2.5), there is a torque applied at the mid-point of the torsion axis due to electrostatic actuation of the micromirror and thus a torsional angular displacement is considered and denoted as α. The bending displacement z at the same location is also resulting from the electrostatic force. These two deformations (z, α) are able to fully define the movement of the micromirror. The equations of motion can be deduced using the flexibility matrix as

$$\begin{Bmatrix} z \\ \alpha \end{Bmatrix} = \begin{bmatrix} \dfrac{l^3}{6EI_y} & 0 \\ 0 & \dfrac{l}{2GI_p} \end{bmatrix} \begin{Bmatrix} F_e \\ T_e \end{Bmatrix} \tag{2.70}$$

where l is the length of a side beam; I_y and I_p are the cross-sectional moment and polar moment of inertia of the beams, respectively.

2.3.4 Stiffness Matrix Method

In an in-plane rectangle grid, any beam segment can be recognized as a cantilever beam with one free end and the other end fixed. This free end acts at the same time as the fixed end for the next beam segment, and the fixed end is the free end for the previous beam segment. Stiffness constant is equal to the magnitude of the force that is required to perform unit displacement and the following *3*×*3* stiffness matrix is thus resulted for a beam member in the planar rectangle grid as:

$$K_{mi} = \begin{bmatrix} \frac{GJ}{L} & 0 & 0 \\ 0 & \frac{4EI}{L} & -\frac{6EI}{L^2} \\ 0 & -\frac{6EI}{L^2} & \frac{12EI}{L^3} \end{bmatrix} \tag{2.71}$$

where L is the length of the beam; I and J are the cross-sectional and polar moments of inertia of the beam with respect to bending displacement and torsion, respectively; G and E are the shear modulus and Young's modulus of the beam, respectively.

If the grid is composed of m beam segments, the complete joint stiffness matrix K_j can be derived from multiplication of the stiffness matrices as it follows:

$$K_j = B_{mj}^T K_m B_{mj} \tag{2.72}$$

where

$$K_m = \begin{bmatrix} k_{m1} & 0 & 0 & 0 & 0 \\ 0 & \ldots & 0 & 0 & 0 \\ 0 & 0 & k_{mi} & 0 & 0 \\ 0 & 0 & 0 & \ldots & 0 \\ 0 & 0 & 0 & 0 & k_{mm} \end{bmatrix} \tag{2.73}$$

with K_m the unassembled matrix consisting of the diagonally arranged sub-matrices K_{mi}; and K_{mi} the stiffness matrix for the individual beam i. The structural matrix B_{mj} is constructed according to the arrangement of joints and nodes in the structure. It helps to transform the member matrix K_m to the joint matrix K_j. The structural matrix relates joint deflections with member deflections as:

$$D_m = B_{mj} D_j = \begin{bmatrix} B_{mf} & B_{mr} \end{bmatrix} \begin{bmatrix} D_f \\ D_r \end{bmatrix} \tag{2.74}$$

where D_m is an array of displacements for all beams at their ends; D_j is an array of displacements for all joints. D_j can be divided into two sub-matrices, D_f and D_r as shown in (2.74), where D_f is the array of displacements for joints that can move freely, whereas D_r is for the joints that have restraints. B_{mj} is determined from the structural compatibility of all members in the grid and can be partitioned into two sub-matrices B_{mf} and B_{mr}. Each column in B_{mf} contains displacements of all members due to a unit displacement performed on a free joint. Each column in the sub-matrix B_{mr} consists of all member displacements due to a unit displacement that occurred at a restraint joint in the structure. The indication for each member in a 3×3 stiffness matrix is shown in Figure 2.9.

The stiffness matrix K_j after assembled can further be partitioned into four sub-matrices; and the equations of motion in matrix form can be written as,

$$\begin{bmatrix} F_f \\ F_r \end{bmatrix} = \begin{bmatrix} K_{ff} & K_{fr} \\ K_{rf} & K_{rr} \end{bmatrix} \begin{bmatrix} D_f \\ D_r \end{bmatrix} \tag{2.75}$$

where $K_{ff}= B_{mf}^T K_m B_{mf}$, $K_{fr}= B_{mf}^T K_m B_{mr}$, $K_{rf}= B_{mr}^T K_m B_{mf}$, $K_{rr}= B_{mr}^T K_m B_{mr}$. Displacements at all free joints can be solved by

$$D_f = K_{ff}^{-1}(F_f - K_{fr}D_r) \tag{2.76}$$

The displacements at restraint joints are usually equal to zero, i.e., $D_r=0$; thus stiffness matrix K_{ff} can be formulated for the complete stiffness matrix of the grid.

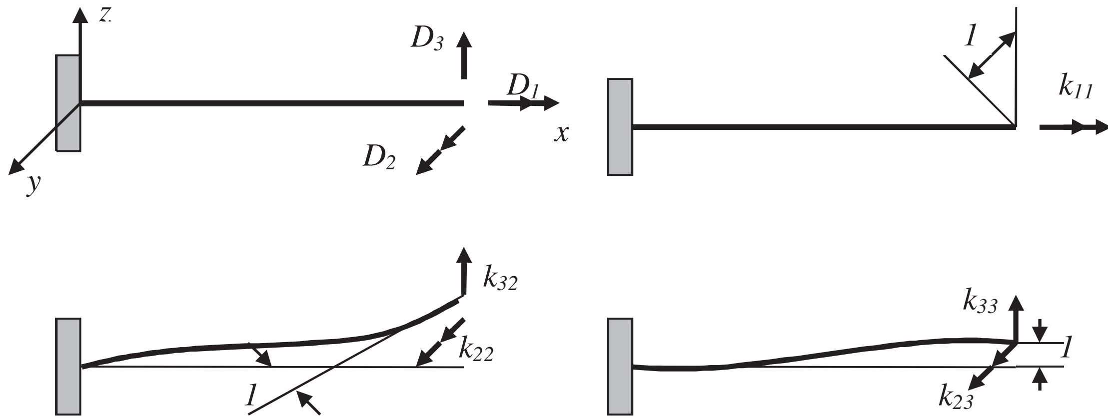

Figure 2.9 Indications of the related terms in a stiffness matrix for a planar frame beam member. k_{11} is the axial stiffness of the beam against the torque; k_{32} and k_{22} are the stiffness constants resisting the angular displacement due to the force along z-axis and the bending moment along y-axis; k_{33} and k_{23} are the stiffness constants resisting the vertical force and the bending moment along y-axis.

2.4 Pseudo Rigid Body Model Method

The pseudo rigid body model (PRBM, hereafter) could be used to approximate a lengthy beam in a framed mechanism for analysis and was reported in literature in the past decade [122, 123, 179 and 181]. It is one of analytical methods dealing with structural nonlinearity due to large deflections. Thus in this section a detailed review of PRBM method is given first, then an analysis using this method for the typical example given in Figure 2.1, the torsional micromirror suspended by two side beams is provided.

2.4.1 Pseudo Rigid Body Model

Pseudo rigid body model method aims to solve the load-displacement relations for mechanisms involved with compliant beam members. In general, PRBM method usually separates a lengthy beam into two or three beam sections and uses one or two spring constants to approximate the deformations in the beam. This method has been reported to solve for load-displacement relations in compliant mechanisms made of compliant hinges at macro size [179]. The use of PRBM method for the analysis of micromechanisms capable of out-of-plane motions with compliant beams represents one of the contributions of this work.

The performance of a cantilever subjected to a bending moment can be expressed by Bernoulli-Euler equation as shown in Equation (2.50), where the square term $(y')^2$ can not be neglected in large deflection analysis of beams. Instead this kind of beams can be assumed to comprise two or three rigid links that are connected with each other by virtual pivots. This is the main theory on which the PRBM method is based on.

Depending on different loading conditions at the free end of a cantilever, models with two and three separations respectively of the cantilever are used in PRBM method. The two separation model is constructed by one short link, one long link and a pivot as shown in Figure 2.10 (*c*). The ratio of the short and long segments is defined below based on the best match to the possible deflection due to the applied load. This model represents a cantilever deflected by a vertical force with or without a synclastic deflection due to a

bending moment at the free end. A rotational spring is assumed for the pivot. This pivot is also called characteristic joint. Another PRBM model is constructed by three rigid links and two pivots, representing for a cantilever subjected to a vertical force plus an opposite bending moment, as shown in Figure 2.10 (*d*). Notations of geometric dimensions, loads and deformations of a cantilever are indicated in Figure 2.10 (*a*). A diagram indicating the internal bending moment along the cantilever is shown in Figure 2.10 (*b*). The PRBM model shown in Figure 2.10 (*c*) can also represents for a cantilever subjected to both a vertical force and a bending moment that induces a deflection component in the same direction as that of the vertical force. An inflection point happens at a cross-section along the cantilever where the resultant moment is zero due to the equal amount of the moments acting in opposite direction transferred from the vertical force and the moment applied at the free end. For example, the inflection point is located in between the two pivots of the PRBM model in Figure 2.10 (*d*). The deductions based on the two PRBM models for a compliant beam are given below.

PRBM Method for Cantilevers of Synclastic Deformations

As mentioned, this model represents for the cantilevers subjected to either a vertical force alone or a vertical force with a moment leading to deformation at the same direction (as shown in Figure 2.10 (*c*)). The characteristic joint of this kind of cantilevers is located at a distance of $(1-\gamma)\times l$ from the fixed end. The two rigid links are connected together at this joint by a rotational resistant spring. Herein length of the rigid link γl is also called as the characteristic radius where γ is the characteristic radius factor, which is correlated to the orientation of the force at the end and should be an optimal value to approximate the trail

of the cantilever end. γ is approximated to be 0.8517 [123] if there is only one vertical force at the end ($n=F_x/F_y=0$). κ_θ herein is the rotational spring factor that also depends on the ratio n of the vertical component against the horizontal component of the end-force whereas Θ is the pseudo-rigid-body angle. The values or factors such as γ, κ_θ, etc for PRBM models in conjunction with few values of n are listed below in Table 2.4. c_θ in the table is a parametric angle factor for linearization of the PRBM angle Θ, with a correlation of $\theta_0=C_\theta\Theta$. More details are given in the reference [123].

Table 2.4 Coefficients γ , κ_θ, c_θ with different end forces [123]

n	γ	c_θ	κ_θ
0.0	0.8517	1.2385	2.67617
0.5	0.8430	1.2430	2.63744
1.0	0.8360	1.2467	2.61259
-0.5	0.8612	1.2348	2.69320
-1.0	0.8707	1.2323	2.72816

As mentioned, two cases of loading conditions are used for this type of PRBM models (Figure 2.11). The first case (Figure 2.11 (*a*)) consists of only one vertical force applied at the free end and no other moment or horizontal force is considered. The rotational spring constant of the characteristic joint is given as:

$$K_R = \gamma\kappa_\theta \frac{EI}{l} \tag{2.86}$$

where K_R is the rotational spring constant, EI and l are the flexural rigidity and the length of the long link. According to the geometry shown in Figure 2.10, the vertical out-of-plane deflection at the free end of the cantilever can thus be written as:

$$\delta = b = \gamma l \sin\Theta \tag{2.87}$$

For small angular deflections, the above equation is rewritten as

$$\delta = \gamma \, l \, \Theta \tag{2.88}$$

Thus the vertical bending (out-of-plane) stiffness is derived as it follows:

$$K_{\delta} = \frac{\kappa_{\theta} EI}{\gamma l^3} \tag{2.89}$$

However, for very large deflections this linearization is not applicable and Equation (2.87) instead of Equation (2.88) has a better performance in dealing with nonlinearity, with which an implicit form of stiffness constant is deduced. Nevertheless, the angular deflection is linearly proportional to the applied force, shown as

$$F = \frac{K_R \Theta}{\gamma l} = \frac{\kappa_{\theta} EI}{l^2} \Theta \tag{2.90}$$

This expression may be useful for characterizing a planar frame that is made of one or more compliant beam segments. Linearity is obtained by replacing the vertical displacement with the angular deflection (the pseudo-rigid-body angle, Θ).

Another case of loading condition on this PRBM model consists of a vertical force and a bending moment that both act in the same direction (see Figure 2.11 (*b*)), thus both in-plane and out-of-plane deflections of the cantilever (denoted as a, b in Figure 2.10 (*a*)) due to the applied external loads can be derived as follows [123]:

$$\begin{cases} a = (1 - \gamma + \rho \cos \Theta) l \\ b = \rho l \sin \Theta \end{cases} \tag{2.91}$$

where

$$\rho^2 = \left[\left(\frac{a_i}{l} - (1 - \gamma) \right)^2 + \left(\frac{b_i}{l} \right)^2 \right] \tag{2.92}$$

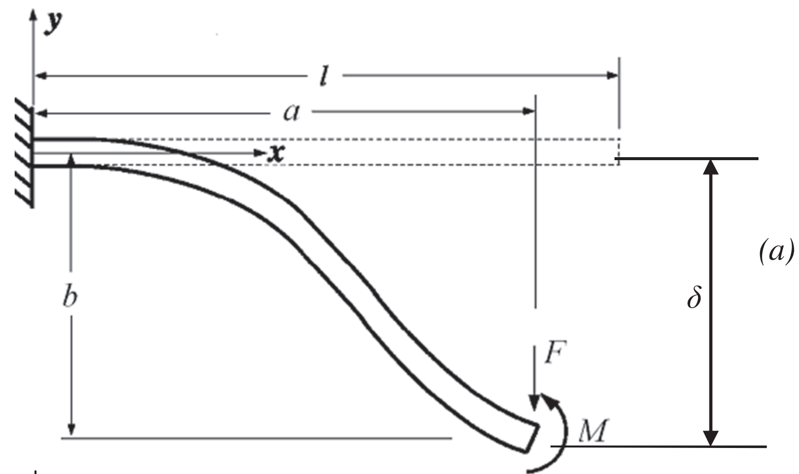

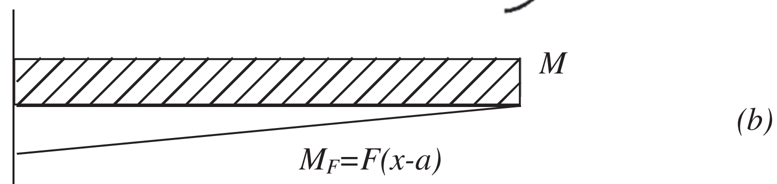

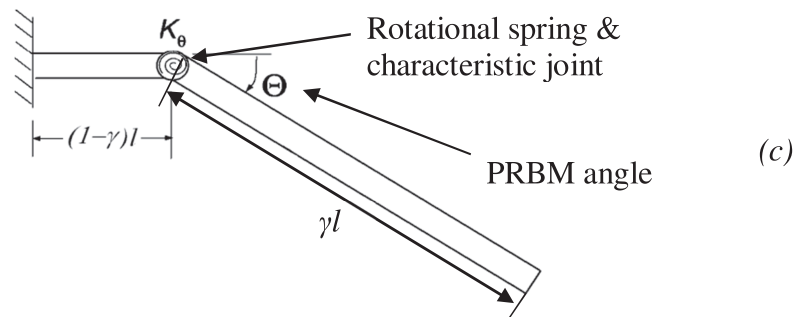

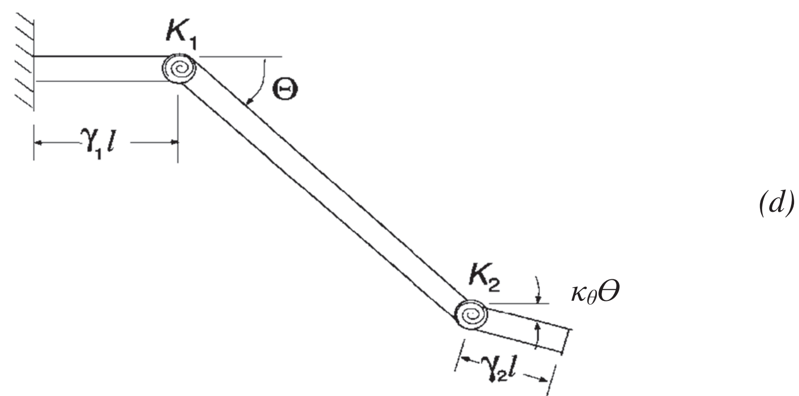

Figure 2.10 (*a*) A compliant cantilever beam with loads at free end; (*b*) The diagram of the applied external loads; (*c*) The equivalent PRBM model when *M* is void (two rigid links and a rotational spring); (*d*) The equivalent PRBM model when *M* exists (three rigid links and two rotational springs).

$$a_i = R_i \sin\frac{l}{R_i} \tag{2.93}$$

$$b_i = R_i(1-\cos\frac{l}{R_i}) \tag{2.94}$$

$$\frac{1}{R_i} = \frac{M_0 l}{EI} \tag{2.95}$$

The rotational spring constant in this case is written as

$$K_R = \rho\kappa_\theta \frac{EI}{l} \tag{2.96}$$

The above found formulae can be applied in cantilevers with attached mass plates and subjected to electrostatic actuation. One of these examples in MEMS, a cantilevered electrostatic actuated micromirror is presented in [182].

PRBM Method for Guided-End Cantilevers

If the applied moment is opposite in its direction to the vertical force, then the PRBM model with two rotational joints and three rigid segments is more suitable for accurate approximation (shown in Figure 2.10 (*d*) and 2.11 (*c*)). In this PRBM model there exists an inflection point (the bending moment at this cross-section is zero) in the length of the cantilever. As shown in Figure 2.10 (*d*), K_1, K_2 herein are the rotational spring constants at joints *1* and *2*, while Θ, κ_θ, $\gamma_1 l$ and $\gamma_2 l$ are the PRBM angle, ratio of the PRBM angles and lengths of the two rigid segments in the initial and the final sections of the cantilever. In a completely guided-end cantilever, the inflection point is known to be located at the mid-point of the cantilever according to the Bernoulli-Euler beam theory (where the moment is zero, the curvature is also zero). Therefore, for completely guided-end

cantilevers ($\gamma_1 = \gamma_2 = (1-\gamma)/2$), the two rotational angles at both joints are equal (κ_θ=1) and the length of the central part in the PRBM model can be represented by γl (γ=0.85) [123]. The rotational spring constants K_1 and K_2 are also equal and are given by

$$K = K_1 = K_2 = 2\gamma K_\theta \frac{EI}{l} \tag{2.97}$$

where K_θ is the rotational spring factor with this kind of end-loads (K_θ =2.65) [123]. The rotational moment M_0 in this PRBM model has a relation with the PRBM angle Θ as $M_0=K\,\Theta$. Thus the deformed in-plane and out-of-plane dimensions for the cantilever are derived as

$$\begin{cases} a = (1-\gamma(1-\cos\Theta))l \\ b = \gamma l \sin\Theta \end{cases} \tag{2.98}$$

The vertical bending stiffness of the cantilever can be written as

$$K_\delta = \frac{2\kappa_\theta EI}{\gamma l^3} \tag{2.99}$$

Two more loading conditions could be formulated for this kind of PRBM models. They apply to the partially guided-end cantilevers due to a large vertical force and a reduced moment applied at the free end, and the overly guided-end cantilevers due to a less vertical force and a large moment loaded at the free end. In both cases, the two PRBM angles are not equal ($\kappa_\theta \neq 1$) and their rotational spring constants K_1 and K_2 are not equal too. Thus, accordingly, the shapes of deflection are different due to shift of the inflection point [183].

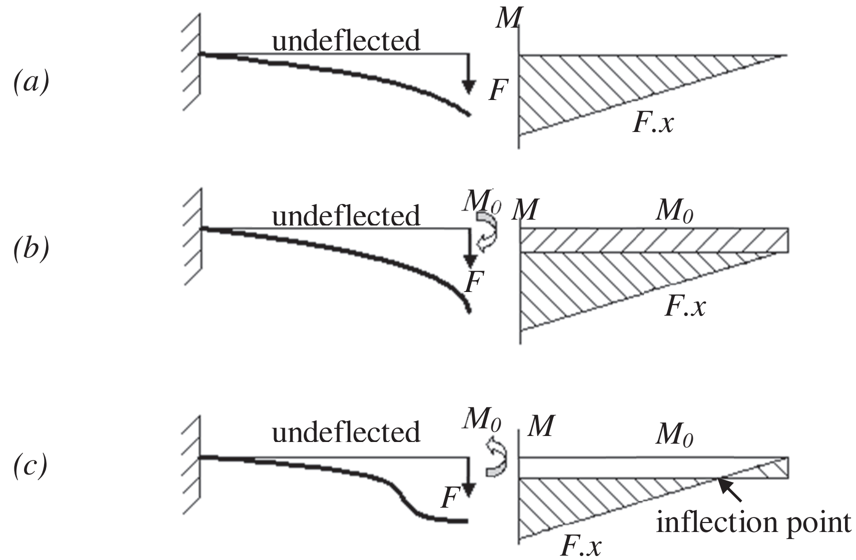

Figure 2.11 Deflection diagrams of a cantilever subjected to three kinds of loads at the free end: (*a*) a vertical force; (*b*) a vertical force with a synclastic moment; and (*c*) a vertical force along with a moment in opposite direction.

However, the compliant cantilevers in the out-of-plane movable MEMS are usually loaded with one vertical force alone or with a small bending moment at the free end. The torsional micromirror given in Figure 2.1 represents one of the examples. This structure can be modeled using PRBM method as shown in Figure 2.15. Due to the symmetry of the structure and the rigidity of the mirror plate, total mirror plate can be levelly pulled toward the opposite substrate by the uniformly distributed electrostatic actuation; thus the free ends of both cantilevers must be kept in horizontal position to form a smooth profile of deformation from both edges of the mirror plate. Both fixed ends of the cantilevers are also kept horizontal and smooth from their anchorages. Thus it is concluded the inflection point is located in the midpoint of the cantilever. This is the case happened to the fully guided-end cantilevers.

In summary, the PRBM model with two joints and three rigid links has a better approximation to a compliant cantilever than the PRBM model with only one joint and two rigid links. The rotational spring constants K_1 and K_2, the ratio of PRBM angles (κ_θ), and the lengths of the two short rigid links can be determined according to different loading conditions and their ratios with each other [183].

2.4.2 Comparison of PRBM and FEM

The load-displacement analysis using PRBM methods is compared here with the results obtained from using other methods such as the finite element analysis (FEA) and the conventional linear method. The comparison is performed on a compliant cantilever of 221μm in length and 8×10 μm^2 in the cross-sectional dimensions and subjected to three different cases of loading at the free end.

Case 1: Cantilevers subjected to a vertical force at free end

This case represents a compliant cantilever loaded with a vertical force alone (shown in Figures 2.10 (*c*) and 2.11 (*a*)). The out-of-plane bending stiffness constant at the free end can be written according to the linear beam theorem as (also refer to Table 2.1):

$$K_b = \frac{3EI}{l^3} \tag{2.100}$$

whereas in PRBM method it has been derived in Equation (2.89) and can be rewritten here:

$$K_{\delta} = \frac{\kappa_{\theta} EI}{\gamma l^3} \tag{2.101}$$

where $\kappa_{\Theta} = 2.65$ and $\gamma = 0.8517$, for example [123]. Comparing these two formulae one can infer that the PRBM beam model is stiffer than the linear beam model. However they all have linear load-displacement relations. This is the reason it is called a linear PRBM beam model.

The cantilever model is also simulated in ANSYS (a kind of commercial software for FEA) using BEAM4 element to mesh the whole structure and loading conditions. BEAM4 is a uniaxial elastic beam element with two nodes at both ends. Each node has six degrees of freedom: translations in the nodal *x*, *y*, and *z* directions and rotations about the nodal *x*, *y*, and *z* axes. Stress stiffening and large deflection capabilities are included. Hence this is appropriate for simulation of the mentioned thin and lengthy cantilever beams. A load-displacement curve at the free end of the cantilever subjected to various magnitudes of a vertical force is then obtained. Figure 2.12 shows the three load-displacement curves resulted from using the above three methods. As comparison, one of the nonlinear curves named Nonlinear PRBM in Figure 2.12 is obtained using Equation (2.87). It is thus observed that larger nonlinearity of deflections can be caused by larger forces applied. The flexibility or compliance of a cantilever is decided by either the ratio of its length over its cross-section or the magnitude of the applied force. Within a certain magnitude of the forces (for example, 1500μN for the given cantilever), both the linear and nonlinear PRBM beam models demonstrate good approximation to the results obtained from using FEA. Three zones of load-displacement relations are identified from the analysis of the results (see Figure 2.12). The first zone is linear where the linear beam

theory with the assumption of small deflections is applicable and the deviations thus caused are acceptable; while the third zone of the curves shows large deviations are resulted from using any of the methods indicated in the figure; the second zone for all of the curves in the figure demonstrates PRBM method has a better approximation than the results obtained from linear beam theory.

Case 2: Cantilevers subjected to a vertical force plus a synclastic moment

A vertical force and a synclastic moment applied on the tip of a cantilever are assumed in this case as shown in Figure 2.12(*c*) and Figure 2.13(*b*). The vertical deflection and slope angle at the free end can be deduced using linear matrix method (see Section 2.3), which is rewritten here as follows (F and M_0 are denoted to the applied force and the moment).

$$\begin{Bmatrix} \delta \\ \Theta \end{Bmatrix} = \begin{bmatrix} \dfrac{l^3}{3EI} & \dfrac{l^2}{2EI} \\ \dfrac{l^2}{2EI} & \dfrac{l}{EI} \end{bmatrix} \begin{Bmatrix} F \\ M_0 \end{Bmatrix} \tag{2.102}$$

where δ and Θ are the vertical deflection (or out-of-plane bending deflection) and the angular deflection at free end of the cantilever. Note that this matrix equation can also be applied in any cantilever subjected to any combination of force and moment at the free end. Comparatively, the matrix eqauation of motion using linear PRBM models can be derived as:

$$\begin{Bmatrix} \delta \\ \Theta \end{Bmatrix} = \begin{bmatrix} \dfrac{\gamma_1 l^3}{K_{\theta 1} EI} & \dfrac{l^2}{K_{\theta 2} EI} \\ \dfrac{l^2}{\gamma_1 K_{\theta 1} EI} & \dfrac{l}{\gamma_2 K_{\theta 2} EI} \end{bmatrix} \begin{Bmatrix} F \\ M_0 \end{Bmatrix} \tag{2.103}$$

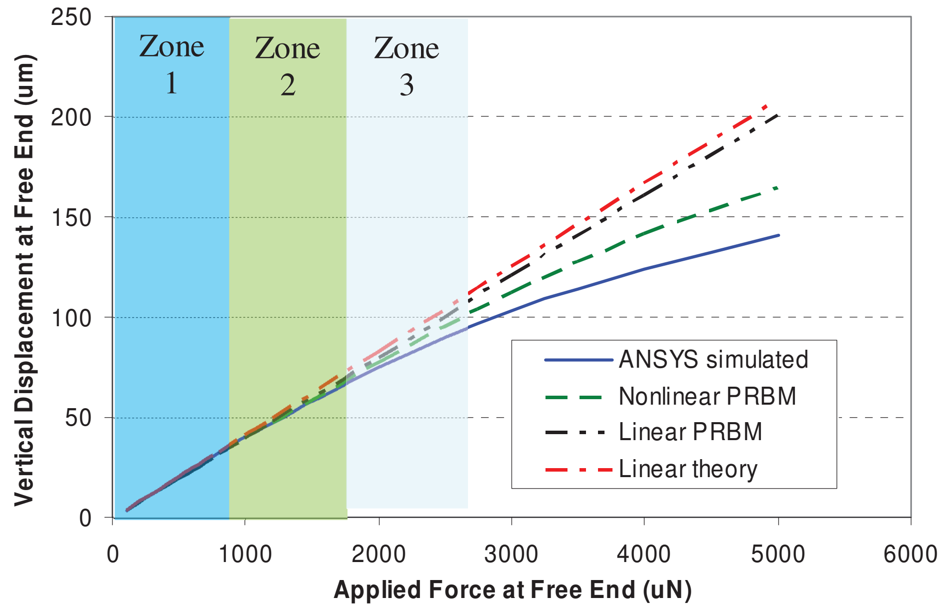

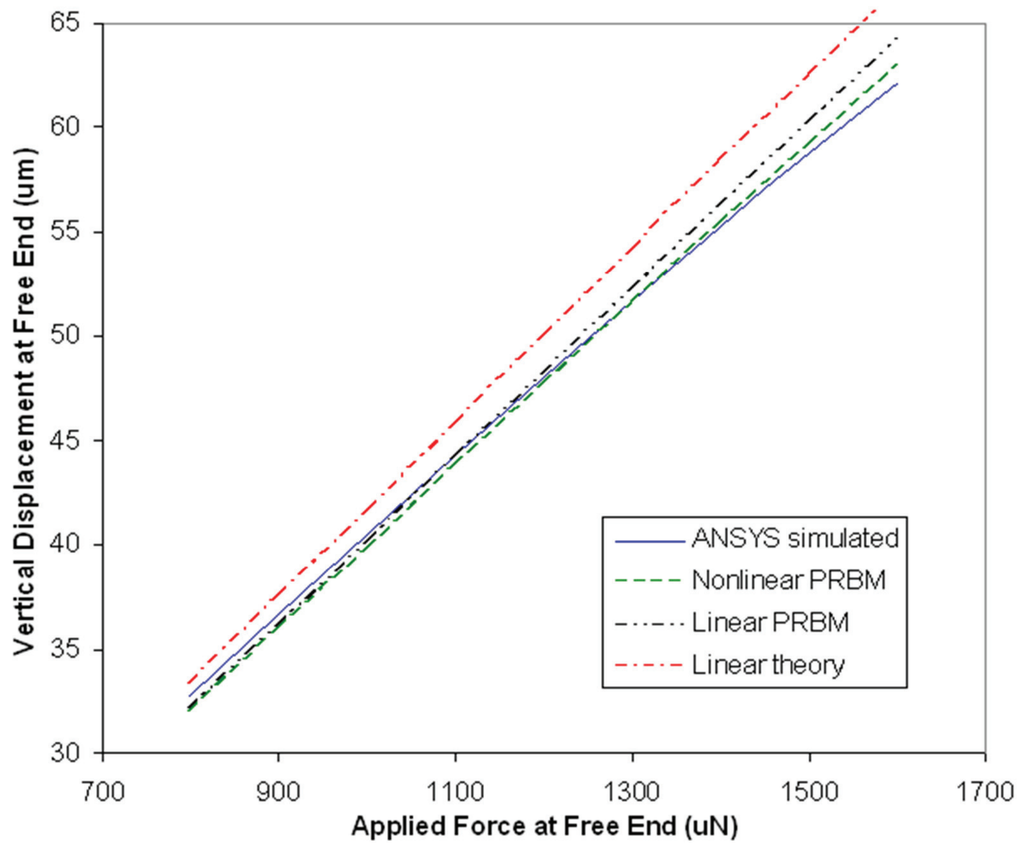

Figure 2.12 The load-displacement curves of a cantilever beam at the free end subjected to a vertical force, obtained by using linear beam theory, linear PRBM, nonlinear PRBM and FEA simulation.

where γ_1 and γ_2 are the characteristic coefficients due to the vertical force and the moment, respectively (γ_1=0.8517 and γ_2= 0.7346); $K_{\Theta 1}$ and $K_{\Theta 2}$ are rotational spring coefficients due to the force and the moment ($K_{\Theta 1} = 2.65$ and $K_{\Theta 2} = 2.0643$). Substitution of the given coefficients into Equation (2.103) gives the following static equation of motion:

$$\begin{Bmatrix} \delta \\ \Theta \end{Bmatrix} = \begin{bmatrix} \dfrac{l^3}{3.1114EI} & \dfrac{l^2}{2.0643EI} \\ \dfrac{l^2}{2.257EI} & \dfrac{l}{1.5164EI} \end{bmatrix} \begin{Bmatrix} F \\ M_0 \end{Bmatrix} \tag{2.104}$$

Compared to Equation (2.102), the flexibility matrix in Equation (2.104) has lower values of coefficients for all of the four matrix members, which demonstrates that smaller deflections can be derived from the linearized PRBM model. This can also be observed from Figure 2.15.

Case 3: Cantilevers subjected to a vertical force with an opposite moment

Conversely to Case 2, the moment applies in an opposite direction to the deflection produced by the force at the free end of a cantilever. The deflections thus induced can be obtained by using the same equations as in Case 2. This case is representative for most of the cantilevers used in suspensions for out-of-plane movable micromirrors and micro-platforms due to their symmetric structures involved. As a typical example, in Figure 2.1 the central mirror plate is suspended symmetrically by the two lengthy beams at its both sides.

(a)

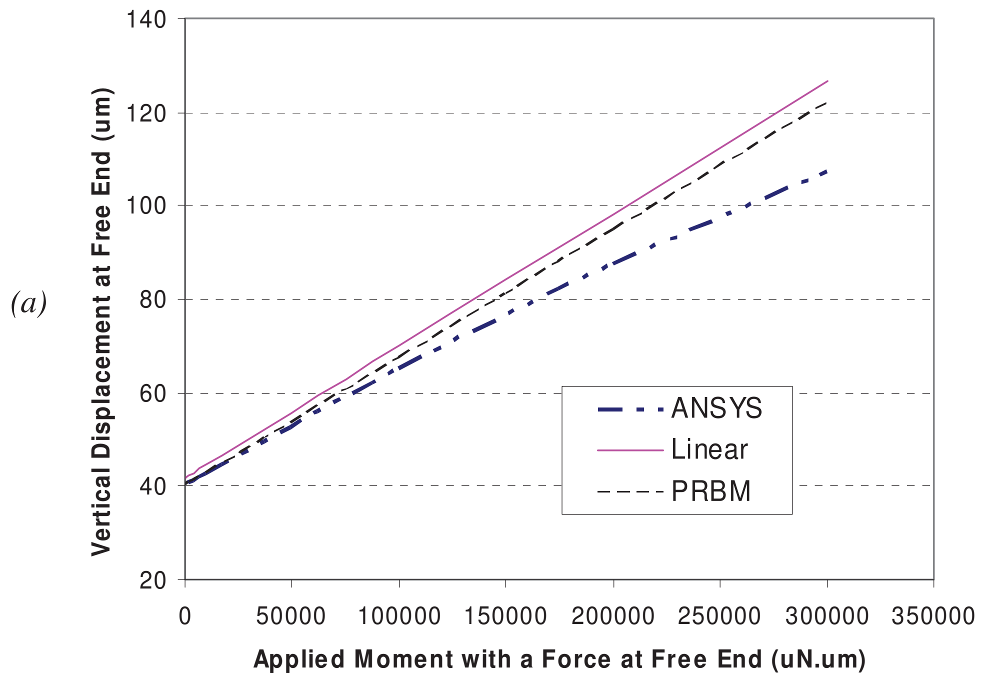

(b)

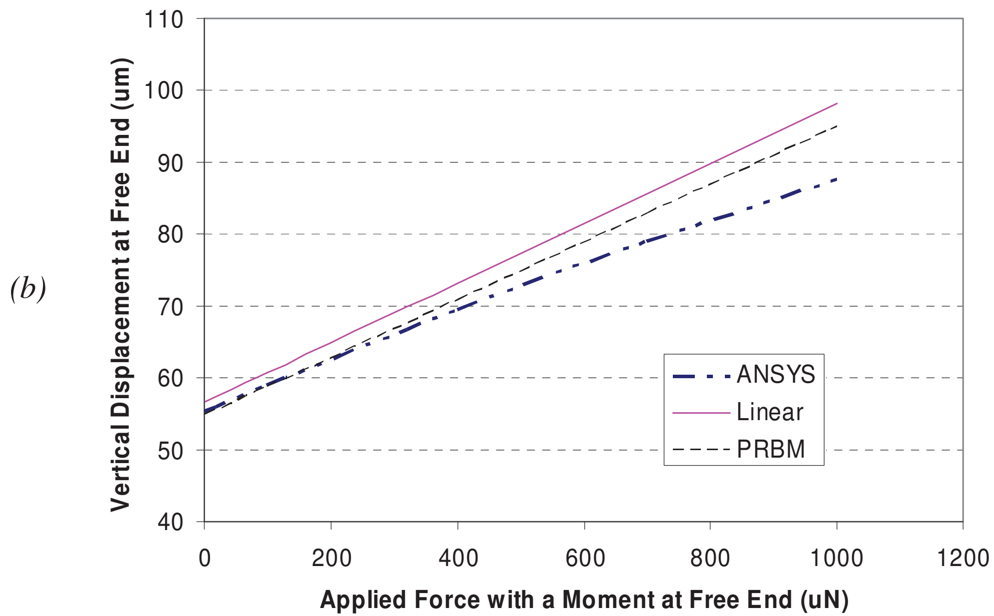

Figure 2.13 Different load-deflection curves of a cantilever at free end are simulated using linear beam theory, PRBM and FEM software: the curves in (*a*) are resulted from a range of moment with a fixed force; and the curves in (*b*) are resulted from a range of force with a fixed moment.

Three load-deflection curves obtained from using linear beam theory, PRBM method and finite element method respectively for the cantilever applied by the assumed loads are shown in Figure 2.14. The upper part in the figure is plotted as if the cantilever is applied at its free end by a variable value of force with a fixed amount of moment in the opposite direction. For example, M_0 is assumed at 0.2μN.m according to the electrostatic torque estimated from the micromirror given in Figure 2.1 and its applied voltage. The lower graph is plotted when the cantilever is loaded by a variable amount moment with a fixed value of vertical force (F=1000μN) in the opposite direction. It is noted from Figure 2.14 that with a fixed upward moment, the vertical deflection is positive or upward if the downward force is less than a value. No displacement can be resulted if the downward deflection arising from the downward force equals the upward deflection caused by the upward moment. The simulated results for the cantilever, for example, show that the zero displacement happens when the applied force is around 1850μN and the corresponding moment is fixed at 0.2μN.m; or it occurs when the applied moment is around 0.113μN.m with the fixed force at around 1000μN (see the red lines shown in Figure 2.14). Both cases (either a variable force with a fixed moment or a variable moment with a fixed force) represent for the guided-end cantilevers. Moreover, it is noted the three curves in Figure 2.14 are very close to each other, with the FEM simulated curve located in between the linear and the PRBM curves. The reason is that the two opposite loads, downward force and upward moment, or vice versa, compress the resultant displacements in the range of small deflections. Linearized curves can thus be resulted. This in the other hand demonstrates both linear PRBM method and linear beam theorem can be applied in the analysis for guided-end cantilevers.

All load-displacement curves in Figures 2.12, 2.13 and 2.14 indicate that the PRBM method is able to give a closer result to that of FEA simulation than using linear beam theorem. For small deflections both linear and PRBM method are applicable. In case of very large deflection, neither linear modeling nor PRBM modeling method is applicable for approximation. Nevertheless, the cantilevers with very large delfections are rare in the actual planar micro-mechanisms. As such, the derived PRBM method is appropriate to solve for most of micro-cantilever problems.

2.4.3 Analysis of Torsional Micromirror Using PRBM Method

The torsional out-of-plane motion of the micromirror given in Figure 2.1 is analyzed in this sub-section using PRBM method. The vertical force is resulted from the electrostatic actuation that is uniformly distributed in the space between the two parallel plates (the micromirror and the substrate electrode) and applied on the micromirror as a distribution force. Thus the force, the moment and the torque concentrated at an end of the two beams are halves of their entire amplitude due to the symmetric geometry. The concentrated moment and torque at the ends are thus generated. The geometric symmetry and the assumed rigidity of the micromirror (see Figure 2.15) indicate the three links plus two joint PRBM model has a better approximation.

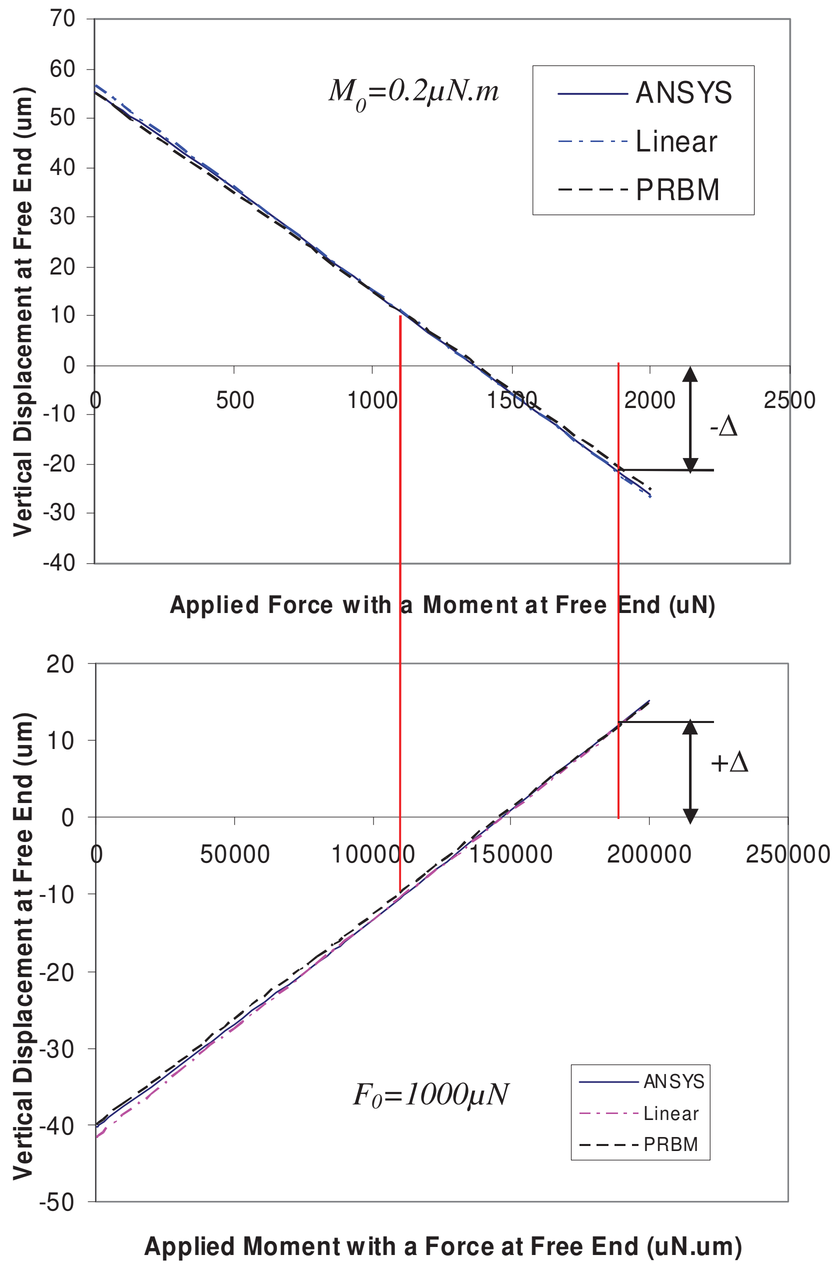

Figure 2.14 Vertical deflections at free end of a cantilever resulted from a varied force or moment along with the conversely applied and fixed moment or force using linear bem theory, PRBM, and FEA simulation.

Each side beam of the micromirror can be approximated by a cantilever having three degrees of freedom of motion, that is, the torsional deflection α along its torsion axis, the vertical deflection δ and the bending slope angle θ caused by electrostatic actuation. The

torsion of the two beams is expressed as a linear relation between load and displacement and it is independent from other two degrees of motion (Section 2.2). The vertical and the angular slope deflections are correlated to each other. Thus both side beams can be represented by the fully guided-end cantilevers. Their equivalent PRBM models are composed of three rigid links and two rotational joints, as shown in Figure 2.17. Using Equation (2.103), a matrix equation of quasi-static motion of the torsional micromirror can be written as follows,

$$\begin{Bmatrix} \delta \\ \theta \\ \alpha \end{Bmatrix} = \begin{bmatrix} \dfrac{\gamma_1 l^3}{K_{\theta 1} EI} & \dfrac{l^2}{K_{\theta 2} EI} & 0 \\ \dfrac{l^2}{\gamma_1 K_{\theta 1} EI} & \dfrac{l}{\gamma_2 K_{\theta 2} EI} & 0 \\ 0 & 0 & \dfrac{2l}{GJ} \end{bmatrix} \begin{Bmatrix} F \\ M_y \\ T \end{Bmatrix} \tag{2.105}$$

The end loads for the equivalent cantilever include the downward force F_z (equal to $F_e/2$), the moment in the opposite direction M_y (equal to M_0) arising from the difference of the moment arms, and the torque T_x caused by the distance of the electrostatic force to the torsional axis. There may be no deflected slope angle at the free end of the cantilver because of the assumed rigidity of the mirror plate compared to the relatively compliant cantilevers. The flexibility matrix for the micromirror can be solved as shown in Equation (2.105). Depending on different loading conditions at the free end of a compliant cantilever in a micro-mechanism, the PRBM models with different numbers and lengths for rigid links can be found and the whole micro-mechanism which may include both the short rigid beam members and the lengthy compliant beams can thus be linearized and analyzed and a model built.

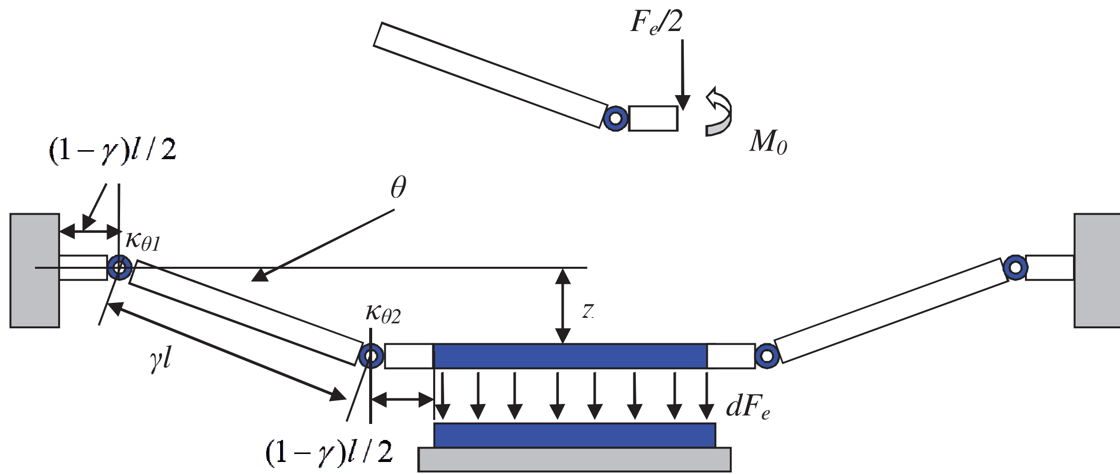

Figure 2.15 The approximated PRBM models for the two cantilever beams in the given torsional micromirror.

2.5 Summary

Planar micro-mechanisms and compliant suspensions were first discussed in this chapter. A typical planar micro-mechanism which is represented by a torsional micromirror suspended by two lengthy side beams was assumed as linear and further analyzed using linear energy method. Electrostatic potential energy, the strain energy, the electrostatic nonlinearity, the pull-in phenonmenon and static and dynamic performances of the micromirror were reviewed. Structural effects due to large deflection, shear strain, axial load stiffening and shear force loosening were also discussed in the second part.

Origination of the matrix method and its applications in planar micro-mechanisms were reviewed and followed by a general formulation of the matrix equations for the framed structures in the third part. Based on the linear assumption, matrix methods via both

flexibility and stiffness matrices were given thereafter. The detail introduction includes the individual stiffness matrices and the equations of motion for static analysis of a torsional micromirror given in the beginning of the chapter. The results were also compared with the simulated results acquired from using commercial FEM software.

As an alternative of analytical methods in dealing with compliant beams, the pseudo rigid body model (PRBM) is utilized to model nonlinear mechanisms due to large deflections. Two types of PRBM models with their criteria and characteristics were presented. Structural features and formulation of the PRBM models with three kinds of end-loads were discussed.The PRBM method was then applied for static analysis of the given torsional micromirror. The results obtained from using different PRBM models were compared with those achieved from using linear beam theorem and commercial FEM software ANSYS.

As a conclusion and in consideration of the characteristics of the compliant beams in the planar framed micro-mechanisms, both linear matrix method and PRBM method are very helpful in modeling and analysis of out-of-plane movable MEMS that comprise compliant beam members.

Chapter 3: Torsional Micromirrors with Serpentine Springs

3.1 Introduction

As previously introduced, the electrostatic actuated torsional micromirrors represent a topic of interest among optical MEMS devices due to the following advantages: they can be easily made in large batches using SOI wafers; their major components, the mirror plates, demonstrate uniformity and flatness in surface for efficient light reflection; their structures are stable and reliable for long life expectancy due to the thick silicon film used for the structural layers; they can be easily controlled by simple electronic circuits; above all they are the essential components in constructing many of micro-optical devices. However, concerns are raised given the hard to satisfy for structural compactness and the large drive voltage needed for electrostatic actuation. It is therefore necessary to model and design compliant suspensions for micromirrors, aiming to incorporate more devices on the micro-chip and to reduce the drive voltage.

Using short beams as hinges to suspend torsional micromirrors was previously discussed [184-187]. Although the lengthy beams have to be adopted if flexible movement of the proof mass plates is desired, they are actually not easy to produce due to sinking or stiction problems during or after fabrication. To avoid such issues, a variety of planar suspensions have been developed although they are all comprised by different lengths of beams. The geometry for these suspensions can take L-shape, U-shape, sagittal shape, or other compositions of multiple beams, as illustrated in Figure 3.1. With symmetric

arrangement in geometry, most of them are used for in-plane motion of the micro-platforms. However, the bridge and the classical serpentine spring shown in Figure 3.1 (*a*) and (*e*) can also be used for out-of-plane torsional motion of micromirrors given the low torsional stiffness constants.

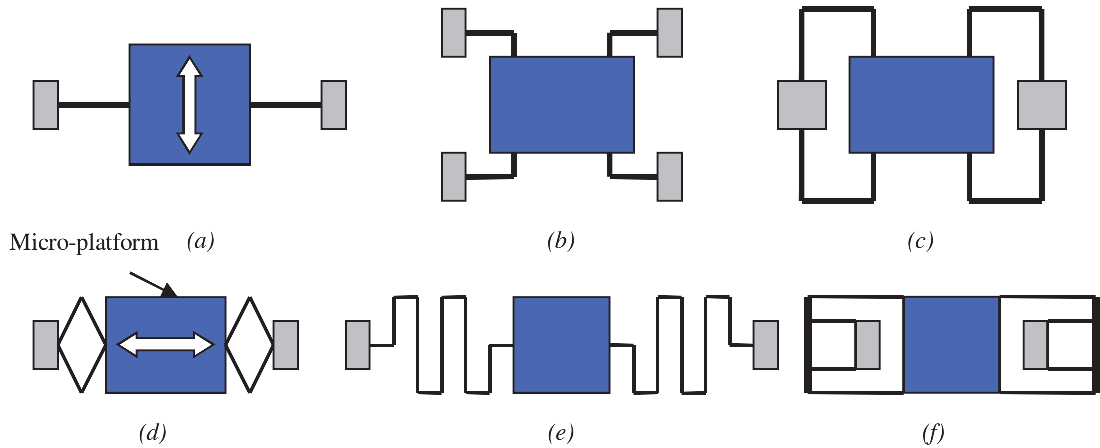

Figure 3.1 Suspensions for micro-platforms: (*a*) a bridge by two cantilevers; (*b*) L-type folded beams; (*c*) U-type folded beams; (d) Sagittal springs; (*e*) Classical serpentine springs; (*f*) Double L-type folded beams.

Although few planar springs have been reported to adapt for the suspensions of platforms [188], they are too stiff to adapt for the suspensions of torsional micromirrors. Recently two kinds of ortho-planar springs in micro size for micro-mechanism applications, the so-called classical seperpentine springs and rotational serpentine springs were reported in literature [86, 157 and 158]. As reported, the spring constants for the out-of-plane bending, the in-plane bending and the out-of-plane torsion modes are in the same order of values for the classical serpentine springs, while the rotational serpentine spring exhibits more flexible torsion and an increased stiffeness in the out-of-plane bending. This indicates that rotational serpentine springs are more appropriate to construct the suspension structure for a torsional micromirror that requires flexible torsion and stiff

bending. Thus in this chapter, torsional micromirrors symmetrically suspended by two side rotational serpentine springs and actuated by parallel field electrostatic actuation are analyzed using various modeling methods such as the linear energy method, the linear matrix method, the PRBM method, the matrix method with PRBM models and FEM simulation.

3.2 Planar Serpentine Springs

A planar serpentine spring consists of multiple beam segments that are consecutively connected. Two or more serpentine springs may join together to form a strengthened suspension. Figure 3.2 shows several types of planar serpentine springs, in which (*a*) is a serpentine spring composed of multiple loops of rotational serpentine elements; (*b*) is a serpentine spring with a few periods of classical serpentine elements; whereas (*e*) is a serpentine spring having only one rotational serpentine loop. These three serpentine springs belong to ortho-planar springs. Two other types of planar serpentine springs, the zigzag serpentine spring and the rounded orthogonal serpentine spring are also shown in Figure 3.2 (*c*) and (*d*). Because of the folded beam structures, these springs occupy much less areas than they may need for the straight beams with the same length. The compactness is thus obvious.

As mentioned previously, a framed structure composed of serpentine springs can be regarded as a grid, capable of out-of-plane translation, slope angular deflection due to the bending moment, and axial torsion. The axial deformations and the in-plane lateral

deformations for individual beam segments are assumed negligible. Compared to orthogonal serpentine springs, the zigzag and the rounded serpentine springs are more difficult to fabricate due to selective etching nature of silicon. Thus in actual applications, only rotational serpentine springs or classical serpentine springs are chosen for suspensions of out-of-plan movable MEMS. Rotational serpentine springs are therefore chosen for suspensions of compliant torsional micromirrors due to their advantages in structural compactness, stiffened bending, and more compliant torsion. All analyses using different methods hereafter in this chapter are focused on the torsional micromirrors supported by rotational serpentine springs.

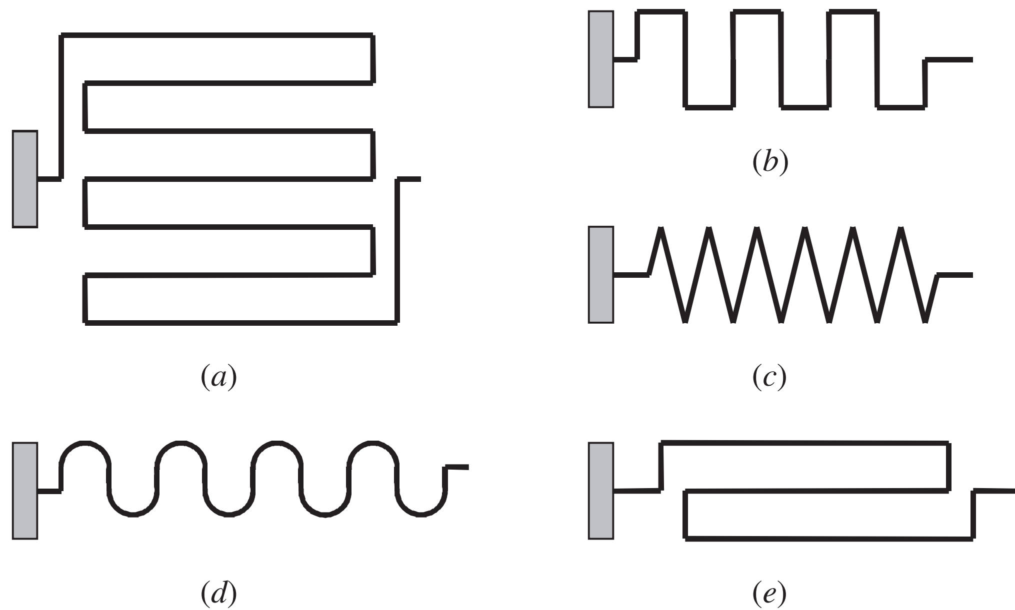

Figure 3.2 Several types of planar serpentine springs: (*a*) one with multiple loops of rotational serpentine; (*b*) one with multiple loops of classical serpentine; (*c*) one zigzag classical serpentine; (*d*) one with rounded classical serpentine; (*e*) a rotational serpentine spring with one serpentine loop.

3.3 Modeling by the Energy Method

The schematic views (both top and side views) of a torsional micromirror suspended by two identical rotational serpentine springs are shown in Figure 3.3 (*a*) and (*b*), respectively. The two rotational serpentine springs are attached to the micromirror symmetrically at their free-ends and anchored to the substrate at their fixed ends. The micromirror is thus suspended and limited from in-plane movements. The gap g_0 between the bottom electrode on the substrate and the top mirror plate allows for the out-of-plane bending and torsion of the micromirror. The electric field is created by application of the electrical bias on the pair of electrodes. The top mirror plate can thus be driven to rotate by an angle α about the torsion axis while the torsion beam can be deflected by a vertical translation z. Small deflections, non residual strains, the overlapped upper and lower plates, and no fringe effect of the electrical field between the two plates, are all assumed in the model and used for performance analysis in this section.

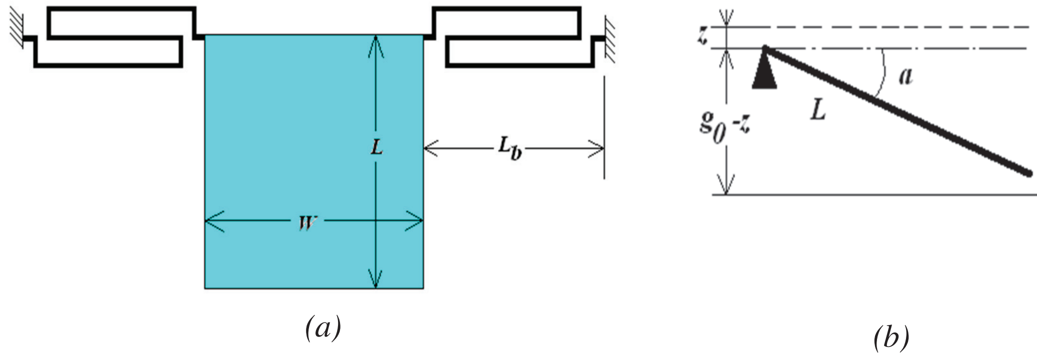

Figure 3.3 Schematic views of a torsional micromirror suspended by two rotational serpentine springs: (a) top view; (b) side view.

3.3.1 Formulation of Stiffness for Rotational Serpentine Springs

As shown in Figures 3.3 and 3.4, due to the structural symmetry, two side springs counteract on each other with equal forces along the torsion axis, such that no axial displacement for any side spring occurs. Meanwhile, the individual axial elongations or stretches along the four short segments (segments #2, #4, #6 and #8 in Figure 3.4) can be cancelled out each other because of their symmetric arrangement along the torsion axis. And the individual elongations or stretches along the three long segments (segments #3, #5 and #7 in Figure 3.4) of each side spring can merge together to behave as a cantilever beam due to the symmetric structure and the uniformity in cross-section and material. Therefore, the two side spring can be regarded as the cantilever serpentine springs with fully guided-end loading condition due to the rigidity of the micromirror and the symmetry of the entire structure. The force diagram for such a rotational serpentine spring element is shown in Figure 3.4 (*a*), in which l_p, l_o, l_i, l_f and d_i are denoted for lengths of the parallel long segments, the orthogonal short segments, the initial segment at the fixed end, the final segment at the end attached to the mirro plate and the distance between the two neighbor short segments in the serpentine spring.

According to Castigliano's theorems, the total strain energy stored in any beam segment of a spring subjected to a general load that includes the components of bending, shear, axial force, and torque, can be summed up as:

$$U = U_{bending} + U_{shearing} + U_{axial} + U_{torsion} \tag{3.1}$$

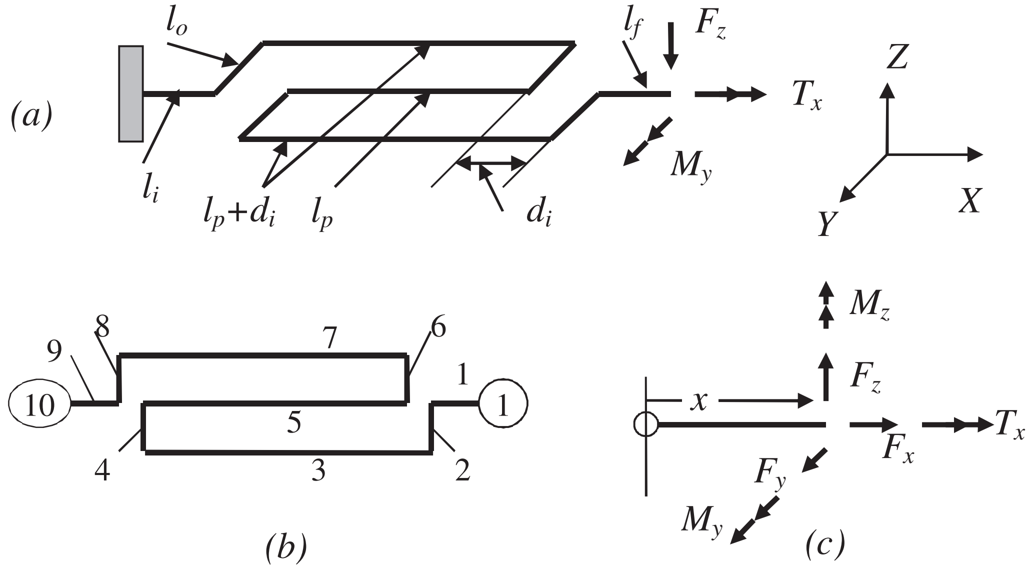

Figure 3.4 Schematic diagrams for a rotational serpentine spring. (*a*) the free body diagram of a rotational serpentine spring with applied loads and geometry notations; (*b*) the joint and segment numbering of the spring; (*c*) the internal loads on a segment.

Since the force components M_z, F_x and F_y for the in-plane deflections are assumed negligible, thus the term U_{axial} is neglected. The other terms in Equation (3.1) are expressed as:

$$U_{bending} = U_{bending,y} + U_{bending,z} = \int_L \frac{M_y^2}{2EI_y} ds + \int_L \frac{M_z^2}{2EI_z} ds \tag{3.2}$$

$$U_{shearing} = U_{shearing,z} = \int_L \frac{f_s F_z^2}{2GA} ds \tag{3.3}$$

$$U_{torsion} = U_{torsion,x} = \int_L \frac{T_x^2}{2GJ} ds \tag{3.4}$$

where f_s in Equation (3.3) is a coefficient that depends on the cross-sectional geometry; I_y and I_z are cross-sectional moments of inertia with respect to the *y*-axis and the *z*-axis, respectively while all integrations are carried out along the length of individual segments.

L, A, G, J and ds are the length, the cross-sectional area, the shear modulus, the cross-sectional polar moment and the infinitesimal element of length of the beam.

The assumptions of no shear strain, no axial strain and no lateral bending moment (M_z) are reasonable according to the applied loads and the characteristics of a planar grid. Thus the corresponding terms of the strain energy on the assumed negligible motion directions can be neglected. The total strain energy for each segment in Equation (3.1) can be simplified to two terms only: bending and torsion strain energies. Thus the total strain energy for a serpentine spring consisting of nine segments and subjected to T_x, M_y and F_z at the free end (shown in Figure 3.4 (*a*)) can be simplified to

$$U = \sum_{i=1}^{9} \int \frac{M_i^2}{2EI_i} d\xi + \sum_{i=1}^{9} \int \frac{T_i^2}{2GJ_i} d\xi \tag{3.5}$$

According to Castigliano's second theorem, the bending slope φ_0, the torsional angle ψ_0, and the vertical displacement δ_0 can therefore be determined by

$$\alpha_0 = \frac{\partial U}{\partial T_x}, \quad \varphi_0 = \frac{\partial U}{\partial M_y}, \quad and \quad \delta_0 = \frac{\partial U}{\partial F_z} \tag{3.6}$$

Thus all of the three stiffness constants can be derived by forcing two of the equations equal to zero and solving the remaining one in Equation (3.6). For an example, the torsional stiffness k_t at the free end of a side spring is derived from setting φ_0=0 and δ_0=0 such that a relation between the applied torque and the torsional angle is obtained. The other two stiffness constants can be similarly obtained.

Table 3.1 lists the corresponding internal loads for all of the nine segments due to the external loads applied at the free end of a serpentine spring. The geometric denotations in

the table can be found in Figure 3.4. The variable *x* in the table represents a longitudinal distance from the initial node in a beam segment, shown in Figure 3.4 (*c*). The constant cross-section and the uniform material properties are assumed in the analysis. The three deflections at the free end of the spring are then derived from solving Equations (3.5) and (3.6) as follows.

Table 3.1 Internal moments and torques for individual segments

Segment Number (*length*)	Moment	Torque
1 (l_f)	$M_y+F_z x$	T_x
2 (l_0)	$T_x-F_z x$	$M_y+F_z l_f$
3 (l_p+d_i)	$M_y+F_z(l_f+x)$	$T_x-F_z l_0$
4 (l_0)	$T_x-F_z(l_0-x)$	$M_y+F_z(l_f+l_p+d_i)$
5 (l_p)	$M_y+F_z(l_f+l_p+d_i-x)$	T_x
6 (l_0)	$T_x+F_z x$	$M_y+F_z(l_f+d_i)$
7 (l_p+d_i)	$M_y+F_z(l_f+d_i+x)$	$T_x+F_z l_0$
8 (l_0)	$T_x+F_z(l_0-x)$	$M_y+F_z(l_f+l_p+2d_i)$
9 (l_i)	$M_y+F_z(l_f+l_p+2d_i+x)$	T_x

$$\alpha_0 = T_x\left(\frac{l_f + l_i + 2d_i + 3l_p}{GJ} + \frac{4l_0}{EI}\right) \tag{3.7}$$

$$\begin{aligned}\varphi_0 = &\left(\frac{l_f^2 + 3l_p^2 + 4l_i l_p + 4d_i^2 + 4l_i d_i + 6l_f l_p + 4l_f d_i + 8l_p d_i}{2EI} + \frac{2l_0 l_p + 4l_0 d_i + 4l_0 l_f}{GJ}\right)F_z \\ &+\left(\frac{l_f + l_i + 2d_i + 3l_p}{EI} + \frac{4l_0}{GJ}\right)M_y\end{aligned} \tag{3.8}$$

$$\delta_0 = \left(\frac{\left\{\begin{aligned}&4l_0^3 + 3(l_f + 2d_i + l_p)l_i^2 + 3(l_f + 2d_i + l_p)^2 l_i + 3(l_f + l_p + d_i)^2 l_p + l_p^3 + \\ &l_f^3 + l_i^3 + 3l_f(l_p + d_i)^2 + 3(l_f + d_i)(l_p + d_i)^2 + 3(l_f + d_i)^2(l_p + d_i) + \\ &3l_f^2(l_p + d_i) + 2(l_p + d_i)^3 - 3(l_f + l_p + d_i)l_p^2\end{aligned}\right.}{3EI} + \frac{2(l_p + d_i)l_0^2 + (l_f + d_i)^2 l_0 + (l_f + l_p + d_i)^2 l_0 + l_f^2 l_0 + (l_f + 2d_i + l_p)^2 l_0}{GJ}\right)F_z$$

$$+\left(\frac{\begin{cases} 2l_f^2 + l_i^2 + 2l_i(l_f + 2d_i + l_p) + 2l_p(l_f + d_i + l_p) \\ + 2l_p(l_f + d_i + l_p) + 2(l_p + d_i)^2 \\ + 2(l_p + d_i)(l_f + d_i) + 2l_f(l_p + d_i) - l_p^2 \end{cases}}{2EI} + \frac{\begin{cases} (l_f + d_i)l_0 + \\ (l_f + l_p + d_i)l_0 + l_f l_0 \\ + (l_f + 2d_i + l_p)l_0 \end{cases}}{GJ} \right) M_y \qquad (3.9)$$

Equation (3.7) indicates the torsional deformation at the free end of the spring solely depends on the external torque applied, while the slope angle and transverse bending deflection at the free end depend on both the applied vertical force and the bending moment, as given by Equations (3.8) and (3.9). These two equations can be rewritten as:

$$\begin{aligned} \varphi_0 &= C_{11}F_z + C_{12}M_y \\ \delta_0 &= C_{21}F_z + C_{22}M_y \end{aligned} \qquad (3.10)$$

where coefficients C_{11}, C_{12}, C_{21}, C_{22} are the members for the flexibility matrix for the spring. The torsional stiffness k_t for a rotational serpentine spring with only one serpentine loop is therefore derived from Equation (3.7):

$$k_t = \left(\frac{l_i + l_f + 2d_i + 3l_p}{GJ} + \frac{4l_0}{EI} \right)^{-1} \qquad (3.11)$$

Meanwhile, due to the assumption of the rigid mirror plate and the balanced moment at the free end of a side spring, the bending slope φ_0 at this point is zero (φ_0=0). Substituting this boundary condition into Equation (3.10) yields the out-of-plane bending stiffness at the free end of the side spring. Other stiffness coefficients can be similarly derived by solving Equation (3.10), which are shown below:

$$k_{\varphi} = \frac{C_{21}}{C_{12}C_{21} - C_{11}C_{22}} \qquad k_{\delta} = \frac{C_{12}}{C_{12}C_{21} - C_{11}C_{22}}$$
$$k_{\varphi z} = \frac{C_{22}}{C_{11}C_{22} - C_{12}C_{21}} \qquad k_{z\varphi} = \frac{C_{11}}{C_{11}C_{22} - C_{12}C_{21}} \tag{3.12}$$

where k_{φ} is the stiffness constant to the bending slope at the free end resisting against the out-of-plane bending moment; k_{δ} is the bending stiffness resisting against the vertical force; $k_{\varphi z}$ and $k_{z\varphi}$ are the stiffness constants indicating the coupled relations between the two deflection modes: the bending component due to moment M_y and the bending due to the vertical force F_z. As mentioned, since $\varphi_0=0$ and $M_y=0$, the out-of-plane bending stiffness for a side spring is thus found from Equation (3.10).

3.3.2 Static Analysis of Torsional Micromirrors

Structural symmetry with respect to the centre of the micromirror can be observed from the given torsional micromiror (Figure 3.3). The applied load resulted from electrostatic actuation can be equally divided onto the two side springs. Therefore the torsional stiffness constant for the complete micromirror is two times of each torsional spring constant,

$$K_t = 2k_t = 2\left(\frac{l_i + l_f + 2d_i + 3l_p}{GJ} + \frac{4l_0}{EI}\right)^{-1} \tag{3.13}$$

Similarly, as indicated by the structural symmetry, the out-of-plane bending stiffness constant for the complete suspension of the micromirror is also a two-fold of the corresponding stiffness for one side spring, that is, $K_b=2k_{\delta}$, where k_{δ} can be directly solved from Equation (3.9).

As above discussed, in consideration of the soft serpentine springs and the non-deformable mirror plate, it is reasonable to approximate the torsional micromirror with a decoupled 2-DOF model, thus the static equations for this micromirror can be re-written here:

$$K_b z = F_e \quad and \quad K_t \alpha = T_e \tag{3.14}$$

where F_e and T_e are the vertical force and the torque applied on the mirror plate arising from the electrostatic actuation. The solving process for Equations (3.14) and the expressions for the two electrostatic forces are provided in Section 2.2 of the thesis.

Similarly, the total strain energy for a serpentine spring comprising multiple loops of rotational serpentines can be solved by integration of all segments involved. Thus stiffness constants and static equations of motion for the torsional micromirror can be derived.

3.4 Modeling by Structural Matrix Method

Structural matrix method has been previously introduced. Compared to the linear energy method presented above, the structural matrix method is easy to be implemented and structured in an algorithm. The method is thus useful for complex framed structures. The complexity of modeling the framed micro-mechanism is increased if non-symmetric factors or unexpected phenomena are present to a microstructure, such as misalignment, undercut, non-uniform deposition, over-etch, tilt, warp and etc. during the microfabrication (Figure 3.5). However, this can be conveniently addressed by using the

structural matrix method. The derivation for the structural stiffness matrix at the free end of a planar rotational spring is provided in this section. The similar process of derivation can be applied to other types of framed structures, such as the planar grids or spatial frames.

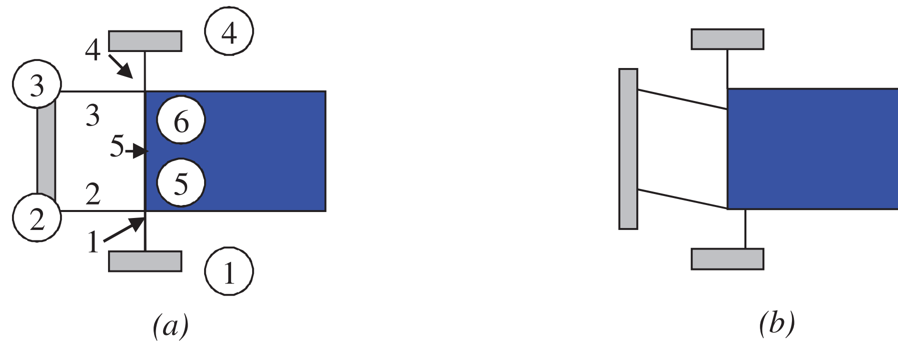

Figure 3.5 Schematic of micromirrors suspended by framed suspensions: (*a*) the ideally fabricated microstructure with numbering of nodes and beam segments; (*b*) the possible deviation of the fabricated microstructure.

The rotational serpentine spring shown in Figure 3.4 has only one rotational serpentine element connected with the initial part that is attached to the substrate in the other end and the final part that is connected with the mirror plate at the free end. However, a general rotational serpentine spring may consist of multiple elements of rotational serpentines. It can be decomposed to three parts: the initial part, the final part and the rotational serpentine elements, as shown in Figure 3.6. This separation is to reduce the order of the matrices needed for the analysis. Moreover, the matrix equation for the multiple rotational serpentine elements can be obtained by multiplication of all identical elements. Therefore the static matrix equations for the three parts of a rotational serpentine spring are derived in three separate sections below.

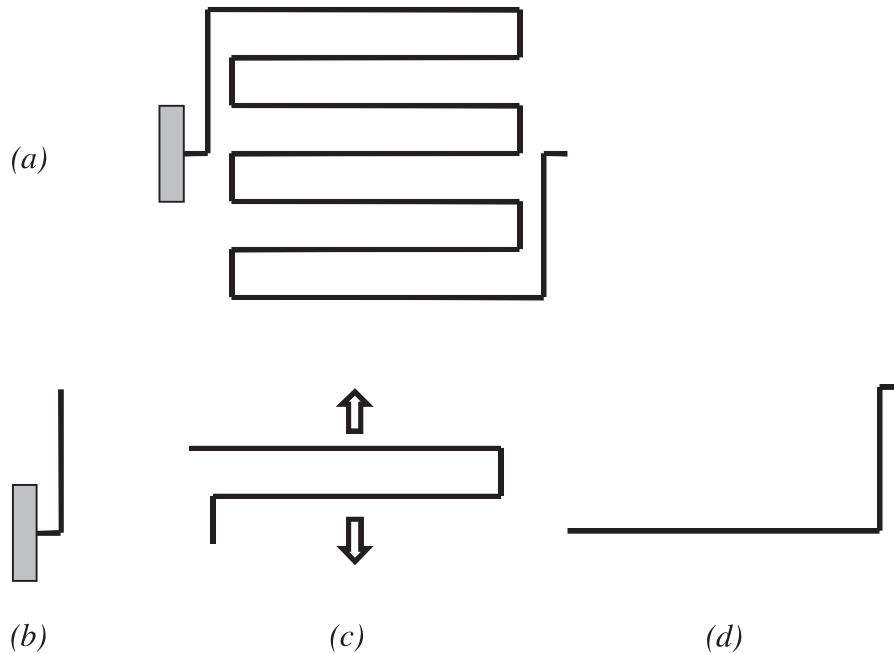

Figure 3.6 The schematic diagrams for (*a*) a serpentine spring with multiple loops of rotational serpentine; (*b*) the initial part attached to the substrate; (*c*) one rotational serpentine loop and (*d*) the final part attached with the mirror plate.

3.4.1 The Static Equation for a Rotational Serpentine Element

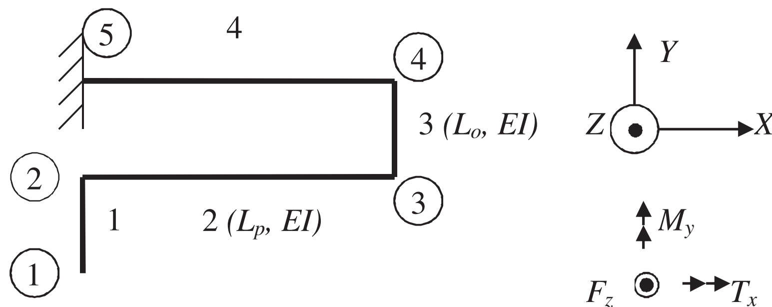

Figure 3.7 A basic serpentine element with four segments and five nodes

One rotational serpentine element extracted from the general rotational serpentine spring (Figure 3.5) is shown in Figure 3.7 with new numbering for the segments and nodes. Any rotational serpentine spring is formed by one or more of such elements with the initial part and the final part. This section provides only the deduction of static matrix equations of the element or loop. The global coordinates and the internal loads on any node are also shown in Figure 3.8. This planar frame is subjected to a torque, a moment and a vertical force transferred at the free end (Node #1) and each node or restraint joint is loaded internally by a vertical force, a torque and an out-of-plane bending moment (F_z, T_x, M_y). The corresponding displacements will be in an order of (Δ_z, Θ_x, Θ_y). The member stiffness matrix K_{mi} in the local Cartesian coordinates for a beam segment that has the initial joint/node and the free joint/node at its ends can be written and arranged as shown in Figure 3.8, where *EI*, *L*, *G* and *J* are the flexural rigidity, length, shear modulus, and cross-sectional polar moment of inertia of the beam in the loop respectively.

Thus the structural stiffness matrix in the global Cartesian for the member can be obtained by transforming the local member stiffness matrix, which is shown as

$$K_{msi} = R_T^T K_{mi} R_T \tag{3.15}$$

where K_{msi} is the member stiffness matrix in the global Cartesian, also called structural member stiffness matrix; R_T^T is the transpose of the transformation matrix R_T. The transformation matrix R_T for a beam member in a planar grid has the form of [163]:

$$R_T = \begin{bmatrix} R & 0 \\ 0 & R \end{bmatrix} \tag{3.16}$$

Equation 3.16 shows that a transformation matrix is composed of two rotation matrices arranged in diagonal. The rotation matrix for a spatial beam member is a multiplication of two rotation matrices:

$$R=R_{\alpha}R_{\beta} \tag{3.17}$$

$$
\begin{array}{cc|cccccc}
 & & \multicolumn{3}{c}{①} & \multicolumn{3}{c}{②} \\
 & & z & x & y & z & x & y \\
\hline
 & z & \frac{12EI}{L^3} & 0 & -\frac{6EI}{L^2} & -\frac{12EI}{L^3} & 0 & -\frac{6EI}{L^2} \\
① & x & 0 & \frac{GJ}{L} & 0 & 0 & -\frac{GJ}{L} & 0 \\
 & y & -\frac{6EI}{L^2} & 0 & \frac{4EI}{L} & \frac{6EI}{L^2} & 0 & \frac{2EI}{L} \\
 & z & -\frac{12EI}{L^3} & 0 & \frac{6EI}{L^2} & \frac{12EI}{L^3} & 0 & \frac{6EI}{L^2} \\
② & x & 0 & -\frac{GJ}{L} & 0 & 0 & \frac{GJ}{L} & 0 \\
 & y & -\frac{6EI}{L^2} & 0 & \frac{2EI}{L} & \frac{6EI}{L^2} & 0 & \frac{4EI}{L}
\end{array}
$$

Figure 3.8 A stiffness matrix for a planar beam segment. The terms in the columns and rows of the matrix are arranged in the same order as the numbering of joints and are set to conform to the order of load and displacement vectors.

where α is defined as the in-plane rotation angle of the beam and β is the out-of-plane rotation angle of the beam; R_{α} is the rotation matrix of the beam at an angle α; R_{β} is the rotation matrix at an angle of β. According to the planar grid in Figure 3.6, the local coordinates and the global coordinates share z-axis, thus there is no out-of-plane rotation (β=0). Then rotation matrix R in Equation (3.16) is a matrix with one in-plane rotation, thus $R=R_{\alpha}$. Given the orthogonal structure, the rotation angle is equal to either 90º or 0º (positive value for the counter-clockwise rotation). As a result the rotation matrices for

members 1 and 3 are equal because of the right angle of orientation with respect to the global X-axis ($\alpha=90°$). The rotation matrices and the transformation matrices for these two members in 3-DOF can be written as

$$R_1 = R_3 = \begin{bmatrix} 1 & 0 & 0 \\ 0 & \cos\alpha & \sin\alpha \\ 0 & -\sin\alpha & \cos\alpha \end{bmatrix}_{\alpha=90^\circ} = \begin{bmatrix} 1 & 0 & 0 \\ 0 & 0 & 1 \\ 0 & -1 & 0 \end{bmatrix} \tag{3.18}$$

$$R_{T1} = R_{T3} = \begin{bmatrix} R & 0 \\ 0 & R \end{bmatrix} = \begin{bmatrix} 1 & 0 & 0 & 0 & 0 & 0 \\ 0 & 0 & 1 & 0 & 0 & 0 \\ 0 & -1 & 0 & 0 & 0 & 0 \\ 0 & 0 & 0 & 1 & 0 & 0 \\ 0 & 0 & 0 & 0 & 0 & 1 \\ 0 & 0 & 0 & 0 & -1 & 0 \end{bmatrix} \tag{3.19}$$

It can be seen from Figure 3.6 that members 2 and 4 are opposite in their orientation angles and thus their rotation and transformation matrices can be written accordingly:

$$R_2 = \begin{bmatrix} 1 & 0 & 0 \\ 0 & \cos\alpha & \sin\alpha \\ 0 & -\sin\alpha & \cos\alpha \end{bmatrix} = \begin{bmatrix} 1 & 0 & 0 \\ 0 & 1 & 0 \\ 0 & 0 & 1 \end{bmatrix}_{\alpha=0^\circ} \tag{3.20}$$

$$R_4 = \begin{bmatrix} 1 & 0 & 0 \\ 0 & \cos\alpha & \sin\alpha \\ 0 & -\sin\alpha & \cos\alpha \end{bmatrix} = \begin{bmatrix} 1 & 0 & 0 \\ 0 & -1 & 0 \\ 0 & 0 & -1 \end{bmatrix}_{\alpha=180^\circ} \tag{3.21}$$

According to Equation (3.15) and Figure 3.7, structural member stiffness matrices for individual members in the loop can be derived as:

$$K_{ms1} = K_{ms3} = \begin{bmatrix} \frac{12EI}{L_0^3} & \frac{6EI}{L_0^2} & 0 & -\frac{12EI}{L_0^3} & \frac{6EI}{L_0^2} & 0 \\ \frac{6EI}{L_0^2} & \frac{4EI}{L_0} & 0 & -\frac{6EI}{L_0^2} & \frac{2EI}{L_0} & 0 \\ 0 & 0 & \frac{GJ}{L_0} & 0 & 0 & -\frac{GJ}{L_0} \\ -\frac{12EI}{L_0^3} & -\frac{6EI}{L_0^2} & 0 & \frac{12EI}{L_0^3} & -\frac{6EI}{L_0^2} & 0 \\ \frac{6EI}{L_0^2} & \frac{2EI}{L_0} & 0 & -\frac{6EI}{L_0^2} & \frac{4EI}{L_0} & 0 \\ 0 & 0 & -\frac{GJ}{L_0} & 0 & 0 & \frac{GJ}{L_0} \end{bmatrix} \tag{3.22}$$

$$K_{ms2} = K_{m2} = \begin{bmatrix} \frac{12EI}{L_p^3} & 0 & -\frac{6EI}{L_p^2} & -\frac{12EI}{L_p^3} & 0 & -\frac{6EI}{L_p^2} \\ 0 & \frac{GJ}{L_p} & 0 & 0 & -\frac{GJ}{L_p} & 0 \\ -\frac{6EI}{L_p^2} & 0 & \frac{4EI}{L_p} & \frac{6EI}{L_p^2} & 0 & \frac{2EI}{L_p} \\ -\frac{12EI}{L_p^3} & 0 & \frac{6EI}{L_p^2} & \frac{12EI}{L_p^3} & 0 & \frac{6EI}{L_p^2} \\ 0 & -\frac{GJ}{L_p} & 0 & 0 & \frac{GJ}{L_p} & 0 \\ -\frac{6EI}{L_p^2} & 0 & \frac{2EI}{L_p} & \frac{6EI}{L_p^2} & 0 & \frac{4EI}{L_p} \end{bmatrix} \tag{3.23}$$

$$K_{ms4} = \begin{bmatrix} \frac{12EI}{L_p^3} & 0 & \frac{6EI}{L_p^2} & -\frac{12EI}{L_p^3} & 0 & \frac{6EI}{L_p^2} \\ 0 & \frac{GJ}{L_p} & 0 & 0 & -\frac{GJ}{L_p} & 0 \\ \frac{6EI}{L_p^2} & 0 & \frac{4EI}{L_p} & -\frac{6EI}{L_p^2} & 0 & \frac{2EI}{L_p} \\ -\frac{12EI}{L_p^3} & 0 & -\frac{6EI}{L_p^2} & \frac{12EI}{L_p^3} & 0 & -\frac{6EI}{L_p^2} \\ 0 & -\frac{GJ}{L_p} & 0 & 0 & \frac{GJ}{L_p} & 0 \\ \frac{6EI}{L_p^2} & 0 & \frac{2EI}{L_p} & -\frac{6EI}{L_p^2} & 0 & \frac{4EI}{L_p} \end{bmatrix} \tag{3.24}$$

The structural stiffness matrix method distinguishes it from other matrix methods by enabling the construction of a global stiffness matrix to cover all beam members and all nodes of the structure by summing up all stiffness terms at the same position in the global stiffness matrix instead of multiplying all individual stiffness matrices for beam members. Figure 3.8 shows the assembly and the distribution of each structural member matrix and its terms in the large matrix. The order of the assembled matrix can be found from the number of DOFs for each beam member and the node number. For the structure shown in Figure 3.6, a 15×15 matrix can be resulted (5 nodes by 3 DOFs).

The constraints are denoted by load vector P_r and the vector D_r represents for the displacement of the restrained nodes. F_f and D_f represent for load vector and displacement vector for the free joints. Then the global stiffness matrix can be partitioned into sub-matrices that correspond to the constraints and the free joints. The static equation for the rotational serpentine loop can thus be formulated in matrix form as

$$\begin{Bmatrix} F_f \\ P_r \end{Bmatrix} = \begin{bmatrix} K_{ff} & K_{fr} \\ K_{rf} & K_{rr} \end{bmatrix} \begin{Bmatrix} D_f \\ D_r \end{Bmatrix} \tag{3.25}$$

As one can see from Figure 3.8, the last three rows and columns represent the stiffness matrix at the last joint which is the real restraint for the entire structure. Compared to Equatin (3.25), the matrix K_{ff} is constructed by the 12×12 upper left part of the global matrix, which can be reformed to

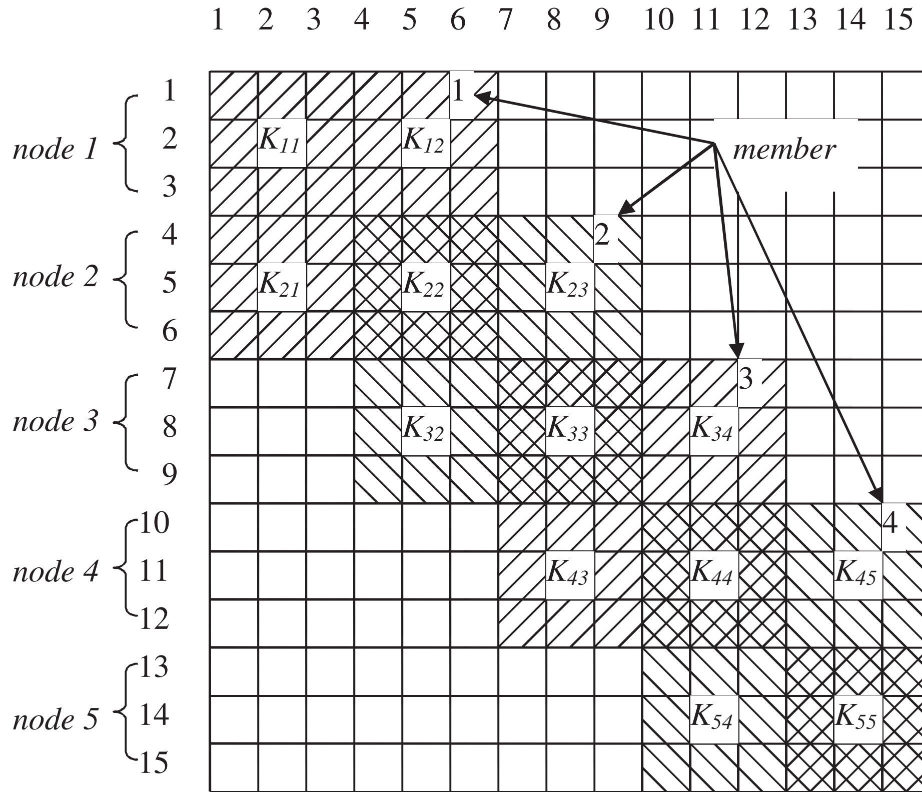

Figure 3.9 The global stiffness matrix for a complete rotational serpentine spring assembled from all individual member stiffness matrices in the global coordinates.

$$K_{ff} = \begin{bmatrix} K_{11} & K_{12} & K_{13} & K_{14} \\ K_{21} & K_{22} & K_{23} & K_{24} \\ K_{31} & K_{32} & K_{33} & K_{34} \\ K_{41} & K_{42} & K_{43} & K_{44} \end{bmatrix} \tag{3.26}$$

Each matrix term in K_{ff} is in an order of 3×3, representing the stiffness matrix for all free joints of a rotational serpentine loop. The non-zero sub-matrices in K_{ff} for the rotational serpentine loop shown in Figure 3.6 are provided as follows (derivation is omitted).

$$K_{11}=\begin{bmatrix}\frac{12EI}{L_0^3} & \frac{6EI}{L_0^2} & 0\\ \frac{6EI}{L_0^2} & \frac{4EI}{L_0} & 0\\ 0 & 0 & \frac{GJ}{L_0}\end{bmatrix},\quad K_{12}=\begin{bmatrix}-\frac{12EI}{L_0^3} & \frac{6EI}{L_0^2} & 0\\ -\frac{6EI}{L_0^2} & \frac{2EI}{L_0} & 0\\ 0 & 0 & -\frac{GJ}{L_0}\end{bmatrix}$$

$$K_{21}=\begin{bmatrix}-\frac{12EI}{L_0^3} & -\frac{6EI}{L_0^2} & 0\\ \frac{6EI}{L_0^2} & \frac{2EI}{L_0} & 0\\ 0 & 0 & -\frac{GJ}{L_0}\end{bmatrix},\quad K_{22}=\begin{bmatrix}\frac{12EI}{L_0^3}+\frac{12EI}{L_p^3} & -\frac{6EI}{L_0^2} & -\frac{6EI}{L_p^2}\\ -\frac{6EI}{L_0^2} & \frac{4EI}{L_0}+\frac{GJ}{L_p} & 0\\ -\frac{6EI}{L_p^2} & 0 & \frac{GJ}{L_0}+\frac{4EI}{L_p}\end{bmatrix}$$

$$K_{23}=\begin{bmatrix}-\frac{12EI}{L_p^3} & 0 & -\frac{6EI}{L_p^2}\\ 0 & -\frac{GJ}{L_p} & 0\\ \frac{6EI}{L_p^2} & 0 & \frac{2EI}{L_p}\end{bmatrix},\quad K_{32}=\begin{bmatrix}-\frac{12EI}{L_p^3} & 0 & \frac{6EI}{L_p^2}\\ 0 & -\frac{GJ}{L_p} & 0\\ -\frac{6EI}{L_p^2} & 0 & \frac{2EI}{L_p}\end{bmatrix}$$

$$K_{33}=\begin{bmatrix}\frac{12EI}{L_p^3}+\frac{12EI}{L_0^3} & \frac{6EI}{L_0^2} & \frac{6EI}{L_p^2}\\ \frac{6EI}{L_0^2} & \frac{GJ}{L_p}+\frac{4EI}{L_0} & 0\\ \frac{6EI}{L_p^2} & 0 & \frac{4EI}{L_p}+\frac{GJ}{L_0}\end{bmatrix},\quad K_{34}=\begin{bmatrix}-\frac{12EI}{L_0^3} & \frac{6EI}{L_0^2} & 0\\ -\frac{6EI}{L_0^2} & \frac{2EI}{L_0} & 0\\ 0 & 0 & -\frac{GJ}{L_0}\end{bmatrix}$$

$$K_{43}=\begin{bmatrix}-\frac{12EI}{L_0^3} & -\frac{6EI}{L_0^2} & 0\\ \frac{6EI}{L_0^2} & \frac{2EI}{L_0} & 0\\ 0 & 0 & -\frac{GJ}{L_0}\end{bmatrix},\quad K_{44}=\begin{bmatrix}\frac{12EI}{L_0^3}+\frac{12EI}{L_p^3} & -\frac{6EI}{L_0^2} & \frac{6EI}{L_p^2}\\ -\frac{6EI}{L_0^2} & \frac{4EI}{L_0}+\frac{GJ}{L_p} & 0\\ \frac{6EI}{L_p^2} & 0 & \frac{GJ}{L_0}+\frac{4EI}{L_p}\end{bmatrix}$$

$$K_{54} = \begin{bmatrix} -\frac{12EI}{L_p^3} & 0 & -\frac{6EI}{L_p^2} \\ 0 & -\frac{GJ}{L_p} & 0 \\ \frac{6EI}{L_p^2} & 0 & \frac{2EI}{L_p} \end{bmatrix}$$

Thus the serpentine loop has the following static equation that relates the forces with the deformations:

$$\begin{Bmatrix} F_{f1} \\ F_{f2} \\ F_{f3} \\ F_{f4} \\ F_{r5} \end{Bmatrix} = \begin{bmatrix} K_{11} & K_{12} & 0 & 0 & 0 \\ K_{21} & K_{22} & K_{23} & 0 & 0 \\ 0 & K_{32} & K_{33} & K_{34} & 0 \\ 0 & 0 & K_{43} & K_{44} & K_{45} \\ 0 & 0 & 0 & K_{54} & K_{55} \end{bmatrix} \begin{Bmatrix} D_{f1} \\ D_{f2} \\ D_{f3} \\ D_{f4} \\ D_{r5} \end{Bmatrix} \tag{3.27}$$

where $F_{f1}=(F_Z, T_X, M_y)^T$, $F_{f2}=0$, $F_{f3}=0$, $F_{f4}=0$ and $D_{r5}=0$ since there is no external load applied at the internal nodes of the structure except at the free end (Node #1) and also no displacement is assumed at the restraint (Node #5). Thus the global equation of motion for the free end of the structure can be expressed from Equation (3.27) as:

$$F_{f1} = \begin{Bmatrix} F_z \\ T_x \\ M_y \end{Bmatrix} = \left[K_{11} + \frac{K_{12}K_{21}(K_{33}K_{44} + K_{34}K_{43})}{K_{23}K_{32}K_{44} + K_{22}K_{34}K_{43} - K_{22}K_{33}K_{44}} \right] D_{f1} \tag{3.28}$$

Similarly, the reaction force vector F_{r5} at the assumed fixed end of the serpentine element can be solved by letting $D_{r5}=0$ in Equation (3.27), that is

$$F_{r5} = \frac{K_{32}K_{43}K_{54}}{K_{33}K_{44} - K_{43}K_{34}} \frac{F_{f1} - K_{11}D_{f1}}{K_{12}} \tag{3.29}$$

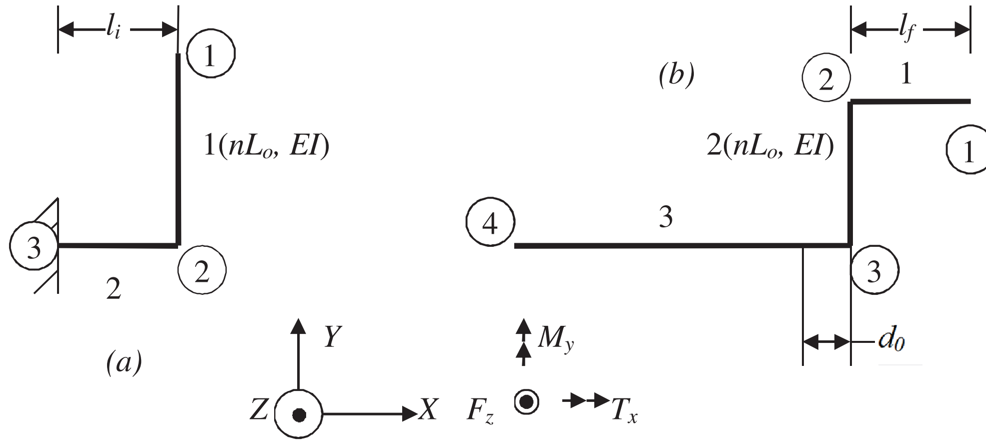

Figure 3.9 The schematic diagrams for (*a*) the initial part and (*b*) the final part of a rotational serpentine spring.

3.4.2 Static Matrix Equations for Initial and Final Parts

The total stiffness matrix for a torsional serpentine spring shown in Figure 3.4 should include the contributions from the initial part (composed of two segments) and the final part (composed of three segments), as shown in Figure 3.9 (*a*) and (*b*), respectively. The external applied loads at Node #1 in the initial part have been derived as F_r from Equation (3.29) in the previous sub-section and the boundary conditions for the fixed joint (Node #3) of this part can be described as D_3=0. The rotation matrices R_1 and R_2 for the two members are given as:

$$R_1 = \begin{bmatrix} 1 & 0 & 0 \\ 0 & 0 & -1 \\ 0 & 1 & 0 \end{bmatrix}_{\alpha=-90^\circ} \quad , \quad R_2 = \begin{bmatrix} 1 & 0 & 0 \\ 0 & -1 & 0 \\ 0 & 0 & -1 \end{bmatrix}_{\alpha=180^\circ} \tag{3.30}$$

Thus the two structural member stiffness matrices transferred from their local coordinates to the global Cartesian can be similarly derived. The elements are numbered for derivations. Here, L_o is the length of one of the orthogonal segments; n is the loop number of the spring, whereas L_i and L_f are lengths as shown. If only one loop is used, n=1. The structural stiffness matrices for segments #1 and #2 in the initial part can be expressed as

$$K_{ms1}^{i} = \begin{bmatrix} \frac{12EI}{L_0^3} & -\frac{6EI}{L_0^2} & 0 & -\frac{12EI}{L_0^3} & -\frac{6EI}{L_0^2} & 0 \\ -\frac{6EI}{L_0^2} & \frac{4EI}{L_0} & 0 & \frac{6EI}{L_0^2} & \frac{2EI}{L_0} & 0 \\ 0 & 0 & \frac{GJ}{L_0} & 0 & 0 & -\frac{GJ}{L_0} \\ -\frac{12EI}{L_0^3} & \frac{6EI}{L_0^2} & 0 & \frac{12EI}{L_0^3} & \frac{6EI}{L_0^2} & 0 \\ -\frac{6EI}{L_0^2} & \frac{2EI}{L_0} & 0 & \frac{6EI}{L_0^2} & \frac{4EI}{L_0} & 0 \\ 0 & 0 & -\frac{GJ}{L_0} & 0 & 0 & \frac{GJ}{L_0} \end{bmatrix} \tag{3.31}$$

$$K_{ms2}^{i} = \begin{bmatrix} \frac{12EI}{L_i^3} & 0 & \frac{6EI}{L_i^2} & -\frac{12EI}{L_i^3} & 0 & \frac{6EI}{L_i^2} \\ 0 & \frac{GJ}{L_i} & 0 & 0 & -\frac{GJ}{L_i} & 0 \\ \frac{6EI}{L_i^2} & 0 & \frac{4EI}{L_i} & -\frac{6EI}{L_i^2} & 0 & \frac{2EI}{L_i} \\ -\frac{12EI}{L_i^3} & 0 & -\frac{6EI}{L_i^2} & \frac{12EI}{L_i^3} & 0 & -\frac{6EI}{L_i^2} \\ 0 & -\frac{GJ}{L_i} & 0 & 0 & \frac{GJ}{L_i} & 0 \\ \frac{6EI}{L_i^2} & 0 & \frac{2EI}{L_i} & -\frac{6EI}{L_i^2} & 0 & \frac{4EI}{L_i} \end{bmatrix} \tag{3.32}$$

where the superscript i rmeans the initial part. Thus the static matrix equation of motion for the initial part can be written as

$$\begin{Bmatrix} F_{f1} \\ F_{f2} \\ F_{r3} \end{Bmatrix}_i = \begin{bmatrix} K_{11} & K_{12} & 0 \\ K_{21} & K_{22} & K_{23} \\ 0 & K_{32} & K_{33} \end{bmatrix}_i \begin{Bmatrix} D_{f1} \\ D_{f2} \\ D_{r3} \end{Bmatrix}_i \tag{3.33}$$

Since external loads applied on Node 2 are zero ($F_{f2}=0$) and displacements for the restraint are also zero ($D_{r3}=0$), static equations for Node 1 (the free end for the initial part) and reactive loads at Node 3 (the assumed fixed end of the initial part) of zero displacements can be solved as

$$F_{f1}^i = \left(K_{11}^i - \frac{K_{12}^i K_{21}^i}{K_{22}^i} \right) D_{f1}^i \tag{3.34}$$

in which the resultant matrix in the parenthesis is the global structural stiffness matrix for the initial part of the spring. All other non-zero sub-matrices are listed below:

$$K_{11}^i = \begin{bmatrix} \frac{12EI}{L_0^3} & -\frac{6EI}{L_0^2} & 0 \\ -\frac{6EI}{L_0^2} & \frac{4EI}{L_0} & 0 \\ 0 & 0 & \frac{GJ}{L_0} \end{bmatrix}, \quad K_{12}^i = \begin{bmatrix} -\frac{12EI}{L_0^3} & -\frac{6EI}{L_0^2} & 0 \\ \frac{6EI}{L_0^2} & \frac{2EI}{L_0} & 0 \\ 0 & 0 & -\frac{GJ}{L_0} \end{bmatrix},$$

$$K_{21}^i = \begin{bmatrix} -\frac{12EI}{L_0^3} & \frac{6EI}{L_0^2} & 0 \\ -\frac{6EI}{L_0^2} & \frac{2EI}{L_0} & 0 \\ 0 & 0 & -\frac{GJ}{L_0} \end{bmatrix}, \quad K_{22}^i = \begin{bmatrix} \frac{12EI}{L_0^3} + \frac{12EI}{L_i^3} & \frac{6EI}{L_0^2} & \frac{6EI}{L_i^2} \\ \frac{6EI}{L_0^2} & \frac{4EI}{L_0} + \frac{GJ}{L_i} & 0 \\ \frac{6EI}{L_i^2} & 0 & \frac{GJ}{L_0} + \frac{4EI}{L_i} \end{bmatrix}$$

$$K_{23}^{i}=\begin{bmatrix} -\frac{12EI}{L_i^3} & 0 & \frac{6EI}{L_i^2} \\ 0 & -\frac{GJ}{L_i} & 0 \\ -\frac{6EI}{L_i^2} & 0 & \frac{2EI}{L_i} \end{bmatrix},\ K_{32}^{i}=\begin{bmatrix} -\frac{12EI}{L_i^3} & 0 & -\frac{6EI}{L_i^2} \\ 0 & -\frac{GJ}{L_i} & 0 \\ \frac{6EI}{L_i^2} & 0 & \frac{2EI}{L_i} \end{bmatrix},$$

$$K_{33}^{i}=\begin{bmatrix} \frac{12EI}{L_i^3} & 0 & -\frac{6EI}{L_i^2} \\ 0 & \frac{GJ}{L_i} & 0 \\ -\frac{6EI}{L_i^2} & 0 & \frac{4EI}{L_i} \end{bmatrix}$$

Finally in Figure 3.9 (*b*), one can see that the final part of a torsional serpentine spring consists of three folded segments. The structural stiffness matrix for this part can be derived in the same way. The real external loads (F_Z, T_X, M_Y) are applied at Node 1 in this part. Though segments #1 and #3 are at the same orientation and have the same form of transformation matrices, their structural member stiffness matrices are different because of the different lengths. The structural member stiffness matrices in the global Cartesians for the three members are therefore deduced:

$$K_{ms1}^{f}=\begin{bmatrix} \frac{12EI}{L_f^3} & 0 & \frac{6EI}{L_f^2} & -\frac{12EI}{L_f^3} & 0 & \frac{6EI}{L_f^2} \\ 0 & \frac{GJ}{L_f} & 0 & 0 & -\frac{GJ}{L_f} & 0 \\ \frac{6EI}{L_f^2} & 0 & \frac{4EI}{L_f} & -\frac{6EI}{L_f^2} & 0 & \frac{2EI}{L_f} \\ -\frac{12EI}{L_f^3} & 0 & -\frac{6EI}{L_f^2} & \frac{12EI}{L_f^3} & 0 & -\frac{6EI}{L_f^2} \\ 0 & -\frac{GJ}{L_f} & 0 & 0 & \frac{GJ}{L_f} & 0 \\ \frac{6EI}{L_f^2} & 0 & \frac{2EI}{L_f} & -\frac{6EI}{L_f^2} & 0 & \frac{4EI}{L_f} \end{bmatrix} \tag{3.35}$$

$$K_{ms2}^f = \begin{bmatrix} \frac{12EI}{L_0^3} & -\frac{6EI}{L_0^2} & 0 & -\frac{12EI}{L_0^3} & -\frac{6EI}{L_0^2} & 0 \\ -\frac{6EI}{L_0^2} & \frac{4EI}{L_0} & 0 & \frac{6EI}{L_0^2} & \frac{2EI}{L_0} & 0 \\ 0 & 0 & \frac{GJ}{L_0} & 0 & 0 & -\frac{GJ}{L_0} \\ -\frac{12EI}{L_0^3} & \frac{6EI}{L_0^2} & 0 & \frac{12EI}{L_0^3} & \frac{6EI}{L_0^2} & 0 \\ -\frac{6EI}{L_0^2} & \frac{2EI}{L_0} & 0 & \frac{6EI}{L_0^2} & \frac{4EI}{L_0} & 0 \\ 0 & 0 & -\frac{GJ}{L_0} & 0 & 0 & \frac{GJ}{L_0} \end{bmatrix} \tag{3.36}$$

$$K_{ms3}^f = \begin{bmatrix} \frac{12EI}{(L_p+d_0)^3} & 0 & \frac{6EI}{(L_p+d_0)^2} & -\frac{12EI}{(L_p+d_0)^3} & 0 & \frac{6EI}{(L_p+d_0)^2} \\ 0 & \frac{GJ}{L_p+d_0} & 0 & 0 & -\frac{GJ}{L_p+d_0} & 0 \\ \frac{6EI}{(L_p+d_0)^2} & 0 & \frac{4EI}{L_p+d_0} & -\frac{6EI}{(L_p+d_0)^2} & 0 & \frac{2EI}{L_p+d_0} \\ -\frac{12EI}{(L_p+d_0)^3} & 0 & -\frac{6EI}{(L_p+d_0)^2} & \frac{12EI}{(L_p+d_0)^3} & 0 & -\frac{6EI}{(L_p+d_0)^2} \\ 0 & -\frac{GJ}{L_p+d_0} & 0 & 0 & \frac{GJ}{L_p+d_0} & 0 \\ \frac{6EI}{(L_p+d_0)^2} & 0 & \frac{2EI}{L_p+d_0} & -\frac{6EI}{(L_p+d_0)^2} & 0 & \frac{4EI}{L_p+d_0} \end{bmatrix} \tag{3.37}$$

The assembled structural stiffness matrix and the static equation for this part are written below:

$$\begin{Bmatrix} F_{f1} \\ F_{f2} \\ F_{f3} \\ F_{r4} \end{Bmatrix}_f = \begin{bmatrix} K_{11} & K_{12} & 0 & 0 \\ K_{21} & K_{22} & K_{23} & 0 \\ 0 & K_{32} & K_{33} & K_{34} \\ 0 & 0 & K_{43} & K_{44} \end{bmatrix}_f \begin{Bmatrix} D_{f1} \\ D_{f2} \\ D_{f3} \\ D_{r4} \end{Bmatrix}_f \tag{3.38}$$

where the similar partition to the global stiffness matrix gives the form of matrices in Equation (3.25) as follows.

$$K_{ff}^f = \begin{bmatrix} K_{11} & K_{12} \\ K_{21} & K_{22} \end{bmatrix}_f, \quad K_{fr}^f = \begin{bmatrix} 0 \\ K_{23} \end{bmatrix}_f, \quad K_{rf}^f = \begin{bmatrix} 0 & K_{32} \end{bmatrix}_f, \quad K_{rr}^f = K_{33}^f$$

Since there is no external load for nodes #2 and #3, i. e. F_{f2}=0 and F_{f3}=0, and D_{r4}=0 due to the assumed fixed end, then solving Equation (3.38) results in the static matrix equation for the free node:

$$F_{r4}^f = \frac{K_{21}^f K_{32}^f K_{43}^f}{K_{11}^f (K_{22}^f K_{33}^f - K_{23}^f K_{32}^f) - K_{12}^f K_{21}^f K_{33}^f} F_{f1}^f \tag{3.39}$$

$$D_{f1}^f = \frac{K_{22}^f K_{33}^f - K_{23}^f K_{32}^f}{K_{11}^f (K_{22}^f K_{33}^f - K_{23}^f K_{32}^f) - K_{12}^f K_{21}^f K_{33}^f} F_{f1}^f \quad or \quad F_{f1}^f = \left(K_{11}^f - \frac{K_{12}^f K_{21}^f K_{33}^f}{K_{22}^f K_{33}^f - K_{23}^f K_{32}^f} \right) D_{f1}^f \tag{3.40}$$

where

$$K_{11}^f = \begin{bmatrix} \frac{12EI}{L_f^3} & 0 & \frac{6EI}{L_f^2} \\ 0 & \frac{GJ}{L_f} & 0 \\ \frac{6EI}{L_f^2} & 0 & \frac{4EI}{L_f} \end{bmatrix}, \quad K_{12}^f = \begin{bmatrix} -\frac{12EI}{L_f^3} & 0 & \frac{6EI}{L_f^2} \\ 0 & -\frac{GJ}{L_f} & 0 \\ -\frac{6EI}{L_f^2} & 0 & \frac{2EI}{L_f} \end{bmatrix},$$

$$K_{21}^f = \begin{bmatrix} -\frac{12EI}{L_f^3} & 0 & -\frac{6EI}{L_f^2} \\ 0 & -\frac{GJ}{L_f} & 0 \\ \frac{6EI}{L_f^2} & 0 & \frac{2EI}{L_f} \end{bmatrix}, K_{22}^f = \begin{bmatrix} \frac{12EI}{L_f^3} + \frac{12EI}{L_0^3} & -\frac{6EI}{L_0^2} & -\frac{6EI}{L_f^2} \\ -\frac{6EI}{L_0^2} & \frac{GJ}{L_f} + \frac{4EI}{L_0} & 0 \\ -\frac{6EI}{L_f^2} & 0 & \frac{4EI}{L_f} + \frac{GJ}{L_0} \end{bmatrix},$$

$$K_{23}^f = \begin{bmatrix} -\frac{12EI}{L_0^3} & -\frac{6EI}{L_0^2} & 0 \\ \frac{6EI}{L_0^2} & \frac{2EI}{L_0} & 0 \\ 0 & 0 & -\frac{GJ}{L_0} \end{bmatrix}, \quad K_{32}^f = \begin{bmatrix} -\frac{12EI}{L_0^3} & \frac{6EI}{L_0^2} & 0 \\ -\frac{6EI}{L_0^2} & \frac{2EI}{L_0} & 0 \\ 0 & 0 & -\frac{GJ}{L_0} \end{bmatrix},$$

$$K_{33}^{f}=\begin{bmatrix} \frac{12EI}{L_0^3}+\frac{12EI}{(L_p+d_0)^3} & \frac{6EI}{L_0^2} & \frac{6EI}{(L_p+d_0)^2} \\ \frac{6EI}{L_0^2} & \frac{4EI}{L_0}+\frac{GJ}{L_p+d_0} & 0 \\ \frac{6EI}{(L_p+d_0)^2} & 0 & \frac{GJ}{L_0}+\frac{4EI}{L_p+d_0} \end{bmatrix},$$

$$K_{34}^{f}=\begin{bmatrix} \frac{-12EI}{(L_p+d_0)^3} & 0 & \frac{6EI}{(L_p+d_0)^2} \\ 0 & \frac{-GJ}{L_p+d_0} & 0 \\ \frac{-6EI}{(L_p+d_0)^2} & 0 & \frac{2EI}{L_p+d_0} \end{bmatrix}, \quad K_{43}^{f}=\begin{bmatrix} \frac{-12EI}{(L_p+d_0)^3} & 0 & \frac{-6EI}{(L_p+d_0)^2} \\ 0 & \frac{-GJ}{L_p+d_0} & 0 \\ \frac{6EI}{(L_p+d_0)^2} & 0 & \frac{2EI}{L_p+d_0} \end{bmatrix},$$

and

$$K_{44}^{f}=\begin{bmatrix} \frac{12EI}{(L_p+d_0)^3} & 0 & \frac{-6EI}{(L_p+d_0)^2} \\ 0 & \frac{GJ}{L_p+d_0} & 0 \\ \frac{-6EI}{(L_p+d_0)^2} & 0 & \frac{4EI}{L_p+d_0} \end{bmatrix}$$

3.4.3 Static Matrix Equation of Motion for a Side Spring

Now that equations of motion for all three portions of a rotational serpentine spring have been derived, the global static equation of motion can be deduced similarly. As shown in Figure 3.10, since all equations for the three parts of a rotational serpentine spring have been transformed into the global coordinates, and each segment has been assumed as a cantilever during derivation, the total displacements at the free end of the spring equal the summation of all individual amounts, which is expressed by

$$D_f = D_1 + D_2 + D_3 = \frac{F_1}{K_1} + \frac{F_2}{K_2} + \frac{F_3}{K_3} = \frac{F_{f1}^i}{K_1} + \frac{F_{f1}}{K_2} + \frac{F_{f1}^f}{K_3} \tag{3.41}$$

As can be seen in Figure 3.10, K_1, K_2 and K_3 are the structural stiffness matrices in Equations (3.34), (3.40) and (3.28), respectively, whereas F_3 or F_{f1}^f is an external load matrix F_f applied at the free end of the spring. Derivation of the internal loads F_1 and F_2 yields

$$F_1 = \frac{K_{21}K_{32}K_{43}K_{54}(K_{33}K_{44} + K_{34}K_{43})F_2}{(K_{34}K_{43} - K_{33}K_{44})[K_{11}(K_{23}K_{32}K_{44} - K_{22}K_{33}K_{44} + K_{22}K_{34}K_{43}) + K_{12}K_{21}(K_{33}K_{44} + K_{34}K_{43})]}$$

$$F_2 = \frac{K_{21}^f K_{32}^f K_{43}^f F_f}{K_{12}^f K_{21}^f K_{33}^f - K_{11}^f K_{22}^f K_{33}^f + K_{11}^f K_{23}^f K_{32}^f}$$

Substitution of K_1, K_2, K_3 and F_1, F_2 into Equation (3.41) yields the global flexibility matrix or the inversion of structural stiffness matrix as well as an equation of motion for the free end of the spring, that is

$$D_f = CF_f = K^{-1}F_f \quad or \quad F_f = KD_f \tag{3.42}$$

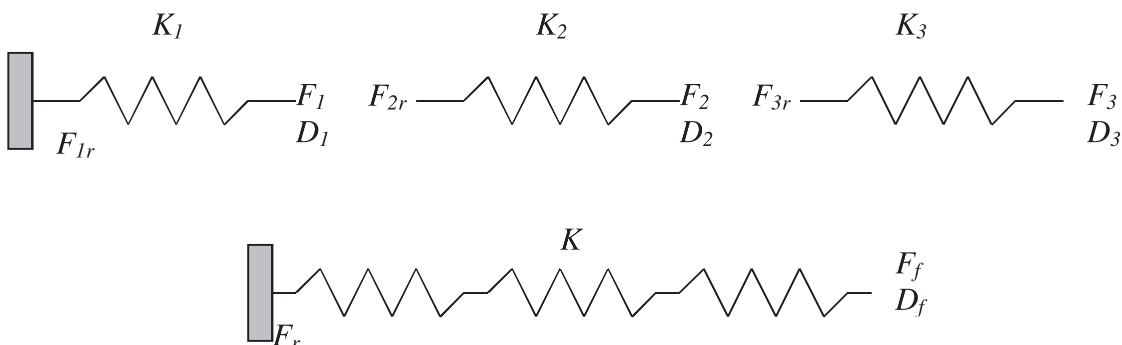

Figure 3.11 A schematic diagram to assemble the global static equation of motion from sub-equations of the three parts for a serpentine spring.

If a rotational serpentine spring is composed of only one or two loops of serpentine beams, the global stiffness matrix and the general static equation can be derived using the same process as shown in Section 3.4.1 and the stiffness matrix map in Figure 3.7. The derived equation is shown in Equation (3.43). Solving this equation yields the static matrix equation of motion for the free end of the spring, that is, $F_f = KD_1$. The global structural stiffness matrix for the free end of the spring K is also derived and shown in Equation (3.44), where K_{11}, …, K_{00} are defined in Section 3.4.1 and Figure 3.8. The arrangement of the terms in the stiffness matrix indicates an algorithm which is very helpful in analyzing other types of serially and orthogonally connected planar frames or springs. The stiffness matrix layout and the form of the global equation are also applicable in analysis of other serially connected springs, such as the classical serpentine springs, the zigzag springs, or spatial springs. The difference in using this method for different serpentine springs consists in the derivation of the rotation matrices due to different orientations of the beam members.

$$\begin{bmatrix} F_f \\ 0 \\ 0 \\ 0 \\ 0 \\ 0 \\ 0 \\ 0 \\ 0 \\ F_r \end{bmatrix} = \begin{bmatrix} K_{11} & K_{12} & & & & & & & & \\ K_{21} & K_{22} & K_{23} & & & & & & & \\ & K_{32} & K_{33} & K_{34} & & & & & & \\ & & K_{43} & K_{44} & K_{45} & & & & & \\ & & & K_{54} & K_{55} & K_{56} & & & & \\ & & & & K_{65} & K_{66} & K_{67} & & & \\ & & & & & K_{76} & K_{77} & K_{78} & & \\ & & & & & & K_{87} & K_{88} & K_{89} & \\ & & & & & & & K_{98} & K_{99} & K_{90} \\ & & & & & & & & K_{09} & K_{00} \end{bmatrix} \begin{bmatrix} D_1 \\ D_2 \\ D_3 \\ D_4 \\ D_5 \\ D_6 \\ D_7 \\ D_8 \\ D_9 \\ 0 \end{bmatrix} \tag{3.43}$$

$$K = K_{11} - \cfrac{K_{21}K_{12}}{K_{22} - \cfrac{K_{23}K_{32}}{K_{33} - \cfrac{K_{34}K_{43}}{K_{44} - \cfrac{K_{45}K_{54}}{K_{55} - \cfrac{K_{56}K_{65}}{K_{66} - \cfrac{K_{67}K_{76}}{K_{77} - \cfrac{K_{78}K_{87}}{K_{88} - \cfrac{K_{89}K_{98}}{K_{99}}}}}}}}} \tag{3.44}$$

Because of the symmetry of the two side springs with respect to the central point of the mirror plate on the torsion axis and the symmetry of the orthogonally connected side spring with respect to the torsion axis, slope bending at the free end of a side spring will not transmit to the whole structure and the stiffness for slope bending deflection can be neglected, leading to a static equation with only two degrees of freedom (torsion and translation bending). This is in agreement with the results acquired using the linear energy method in Section (2.2.4). And the static equation of motion for a torsional micromirror with one or multiple loops of rotational serpentine springs and electrostatic actuation can thus be solved using the same formulation as it has been shown in Section 3.4.1.

3.5 Modeling by Matrix Method with PRBM Models

The PRBMs (Pseudo Rigid Body Models) are used to approximate lengthy beam members (also called compliant beam members) in a framed structure. In the example shown in Figure 3.11, the rotational serpentine spring for torsional micromirror suspensions is composed of both short and long beams. For compliant suspensions, the three parallel beams (members 3, 5 and 7 in Figure 3.11 (*b*)) may be much longer than

the short beams. Using PRBM models to approximate these lengthy beams (Figure 3.11 (*c*)) in the framed micro-mechanism helps enhance analytical accuracy. Due to complexity of framed structures, a hybrid method involving both matrix method and the PRBM model is utilized in analysis of the planar framed micro-structures.

3.5.1 Structural Member Stiffness Matrices

The structural member stiffness matrices in the global coordinates for members 1, 2, 4, 6, 8 and 9 in Figure 3.11 have been found in the previous section (see Equations (3.22), (3.31), (3.32), (3.35), (3.36)). Since the length of these beams is much shorter than the parallel segments, they can be recognized as linear beams with very small deflections. Approximation of PRBM models for these orthogonal beams and the initial and final segments is not considered. However, due to their length and the thin cross-section of the parallel beams, it is more likely for them to perform large deflections. The structural member stiffness matrices for all short beams are rewritten here for convenience.

Lengths, spring constants, applied loads, and beam numbering used in the following matrices are denoted and shown in Figure 3.11. EI and GJ are the flexural rigidity and the twisting rigidity, respectively. One of the assumptions is that all beams share the same cross-section and material properties. K_{ms} is made and the structural member stiffness matrix is found. Since the final section and the initial section of the spring have the same orientation but different lengths (L_f or L_i), thus they share the same format of matrices:

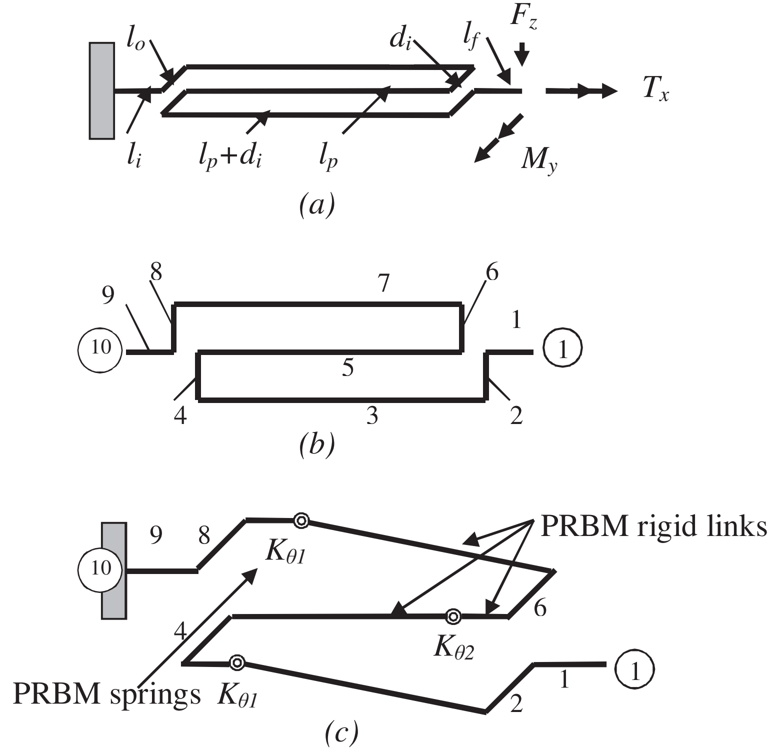

Figure 3.12 The free diagrams for a rotational serpentine spring with a single serpentine loop, where (*c*) is the equivalent structure after PRBM approximation for the three long segments.

$$K_{ms1} = \begin{bmatrix} \frac{12EI}{L_f^3} & 0 & \frac{6EI}{L_f^2} & -\frac{12EI}{L_f^3} & 0 & \frac{6EI}{L_f^2} \\ 0 & \frac{GJ}{L_f} & 0 & 0 & -\frac{GJ}{L_f} & 0 \\ \frac{6EI}{L_f^2} & 0 & \frac{4EI}{L_f} & -\frac{6EI}{L_f^2} & 0 & \frac{2EI}{L_f} \\ -\frac{12EI}{L_f^3} & 0 & -\frac{6EI}{L_f^2} & \frac{12EI}{L_f^3} & 0 & -\frac{6EI}{L_f^2} \\ 0 & -\frac{GJ}{L_f} & 0 & 0 & \frac{GJ}{L_f} & 0 \\ \frac{6EI}{L_f^2} & 0 & \frac{2EI}{L_f} & -\frac{6EI}{L_f^2} & 0 & \frac{4EI}{L_f} \end{bmatrix}, \quad K_{ms9} = K_{ms1}(L_i) \quad (3.45)$$

Similarly, members #2 and #8 share exactly the same stiffness matrix due to the same orientation and the same length:

$$K_{ms2} = K_{ms8} = \begin{bmatrix} \frac{12EI}{L_0^3} & -\frac{6EI}{L_0^2} & 0 & -\frac{12EI}{L_0^3} & -\frac{6EI}{L_0^2} & 0 \\ -\frac{6EI}{L_0^2} & \frac{4EI}{L_0} & 0 & \frac{6EI}{L_0^2} & \frac{2EI}{L_0} & 0 \\ 0 & 0 & \frac{GJ}{L_0} & 0 & 0 & -\frac{GJ}{L_0} \\ -\frac{12EI}{L_0^3} & \frac{6EI}{L_0^2} & 0 & \frac{12EI}{L_0^3} & \frac{6EI}{L_0^2} & 0 \\ -\frac{6EI}{L_0^2} & \frac{2EI}{L_0} & 0 & \frac{6EI}{L_0^2} & \frac{4EI}{L_0} & 0 \\ 0 & 0 & -\frac{GJ}{L_0} & 0 & 0 & \frac{GJ}{L_0} \end{bmatrix} \tag{3.46}$$

Other two orthogonal segments, namely, members #4 and #6 also have the same length and the same orientation in the global coordinates, thus their stiffness matrix is shown in Equation (3.47) below. However, some terms in the map for a structural stiffness matrix of the lengthy beam in Figure 3.7 have to be adjusted to adapt to the current PRBM beams. The new map involving PRBM models is shown in Figure 3.12 as follows. This structural member stiffness matrix is arranged in an order of vertical force along *z*-axis, moment along *x*-axis and moment along *y*-axis or in an order of vertical translation, angular deflection along *x*-axis and angular deflection along *y*-axis according to the global coordinates of (*Z*, *X*, *Y*) in Figure 3.11.

$$K_{ms4} = K_{ms6} = \begin{bmatrix} \frac{12EI}{L_0^3} & \frac{6EI}{L_0^2} & 0 & -\frac{12EI}{L_0^3} & \frac{6EI}{L_0^2} & 0 \\ \frac{6EI}{L_0^2} & \frac{4EI}{L_0} & 0 & -\frac{6EI}{L_0^2} & \frac{2EI}{L_0} & 0 \\ 0 & 0 & \frac{GJ}{L_0} & 0 & 0 & -\frac{GJ}{L_0} \\ -\frac{12EI}{L_0^3} & -\frac{6EI}{L_0^2} & 0 & \frac{12EI}{L_0^3} & -\frac{6EI}{L_0^2} & 0 \\ \frac{6EI}{L_0^2} & \frac{2EI}{L_0} & 0 & -\frac{6EI}{L_0^2} & \frac{4EI}{L_0} & 0 \\ 0 & 0 & -\frac{GJ}{L_0} & 0 & 0 & \frac{GJ}{L_0} \end{bmatrix} \tag{3.47}$$

$$\begin{array}{cc} & \overbrace{z \quad x \quad y}^{①} \quad \overbrace{z \quad x \quad y}^{②} \\ \begin{array}{c} ① \left\{ \begin{array}{c} z \\ x \\ y \end{array} \right. \\ ② \left\{ \begin{array}{c} z \\ x \\ y \end{array} \right. \end{array} & \begin{bmatrix} \frac{4\kappa_\theta EI}{\gamma L^3} & 0 & -\frac{2\kappa_\theta EI}{L^2} & -\frac{4\kappa_\theta EI}{\gamma L^3} & 0 & -\frac{2\kappa_\theta EI}{L^2} \\ 0 & \frac{GJ}{L} & 0 & 0 & -\frac{GJ}{L} & 0 \\ -\frac{2\kappa_\theta EI}{L^2} & 0 & \frac{2\gamma\kappa_\theta EI}{L} & \frac{2\kappa_\theta EI}{L^2} & 0 & \frac{\gamma\kappa_\theta EI}{L} \\ -\frac{4\kappa_\theta EI}{\gamma L^3} & 0 & \frac{2\kappa_\theta EI}{L^2} & \frac{4\kappa_\theta EI}{\gamma L^3} & 0 & \frac{2\kappa_\theta EI}{L^2} \\ 0 & -\frac{GJ}{L} & 0 & 0 & \frac{GJ}{L} & 0 \\ -\frac{2\kappa_\theta EI}{L^2} & 0 & \frac{\gamma\kappa_\theta EI}{L} & \frac{2\kappa_\theta EI}{L^2} & 0 & \frac{2\gamma\kappa_\theta EI}{L} \end{bmatrix} \end{array}$$

Figure 3.13 A stiffness matrix for a PRBM equivalent beam. The columns and rows of the matrix are arranged in the order of local coordinates and the numbering for joints.

The terms in the adjusted matrix for a parallel beam have been given in Equations (2.90), (2.97) and (2.99) in Chapter 2, which can be rewritten here:

$$F = \frac{\kappa_\theta EI}{\gamma l^3}\delta, \quad M = \frac{\kappa_\theta EI}{l^2}\delta; \quad F = \frac{\kappa_\theta EI}{l^2}\theta, \quad M = \frac{\gamma\kappa_\theta EI}{l}\theta \tag{3.48}$$

where κ_θ and γ are a rotational spring factor and a characteristic radius factor that are related to the orientation of the external force at the free end of a beam. If there is only one vertical force, κ_θ and γ are usually equal to 2.65 and 0.8517, respectively.

According to Figure 3.12 and transformation matrices for the three long beams (#3, #5 and #7 in Figure 3.11 (*c*)), their structural member stiffness matrices are given as follows. Beam members #3 and #7 share the same matrix due to the same orientation and length. The structural member stiffness matrix for beam member #5 is shown in Equation (3.50) below. The structural member stiffness matrices for the 9 beam segments of a rotational serpentine spring are thus derived.

$$K_{ms3} = K_{ms7} =$$
$$\begin{bmatrix} \frac{4\kappa_\theta EI}{\gamma(L_p+d_0)^3} & 0 & \frac{2\kappa_\theta EI}{(L_p+d_0)^2} & -\frac{4\kappa_\theta EI}{\gamma(L_p+d_0)^3} & 0 & \frac{2\kappa_\theta EI}{(L_p+d_0)^2} \\ 0 & \frac{GJ}{L_p+d_0} & 0 & 0 & -\frac{GJ}{L_p+d_0} & 0 \\ \frac{2\kappa_\theta EI}{(L_p+d_0)^2} & 0 & \frac{2\gamma\kappa_\theta EI}{L_p+d_0} & -\frac{2\kappa_\theta EI}{(L_p+d_0)^2} & 0 & \frac{\gamma\kappa_\theta EI}{L_p+d_0} \\ -\frac{4\kappa_\theta EI}{\gamma(L_p+d_0)^3} & 0 & -\frac{2\kappa_\theta EI}{(L_p+d_0)^2} & \frac{4\kappa_\theta EI}{\gamma(L_p+d_0)^3} & 0 & -\frac{2\kappa_\theta EI}{(L_p+d_0)^2} \\ 0 & -\frac{GJ}{L_p+d_0} & 0 & 0 & \frac{GJ}{L_p+d_0} & 0 \\ \frac{2\kappa_\theta EI}{(L_p+d_0)^2} & 0 & \frac{\gamma\kappa_\theta EI}{L_p+d_0} & -\frac{2\kappa_\theta EI}{(L_p+d_0)^2} & 0 & \frac{2\gamma\kappa_\theta EI}{L_p+d_0} \end{bmatrix} \tag{3.49}$$

$$K_{ms5}=\begin{bmatrix} \frac{4\kappa_\theta EI}{\gamma L_p^3} & 0 & -\frac{2\kappa_\theta EI}{L_p^2} & -\frac{4\kappa_\theta EI}{\gamma L_p^3} & 0 & -\frac{2\kappa_\theta EI}{L_p^2} \\ 0 & \frac{GJ}{L_p} & 0 & 0 & -\frac{GJ}{L_p} & 0 \\ -\frac{2\kappa_\theta EI}{L_p^2} & 0 & \frac{2\gamma\kappa_\theta EI}{L_p} & \frac{2\kappa_\theta EI}{L_p^2} & 0 & \frac{\gamma\kappa_\theta EI}{L_p} \\ -\frac{4\kappa_\theta EI}{\gamma L_p^3} & 0 & \frac{2\kappa_\theta EI}{L_p^2} & \frac{4\kappa_\theta EI}{\gamma L_p^3} & 0 & \frac{2\kappa_\theta EI}{L_p^2} \\ 0 & -\frac{GJ}{L_p} & 0 & 0 & \frac{GJ}{L_p} & 0 \\ -\frac{2\kappa_\theta EI}{L_p^2} & 0 & \frac{\gamma\kappa_\theta EI}{L_p} & \frac{2\kappa_\theta EI}{L_p^2} & 0 & \frac{2\gamma\kappa_\theta EI}{L_p} \end{bmatrix} \tag{3.50}$$

3.5.2 Global Stiffness Matrix and the Equations of Motion

Since the rotational serpentine spring has 9 beam members and 10 nodes in the structure, and each node has three DOFs, therefore the global stiffness matrix has an order of 30×30 terms arranged in 9 columns and rows. The matrix can be assembled similarly as the previous distribution map shown in Figure 3.8 because of the serially connected chain of beams. By adding up all matrix terms located at the same positions in the assembled matrix, sub-matrices K_{ij} shown in Equations (3.43) or (3.44) can also be resulted. Thus static equation for the complete rotational serpentine spring can be written in the similar form as in Equation (3.43). The sub-matrices are listed as follows.

$$K_{11}=\begin{bmatrix} \frac{12EI}{L_f^3} & 0 & \frac{6EI}{L_f^2} \\ 0 & \frac{GJ}{L_f} & 0 \\ \frac{6EI}{L_f^2} & 0 & \frac{4EI}{L_f} \end{bmatrix},\quad K_{12}=\begin{bmatrix} -\frac{12EI}{L_f^3} & 0 & \frac{6EI}{L_f^2} \\ 0 & -\frac{GJ}{L_f} & 0 \\ -\frac{6EI}{L_f^2} & 0 & \frac{2EI}{L_f} \end{bmatrix}$$

$$K_{21}=\begin{bmatrix} -\frac{12EI}{L_f^3} & 0 & -\frac{6EI}{L_f^2} \\ 0 & -\frac{GJ}{L_f} & 0 \\ \frac{6EI}{L_f^2} & 0 & \frac{2EI}{L_f} \end{bmatrix},\quad K_{22}=\begin{bmatrix} \frac{12EI}{L_f^3}+\frac{12EI}{L_0^3} & -\frac{6EI}{L_0^2} & -\frac{6EI}{L_f^2} \\ -\frac{6EI}{L_0^2} & \frac{GJ}{L_f}+\frac{4EI}{L_0} & 0 \\ -\frac{6EI}{L_f^2} & 0 & \frac{4EI}{L_f}+\frac{GJ}{L_0} \end{bmatrix}$$

$$K_{23}=\begin{bmatrix} -\frac{12EI}{L_0^3} & -\frac{6EI}{L_0^2} & 0 \\ \frac{6EI}{L_0^2} & \frac{2EI}{L_0} & 0 \\ 0 & 0 & -\frac{GJ}{L_0} \end{bmatrix},\quad K_{32}=\begin{bmatrix} -\frac{12EI}{L_0^3} & \frac{6EI}{L_0^2} & 0 \\ -\frac{6EI}{L_0^2} & \frac{2EI}{L_0} & 0 \\ 0 & 0 & -\frac{GJ}{L_0} \end{bmatrix}$$

$$K_{33}=\begin{bmatrix} \frac{12EI}{L_0^3}+\frac{4\kappa_\theta EI}{\gamma(L_p+d_0)^3} & \frac{6EI}{L_0^2} & \frac{2\kappa_\theta EI}{(L_p+d_0)^2} \\ \frac{6EI}{L_0^2} & \frac{4EI}{L_0}+\frac{GJ}{L_p+d_0} & 0 \\ \frac{2\kappa_\theta EI}{(L_p+d_0)^2} & 0 & \frac{GJ}{L_0}+\frac{2\gamma\kappa_\theta EI}{L_p+d_0} \end{bmatrix}$$

$$K_{34}=\begin{bmatrix} -\frac{4\kappa_\theta EI}{\gamma(L_p+d_0)^3} & 0 & \frac{2\kappa_\theta EI}{(L_p+d_0)^2} \\ 0 & -\frac{GJ}{L_p+d_0} & 0 \\ -\frac{2\kappa_\theta EI}{(L_p+d_0)^2} & 0 & \frac{\gamma\kappa_\theta EI}{L_p+d_0} \end{bmatrix}$$

$$K_{43}=\begin{bmatrix} -\frac{4\kappa_\theta EI}{\gamma(L_p+d_0)^3} & 0 & -\frac{2\kappa_\theta EI}{(L_p+d_0)^2} \\ \frac{6EI}{L_0^2} & -\frac{GJ}{L_p+d_0} & 0 \\ \frac{2\kappa_\theta EI}{(L_p+d_0)^2} & 0 & \frac{\gamma\kappa_\theta EI}{L_p+d_0} \end{bmatrix}$$

$$K_{44}=\begin{bmatrix} \frac{4\kappa_\theta EI}{\gamma(L_p+d_0)^3}+\frac{12EI}{L_0^3} & \frac{6EI}{L_0^2} & -\frac{2\kappa_\theta EI}{(L_p+d_0)^2} \\ \frac{6EI}{L_0^2} & \frac{GJ}{L_p+d_0}+\frac{4EI}{L_0} & 0 \\ -\frac{2\kappa_\theta EI}{(L_p+d_0)^2} & 0 & \frac{2\gamma\kappa_\theta EI}{L_p+d_0}+\frac{GJ}{L_0} \end{bmatrix}$$

$$K_{45}=\begin{bmatrix} -\frac{12EI}{L_0^3} & \frac{6EI}{L_0^2} & 0 \\ -\frac{6EI}{L_0^2} & \frac{2EI}{L_0} & 0 \\ 0 & 0 & -\frac{GJ}{L_0} \end{bmatrix}, \quad K_{54}=\begin{bmatrix} -\frac{12EI}{L_0^3} & -\frac{6EI}{L_0^2} & 0 \\ \frac{6EI}{L_0^2} & \frac{2EI}{L_0} & 0 \\ 0 & 0 & -\frac{GJ}{L_0} \end{bmatrix}$$

$$K_{55}=\begin{bmatrix} \frac{12EI}{L_0^3}+\frac{4\kappa_\theta EI}{\gamma L_p^3} & -\frac{6EI}{L_0^2} & -\frac{2\kappa_\theta EI}{L_p^2} \\ -\frac{6EI}{L_0^2} & \frac{4EI}{L_0}+\frac{GJ}{L_p} & 0 \\ -\frac{2\kappa_\theta EI}{L_p^2} & 0 & \frac{GJ}{L_0}+\frac{2\gamma\kappa_\theta EI}{L_p} \end{bmatrix}$$

$$, \quad K_{56}=\begin{bmatrix} -\frac{4\kappa_\theta EI}{\gamma L_p^3} & 0 & -\frac{2\kappa_\theta EI}{L_p^2} \\ 0 & -\frac{GJ}{L_p} & 0 \\ \frac{2\kappa_\theta EI}{L_p^2} & 0 & \frac{\gamma\kappa_\theta EI}{L_p} \end{bmatrix}, \quad K_{65}=\begin{bmatrix} -\frac{4\kappa_\theta EI}{\gamma L_p^3} & 0 & \frac{2\kappa_\theta EI}{L_p^2} \\ -\frac{6EI}{L_0^2} & -\frac{GJ}{L_p} & 0 \\ -\frac{2\kappa_\theta EI}{L_p^2} & 0 & \frac{\gamma\kappa_\theta EI}{L_p} \end{bmatrix}$$

$$K_{66}=\begin{bmatrix} \frac{4\kappa_\theta EI}{\gamma L_p^3}+\frac{12EI}{L_0^3} & \frac{6EI}{L_0^2} & \frac{2\kappa_\theta EI}{L_p^2} \\ \frac{6EI}{L_0^2} & \frac{GJ}{L_p}+\frac{4EI}{L_0} & 0 \\ \frac{2\kappa_\theta EI}{L_p^2} & 0 & \frac{2\gamma\kappa_\theta EI}{L_p}+\frac{GJ}{L_0} \end{bmatrix}$$

$$K_{67} = \begin{bmatrix} -\frac{12EI}{L_0^3} & \frac{6EI}{L_0^2} & 0 \\ -\frac{6EI}{L_0^2} & \frac{2EI}{L_0} & 0 \\ 0 & 0 & -\frac{GJ}{L_0} \end{bmatrix}, \quad K_{76} = \begin{bmatrix} -\frac{12EI}{L_0^3} & -\frac{6EI}{L_0^2} & 0 \\ \frac{6EI}{L_0^2} & \frac{2EI}{L_0} & 0 \\ 0 & 0 & -\frac{GJ}{L_0} \end{bmatrix}$$

$$K_{77} = \begin{bmatrix} \frac{12EI}{L_0^3} + \frac{4\kappa_\theta EI}{\gamma(L_p + d_0)^3} & -\frac{6EI}{L_0^2} & \frac{2\kappa_\theta EI}{(L_p + d_0)^2} \\ -\frac{6EI}{L_0^2} & \frac{4EI}{L_0} + \frac{GJ}{L_p + d_0} & 0 \\ \frac{2\kappa_\theta EI}{(L_p + d_0)^2} & 0 & \frac{GJ}{L_0} + \frac{2\gamma\kappa_\theta EI}{L_p + d_0} \end{bmatrix}$$

$$K_{78} = \begin{bmatrix} -\frac{4\kappa_\theta EI}{\gamma(L_p + d_0)^3} & 0 & \frac{2\kappa_\theta EI}{(L_p + d_0)^2} \\ 0 & -\frac{GJ}{L_p + d_0} & 0 \\ -\frac{2\kappa_\theta EI}{(L_p + d_0)^2} & 0 & \frac{\gamma\kappa_\theta EI}{L_p + d_0} \end{bmatrix}$$

$$K_{87} = \begin{bmatrix} -\frac{4\kappa_\theta EI}{\gamma(L_p + d_0)^3} & 0 & -\frac{2\kappa_\theta EI}{(L_p + d_0)^2} \\ 0 & -\frac{GJ}{L_p + d_0} & 0 \\ \frac{2\kappa_\theta EI}{(L_p + d_0)^2} & 0 & \frac{\gamma\kappa_\theta EI}{L_p + d_0} \end{bmatrix}$$

$$K_{88} = \begin{bmatrix} \frac{4\kappa_\theta EI}{\gamma(L_p + d_0)^3} + \frac{12EI}{L_0^3} & -\frac{6EI}{L_0^2} & -\frac{2\kappa_\theta EI}{(L_p + d_0)^2} \\ -\frac{6EI}{L_0^2} & \frac{GJ}{L_p + d_0} + \frac{4EI}{L_0} & 0 \\ -\frac{2\kappa_\theta EI}{(L_p + d_0)^2} & 0 & \frac{2\gamma\kappa_\theta EI}{L_p + d_0} + \frac{GJ}{L_0} \end{bmatrix}$$

$$K_{89}=\begin{bmatrix} -\frac{12EI}{L_0^3} & -\frac{6EI}{L_0^2} & 0 \\ \frac{6EI}{L_0^2} & \frac{2EI}{L_0} & 0 \\ 0 & 0 & -\frac{GJ}{L_0} \end{bmatrix}, \quad K_{98}=\begin{bmatrix} -\frac{12EI}{L_0^3} & \frac{6EI}{L_0^2} & 0 \\ -\frac{6EI}{L_0^2} & \frac{2EI}{L_0} & 0 \\ 0 & 0 & -\frac{GJ}{L_0} \end{bmatrix}$$

$$K_{99}=\begin{bmatrix} \frac{12EI}{L_0^3}+\frac{12EI}{L_i^3} & \frac{6EI}{L_0^2} & \frac{6EI}{L_i^2} \\ \frac{6EI}{L_0^2} & \frac{4EI}{L_0}+\frac{GJ}{L_i} & 0 \\ \frac{6EI}{L_i^2} & 0 & \frac{GJ}{L_0}+\frac{4EI}{L_i} \end{bmatrix}, \quad K_{90}=\begin{bmatrix} -\frac{12EI}{L_i^3} & 0 & \frac{6EI}{L_i^2} \\ 0 & -\frac{GJ}{L_i} & 0 \\ -\frac{6EI}{L_i^2} & 0 & \frac{2EI}{L_i} \end{bmatrix}$$

$$K_{09}=\begin{bmatrix} -\frac{12EI}{L_i^3} & 0 & -\frac{6EI}{L_i^2} \\ 0 & -\frac{GJ}{L_i} & 0 \\ \frac{6EI}{L_i^2} & 0 & \frac{2EI}{L_i} \end{bmatrix}, \quad K_{00}=\begin{bmatrix} \frac{12EI}{L_i^3} & 0 & -\frac{6EI}{L_i^2} \\ 0 & \frac{GJ}{L_i} & 0 \\ -\frac{6EI}{L_i^2} & 0 & \frac{4EI}{L_i} \end{bmatrix}$$

The stiffness matrix and the static equation for a torsional micromirror with rotational serpentine springs can thus be expressed as two times of the global stiffness matrix in the corresponding equation. The same process and equations can be found in the previous section thus the derivations are not repeated herein. It is noted that due to the symmetric structrure and the freedom in angular bending deflection for each beam, no angular bending deflection or slope for the two side springs is resulted during deduction. The final static equation of motion for the torsional micromirror is thus a system of 2-DOFs (vertical bending and torsion).

3.6 Numerical Simulation, Analysis and Comparison

Numerical simulation of torsional micromirrors with compliant suspensions composed of two symmetric rotational serpentine springs was performed through the commercial FEM software, ANSYS. Similar work was carried out using commercial software COMSOL [189].

3.6.1 Numerical Simulation

In consideration of the structural features and the coupled electrical field, the structural meshing elements SOLID45, SOLID95 and BEAM4 in ANSYS Multiphysics are used respectively to mesh the proposed torsional micromirrors. SOLID45 is a 3-D cubic element that is defined by the eight nodes at corners, with each node having three degrees of freedom: translations in x, y, and z directions. Electrostatic field is applied as a surface load uniformly distributed on all nodes on the bottom surface of the top mirror plate. Compared to SOLID45, SOLID95 is a higher order structural meshing element with additional 12 nodes on the midpoints between the 8 nodes of the SOLID45 element. Thus, it tolerates more irregular shapes of solid structures without much loss of accuracy. Since each surface on the SOLID95 element has 4 more nodes than that of the SOLID45 element, the finer presentation of electrostatic pressure can be built on SOLID95 thus a better simulation may be resulted if the structure is meshed in the same size of finite elements. BEAM4 is a uniaxial element for a slender beam; it has only two nodes at its both ends and each node has the complete six degrees of freedom. This element is very

useful in meshing Euler beams, but it can not represent properly the surface pressure such as the electrostatic force on the mirror plate. Since the proposed micromirror is composed of both the beams and the plates, meshing of the entire structure has to be realized by using a SOLID element along with the beam element. In consideration that the short beam segments exist in the rotational serpentine springs, BEAM4 is not used. Instead, either SOLID45 or SOLID95 is used for simulation of the given example. Finer meshing for structural corners is required for higher accuracy.

Coupling of electrical field with mechanical structures is created by using the transducer element TRANS126 in ANSYS. This is a point-to-point or a line element. Denser meshing of the TRANS126 element for the electric field requires higher order structural meshing, and thus more accuaret results may be obtained. However, the maximum number of elements is not unlimited; it depends on the capability of computer used and the type of elements involved. The electrostatic force is applied on the opposite surfaces of a pair of electrodes, that is, the bottom side of the mirror plate and the surface of the opposite electrode in the torsional micromirror. Compared to the generated electrostatic force, electrical fringing effects caused by edges and corners of large mirror plates can be neglected [169, 190].

Eight electrical field lines from the 8 nodes on a surface of SOLID95 elements can be simulated for the electrical field in this area, as compared to only four electrical field lines on a SOLID45 element surface for the same space. Thus a less number of SOLID95 leads to the same quantity of TRANS126 elements and the same accuracy of simulation

for the electrostatic field. Compared to the amount of 9726 elements of SOLID45 in meshing of the given torsional micromirror, much less number of SOLID95 elements (1378 elements) is required for the same structure. Figure 3.13 shows the top view of the meshed micromirror and the lateral view of the micromirror when it is deflected to some angle before snap-down. The given micromirror has dimensions of 500μm × 400μm × 10μm (length×width×thickness) for the mirror plate, 12μm for the gap, 23μm for the length of both the initial and the final segment and 220μm for the length of the parallel beams as well as 10μm distance between the neighbour features of the structure, which results in a distance of 300μm from the anchored point to the attached point on the suspended mirror plate for the side springs. The Young modulus, Poisson ratio, and density of the material for the mirror plate and springs used during simulation are 129.5GPa, 0.21, and 2320kg/m^3, respectively [167, 168].

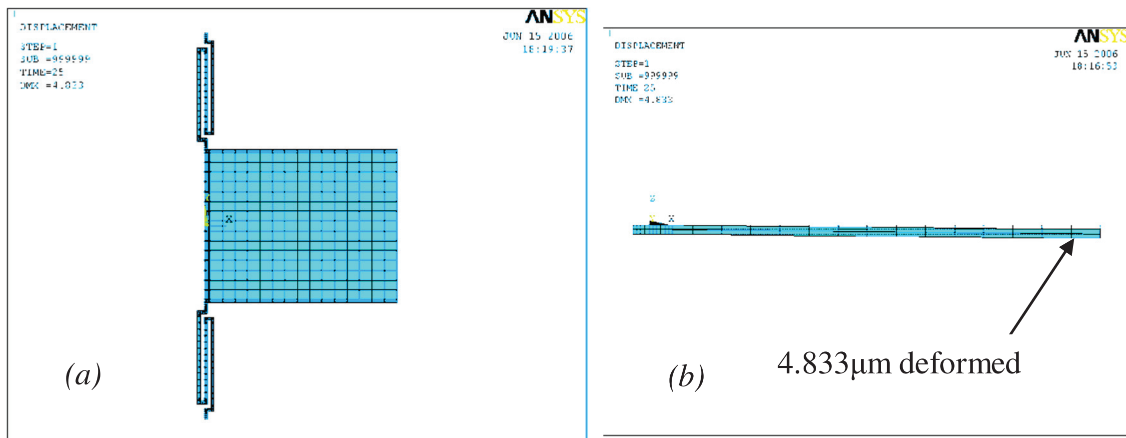

Figure 3.14 The simulated torsional micromirror and the deformation before pull-in: (*a*) the top view of the torsional micromirror meshed using SOLID95 element (1378 elements in total); (*b*) the side view of the deflected micromirror before pull-in.

3.6.2 Analysis and Comparison

Substitution of the geometric dimensions, physical parameters and the PRBM coefficients given in the above example into the sub-matrices K_{11}, K_{12}, …, K_{00} yields the global stiffness matrix in Equation (3.43). Solving this equation yields the 3×3 stiffness matrix for the free end of a side rotational serpentine spring which is formulated in Equation (3.44). The static equation for the free end of the spring has the following form, which is extracted from Equation (3.25):

$$F_f = K_{ff} D_f \tag{3.51}$$

where F_f is a half of the electrostatic force that is applied on the free end of the spring induced by the electrical bias applied on the mirror plate and the bottom electrode on the substrate. It has the three components: F_z, T_x and M_y. Thus Equation (3.51) is rewritten as

$$\begin{Bmatrix} F_z \\ T_x \\ M_y \end{Bmatrix} = K_{ff} \begin{Bmatrix} \delta \\ \alpha \\ \beta \end{Bmatrix} \tag{3.52}$$

where δ, α and β are the vertical deflection, the torsional angle and the slope angle due to bending moment M_y. β equals zero because of the guided-end loading condition, the rigidity of the mirror plate and the symmetric structure along the centre of the mirror plate.

Table 3.2 lists the analyzed and simulated results of the static performance of an electrostatic actuated torsional micromirror suspended symmetrically by two single-loop rotational serpentine springs. Two kinds of meshing elements in ANSYS, BEAM4 and SOLID95 are used in simulation of rotational serpentine springs. The resulted stiffness

constants in the table show some difference. The deviation becomes large as the cross-section of the beam segments increases. However, due to the dominant torsional mode, the effect on pull-in voltage due to this error is not significant.

Table 3.2 Comparison of static performance and pull-in voltage by different methods

Method	Pull-in Voltage (*V*)	Difference (%)	Bending stiffness (kN/m)	Torsion stiffness (kN/rad)
Analyzed	18.3971	-5.66	34.3056	1.2931e-07
BEAM4	17.8927	-8.24	45.1990	1.2571e-07
SOLID95	19.50	0	33.6137	1.3234e-07

Figure 3.15 (*a*) shows the colour view of bending deflections distributed along the total planar structure, whereas Figure 3.15 (*b*) shows the maximum stress locations before snap-on occurs. The vertical displacement of the micromirror at its front edge at this moment is shown to be 4.833μm and the corresponding voltage is 19.5V. When the applied voltage is given a small perturbation, the micromirror will be pulled down to the opposite electrode abruptly. Bending of the planar springs is noted to be almost negligible. Meanwhile, the extreme stress is observed at locations of the concave corners of the serpentine springs. The maximum stress occurs at locations of the inner U-corners near the anchored ends of the springs (as shown in Figure 3.15 (*b*)). Figure 3.16 shows the electrostatic curves obtained from an analytical method (linear energy method) and ANSYS simulation using SOLID95 meshing elements. Both of the resulted pull-in voltages have been shown in Table 3.1 with a difference of around 6%. This error is reasonable due to the assumption of small deflection in analytical modeling. The error becomes larger as the applied voltage is close to the pull-in voltage.

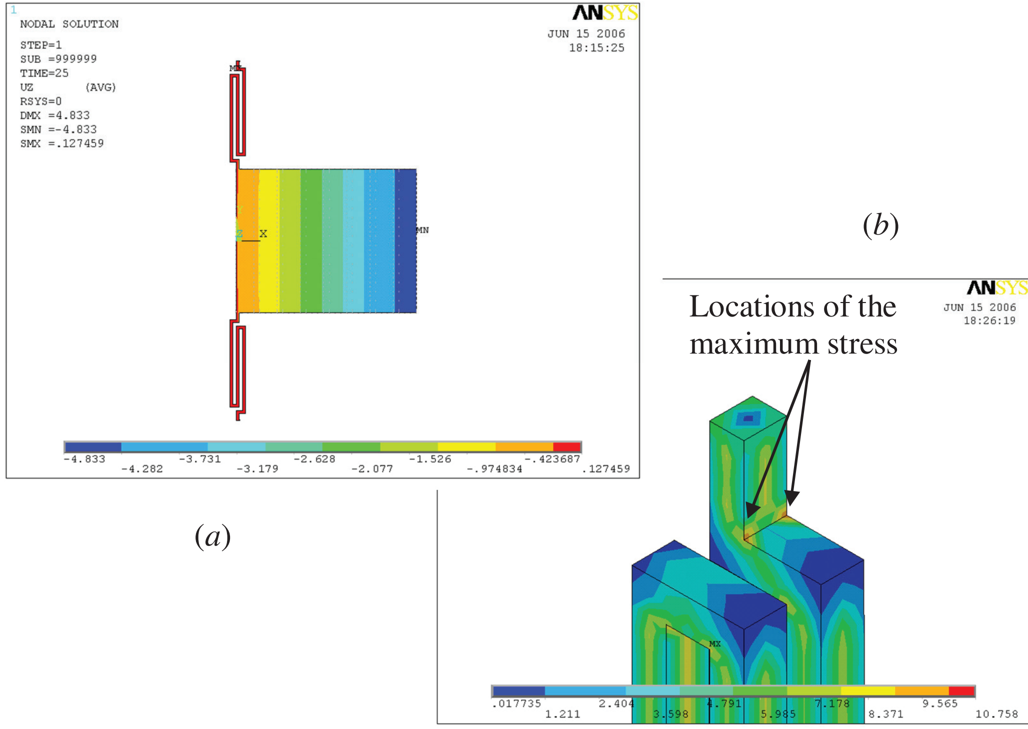

Figure 3.15 FEM simulated results: (*a*) the top view of the stress distribution on the SOLID95 meshed micromirror; (*b)* the simulated maximum stress locations on rotational serpentine springs of the micromirror before pull-in.

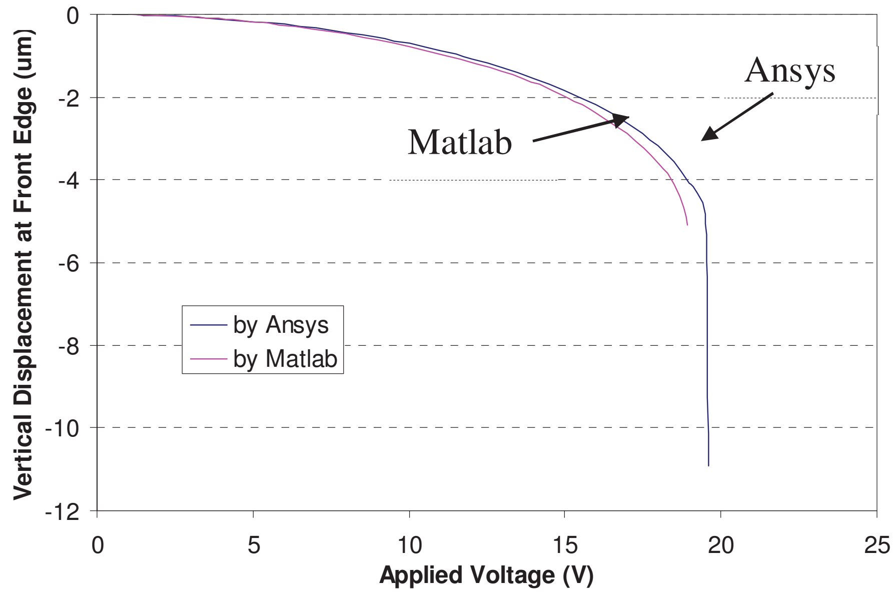

Figure 3.16 Comparison between electrostatic curves obtained using linear energy method and FEM simulation with SOLID95 element.

3.7 Summary

Various planar framed suspensions for proof mass plates compatible with the current SOI wafer based micromachining technology were first reviewed. A concept for designing compliant torsional micromirrors is presented.

The compliance, structural compactness and the stiffened out-of-plane bending of the rotational serpentine springs are identified in the second section. Compared to classical serpentine springs, rotational serpentine springs are soft in torsion but stiff in bending. This advantage helps the rotational serpentine springs avoid such issues as stiction, sinking, or warping of the microstructures occur during microfabrication. The other forms of serpentine springs such as the zigzag and rounded-corner classical serpentine springs are hard to produce because of the limits of micromachining processes.

Analytical modeling of a torsional micromirror symmetrically suspended by rotational serpentine springs and actuated by parallel electrostatic force is presented in the third section. Using a linear energy method, the rotational serpentine springs are analyzed. The structure is equivalent to a cantilever with two degrees of freedom comprised of torsion and out-of-plane bending at the free end due to the symmetric geometry along its central line. The characteristic parameters such as bending stiffness and torsional stiffness are derived, which demonstrated that the induced torsion and bending modes at the free end of a symmetric rotational serpentine spring can be decoupled. The static equation of

motion for the torsional micromirror supported at both sides by two such springs is also derived.

Instead, stiffness matrix method is utilized in analysis of a rotational serpentine spring. It has been noted any rotational serpentine spring is composed of three parts, the initial part, the final part and the part composited by a few loops of rotational serpentines. The matrix method is thus applied for each of them. The matrix construction is further presented. This includes construction of member stiffness matrix and global stiffness matrix. A map to construct the global matrix and the formula to establish the static matrix equations for rotational serpentine springs and the complete torsional micromirror are provided.

In consideration of the lengthy beams involved in compliant micromirrors, PRBM method is also used to approximate or linearize the nonlinearity of these beams. The spring constants from PRBM method dealing with the guided-end cantilevers are used to replace the corresponding terms in the map for the global stiffness matrix. The stiffness matrix and the static equation of motion for the free end of a rotational serpentine are thus derived. Summation of the two stiffness matrices yields the complete stiffness matrix and the static matrix equation of motion for the micromirror.

The FEM simulation in ANSYS for the given micromirror is also presented in the last section. Different structural meshing elements for the structure result in some deviation, in which SOLID95 has demonstrated a better accuracy and thus is recommended for FEA. Comparison of analytical method with numerical method is performed too. Both results

demonstrate very good agreement. This indicates an acceptable error may be resulted from using the analytical method. As for compliant framed microstructures, linear matrix method accompanied by PRBM approximation for the compliant beams in the structures is recommendable. This way helps enhance the accuracy of the results and also enables the embedding in a computer algorithm for the whole process of analysis.

Chapter 4: Micromachining of Torsional Micromirrors

4.1 Introduction

Modeling and design of torsional micromirrors have been discussed in depth in the previous chapters. However, due to the desired compliance of suspensions for micromirrors, fabrication of such MEMS devices is not an easy task. With good understanding of micromachining techniques and materials, development of an easy-to-handle, cost-effective micromachining process and high success rate of production for specific MEMS devices is an important task. Due to the known limitations of bulk micromachining, a feasible fabrication process for the proposed compliant micromirrors has to tolerate their conflicting requirements on the size and volume of components. Two MEMS processes, namely MUMPs (Multi-User MEMS Processes) and MicraGEM (Micralyne GEneralized MEMS), are chosen for fabrication. These two processes belong to the planar or surface micromachining, which is able to obtain the flat micro-platforms or micromirrors for various optical related applications such as optical tele-communication, micro-scanners, projection display, and micro-sensors. The following sections outline the fabrication of miromirrors.

The 2-D layer addition by depositions and bonding processes, and the 2-D layer subtraction by etching methods or removals of sacrifice layers, can generate planar sandwiched 2-D micro-structures. The planarity of these so-called 2-D micro-structures is

due to the successive photo-lithographic patterning of the 2-D layers, the interaction of stacked and patterned 2-D layers and the selective etching characteristic of the layers or the substrates, depending on the materials, the tools and the etchants that are chosen for micro-fabrication. Because of this kind of parallel plate microstructures, an attractive force generated between a pair of plates loaded by an electrical bias is widely used as the electrostatic actuation for MEMS with movable components.

4.2 MUMPs Process

As it has been introduced, MUMPs micromachining process is a kind of surface micromachining processes, suitable for the fabrication of precise and fine planar structures composed of a few thin polysilicon layers. The detailed description of MUMPs can be found in the manuals or instructions that are provided by the company [191]. A brief review of one of MUMPs process, that is, PolyMUMPs is provided herein, which is widely accepted for the production of specific MEMS devices such as micromirrors or micro-platforms.

There are three sophisticated processes of MUMPs, namely, PolyMUMPs, MetalMUMPs and SOIMUMPs, named after the materials that are used for structure layers of MEMS devices. Due to the small dimensions of the micro-structures that can be fabricated, PolyMUMPs (Polysilicon based MUMPs) is selected for the fabrication of micro-platforms with soft suspensions. PolyMUMPs is not suitable for micromachining torsional micromirrors that are needed in our research as they are supposed to have large

dimensions of micromirrors (hundreds of microns) and the corresponding non-symmetric supports for torsional movement. Figure 4.1 shows a typical cross-section of PolyMUMPs process, which is composed of two structural layers, one bottom electrode layer, one external metal wiring layer and three other layers. As shown in this figure, poly-silicon layer Poly 0 is for the electrical ground or bottom electrodes, whereas Poly 1 and Poly 2 are two mechanical structural layers. The two PSG (phosphorous-silicate-glass) deposited oxide layers are sacrificial layers, employed to provide the first gap (1st oxide) between Poly 1 and substrate/nitride and the second gap (2nd oxide) between Poly 2 and Poly 1. Silicon nitride layer is used for isolating the device with the substrate whereas the metal layer is used for wiring of the device for packaging. Thickness for each layer of PolyMUMPs process is fixed as one of the design rules for the standardized process. Table 4.1 lists all thickness values of the process to be used in layout design in order to obtain a successful yield of the MEMS devices. In an overview, PolyMUMPs process uses eight lithography levels to pattern the seven physical layers that have been mentioned [192].

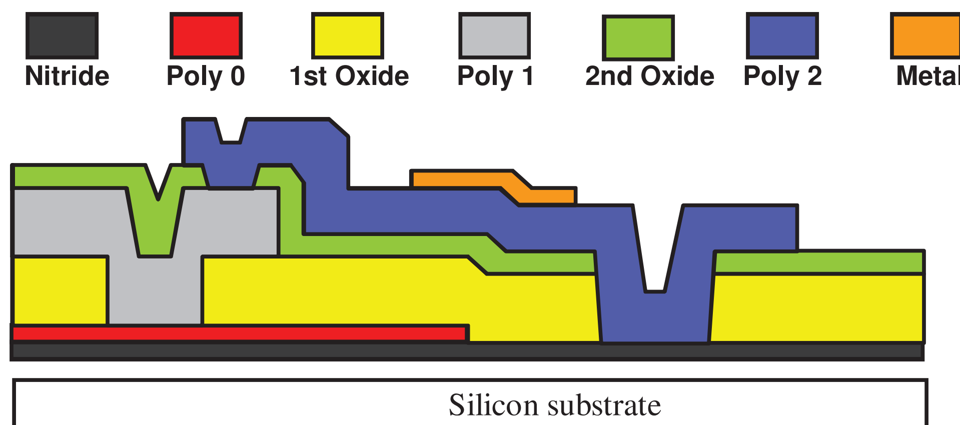

Figure 4.1 Cross-section view of PolyMUMPs micromachining process (Adapted from MUMPs Process [192])

Table 4.1 Layer or material names and individual thicknesses of PolyMUMPs

Material layer	Nitride	Poly 0	1st Oxide	Poly 1	2nd Oxide	Poly 2	Metal
Thickness (μm)	0.6	0.5	2.0	2.0	0.75	1.5	0.5

There are a few compliant micromirrors using MUMPs micromachining process that have been introduced in the first chapter. They all have relatively large plates with very thin thickness (1.5~2μm) based on the design rules provided. Although these devices can perform out-of-plane movement, they all have to be actuated using complicated mechanisms and additional circuits for actuation controls [193-195]. And flatness of mirror surfaces will be deformed after some time. It is therefore the MUMPs is not suitable to fabricate the desired torsional micromirrors that have larger dimensions and will keep flatness of mirror surfaces for the life time. Nevertheless, it is valuable to render this process for fabrication of other kinds of microstructures such as those fully clamped deformable micro-diaphragms or micro-bridges for optical sensing applications (see Figure 4.2) [196]. The design layout for the two kinds of microstructures (the stiff suspension by directly clamped or anchored and the soft suspension by the compliant springs) can be seen in Figure 4.2. Out of these, the two soft suspended micromirrors snapped over time. Moreover, there are only two options of gaps between the bottom electrode (Poly 0) and one of structural layers (either Poly 1 or Poly 2) that can be chosen, i.e., 2μm and 4.75μm for the out-of-plane motion, which is too small for the torsional micromirrors desired for our research even though the compliance of suspensions can be easily obtained. These two drawbacks make the PolyMUMPs process not applicable for fabrication of large torsional micromirrors. In replacement, SOI-MUMPs process has been developed for such kind of applications. And it is also very similar to another SOI wafers based micromachining process such as MicraGEM, as introduced in the first

chapter. MicraGEM process for the desired torsional micromirrors will be provided in the later section.

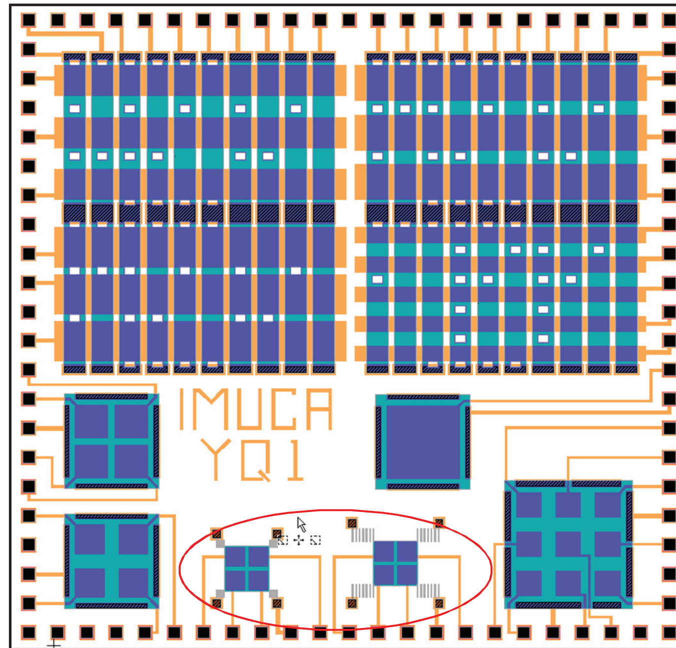

Figure 4.2 A PolyMUMPs design layout showing two compliant micro-platforms, each of which is suspended by four symmetric classical serpentine springs and has four bottom electrodes underneath the platform (see the red circle) [196].

4.3 SOI Wafers and SOI MEMS Fabrication

As shown in introduction, SOI (silicon-on-insulator) wafers are a kind of sandwich structures consisting of three layers: a thin silicon layer on the top, a bulk silicon layer at bottom and an insulator layer in between. There are two extensively employed techniques in producing SOI wafers for both IC and MEMS applications, that is, the silicon fusion bonding (SFB) and the separation by implanted oxygen layer (SIMOX) [61-63].

The main advantages of SOI (SFB) wafers for fabrication of MEMS devices and applications are as follows: 1) the device layer is made of single crystal silicon, which has a very uniform geometry (thickness and flatness) and very good mechanical performances; 2) the insulation layer, the cavities or gaps and the etch stops underneath the device layer can be formed flexibly in various depths and shapes depending on the etching process selected and the patterns designed; 3) the thickness for device layers can also be realized by mechanical wafer thinning processes such as grinding, lapping and polishing of the wafers; 4) due to stable, uniform and high strength mechanical performances of the single crystal silicon and the diversity of its thickness for the device layers, the fabricated mechanical structures can be very flexible, ranging from very high aspect ratio beams (fine cross-section but lengthy beams) to relatively large and heavy plates; 5) it is compatible with IC processes (e.g. CMOS) so as to form micro-electro-mechanical systems on the same chip; and 6) the created devices will have a flat and very fine roughness surface, an essential feature for efficient optical refraction or reflection. Comparisons of silicon surface micromachining, bulk micromachining and SOI wafer based micromachining for MEMS chips were summarized in [197].

4.4 MicraGEM Process

Using bonded SOI-wafers for high aspect ratio MEMS fabrication is an appropriate routine at present, which is especially very suitable for those MEMS devices that need large rigid plates or platforms but relatively weak supports. Based on these concepts, the bonded SOI wafers are the most suitable base material for fabrication of the micromirrors

or microplatforms having large and rigid plates and relatively weak supports. And as has been mentioned before, this belongs to one of the research motives, that is, to obtain a kind of micromirrors with a heavy proof mass but a relatively soft suspension aiming to reduce the resonant frequency of the structure for inertial sensing and positioning applications. MicraGEM process (Micralyne GEneralized MEMS), which is one of the SOI wafer based MEMS processes, is exactly an SOG (Silicon on Glass) MEMS process, in which bulky silicon substrate is replaced by glass plate, an extra thickness of trench is added (2μm, 10μm, or 12μm), and the flip-chip bonding technology is utilized in the process [167]. The details of the process will be given in the later chapter. Because of the availability for Canadian academic researchers owing to the generosity of the technology hosting company Micralyne [168], the torsional micromirrors and other micro-platforms used herein for the research are thus manufactured.

Among SOI MEMS processes that are recently emerged and commercially available, MicraGEM (Micralyne Generalized MEMS, Canada) [167-168] has been well standardized and thus used for fabrication of the robust torsional micromirrors in our research, owing to its availability made by the company and through the network of Canadian Microsystems Corporation to the researchers in Canada. This SOI wafer based process offers not only the three options of gaps (2μm, 10μm, 12μm) between the two silicon layers, but also the metal electrodes for both the substrate and the device layer as well as highly reflective metal surfaces at the top of device layer for micromirrors. The minimum size of a feature is 3μm, almost at the same scale of the fine dimensions made from PolyMUMPs. And the maximum size of a feature by MicraGEM can be up to a

thousand microns according to the maximum allowable aspect ratio of 125:1 in MicraGEM, much larger than that of MUMPs. With such a fine dimension and such a high aspect ratio, a large micromirror with a relatively soft suspension can be easily achieved. Moreover, compared to MUMPs, MicraGEM provides a larger free space or gap (10μm or 12μm as compared to 2μm or 2.75μm of MUMPs) for out-of-plane motion of torsional micromirrors, meaning a larger angle of torsion. Adding that the residual stress in device layer of SOI wafers is negligible and that no etch holes in a device layer are needed for etching sacrifice layer, MicraGEM process demonstrates more versatility and flexibility over other MEMS fabrication techniques at present.

Instead of a bulk silicon wafer, MicraGEM process employs a Pyrex glass as the substrate of SOI MEMS. A cross-sectional view of the process (see Figure 4.3) shows that it not only enables the MEMS devices with a free space or gap between the device silicon layer and the bottom Pyrex substrate but also offers a metal layer via deposition on the Pyrex for the bottom electrodes and another metal layer for the electrodes and electrical connection pads on the top surface of the device layer. The bottom electrodes are led through patterned metal lines or routes to the pads located at peripheral of the Pyrex. The top metal layer provides also reflecting mirror surfaces for functioning of micromirrors. Three Pyrex etching depths of 12μm, 10μm and 2μm for the gaps can be selected in the process to make it more versatile and flexible. This process is briefly presented in Figure 4.3.

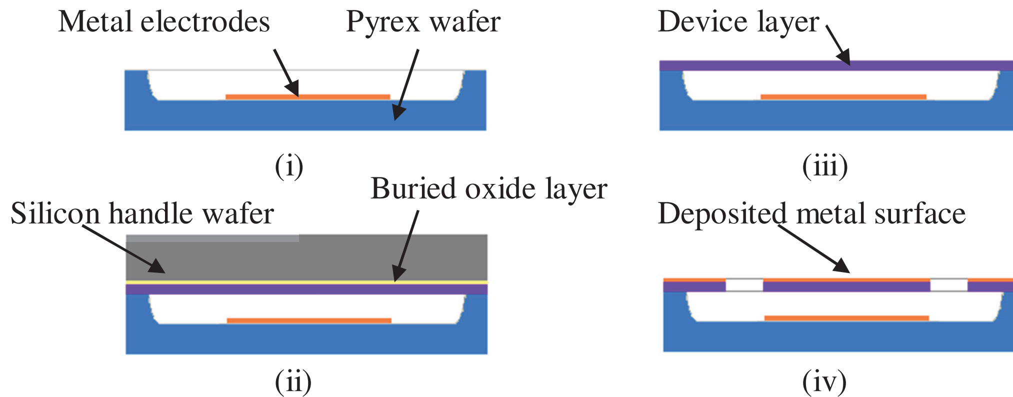

Figure 4.3 A typical process flow for MicraGEM SOI MEMS fabrication, which briefly shows a few main steps of operation, that is, Pyrex glass etching, metal deposition, device layer etching, handle layer etching, and wafer bonding.

- ❖ Pyrex etching and bottom electrode deposition: This first step starts from a glass Pyrex wafer. Patterning with a Pyrex mask (there are 3 mask options: mask 1 is for 2μm shallow etching; mask 2 for 10μm deep etching; and double mask for 12μm deep etching) on the Pyrex wafer, cavities with selected depths are etched in the Pyrex. Thereafter, bottom metal electrodes, lines and bonding pads can be patterned by METAL1 mask;
- ❖ Anodic bonding of a SOI wafer with the Pyrex wafer;
- ❖ Etching of SOI handle wafer and buried oxide layer;
- ❖ Designed silicon structures are patterned by DRIE etching and released. The top electrodes and reflective metal surface for mirrors are deposited and patterned.

Dimensions of a standard MicraGEM chip are 9×5×0.5 mm^3 or 4×5×0.5 mm^3. On such a chip, one can place many individual MEMS designs by rows and columns. As in our research, in order to approach for torsional micromirrors that have relatively low resonant value and flat reflective surface, the dimensions of our torsional micromirrors drop in a

range of a few hundred microns. Because of the availability of this process, fabrication of these micromirrors is focused on the optimum design of the supports or suspensions for large micromirror plates. A typical design and fabrication for one of the torsional micromirrors is obtained and reviewed in the following sections. The dimensions of the micromirror plate were designed to be 500µm long, 400µm wide and 10 µm thick, but the actual dimensions after MicraGEM micromachined are measured using a scanning electronic microscope (SEM) and found to be 506µm×402µm×10µm (Figure 4.4). A very thin metal layer is deposited and patterned on the Pyrex glass substrate to form the bottom electrodes that have the same dimensions and positions with those of individual micromirrors above. Another metal layer is deposited and patterned on the top surface of the chip to cover all the surfaces of micromirrors and surfaces of other structural features in the chip, for example, the suspensions of the micromirrors in the shapes of serpentine springs. Both shallow and deep Pyrex glass etchings (2+10µm) are utilized to form a 12µm gap between the micromirrors and the bottom electrodes on the Pyrex substrate. Each fabricated rotational serpentine spring has a length of 24µm for both the initial and final segments of the spring, a length of 221µm for the long parallel segments, and a gap of 10µm between every close neighbor elements, thus the total length of each side serpentine spring is added up to be 819µm and the distance between the micromirror and the spring anchoring location is measured to be 305µm. All beam segments in the springs are designed to be 8µm in width and 10µm in thickness. SEM pictures of the fabricated micromirror are shown in Figure 4.4.

The metal layer on Pyrex substrate is a combination of titanium, platinum and gold, as the process provider indicated, which provides for a low resistance electrical conductivity. Instead, chrome or gold is deposited on the top of the device layer (SiSC) to enhance optical reflectivity. Lift-off technique is used in both metal layer depositions. The top metal layer is patterned and etched to expose the silicon layer underneath. Figure 4.5 shows SEM pictures for another micromirror with the same designed dimensions as the previous one but different dimensions measured after post-processing. Dimensions of the fabricated micromirror plate are measured to be 495μm in length and 374μm in width showing an error of approximately 1~6% during fabrication. However, it can be observed from both figures (Figures 4.4 and 4.5) that the micromirror surfaces are flat and well polished, having a perfect surface finishing and being very suitable for optical reflective works. Moreover, no curling or sinking of any structural feature is observed in these SEM pictures, due to low residual stress of SOI wafers and the optimum design based on the rules required by the process, even though the design concepts for suspensions and for proof mass plates are contradictive, which demonstrates that MicraGEM is a successful MEMS prototyping process.

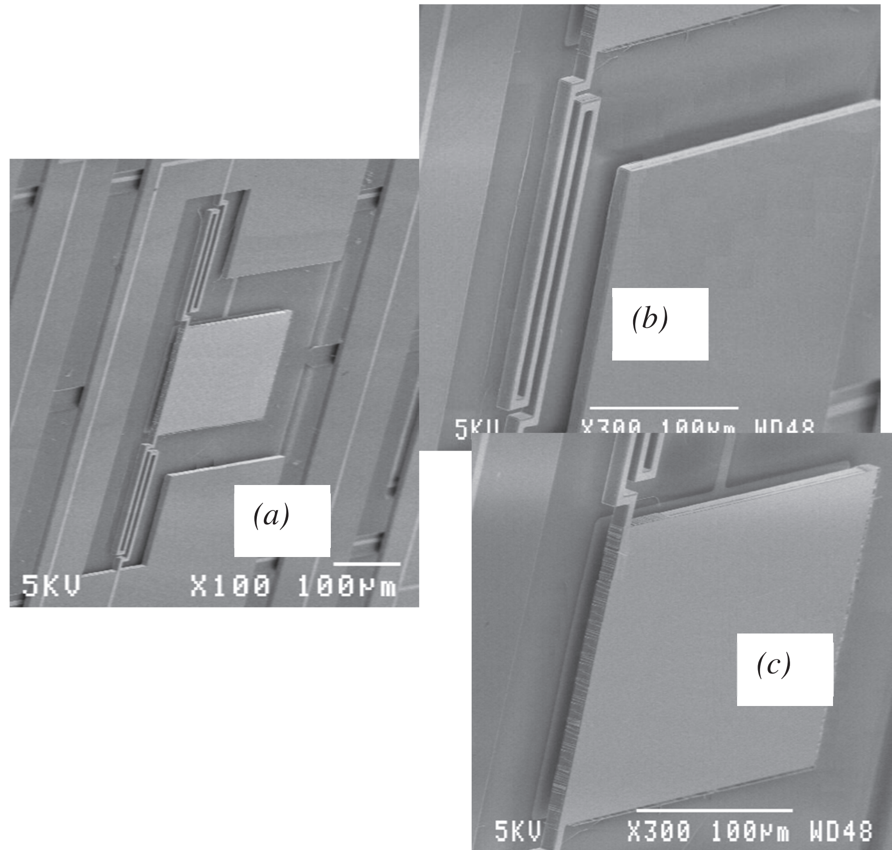

Figure 4.4 SEM photos of the fabricated torsional micromirror with rotational serpentine springs: (*a*) view of the whole mirror; (*b*) view of a side spring; (*c*) view of the mirror plate.

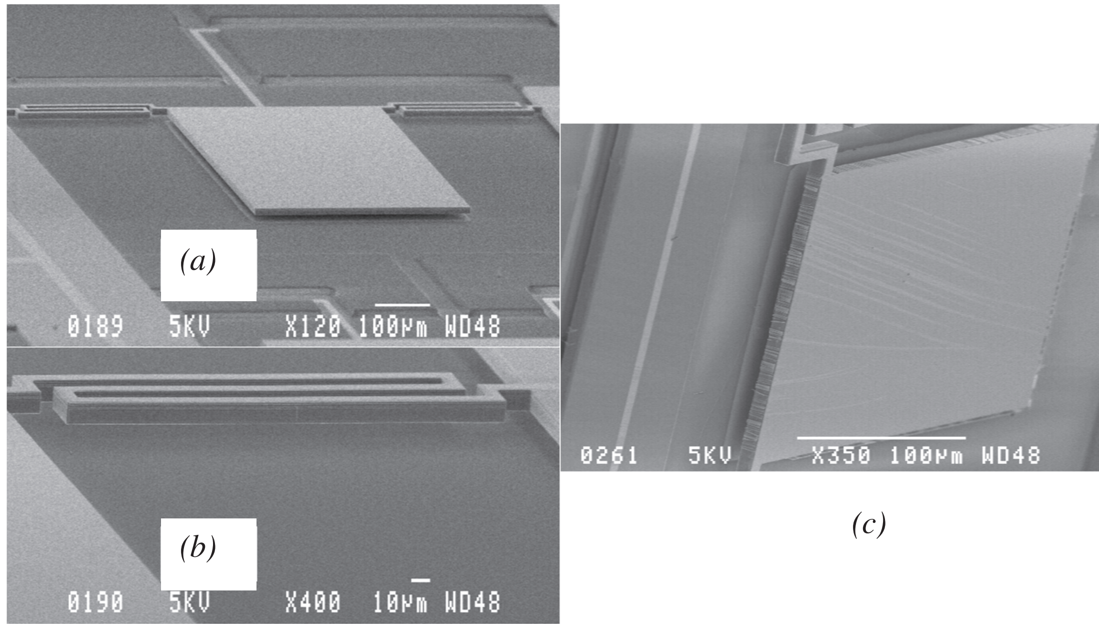

Figure 4.5 SEM pictures of another fabricated micromirror: (a) top view; (b) view of a side spring; (c) view of the uniform gap.

4.5 Layout Design, Wire Bonding, and Packaging

There are a few MEMS layout design tools currently available, such as MEMCAD from M.I.T. and CAEMEMS from University of Michigan while MEMS Pro and IntelliCAD are commercial software from SoftMEMS and IntelliSense, respectively. They all provide system-level synthesis and analysis, structural modeling and numerical analysis, layout editors for MEMS components and devices, and 3D visualization of models. All layout designs in our research were done by using L-Edit editor in MEMS Pro™. As mentioned before, MEMS layout design for a successful fabrication should observe the design rules required by any selected micromachining process such as MUMPs and MicraGEM. Figures 4.6 and 4.7 show the design layouts for a variety of torsional

micromirrors and other suspended micro-devices on the chips with a standard size of $9\times5mm^2$ that follow with MicraGEM process.

These CAD layouts still need to be checked by running DRC (Design Rule Checker) in MEMS Pro to avoid any possible occurrence of costly errors during fabrication. The finished design that has passed through DRC is submitted to the manufacturer (CMC/Micralyne herein) together with a bonding diagram if required for fabrication. Thereafter the finished chip is diced and shipped to the users for further assembly or packaging.

Wire bonding is the last step of preparation before MEMS testing and characterization. The pads on a MEMS chip are connected internally with the corresponding devices inside, and need to connect externally with the pads on a package die, such as those on PGA cavity dies (the ceramic Pin Grid Array cavity dies with options of 84 pins and 68 pins at bottom, named as 84 PGA and 68 PGA, Figure 4.8). Wire bonding in this aspect fulfills this final step. Two bonding types, ball-stitch bonding and wedge-wedge bonding are available, which have been used for IC chip production and based on one of the following three bonding mechanisms: thermo-compression, ultrasonic, and thermo-sonic. A few sophisticated bonding machines in the market can be selected, which can be operated either manually or automatically. The manually operated machine WEST/BOND 7400E is used in our research for wire bonding of the chips (see Figure 4.8), in which either aluminum wires or gold wires with diameters from 17μm to 50μm can be employed for wire bonding. The loose dice is first placed, positioned and attached to the central

platform in the cavity of a PGA die. Wire from the attached coil is threaded through the capillary hole in the wedge by pressurized gas and held by the clamp, allowing automatic feeding by the machine. Aluminum wire bonding operation is implemented using ultrasonic bonding, while gold wire bonding operation needs the work piece on the platform to be heated, which could be detrimental to the movable components on the chip. The cost effective aluminum wire of 20μm diameter was chosen for wire bonding in our work. Common defects or failures may occur in wire bonding due to underlying cause. If the bonding force is too high, peeling of metallic layer may occur to the pads. Conversely, if the bonding force is too low, the bonds may not stick to the pads. Contaminated bonding pads or uneven pad surfaces may also keep them from sticking. Wire breakage during the bonding process is usually the result of imperfections (nicks, scratches, or kinks) in the wire. The high yield and high quality bonding operation can be achieved for an experienced operator. Wire bonding of MEMS chips with the ceramic cavity dies (or containers) is the last step in the fabrication of MEMS devices for laboratory tests and characterization.

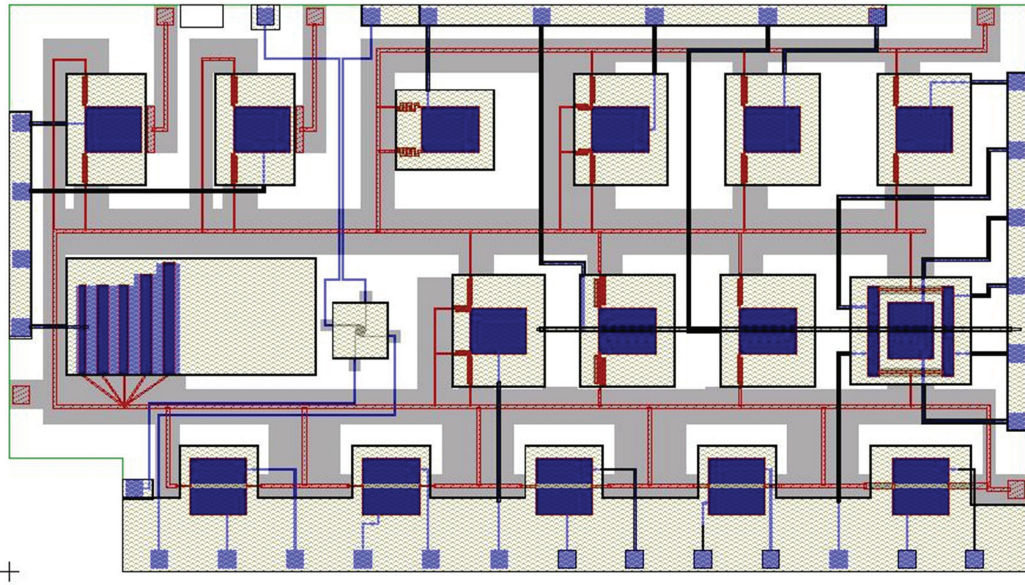

Figure 4.6 Design layout for a variety of torsional micromirrors with the size of the mirror plate at 600μm×500μm on a standard chip of MicraGEM.

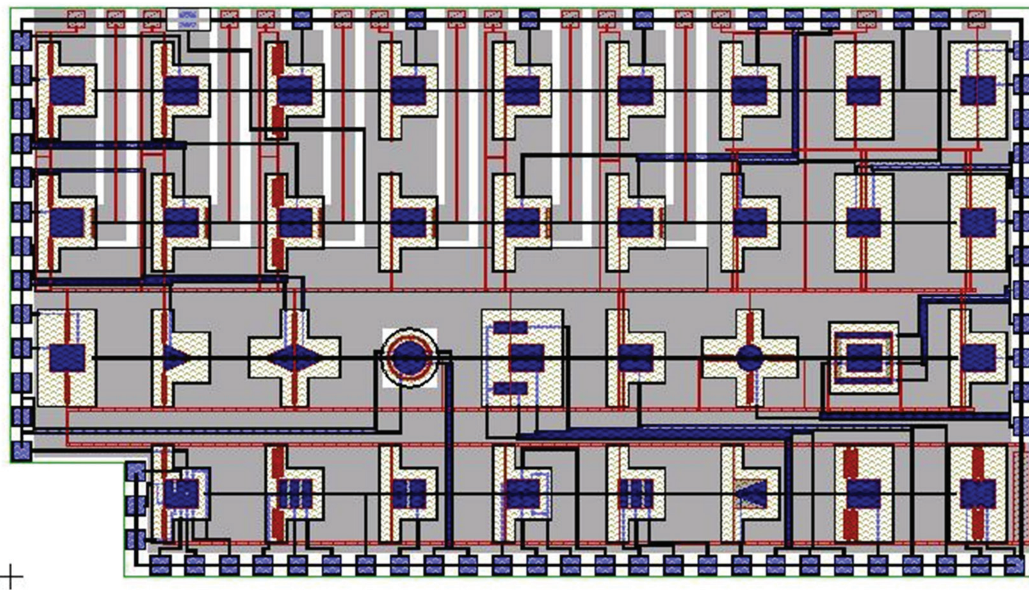

Figure 4.7 Design layouts for a variety of torsional micromirrors with the size of the mirror plate at 300μm×240μm on a standard chip of MicraGEM.

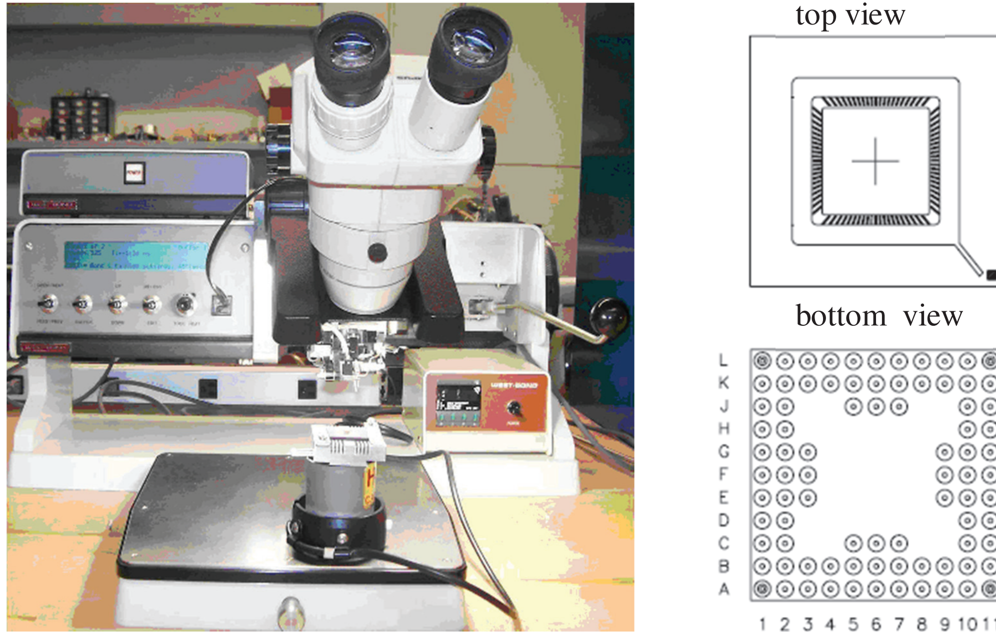

Figure 4.8 The wire bonding machine WEST BOND 7400E and the diagrams of an 84 PGA die with pin number used for packaging of the diced MicraGEM chips.

4.6 Discussion on Limitations

There exist limitations to MEMS fabrication due to limitations of the available micromachining techniques and the specific physical fields. As has been mentioned in the introduction, MEMS fabrication evolves from single layer addition or subtraction (2D micromachining), multiplex planar structures (2D+ micromachining) toward 3D micromachining and nano-scale. The drawbacks arising from 2D micromachining can be solved as the 3D micromachining technology becomes sophisticated in the future. Since the 3D micro-fabrication is still in its initial stage of research, the real 3D MEMS devices are hard to be fabricated. MEMS devices made by surface micromachining still need to be packaged properly for harsh applications. And various physics and physical fields

(electrostatic, magnetic, gravity, etc) may also set to some extent the limitations on the capability of micromachining and applications of these MEMS devices.

4.7 Fabricated Results

The micromirrors or micro-platforms that are non-symmetrically supported by a variety of beams or springs have been successfully fabricated using MiraGEM process, and released and packaged in our lab for testing and characterization. Figure 4.9 provides AFM photos for the two micro-platforms that are supported by a cantilever of serially connected multiple serpentine beam segments. Under each of these micro-platforms there are two equal size bottom electrodes that are symmetrically arranged and isolated with each other. This kind of electrostatically activated micro-platforms has been validated theoretically to be a suitable alternative for spatial optical switches of 1×N routes or ports because of its two degrees of freedom of motion (2-DOFs). The tunable ranges of angles for both torsion and bending slope of the micro-platforms can be designed to be in the same order. Analysis on one of these micro-platforms that are supported by cantilevers has been performed [182] while leaving characterization of these micro-platforms with different supports for further work. Figures 4.10-4.16 provide the SEM photos of several fabricated torsional micromirrors.

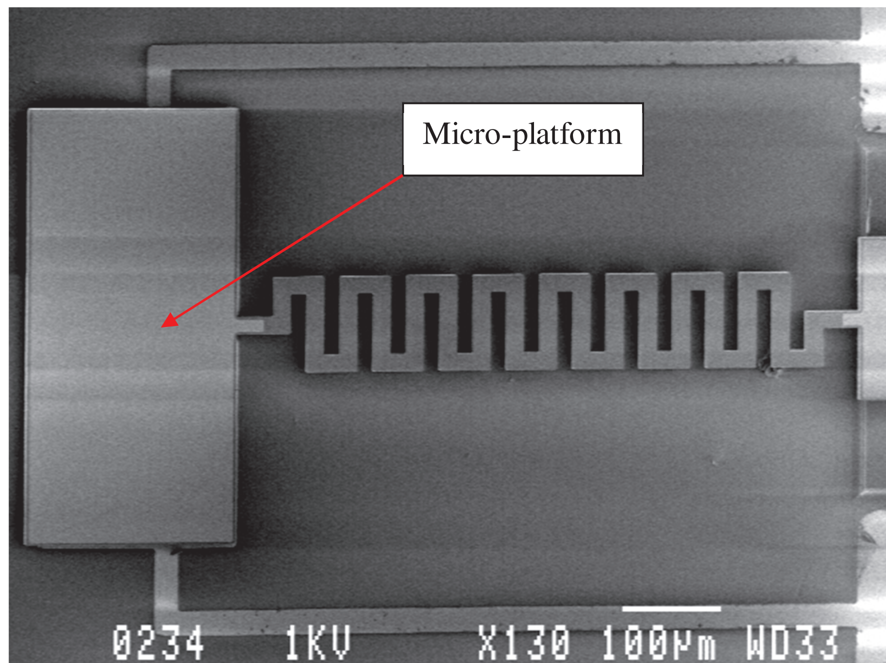

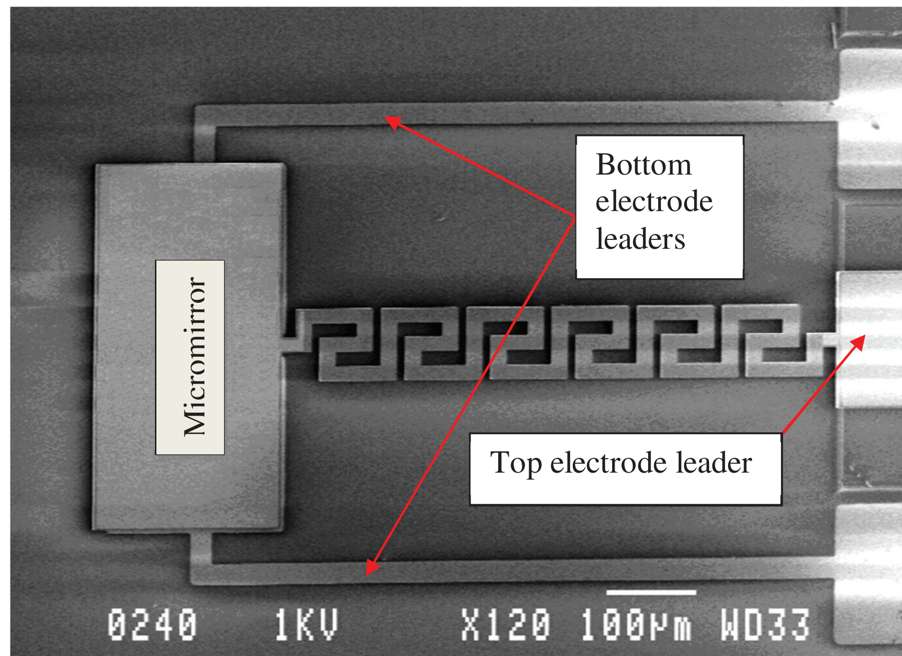

Figure 4.9 AFM pictures of micro-platforms supported by “a cantilever”. This cantilever can be a real cantilever or made of serially connected multiple serpentine beams as shown.

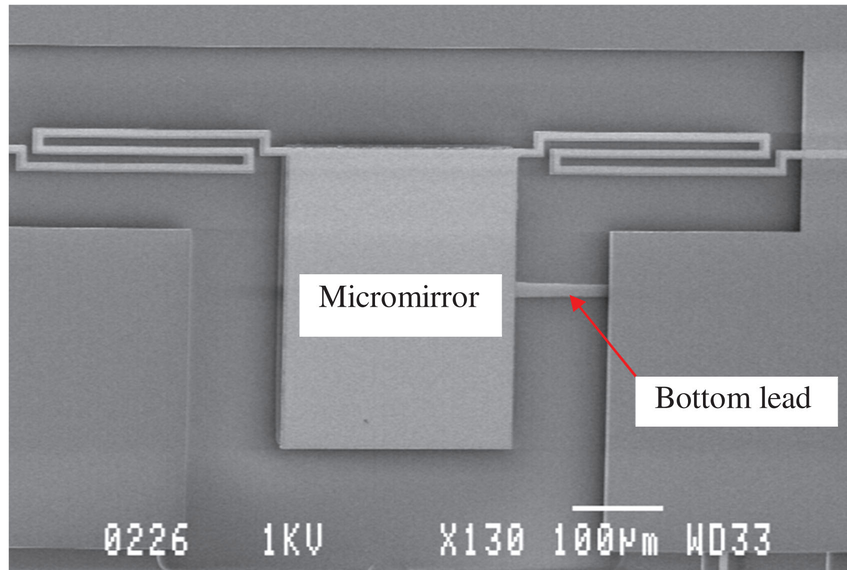

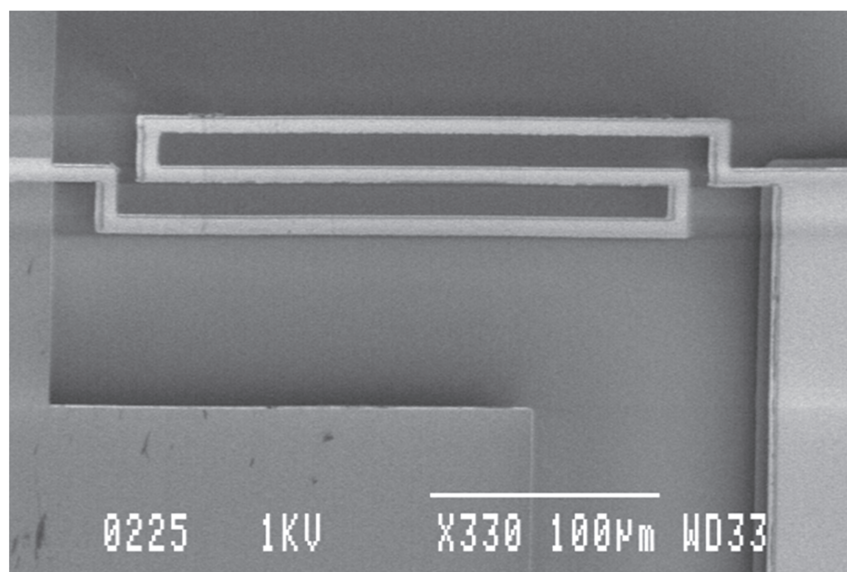

Figure 4.10 AFM pictures of a torsional micromirror in the size of 300μm×240μm suspended symmetrically by two identical rotational serpentine springs. The lower picture shows one of the side springs.

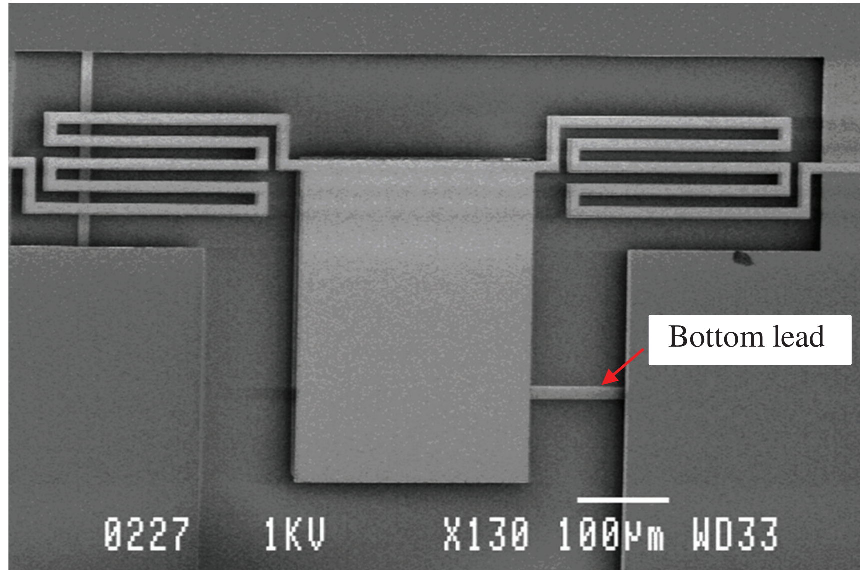

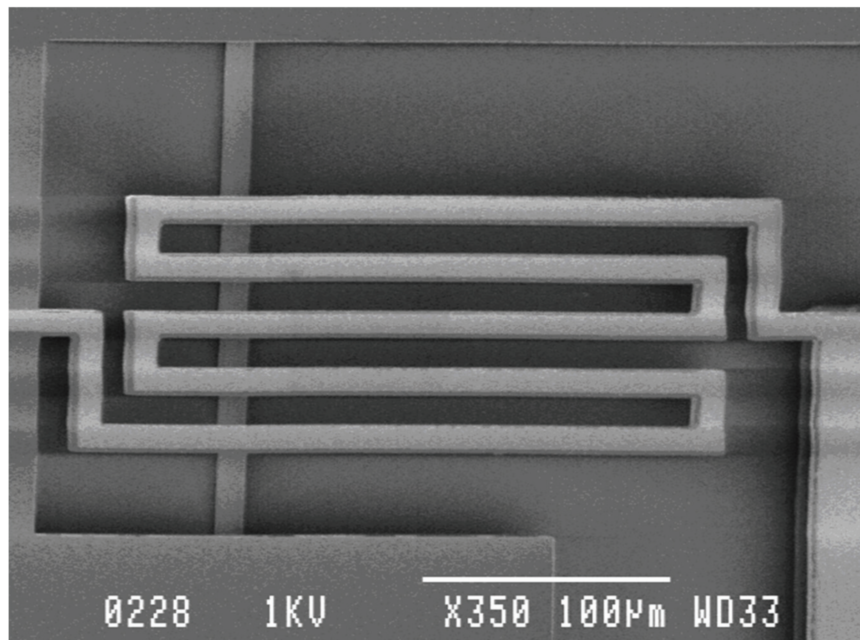

Figure 4.11 AFM pictures of a torsional micromirror with the mirror plate at size of 300µm×240µm symmetrically suspended by two side springs, each of which is made of two rotational serpentine loops. The lower photo shows a side spring.

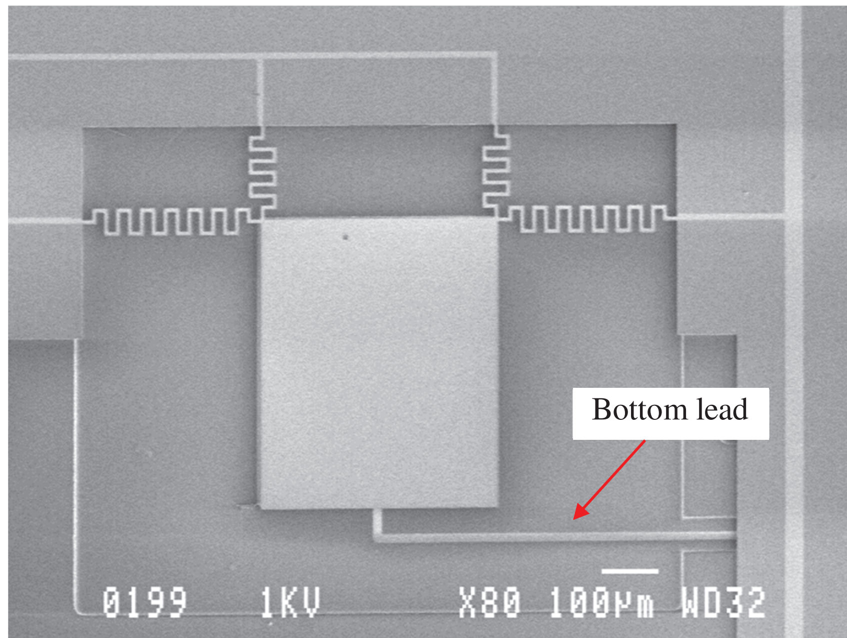

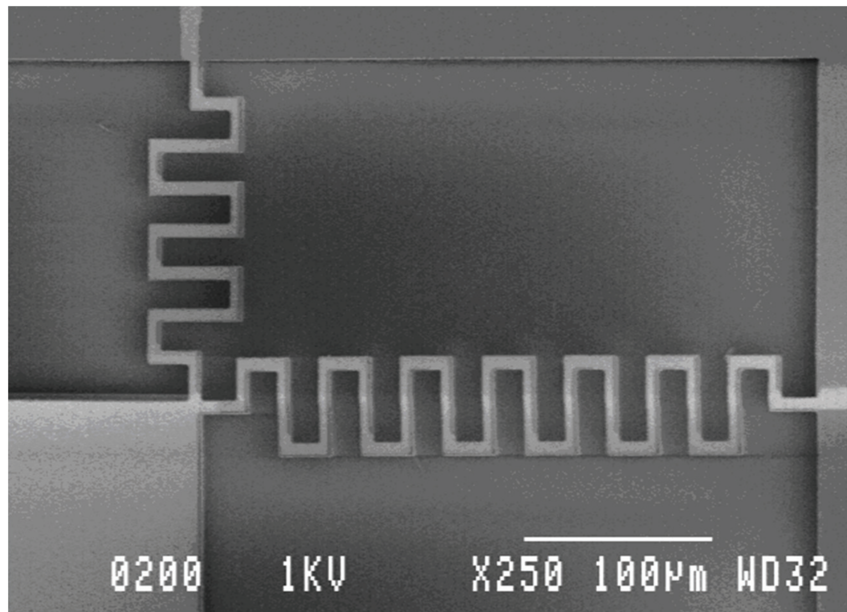

Figure 4.12 AFM pictures of a torsional micromirror with the mirror plate size of 500μm×400μm suspended by two pairs of classical serpentine springs perpendicular to each other for strengthening.

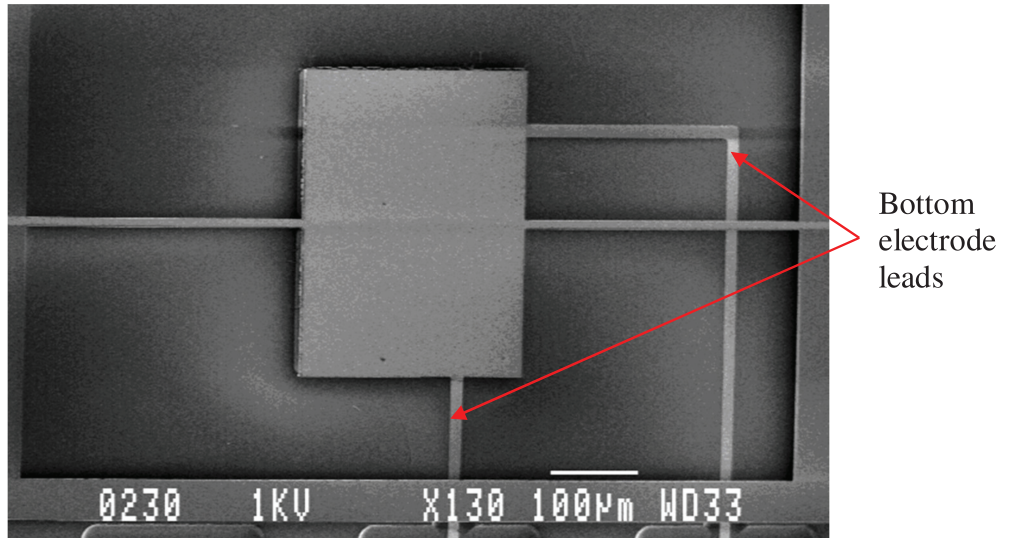

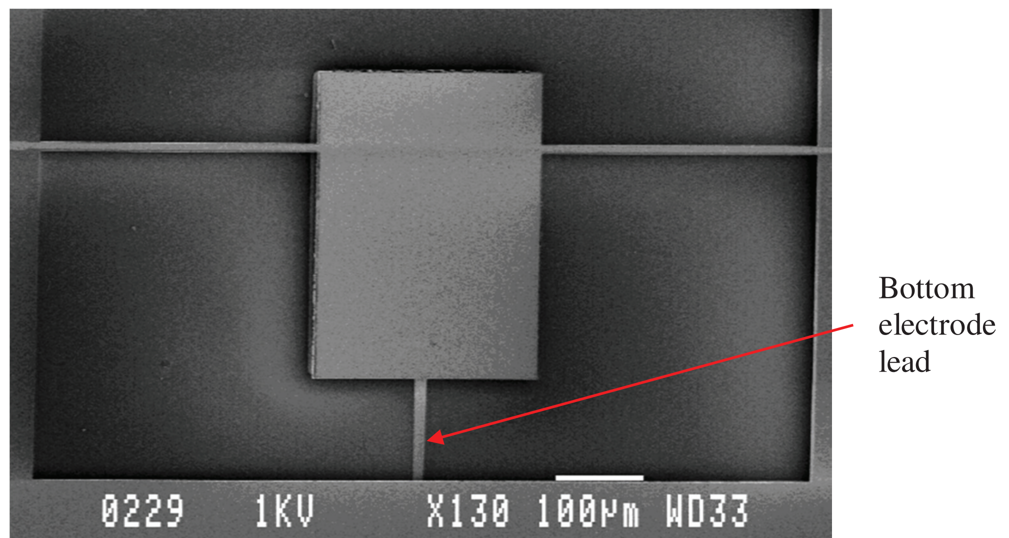

Figure 4.13 AFM pictures of torsional micromirrors with the mirror plate at size of 300µm×240µm symmetrically suspended by two straight beams. The top photo shows the two side beams are lined up with the central line of the mirror plate; the bottom photo shows the torsional axis formed by the two side beams has some eccentric distance to the central line of the mirror plate.

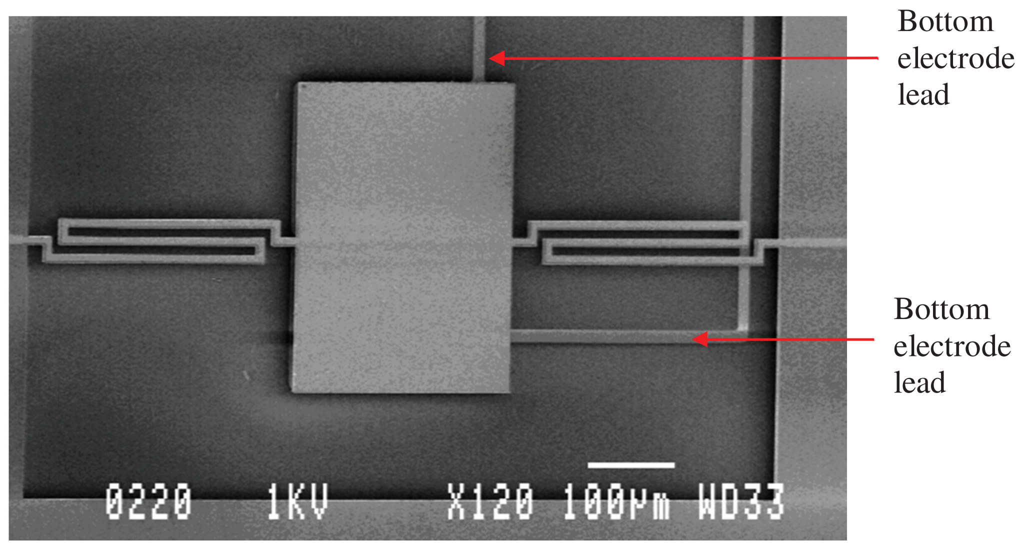

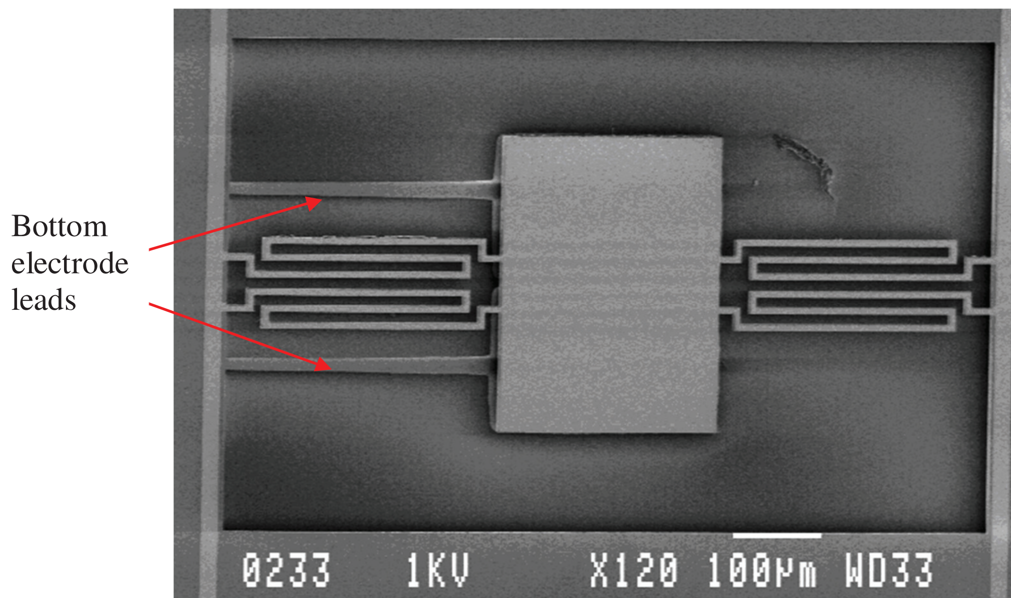

Figure 4.14 AFM pictures of torsional micromirrors with the mirror plate at size of 300μm×240μm symmetrically suspended by two side springs. The top photo shows a single rotational serpentine spring for a side spring; the bottom picture shows each side spring is made of two rotational serpentine springs.

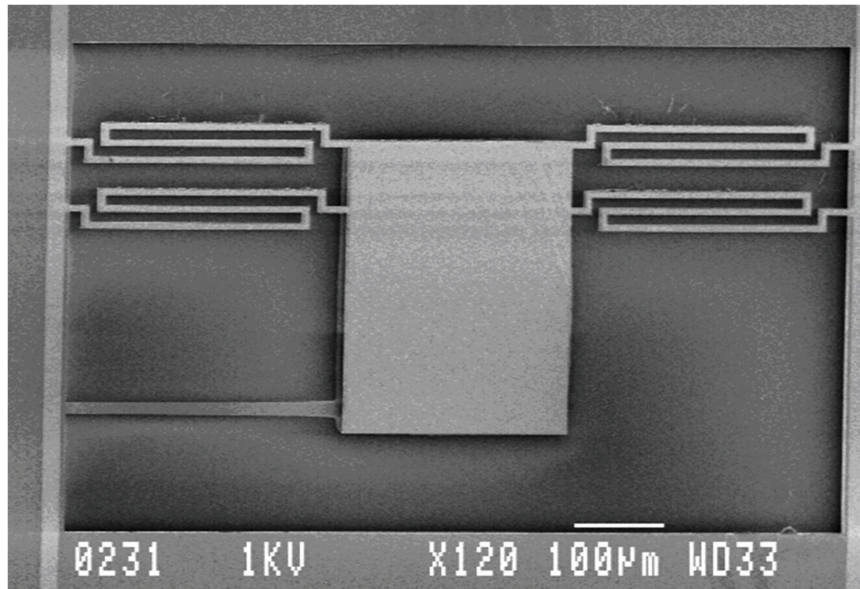

(*a*)

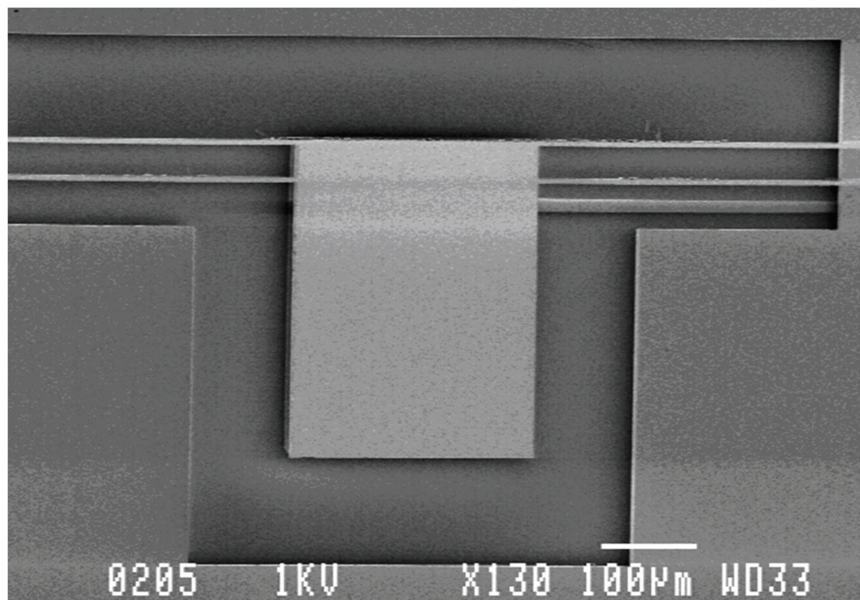

(*b*)

Figure 4.15 AFM pictures of torsional micromirrors at size of 300µm×240µm that are suspended symmetrically by two pairs of rotational serpentine springs (*a*) or two pairs of straight beams (*b*).

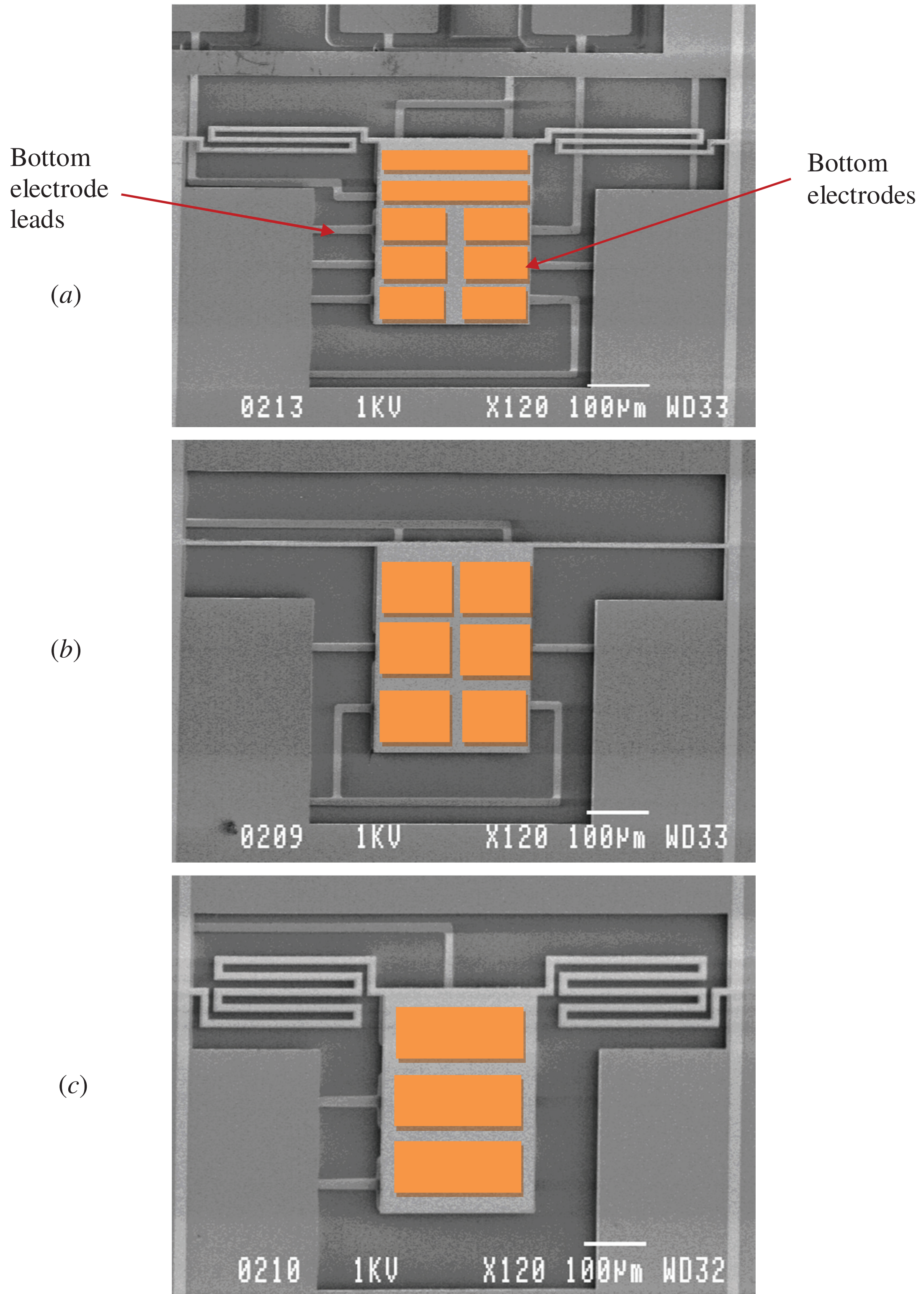

Figure 4.16 AFM pictures of torsional micromirrors at size of 300µm×240µm with their compliant suspensions and the multiple electrodes underneath the micromirrors: (*a*) eight electrodes as shown; (*b*) six equally distributed electrodes; and (*c*) three electrodes.

4.8 Summary

One of surface micromachining processes, MUMPs, its limitations and applications have been briefly reviewed, leading to a presentation on SOI wafer production and the specific process based on SOI wafers including MicraGEM for the fabrication of the proposed torsional micromirrors. Some design rules and design layouts for MicraGEM process, packaging of the fabricated MEMS chips were presented thereafter. Some discussions and SEM photos of the fabricated torsional micromirrors were finally provided.

Chapter 5: Experimental Set-Up and Characterization

5.1 Introduction

There are two types of tests for MEMS characterization: contact and non-contact. In avoidance of any damage that may occur to the micro-structures, the highly integrated circuits and the micro-chips, non-contact testing methods are typically preferable for MEMS and especially for optical MEMS tests. The concept of non-contact herein means there is no direct mechanical contact with the movable parts in a MEMS device because any mechanical contact such as the microprobe, micro-indenter, or other mechanical styluses may lead to the failure of MEMS components. Therefore, the contact test method is limitedly used in characterizing material properties of a microstructure or MEMS [198]. Instead, MEMS tests without external mechanical contact can be realized through either optical or electrical excitation and perception techniques.

Other reasons of using non-contact testing methods are: 1) a highly reflective surface on a movable MEMS component is obtainable, which can be formed by gold plating or coating or other high reflective coating materials; and 2) a laser beam through a group of lenses can be focused into a very small spot on the sensing surface of a movable MEMS part, which then reflects the light beam and projects a light spot on a photo-detector. Many optical sensing components, such as reflecting micromirrors, micro-plates, micro-beams, refracting waveguides and lenses can be integrated in optical MEMS devices.

Optical non-contact test instruments or methods include scanning electron microscope (SEM), laser scanning, stroboscobic interferometry, light scattering and interferometric techniques such as the Tolansky multiple beam interferometry and the two-beam interferometry based on Michelson, Linnik and Mirau. The electrical non-contact test methods include the electrostatic testing method to acquire the capacitance variation of a parallel plate structure under a DC bias, and the resonance measurement along with the responses of MEMS devices under AC excitation. The piezoelectric excitators such as the piezoelectric stacks combined with optical detection method can perform dynamic tests of optical MEMS.

The torsional micromirrors herein fabricated using MicraGEM process discussed in the previous section are usually plated with gold, having a highly reflective surface. This thin deposited layer with the structural device layer (made of silicon or poly-silicon) not only is used as one of the two electrodes but also as the reflecting surface for an incident laser beam. Based on this principle, Laser Doppler Velocimetry (LDV) is adopted in our research for the measurement of dynamic performance for fabricated torsional micromirrors. It is equipped with auxiliary devices such as the signal generator with a range of frequency and other optical equipment. Both optical interference measurement method and PSD (position sensing detector) method are also used in our research for the static testing of micromirrors. Therefore, in this chapter, individual testing set-ups based on these three testing methods will be provided in detail. Then an introduction of a testing method using PSD sensor and Lab-view control algorithm for both static and dynamic measurements of the micromirrors will also be given. This is continued by analysis and

comparison of the tested results with the previous results from either numerical simulations or the established theoretical models. Summary of testing and validation is given in the final section.

5.2 LDV for Dynamic Testing

5.2.1 Doppler Effect

Doppler Effect or Doppler Shift describes that when a laser beam of high frequency is scattered back by an out-of-plane vibrating object, it will undergo a frequency shift that is proportional to the target velocity. Thus to measure the vibrating frequency of the target is to measure the target velocity relative to the motion of the light source. Figure 5.1 shows the schematic of working principle of a Laser Doppler Vibrometer (Type 3544 from Bruel Kjaer) [198], in which a small spot of laser beam emitting from a low power Helium-Neon laser (2mW and 632.8nm in wavelength) is split into two beams by a beam splitter, with one being directed externally to the testing object (the target beam) and the other to the internal rotating disc (the reference beam). Then both the target beam and the reference beam are scattered and reflected back with their corresponding frequency shifts and detected by the photodiode in the instrument. The known frequency shift for the reference beam is realized by the rotating disc with a given rotating speed, whereas the target beam frequency shift is induced by the motion of the testing object. These frequency shifts can be deduced by the formula as $f_{shift} = 2\times v(t)\times cos(\alpha)/\lambda$, where $v(t)$ is the velocity of the spot on the rotating disc or the vibrating target as a function of time, α is the angle between the incident laser beam and the velocity vector, and λ is the

wavelength of the light. Two beams are then mixed and detected by the photodiode or photo-detector in the instrument. Thus the output of the photodiode is a frequency modulated (FM) signal, with the reference beam as the carrier and the target beam as the modulated. The frequency shift of the target beam can be computed through signal demodulation by the signal processor to derive the velocity versus time of the vibrating target, which can be expressed as $f_{target}=abs[(f_o+f_{disc})-(f_o+f_{disc}+f_{target})]$. The original laser beam, the known shifted beam by the rotating disc, the unknown shifted beam (scattered back) by the target, and the signal after modulation are shown clearly in [199] or Figure 5.1. The rotating disc in the LDV set-up used in our experiments has two fixed frequency shifts, meanly, 0.922MHz and 3.456MHz, for the measurement of low and high frequency vibrations of a target, respectively. In other LDV experimental set-ups, the rotating disc is replaced with a Bragg cell [199] to add directly a frequency shift to the original laser beam for both reference and target beams.

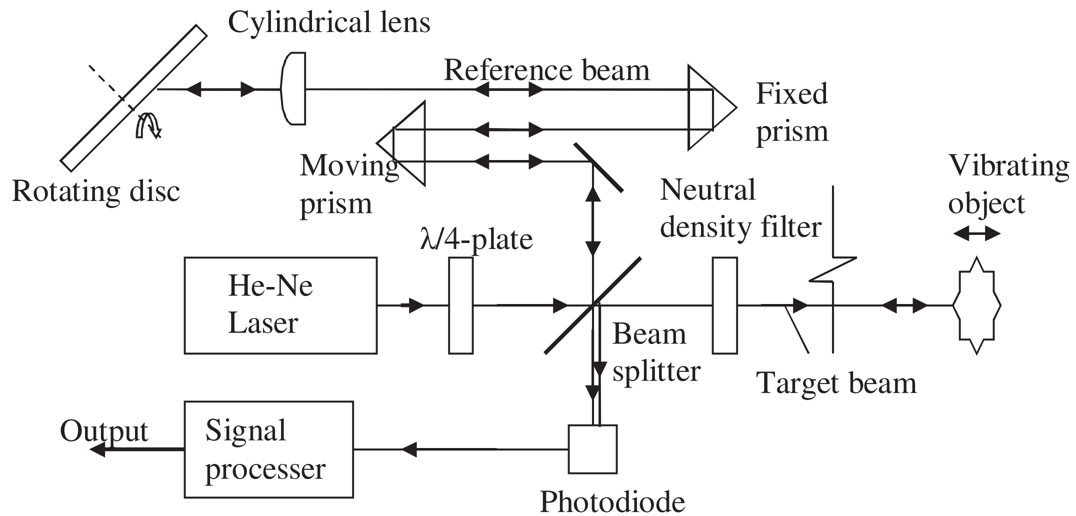

Figure 5.1 The schematic of working principle of a Laser Doppler Vibrometer from B & K using Michelson interferometry (heterodyne interferometry) [199].

5.2.2 Dynamic Test Set-up

The nominal size of the laser beam in LDV is specified by the manufacturer as around 1mm in diameter, which has to be reduced to fit for the MEMS devices through a set of diverging and converging lenses arranged in the light path between the output of the LDV transducer and the target. All individual lenses and beam splitters are mounted on the corresponding XYZ positioners, and the PGA packaged MEMS chip is also positioned on an XYZ positioner with angle tunable platform [200]. The complete experiment set up includes an oscilloscope viewing for the time-domain responses, a frequency spectrum analyzer for reading and recording the frequency spectrums of the LDV output, a vibration source for the MEMS chip, a microscope with a lamp for viewing and adjusting the MEMS chip before test. The vibration for MEMS can be achieved from either electrostatic actuation to the individual micro-device or the attachment of the MEMS chip to a vibrator (this can be an acoustic speaker or a piezoelectric-stack). The vibrator is attached on the platform and adjusted to the right position of the target laser beam. Electrostatic actuation to a MEMS device, a torsional micromirror herein, is realized by connecting the micromirror with an electrical function generator, which outputs an AC power that has an adjustable amplitude and DC floor of voltage and the cyclic varying frequency ranging from zero to the upper limit of frequency defined by the LDV transducer for each cycle. Instead, the vibration of an excitor (either a speaker or a piezo-stack) that has a MEMS chip attached on it can be achieved by connecting the speaker or the stack with the electrical function generator. The frequency set in the function generator can vary from any low frequency (such as DC, the zero frequency) to the upper

frequency limit of the LDV, which is specified to be about 25 kHz. In most of the experiments with electrostatically driven parallel micromirrors like the torsional micromirrors in our research, application of high voltage (may be up to a few hundreds) is necessary to actuate the micromirrors due to their relatively high stiffness of the micro-structures to the out-of-plane motion and large gaps ($\geq$10μm). The high voltage can be obtained by using a DC/AC voltage amplifier. Figure 5.2 shows an overview of the experimental set-up used for the dynamic testing of torsional micromirrors. Positioning of all involved opto-mechanical fixtures starts with aligning He-Ne laser to obtain a circular laser spot on a reflective surface about 1.5m away. The central point of the spot needs to be marked for the alignment of the lenses. And alignment of each lens has to be carried out so that the laser beam targets at the marked central point with a complete round spot. Optimal positioning for the test set-up is achieved until the size and shape of the laser spot on a MEMS device is minimized and perfectly rounded through the adjustment of the distances between all optical components, such as the MEMS device, the converging and diverging lenses, and the laser transducer. For further details, see references in [199].

5.2.3 Excitation Mechanisms

Excitation to electrostatic torsional micromirrors can be done in a direct or indirect way depending on where the mechanical vibration originates. Previously an acoustic speaker is used to provide the vibrating motion from its diaphragm that is subjected to an alternating electrical signal, which belongs to an indirect excitation method. Since most of the packaged MEMS chips are relatively heavy, they are not attachable or bondable to

the diaphragm of a speaker. Only the diced microchips can be bonded or glued to the central flat portion of the diaphragm for the resonance tests. In this way there is no electrostatic deflection that can be resulted because no electrical connection of the MEMS device is possible.

The similar vibrating excitation can be obtained by directly applying a harmonic voltage on a device or a micromirror on a packaged microchip, which belongs to the direct excitation mehod. Thus the direct excitation is straightforward, and can be generated through electrical connection of the testing micromirror with an external unit of a function generator with a voltage amplifier through the embedded electrodes and wiring on the chip and the package. A sinusoidal AC voltage $v(t)$ of small amplitude with sweeping frequency ω with a base DC voltage helps to generate not only a direct vibrating excitation but also a static deflection of the micromirror, in which the excitation can be expressed as $V_0+V \cdot sin\omega t$. In brief, direct excitation method is suitable for the packaged and wired microchips.

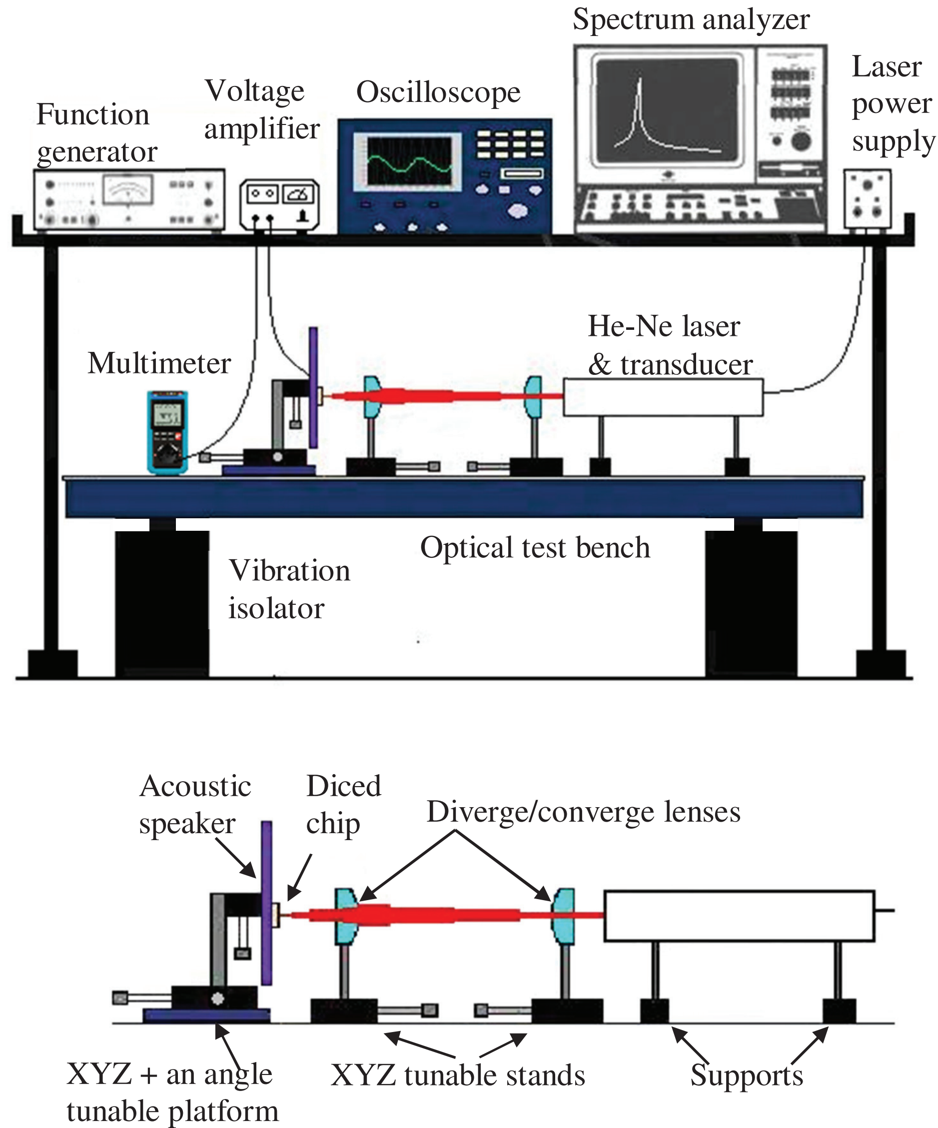

Figure 5.2 An experimental set-up for dynamic tests of torsional micromirrors. The diced MEMS chip with the micromirrors and other microstructures is bonded onto an acoustic speaker (see in the top picture); the bottom picture shows the detail fixtures for alignment of the laser beam. Similar set-up can be found in [205]

There exist other kinds of indirect excitations using piezo-electric actuators or piezo-stacks equipped with drive circuits [201]. Selection of the piezo-stacks needs to satisfy the desired vibrating amplitude, the desired range of sweeping frequencies, and an easy assembly (such as bonding) of it with the packaged micro-chip and the platform. Figure

5.3 gives an example of these piezo-stacks and its voltage–charge amplifier drive circuit. The maximum stroke or amplitude of vibration achievable can be more than 100μm depending on the working range of drive frequency.

In indirect excitation, the actual frequency spectrum of a micromirror is extracted from filtration or subtraction of the frequency response of the MEMS device by that of the microchip or the substrate of the testing device. In this way, all background noises from the test bench or substrate are removed. As long as the bonding of the chip with the flat surface of the vibrator is firm enough, output will be exactly the response from the testing device. As mentioned, since all surfaces on the structural layer of MicraGEM made MEMS device are plated with gold, a high reflective metal, the laser beam can be targeted onto the non-movable portion of the testing device to get the background noise. Comparatively, there is no necessity to perform this subtraction for the direct excitation as long as the test bench has good isolation.

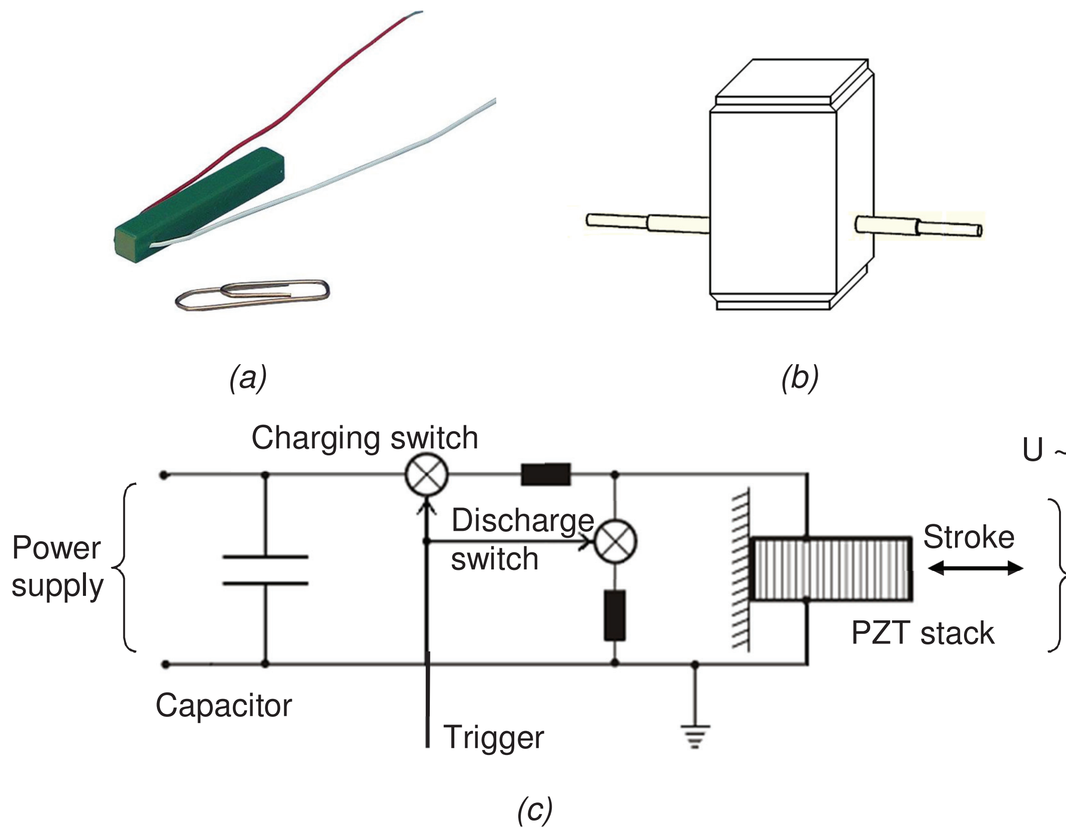

Figure 5.3 Piezo-stack and the drive circuit. (a) a large amplitude (>80μm) of stroke or displacement is obtainable for this stack; (b) the flat top of the stack is suitable for bonding of MEMS chips; (c) a sample of drive circuits for the stacks [208].

5.3 PSD for Static Test

5.3.1 Test Set-up Details

The experimental set-up and its optical path arrangement that involve a PSD sensor (position sensing detector) for quasi-static performance of torsional micromirrors are shown in Figure 5.4. The set-up comes with a He-Ne laser with or without a transducer, a pair of diverging and converging lenses for beam focusing, a PSD sensor, a computer equipped with PSD digital image processing software, and a function generator with

voltage amplification attenuator as well as the necessary positioning fixtures (positioners) for lenses, microchip, and a mirror for optical path adjustment.

The laser beam originated from a He-Ne laser passes through the two focusing lenses and targets at the testing micromirror on the microchip. Then it is reflected by the testing micromirror toward the sensing area of the PSD. The PSD sensor captures the image on it and transmits to the host computer for processing. The coordinates of the center of a laser spot on the digital image or CCD sensing arrays (640×480 pixels) are thus calculated by the software and can be displayed. Due to its high sensitivity in position sensing (sub-micron range) and fast shutter speed (from 1/50 up to 1/10000 per second), both duration and the sampling frequency need to be set in the computer for precise measurement. Depending on these two parameters given, coordinates (x, y) for a static position of the testing object can be obtained and saved in computer for further analysis. It is a common practice that the average of them can represent the current position of the spot. By the comparison of the current position to the original standstill position (0V), and through geometry conversion, one is able to derive the current torsional angle of micromirror. Therefore a relation of the actuated torsional angular deflection of the micromirror versus the DC electrical bias can be obtained through applications of a series of DC voltages (from zero voltage to a voltage before pull-in).

The holder of the microchip is made by an assembly of an XYZ stage and a rotational platform. They are used together for the positioning of the micromirror on the microchip so that the central portion of the movable micromirror is set to be right in the central line

of the optical path and to have a certain angle (for example, 45°) with respect to the incident laser beam. The initial position of the spot on the CCD area has to be carefully adjusted to make sure that the movement of the spot is fully covered by the sensing surface, as shown in Figure 5.4.

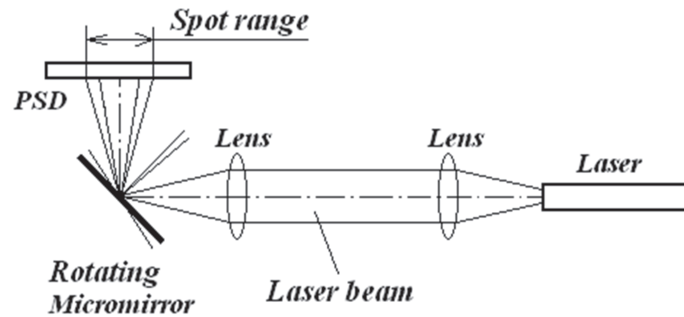

Figure 5.4 The schematic diagram of the test set-up for static performance using PSD sensor.

5.3.2 PSD Sensor and Data Conversion

The PSD sensor mentioned herein is actually a kind of CCD image sensor with integrated matrix arrays of photo-sensing cells. The one used in our research is named as SpotOn CCD by the manufacturer [202], an optical beam positioning measurement system for real time position measurements of single or multiple beams. As briefly introduced, it captures images on the sensing surface and derives the central positions for the light spots on the CCD area using the incorporated software in its host computer. Table 5.1 lists related parameters of the SpotOn PSD sensor while Figure 5.5 shows the SpotOn CCD sensing head and an image of a laser spot on the sensing surface.

Because of the well collimated laser beam, the laser source of the LDV set (see Section 5.2) is selected as the laser source for the PSD static set up. As one can see from the table that wavelength of the chosen He-Ne laser (632.8nm wavelength) is in the spectral response of the CCD camera which is from 350nm to 1100nm. Moreover, stronger light intensity and smaller size of the spot on the CCD area can be obtained if the CCD head is placed closer and more perpendicular to the testing micromirror and the micromirror is placed in a more perpendicular position to the incident laser beam. The spot shape can thus be adjusted to as round as possible in order to maximize the accuracy. The intensity of the laser beam itself can be tuned with an attenuator. Since the wide wavelength of the CCD spectral response range, there may exist some background noise on the image. It is better to place an optical filter in front of the CCD sensing area to avoid any interruption of unwanted light. In this way, the central coordinates can be precisely obtained.

Table 5.1 The related specifications of the SpotOn sensor [202]

Camera type	Monochrome Interline transfer CCD, ½" format
Pixel size	8.6 µm (horizontal)× 8.3 µm (vertical)
Image Resolution	640 × 480
Sensor active area	6.47 mm × 4.83 mm
Position resolution	Sub-micron range
Position accuracy	±5µm deviation edge-to-edge
Spectral response	350 -1100 nm (Model VIS)
Dimensions	64 mm diameter × 34.3 mm depth. Optical aperture has ¾"-32 thread for mounting filters
Communication	RS232
Shutter speed	1/50 to 1/10000 sec

The captured image represents the distribution of light intensity or grey levels along the complete CCD sensing matrix arrays (640×480 pixels). This digitalized image is output and the coordinates (*X*, *Y*) of the center of the spot in the image can be computed by the image processing software installed in the computer using the formula as follows.

$$X = \sum [h \cdot i(h,V)]/I \,,\; Y = \sum [V \cdot i(h,V)]/I \qquad (5.1)$$

where *i(h, V)* is the intensity at a pixel of *(h, V)*, and *I* is the total intensity integrated over total area.

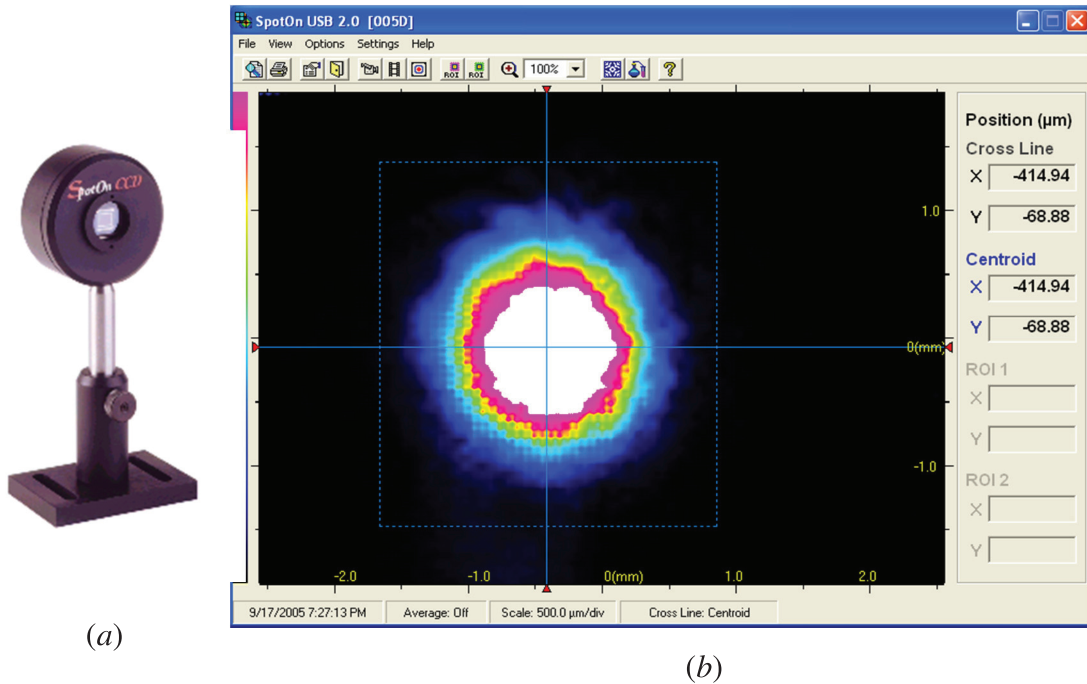

Figure 5.5 (a) The sensing head of the SpotOn CCD sensor; (b) The image in the computer for the laser spot on the PSD sensing area that is reflected by the test micromirror.

As the micromirror might be subjected to transient motion at the moment when it is applied by a step loading of a DC voltage, image capturing should start after some time delay after the mirror reached static equilibrium position. Moreover, the interval between every sampling can be set as long as one second. Duration of 20 seconds can thus provide

20 groups of coordinates for the same position of the micromirror under one applied DC voltage. Average of the values provides the coordinates for the center of the laser spot. The conversion from the coordinates to the deflection of the micromirror can be done based on the geometry of the optical path. And proper arrangement for the complete optical path helps simplify this conversion. Figure 5.6 shows two schematic geometries of the optical path for measurement of vertical and torsional deflections, respectively. Figure 5.6 (a) is used for vertical deflection measurement, while Figure 5.6 (b) is used for the measurement of static performance of the torsional micromirrors that have only non-symmetric suspensions and with an assumption of negligible vertical bending deflection.

As mentioned, the holder of the MEMS chip is an assembly of an XYZ stage and a rotational platform, capable of 3D positioning and an angular positioning. By fine adjusting the MEMS chip holder, the incident laser beam is then targeted at the edge area of the micromirror for easy capture of vibration. Reflected laser spot must be within the sensing area of PSD. As shown in Figure 5.6 (a), if an angle of α for the MEMS chip (the MicraGEM micromirror is in parallel with the chip) and an angle of β for the CCD surface with respect to the incident laser beam are adjusted after fine tuning of their positions, it is possible to predict the relation between the spot position on the CCD sensing surface or captured image and the actual vertical deflection of the micro-stage or micro-platform as:

$$z = \Delta . \sin \alpha \cos \beta \qquad (5.2)$$

where z is the actual vertical deflection of the micro-stage, Δ the spot trip distance on the CCD sensing area or on the image captured by the CCD camera. Similarly, in Figure 5.6

(b), the incident laser spot should be adjusted to the target at a location close to the edge of the rectangular CCD surface such that the full movement of the laser spot is restricted within the sensing area. The distance between the CCD surface and the reflecting micromirror has to be as close as possible to minimize the spot size and the spot movement on CCD surface. All adjusted angles and distances can be measured manually. Thus the actual torsional angle of the torsional micromirror can be derived by the following formula according to the geometry conversion:

$$\tan 2\theta = \frac{\cos(2\alpha - \beta)}{\sin(2\alpha - \beta) + \dfrac{S}{\Delta}} \tag{5.3}$$

where θ is the actual torsion angle of the testing micromirror after deflection; S is the original distance of the optical path before deflection from the micromirror to the CCD sensing surface. Due to the very small angle of the torsional deflection, S can be approximated by the distance between the MEMS chip and the centroid of the CCD surface. In order to compare test results with analytical and finite elemental simulated results, the torsion angle θ is further converted to the vertical displacement by assuming that the vertical deflection at the torsion axis of the micromirror is negligible.

Slow and careful attenuation of the applied voltage is necessary during the test. Pull-in voltage of the micromirror is first estimated by the established analytical model. The applied voltage is tuned step by step from zero until pull-in value. The snapped micromirror recovers to its free position if the applied voltage is switched off. The spot trip Δ can be deduced by subtracting the current coordinates with the original coordinates (zero voltage applied). Thus the torsion angle can be derived by Equation (5.3). The

actual vertical deflection for the front edge of the micromirror can be calculated according to the relation of $z=L\times\theta$, where L is the length of the micromirror from the torsion axis to the front edge.

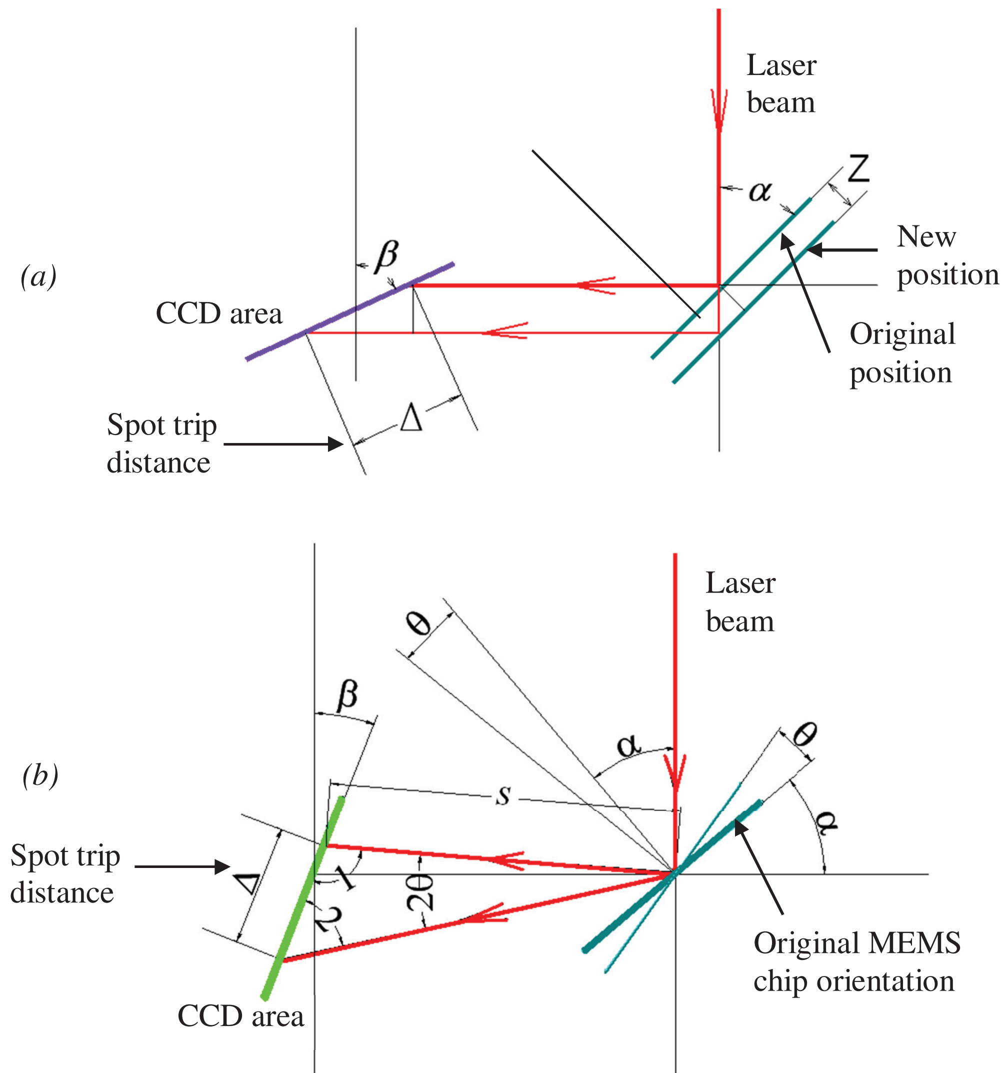

Figure 5.6 The schematic geometries for the optical paths when PSD sensing system is involved in a static test: (*a*) for measurement of vertical bending deflections; (*b*) for measurement of torsional deflections.

5.3.3 Position Sensing Detection

The SpotOn CCD used in static tests belongs to a kind of optical position sensing detectors (PSD) involving matrix arrays of discrete and micron size photo-sensing pixels. However, there have appeared other position sensing detectors (PSDs) that have been involved in MEMS tests, one of which is more economical and employs only a monolithic PIN photodiode as the linear (1-D) or planar (2-D) sensing surface and has a large size of active area (such as $12\times12mm^2$) with uniformly distributed resistance. Compared to those discretely integrated element PSDs, the monolithic silicon PSD has the advantages of high position resolution, fast response speed and simple operating circuits. Some physical parameters of S1880 two dimensional PSD used in our research are listed in Table 5.2 [203]. More details of this PSD can be found in the manufacturer website. Figure 5.7 shows the schematic diagrams for the open-loop static test set-up using PSD and its signal processing circuit module as well as a photo of their assembly. Some views of the complete test set-up are shown in Figure 5.8.

Table 5.2 The related physical parameters of S1880 type 2-D PSD

Parameter	Value
Package type	Ceramic
Active sensing area	12mm×12mm
Spectral response range	320~1060 nm
Photo sensitivity	0.6 A/W
Rise time	1.5μs
The minimum detectable displacement of light spot on the sensing area	1.5μm
Reverse bias voltage	+5V
Output voltage range $V_0(X)$	±6V
Output voltage range $V_0(Y)$	±6V

If the incident light spot is not sufficiently focused on the PSD sensing surface, i.e., the light spot diameter is large and distorted, and falls upon near the edge of the active area, part of the light spot may go outside of the active area, thus degrading the position measurement accuracy. The PSD head is recommended to mount on a module board of signal processing circuit provided by the same manufacturer (see Figure 5.7 (*b*) and (*c*)), such that a range of ±6V output voltages listed in Table 5.2 can be achieved for the *x* and *y* movement of the centroid of the spotlight on the PSD active area when the light spot size is made as small as possible and well within the active area with an adequate intensity of the spotlight. The light spot position is given by the formula below:

$$\frac{2X}{L_X} = \frac{(I_{X2} + I_{Y1}) - (I_{X1} + I_{Y2})}{I_{X1} + I_{X2} + I_{Y1} + I_{Y2}} \tag{5.3}$$

$$\frac{2Y}{L_Y} = \frac{(I_{X2} + I_{Y2}) - (I_{X1} + I_{Y1})}{I_{X1} + I_{X2} + I_{Y1} + I_{Y2}} \tag{5.4}$$

where L_X is the geometry length of the two electrodes at either of the horizontal sides and L_Y is the geometry length of the two electrodes in a vertical side of the sensor (see in Figure 5.9 (*a*), L_X=L_Y=14mm for S1880 PSD), while I_{X1}, I_{X2}, I_{Y1} and I_{Y2} are the output currents from the four electrodes. The schematic of the sensor and the electrodes and its equivalent circuit are shown in Figure 5.9 (*a*). Compared to the digitized image output from the integrated CCD arrays or pixels, this PSD together with its module board of signal processing circuit (SPC) outputs the analog voltage, which can be converted to positional movement of the laser spot. The output resolution is 1mm per output voltage from this PSD sensor, which is not adequate in resolution for the tests of optical MEMS. The actual angle of the targeted torsional micromirror and angular resolution of the set-up can be deduced by geometry relation. Due to the diverging effect of the reflected laser

beam from the micromirror, the PSD sensor have to be placed as close as possible to the micromirror and the optical path between them is better to be approximately perpendicular, such that a small and round spot can be obtained and thus a higher positional resolution can be achieved. Large and distorted spotlight on the PSD active area will cause errors of measurement. Therefore there exists a trade-off in setting the geometry parameters and a calibration for each set up has to be performed. Moreover, photocurrent saturation of the PSD may also introduce some error in the position measurement. In this regard, it is suggested to reduce background light level or to avoid the light beam with strong intensity by using optical filters. Figure 5.9 (*b*) shows a sample of the obtained results during a static test for a torsional micromirror, in which the output voltage needs to be converted into the position of spotlight on PSD active area and then the angular position of the micromirror subjected to a DC voltage can be estimated.

Compared to SpotOn CCD sensors, measurements by using the monolithic photodiode PSD sensors are easily affected by circuits, background light level, and ambient temperature. But it is a better, easier and more economical solution to integrate it within a MEMS device to form a completely packaged optical sensor, for example, the optical cross-connects, the accelerometers, the vibration sensors, etc. Instead, the CCD type PSD sensors are expensive and more accurate. So it is better to use it in tests and characterizations for MEMS research. Nowadays, quite a few manufacturers can provide a variety of monolithic photodiodes to assemble with MEMS devices for various applications.

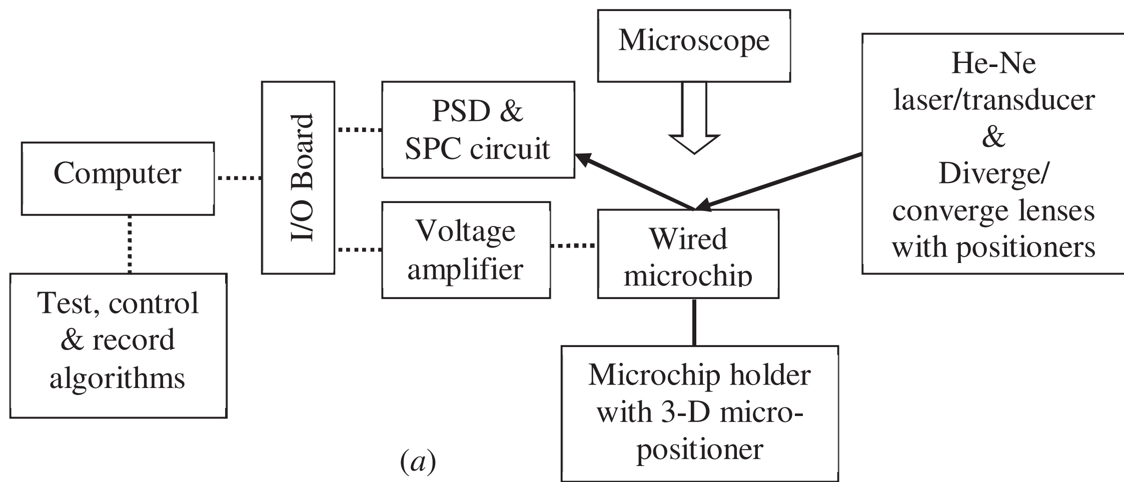

(*a*)

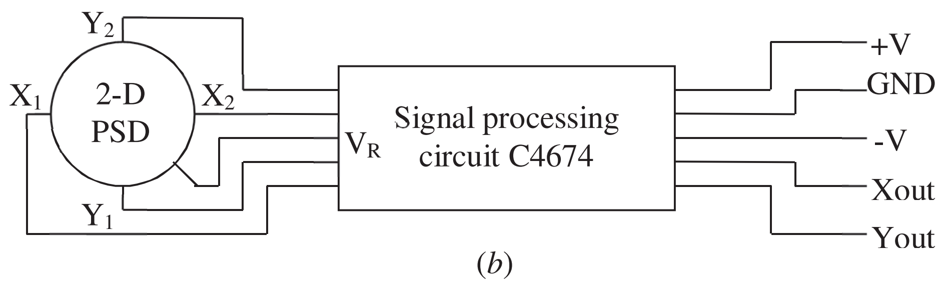

(*b*)

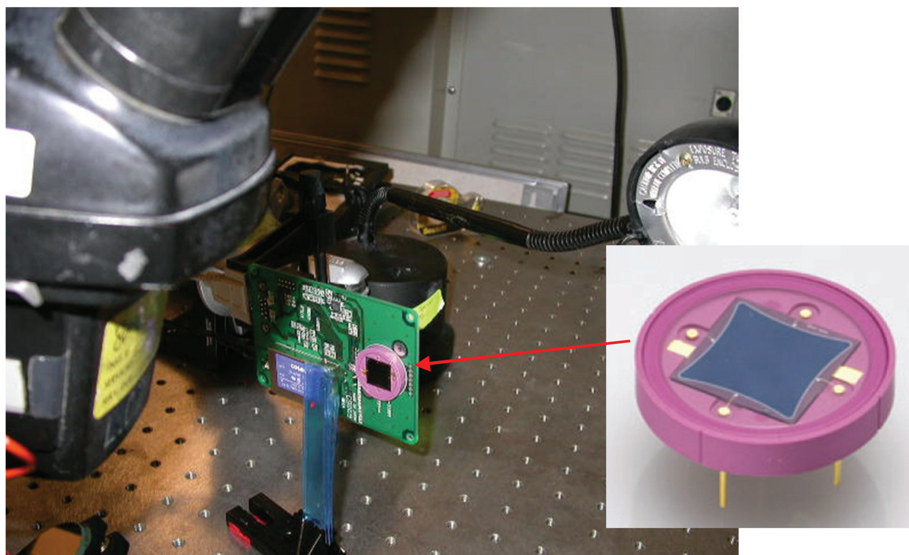

(*c*)

Figure 5.7 Schematic diagrams of PSD based open-loop static test set-up and the signal processing circuit for the PSD as well as a photo of the set-up.

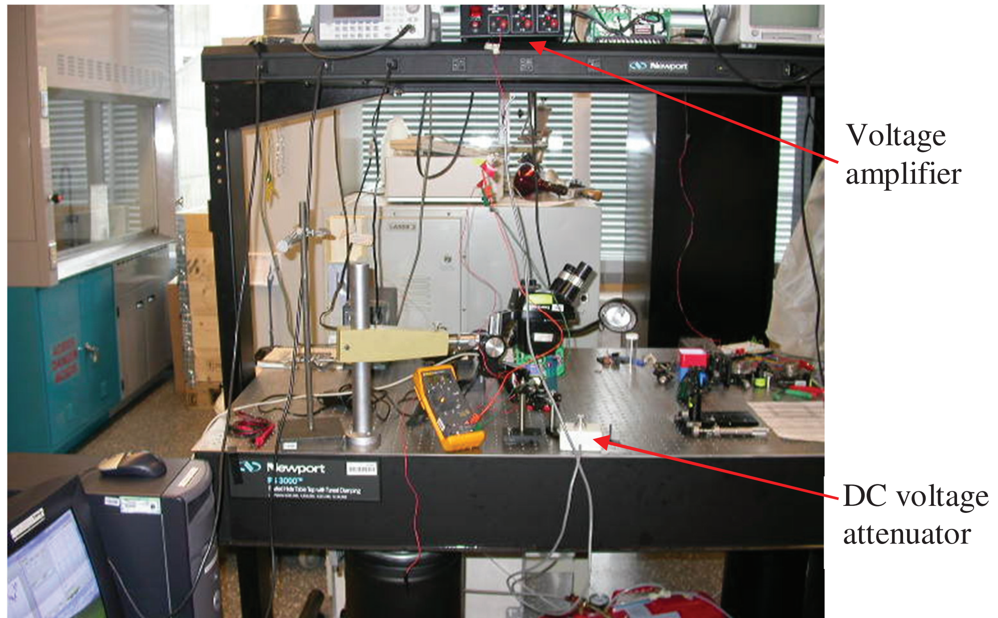

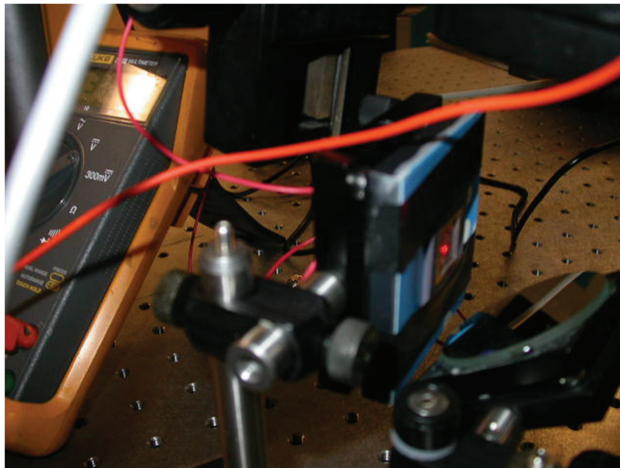

Figure 5.8 Photos of the PSD based static test set up: the bottom left is the mounted micro-chip and the reflecting torsional micromirror; the bottom right is the hosting computer with algorithms for the static tests.

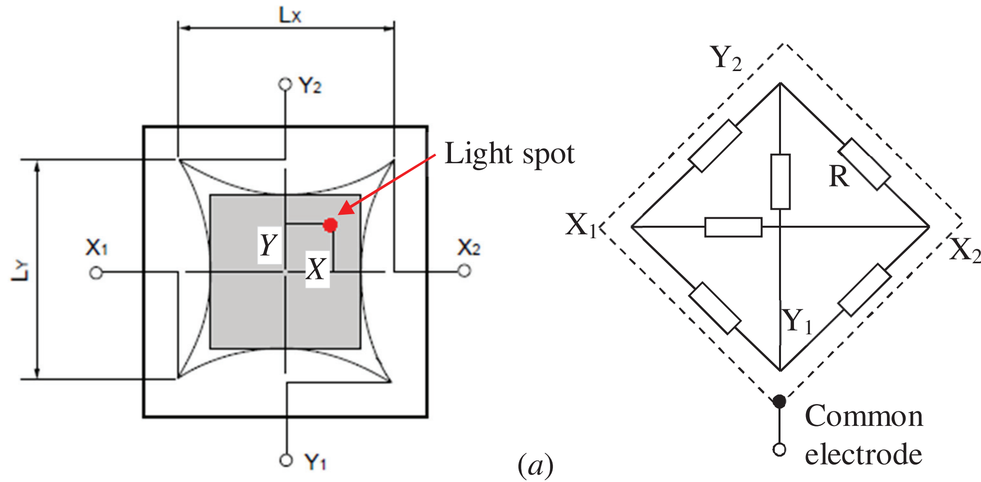

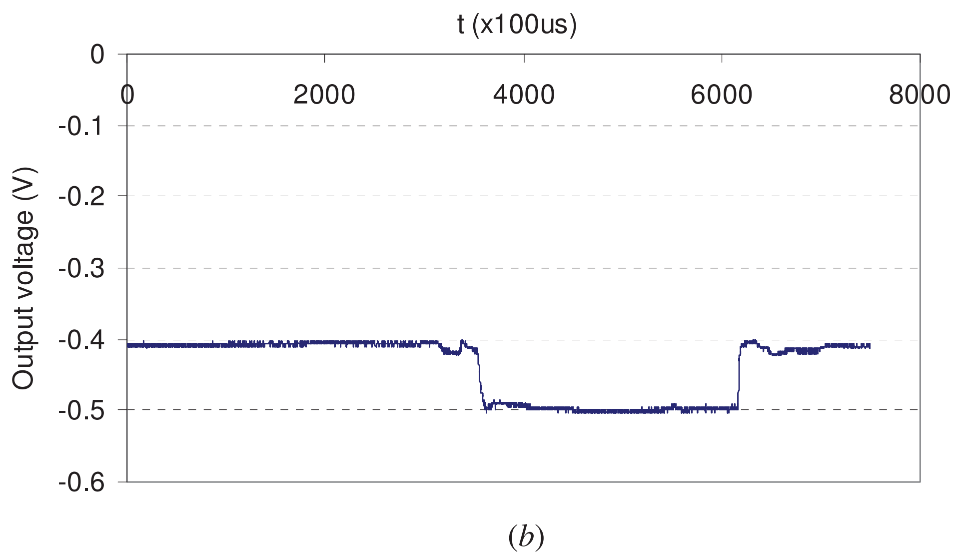

(*b*)

Figure 5.9 (*a*) The schematic diagram for the 2-D PSD and its equivalent circuit and electrodes. (*b*) A sample of the tested results: The *x*-axis represents the time duration with a unit of 100μs and the *y*-axis is the output voltage proportional to the spotlight position on the PSD sensing surface. It shows the micromirror is deflected to an angle when the micromirror is loaded by a DC voltage input.

5.4 Optical Interferometry Technique for Static Test

Non-contact tests that employ interferometric techniques are common for the measurement of static deflection and surface deformation or profile of MEMS devices and other micro-structures. This technique can be further classified as two beam and

multi-beam interferometric techniques. The former can be of many types, such as Michelson interferometry, Linnik or Mirau interferometry, which involve the double beam interferometry technique. Later, some experiment designs were developed based on Tolansky interferometry [204]. The two beam interferometric technique does not emphasize light reflection from the testing surfaces. However, the highly reflective surface of the reference plate is demanded in multiple beam interferometric technique. Because of the simplicity in test platform and high accuracy of measurement, the coaxial interferometric technique, an improved double beam interferometry that is based on Michelson interferometer establishment, is selected in our investigation.

5.4.1 Optical Interference

When two or multiple light beams travel together, they interface each other forming an image or a stripe pattern consisting of successive bright and dark fringes if viewed by an optical instrument at this location. This is called optical interference phenomenon. For two beam interference, there exists a relation among the quantity of the fringes (N), the light wavelength (λ), the refractive index (n), the incident angle of light (Φ), and the thickness (t) of the gap between interference image plane and the testing surface on the object, which is written as [205]

$$N \lambda = 2\, n\, t \cos \Phi \tag{5.5}$$

As is often the case, the incident light is perpendicular to the interference image plane and works in a vacuum or air (the index for air is 1), thus the formula can be simplified by

$$t = N\lambda/2 \tag{5.6}$$

An interference fringe will appear if the thickness of the gap is changed by half a wavelength of the light. The number of interference fringes determines the accuracy level of the measurement. And since the deflections/deformations or surface profiles for MEMS devices are in a range of microns, this submicron level of precision (half a wavelength) is enough for MEMS characterization. Practically, a reference glass plate is placed at the location of the interference image plane, which is usually in contact or close proximity with the object, thus an image of interference fringes can be observed under a microscope. However this reference plate that is almost in contact with the surface of the object is detrimental to the MEMS devices because of possible contamination and mechanical damage.

Compared to the two beam interference, the width of the interference fringes generated from multiple-beam interferometry becomes extremely narrow, and the precision of measurement is around 50 times higher than that of the two beam interference technique, which is thus used for nano-scale measurement for surface topography. The multiple beams are generated by multiple reflections of an incident light beam on two highly reflective surfaces that are placed in close proximity, which include the original non-reflected beam, the twice-reflected beam, the fourfold-reflected beam, and etc (see Figures 5.10 (*a*) and 5.11 (*b*)). These beam waves superimpose each other to form an image of interference fringes when it is collected by a lens and observed in a microscope. It is therefore the width of the fringes is determined by intensities of these beams or the reflectivity of the surfaces. However, due to the same proximity of the two surfaces (the

reference plate and object surface), multiple beam interferometry technique can be used for high precision topography measurements.

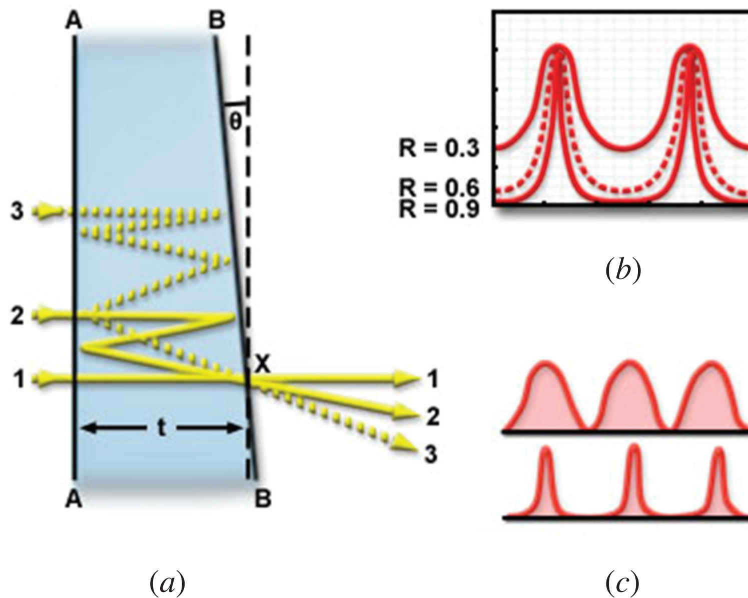

Figure 5.10 Multiple beam reflections and interferometry. (*a*) multiple beams generated due to the high reflectivity of the surfaces; (*b*) the breadth of the fringes depends on the reflectivity levels; (c) the comparison of two beam fringes with the multiple beam fringes or the synthetic light waves by two beams and multiple beams (Adapted from [206]).

5.4.2 Mirau Interferometry

In avoidance of contact or close proximity measurement, it is desirable to develop a non-contact interferometric technique for MEMS characterization. The Michelson type interferometers, due to an appreciable distance between the reference plate (a beam splitter or a half mirror) and the surface of testing object, can be chosen for such kind of measurements. The principle of the double beam interferometric technique can be briefly described as follows: A light beam from source is split by a beam splitter into two beams

of equal intensity and mutual coherence, with one beam being directed onto the reference mirror plate and the other onto the target surface of a MEMS device. The light produced by reflection of these two beams is then made to interfere with each other and generate interference fringes. Based on these interferometric essentials, various test set-ups can be devised depending on the specified requirements and applications. In combination with conventional microscopes, there have appeared a few interference objectives that are so compact that they can be easily screwed into a microscope to perform interferometric measurements for MEMS chips. Because of this, the microscope equipped with an interference objective or Mirau objective is thus called an interferometric microscope.

Mirau objective together with a Nikon microscope is chosen for test characterization of the fabricated torsional micromirrors due to the availability of Nikon's instruments in our lab. The principle of the objective, as illustrated in Figure 5.11 (*b*), relies on placing a reflection reference mirror in the center of the objective lens, and interposing a half mirror between the objective lens and the testing object. These components are so arranged that an interference pattern will appear if the system is focused upon the surface of the object. This fringe image is then captured by a digital camera or a CMOS camera mounted at the top view port of the microscope and stored in the hosting computer for further numerical treatment. The schematic of the interferometric measuring set up that involves a Mirau objective is shown in Figure 5.11 (*a*). The precise alignment of optical path has been incorporated into the compact assembly of Mirau interference objective (see Figure 5.11(*b*)). Due to the coaxial optical path, the interference fringe image will appear along the optical axis at the central portion of the reference mirror plate, thus both

3-D coarse and fine positioning of the testing micromirror with respect to the Mirau objective has to be performed carefully by manual manipulation of the adjusting fixtures on the microscope and the micropositioner placed on the platform of the microscope.

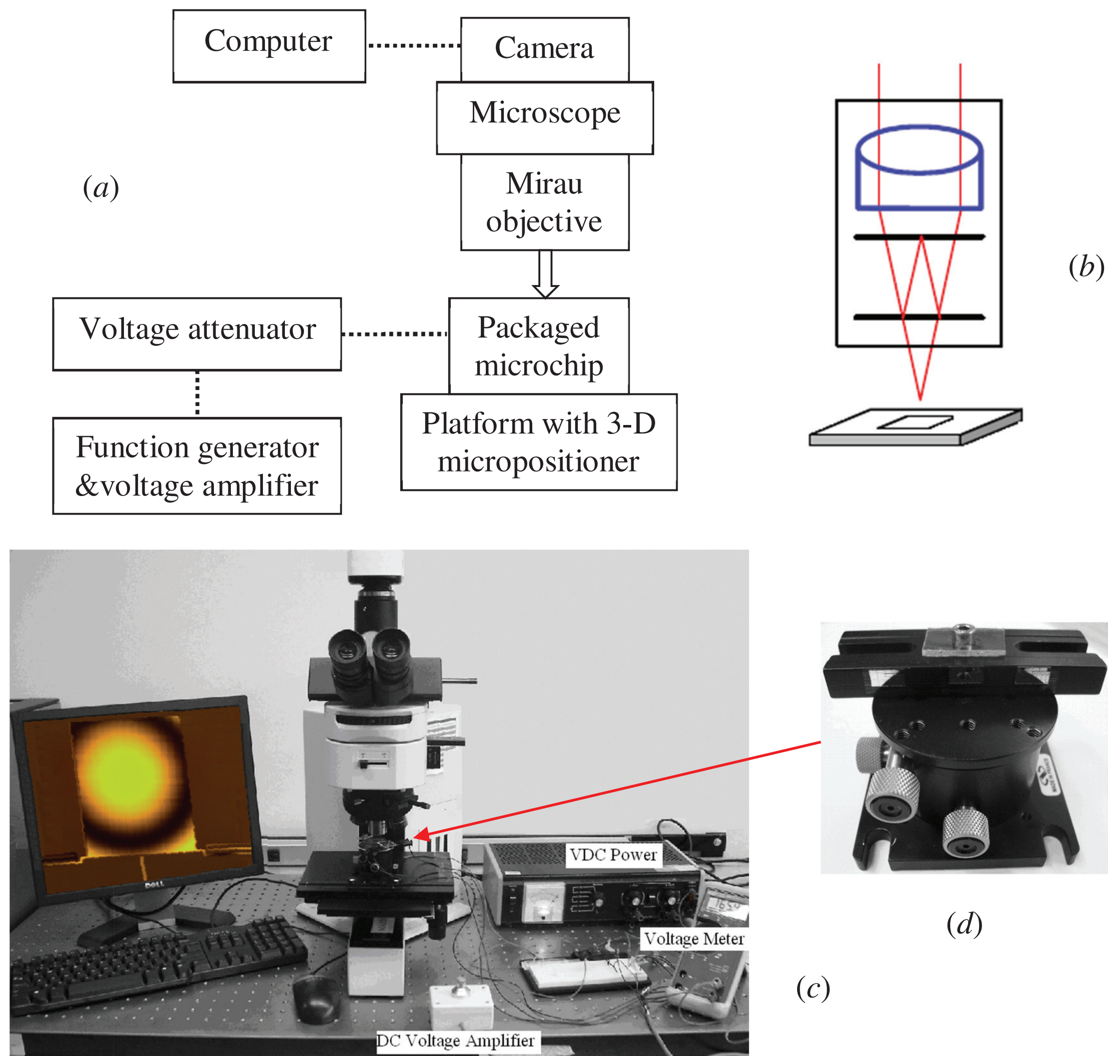

Figure 5.11 The schematic diagrams and views of the two beam interferometric static test set up involving Mirau objective. (*a*) the schematic of the set up; (*b*) the schematic of the Mirau objective; (*c*) the view of the set up; (*d*) the micro-stage used for fine positioning.

5.4.3 Static Test Set-up with Mirau Objective

As has been briefly introduced above and shown in Figure 5.11, the static test set-up including Mirau interference objective is established on the test platform with the microscope capable of 3-D positioning. Fine adjustment of the testing micro-chips can be realized by the micro-stage, which is capable of very fine tuning at translation, tilt and rotation (see Figure 5.11 (*d*)). Mirau objectives adaptable to Nikon microscopes have three magnifications at 10, 20, and 40 times. The one used in the research is with 10 times magnification, accurate enough for MEMS measurement. It is a compact assembly of a beam splitter or a half mirror, a reference mirror and an objective lens. As illustrated previously, two beams reflected by the reference mirror and the testing surface, respectively, superimpose or interfere with each other to form a clear fringe image when the optical path is focused on the testing surface. A light filter is inserted into the slot on the microscope and placed perpendicularly to the optical path in an intention to get a monochromatic light beam in narrow wavelength before it is guided onto the Mirau objective and to obtain clear fringe maps. Figure 5.12 shows the complete set of fringe images taken for a torsional micromirror subjected to a DC voltage that varies from zero to pull-in voltage. The circular stripes or ridges with different radius, breadth and intensity can be observed from these images depending on the magnitude of the voltage applied. The maximum torsional angle can be roughly estimated by counting the number of either the dark or the bright ridges when the micromirror is snapped down under the pull-in voltage. The further precise evaluation of the desired parameters can be performed

by using various digital image processing techniques, which is the content of the following sub-section.

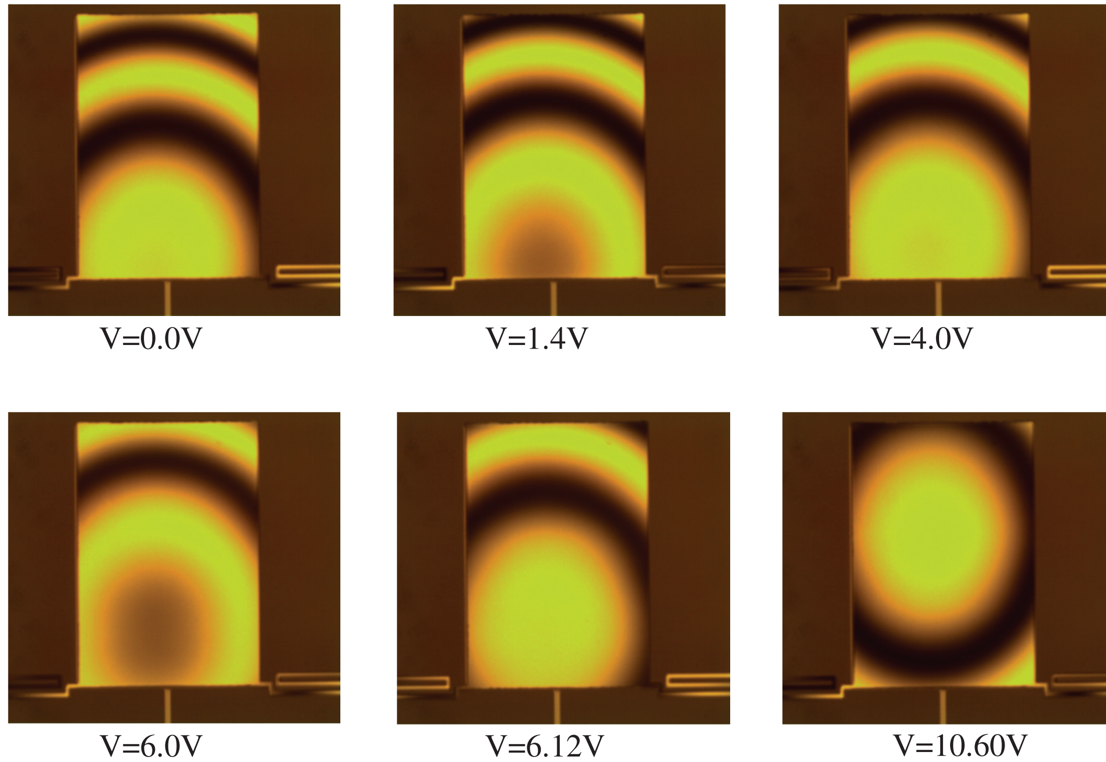

Figure 5.12 (*a*): The interference fringe images captured from the interferometric microscope that has Mirau objective. The voltages are shown for individual images. The last image herein is captured when the micromirror is in perpendicular to the incident light beam (in horizontal level).

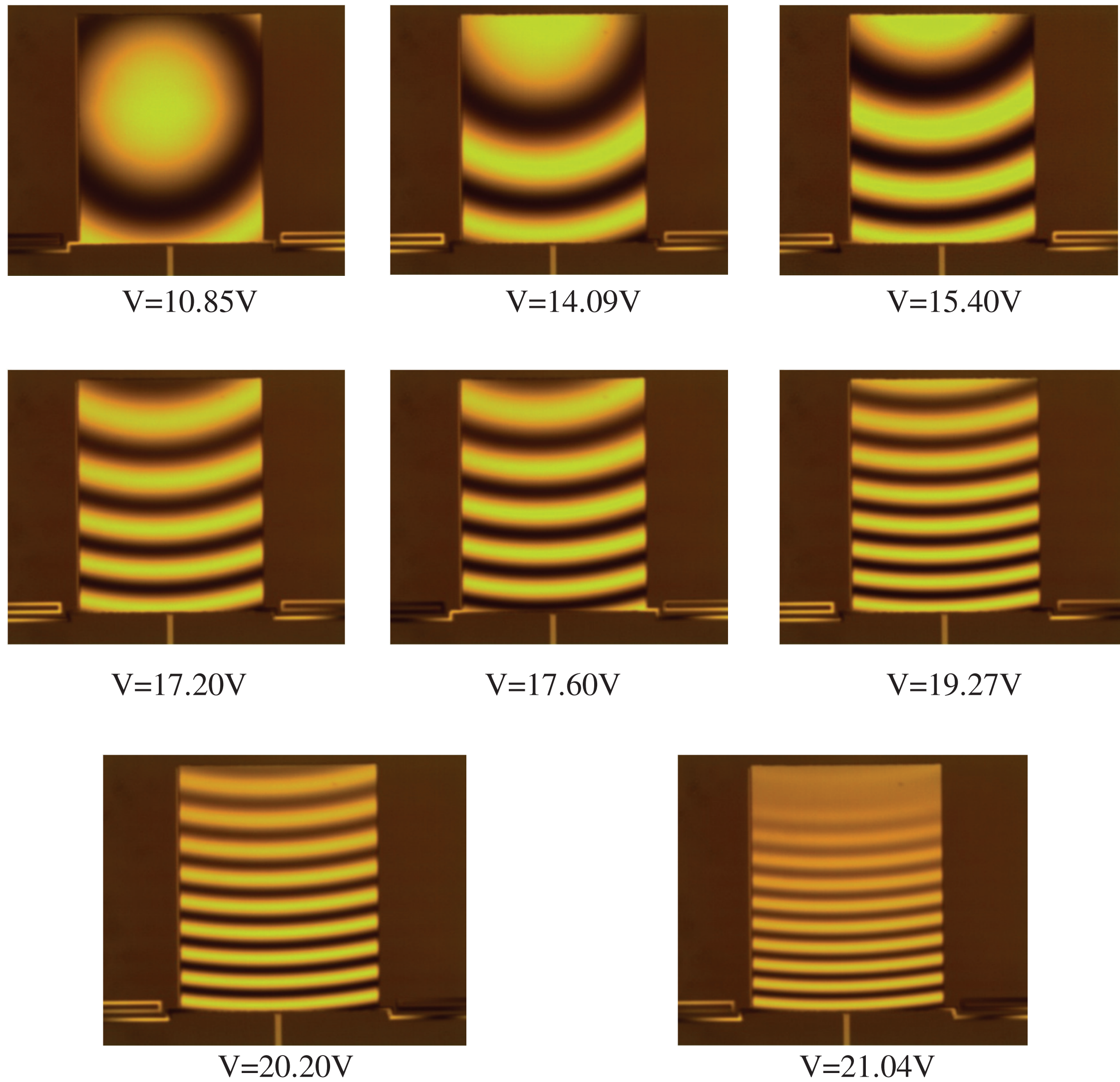

Figure 5.12 (*b*): The interference fringe images captured from the interferometric microscope that has Mirau objective. The voltages are shown for individual images. The first image is captured when the micromirror is in perpendicular to the incident light beam and the last image shows the fringe pattern before pull-in.

5.4.4 Fringe Pattern Processing

The fringe patterns or images captured by a digital camera from an interferometric microscope have to be further processed mathematically to acquire the phase distribution

along the pattern. Then this phase distribution can be converted into the desired parameters, such as the out-of-plane deformations or deflections or surface profile of the object. There are a few methods used for fringe pattern processing, such as the fringe tracking, Fourier-Transform based algorithms, and phase shift techniques. The phase shift technique is sensitive to the background noise on the fringe patterns, requiring multiple fringe patterns to eliminate this noise. The Fourier transform based algorithms are more tolerant to noise, but a signal at one position may affect the signals in other positions. This can be overcome by applying an FT algorithm to a partially representative image or a window adapted from the global fringe pattern. Applying this algorithm (windowed Fourier-Transform, WFT) each time to an individual sub-image, the desired parameters for the complete surface can thus be derived and collected. The fringe tracking technique is very straight forward, which can be applied to read the linear deflection distribution along a rigid plate. Since the torsional micromirrors used in our research are composed of the rigid mirror plates and the soft suspensions, no deformation of the mirror plate itself is considered, and the fringe pattern reflects only the linear deflection or a constant out-of-plane slope along the length of the micromirror. By counting the number of the dark or bright stripes (ridges) on the fringe pattern, a torsional angle or the vertical deflection distribution of the loaded micromirror can be calculated by the formula given in Equation (5.6).

Physically a fringe pattern is a distribution of the light intensity along the testing surface, while mathematically this fringe pattern can be represented by

$$I(x, y) = a(x, y) + b(x, y)\cos[\varphi(x, y)] + n(x, y) \tag{5.7}$$

where $I(x, y)$, $a(x, y)$, and $b(x, y)$ are the recorded intensity, background intensity, and the fringe amplitude, respectively; $\varphi(x, y)$ is the desired phase distribution; and $n(x, y)$ is the noise. The phase distribution can be derived by solving the equation using Fourier transform, which yields a result for the wrapped phase distribution as,

$$\varphi(x, y) = \tan^{-1}\left(\frac{\operatorname{Im} c(x, y)}{\operatorname{Re} c(x, y)}\right) \tag{5.8}$$

A conversion using unwrapping is needed in the translation of the phase distribution to desired parameters such as an out-of-plane deformation at a position in the image. The complete process of WFT algorithm can be done by the hosting computer in the test set up, which is installed with the commercial software, Fringe Processor™ [207], for post-processing of the fringe patterns. The operation procedure to perform WFT algorithm using the software is written here for reference: 1) The image in true color and BMP format captured by the digital camera must be converted into 256 grayscale TIF format; 2) A sub-image or window from the formatted image is taken, which has to be a representation of the original image; 3) The last image is loaded and further converted into 8bit image by the software; 4) This reformatted image is then resized; 5) Low pass filter is applied; 6) The 2D FFT is applied; 7) The wrapped phase distribution is obtained by applying the inverse FFT; 8) The continuous phase distribution is derived by unwrapping; 9) Then the desired parameters are finally achieved by calculation. Figure 5.13 shows a sample of the initial and the post-processed images obtained by using the software. Due to its simplicity, double beam interferometry is therefore also employed in our research to measure for static deflections of the fabricated torsional micromirrors for verification. With the mentioned processing software, the obtained interference patterns

or light strips can be treated to provide the deflections at any point of the micromirror or the slope in an assumption that the micro-mirror plate is rigid enough and flat.

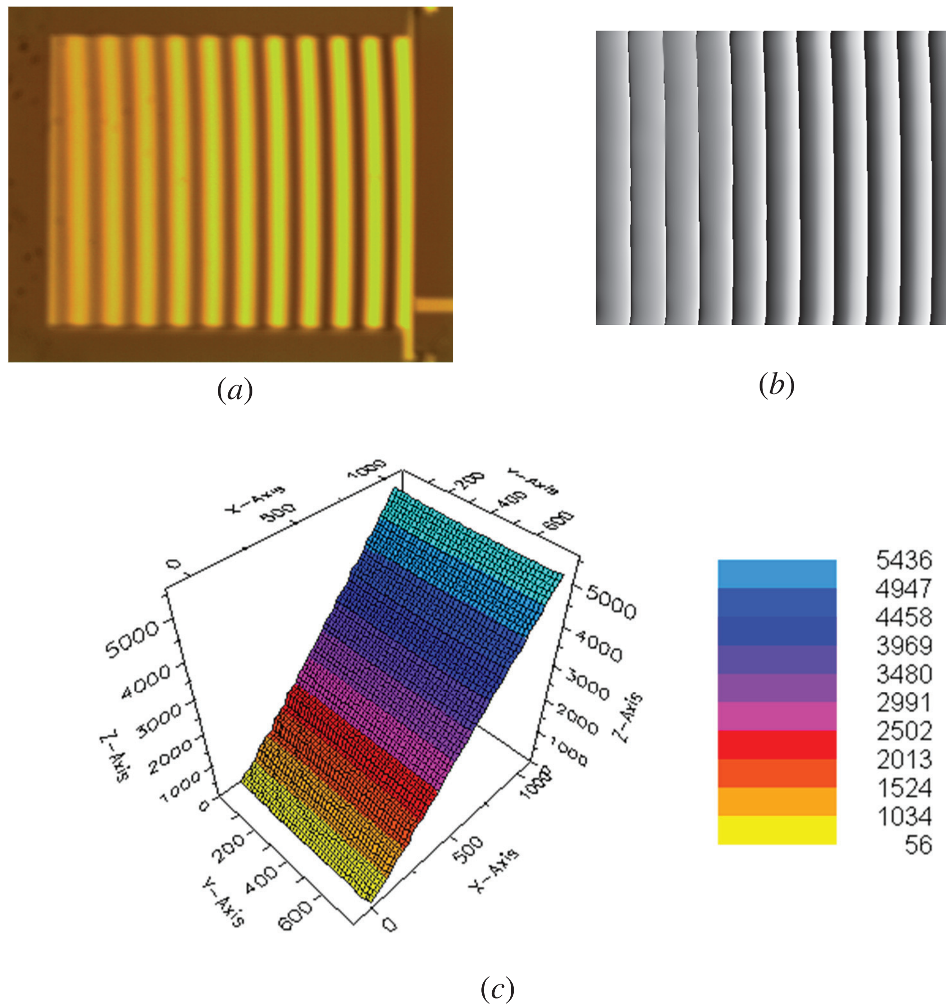

Figure 5.13 (*a*) The interference fringe image captured from Mirau interferometric microscope; (*b*) The processed (wrapped) fringe pattern; (*c*) The 3-D unwrapped phase map showing the bending slope along the micromirror.

5.5 Verification and Discussion

Many tests have been done for the verification of the fabricated torsional micromirrors using the previously proposed test methods. However, due to many reasons such as the

fragileness, deformed structure, and handling error, some of the micromirrors are broken. Therefore, the following analysis and discussion are only on the test results obtained from a few micromirrors and have been verified by repeating the same tests at least twice with the same device. Comparisons and discussions between analysis, simulation and test of these individual micromirrors will be presented. The test methods used in the research are very useful for optical MEMS tests and further investigation and characterization on these test set-ups are another research topic. The physical properties of the micromirrors involved in the following sections are provided by the manufacturer.

5.5.1 Micromirror #1

Table 5.3 presents the design parameters for a torsional micromirror with dimensions of 500μm×400μm×10μm in length L, width W and thickness t, named as Micromirror #1. The static test set-up for the micromirror is based on PSD sensor, that is, the SpotOn CCD, shown in Figure 5.5. The 84 PGA packaged MicraGEM device consisting of the micromirrors is held by a holder placed on micro-positioners. The LDV He-Ne laser source is used to shoot a laser spot on the micromirror device. An optical system consisting of diverging-converging lenses was used in order to reduce the beam diameter and focus the laser beam onto the micromirror. Different laser spot sizes may be obtained by varying the distance between the lenses in order to test devices of different dimensions. The micro-positioners were also used to precisely tune the distance between lenses. Thus the combination of the lens and micro-positioners can be used to get a desired laser spot size. The bias voltage is applied using the designated pins of the

packaged device. Application of a predetermined voltage tilts the micromirror and the amount of tilting can be estimated by the movement of the reflected spot. Figure 5.14 shows a picture of the experiment. The silicon material for all miromirrors tested in the research has the following physical parameters: Young modulus E equals 129.5GPa; Poisson ratio v equals 0.21 and density ρ is 2320kg/m^3 [167, 168].

Table 5.3 The designed dimensions for the torsional micromirror #1

Spring Type	Side Distance (μm)	Cross-section w×t (μm)	Initial Length L_i (μm)	Final Length L_f (μm)	Parallel Length L_p (μm)	Orthogonal Length L_o (μm)	Air Gap (μm)
Rotational Serpentine	300	7×10	23	23	220	17	12

Because the predicted pull-in voltage is around 19V, the applied voltage on the micromirror has to be fixed in the range less than 19V, in order to avoid any unstable deflection or snap-down. Therefore the voltage was tuned from zero to 18V in a constant step increase of 2V. During each voltage step, PSD performs sampling and recording of the spot positions only after the voltmeter settles stably on the desired voltage. Table 5.4 lists both the measured data and converted data. In order to compare, the PSD read-out have been converted into displacement of the front edge of the mirror plate. Figure 5.15 shows the electrostatic curves obtained from Matlab programming based on linear beam theory, FEM simulation based on SOLID95 mesh element in ANSYS and tested results. From Figure 5.15, some differences can be observed. The tested deflections are slightly lower than the numerical predictions. The difference becomes larger when the applied voltage increases. However the tested electrostatic curve is closer to the simulated result than it is to the analytical result. The pull-in voltage from the tested electrostatic curve is estimated to be around 20V, showing a difference of less than 3% from the simulated

value. Thus from this figure, some comments can be derived: 1) the actual pull-in voltage is slightly higher than those obtained from numerical model and linear beam model; 2) the actual structure can have higher stiffness than assumed or less deflection than the predictions. The difference may be caused by fabrication tolerance, structural fillet effect, the metal film deposited on all surfaces of the micromirror and the springs due to the micromachining process used and the stiffening effect (see Section 2.2.7.3).

Table 5.4 PSD read-out and converted deflection

Voltage (V)	PSD readout	Difference	Θ (deg)	z-deflection (μm)
0	83.7991	0	0	0
2	83.3541	-0.445	-0.00093	0.00812
4	85.3343	1.5352	0.0032	-0.02793
6	95.0343	11.2352	0.0234	-0.2042
8	104.383	20.5839	0.0429	-0.37437
10	118.011	34.2119	0.0713	-0.62221
12	135.474	51.6749	0.1077	-0.93986
14	154.035	70.2359	0.1465	-1.27845
16	189.073	105.2739	0.2196	-1.91637
18	240.708	156.9089	0.3273	-2.85623

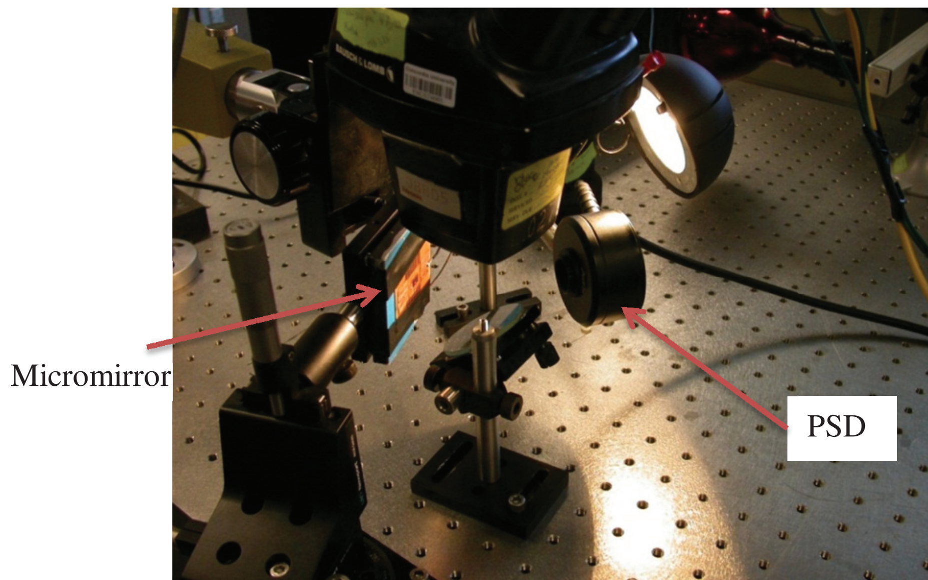

Figure 5.14 A photo of the PSD sensor (Spot-On CCD) based experimantal set-up for static performance test of a torsional micromirror.

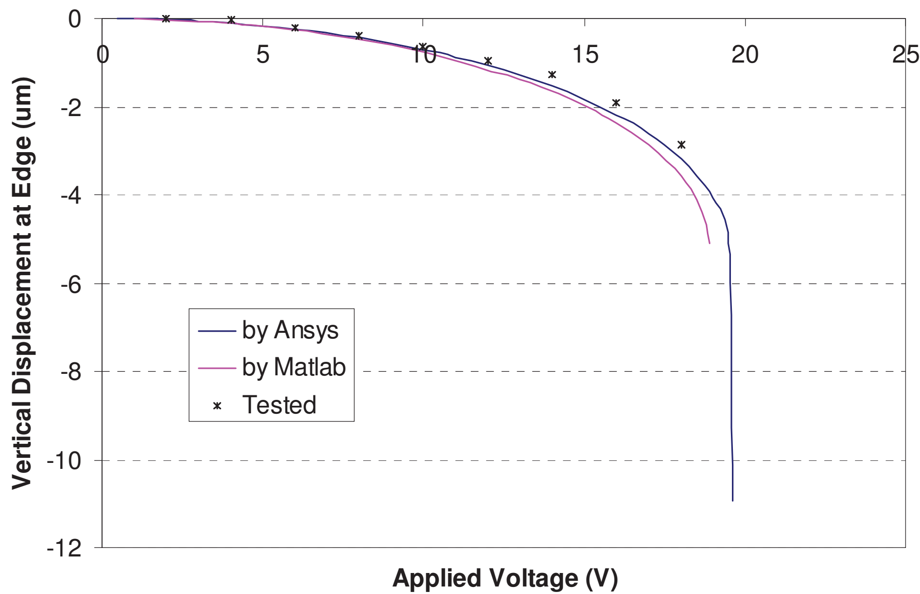

Figure 5.15 Electrostatic curves obtained from the analytical model using linear energy method (Matlab), FEA simulation using SOLID95 element (Ansys) and static test.

5.5.2 Micromirror #2

Table 5.5 The designed dimensions for the torsional micromirror #2

Spring Type	Side Distance (μm)	Cross-section w×t (μm)	Initial Length L_i (μm)	Final Length L_f (μm)	Parallel Length L_p (μm)	Orthogonal Length L_o (μm)	Air Gap (μm)
Rotational Serpentine	300	9×10	22	22	220	18	12

Table 5.5 presents the design dimensions for Micromirror #2. The mirror plate has the same dimensions as Micromirror #1. The electrostatic performance of the micromirror has been analyzed using linear matrix method along with PRBM models for the three long beams in one of the side springs. The analysis process is similar to the one described in Section 3.6.2. Comparison of electrostatic pull-in voltages using different methods is

shown in Table 5.6. The electrostatic characteristics obtained by different methods are shown in Figure 5.16. These methods include the energy method based on linear beam theory, the PRBM along with stiffness matrix method, the FEM simulation in ANSYS and the curve obtained from the tested results. Some observations from the table and the figure are listed below:

- The difference between the established analytical model and the tested results is in an acceptable range;
- The FEM simulation in ANSYS using SOLID45 structural meshing element and TRANS126 electrostatic element yields very close results to the tested results, demonstrating that the established model is successful;
- Torsional motion is the dominant mode of motion for the 2-DOF micromirror, and the variation of out-of-plane bending stiffness shows very less affect on the torsional motion of the mirror plate. In other words, the two modes of motion are almost decoupled.

Table 5.6 Comparison of pull-in parameters using different methods

Method	Normalized Θ_{pin}	Normalized Z_{pin}	Normalized V_{pin}	V_{pin} (V)	Difference (%)
PRBM+Matrix	0.4288	0.0111	0.6325	21.0971	7.27
Ansys Solid45	---	---	---	22.60	0.66
Tested	---	---	---	22.75	---

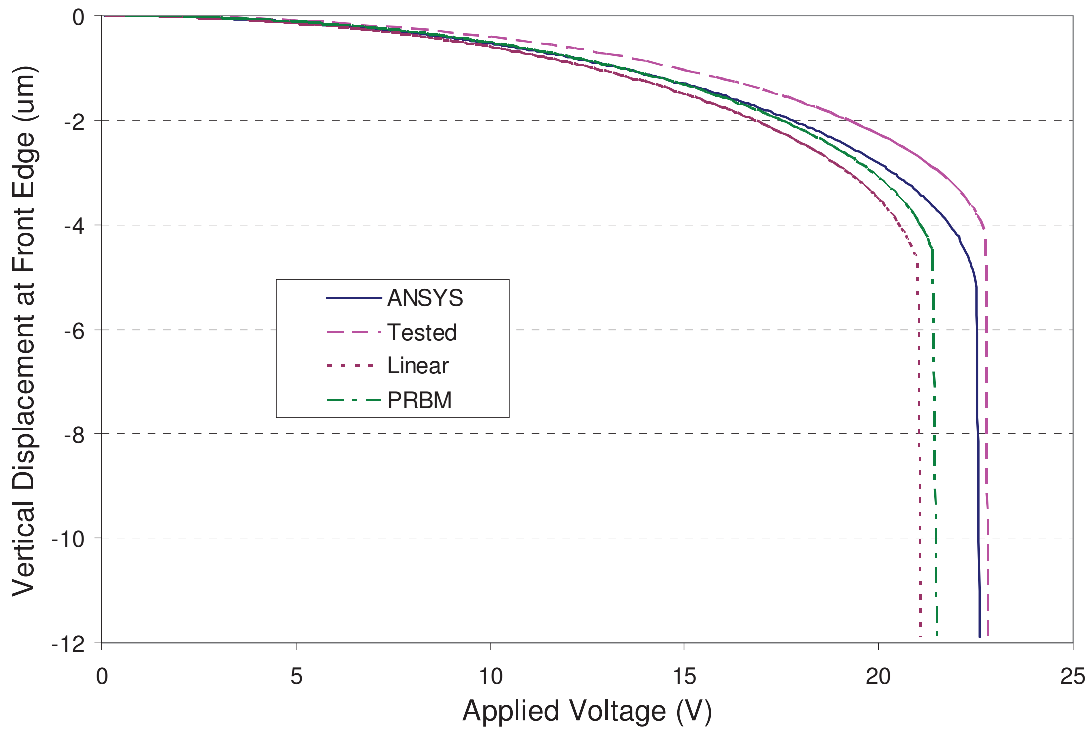

Figure 5.16 The electrostatic curves obtained from using FEM simulation, linear energy method, PRBM with linear matrix method (Hybrid PRBM) and the PSD detector based experimental results for the torsional micromirror #2.

5.5.3 Micromirror #3

Table 5.7 The design dimensions for Micromirror #3

Spring Type	Side Distance (μm)	Cross-section w×t (μm)	Initial Length L_i (μm)	Final Length L_f (μm)	Parallel Length L_p (μm)	Orthogonal Length L_o (μm)	Air Gap (μm)
Rotational Serpentine	300	9×10	22	22	220	18	12

Table 5.7 shows the designed dimensions for Micromirror #3 with its mirror plate's dimensions of 300μm×240μm×10μm in length *L*, width *W* and thickness *t*. Two tests were performed using PSD based test set-up and Mirau objective set-up. The two

electrostatic curves for the micromirror obtained from the two test methods are shown and compared in Figure 5.17. The interferometry test results are post-processed from the fringe maps recorded by a video camera (see Figure 5.11), whereas some conversion or calculation of the acquired data during PSD based static test is needed to produce the electrostatic curve shown in the figure. Again the tested results demonstrate slightly higher stiffness and less deflection than those obtained from FEM simulation.

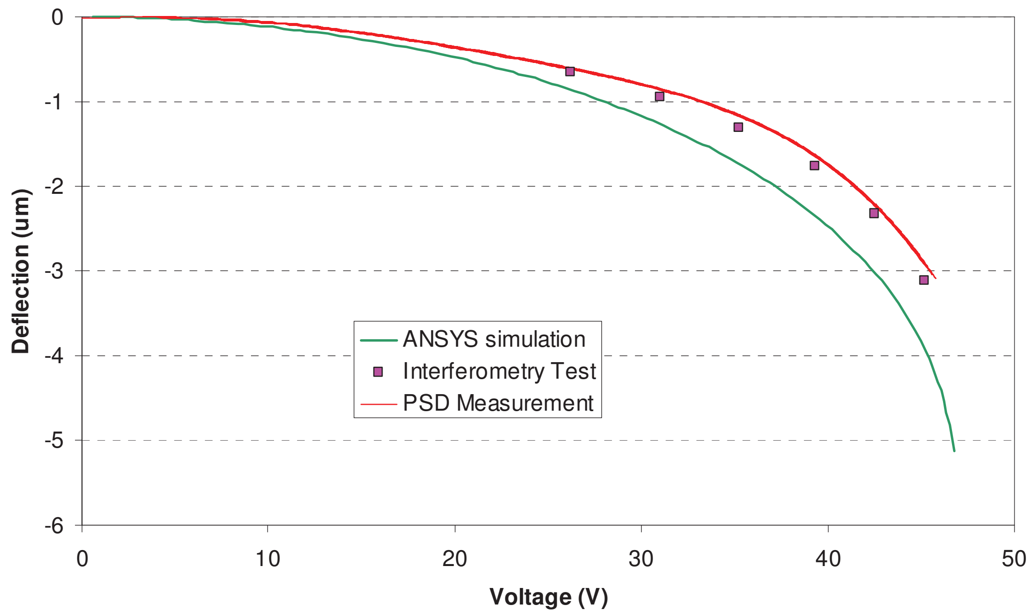

Figure 5.17 The electrostatic curves obtained from using FEM simulation, linear energy method, Pseudo Rigid Body Model with linear matrix method (Hybrid PRBM) and PSD sensor based experimental results for the torsional micromirror #3.

Table 5.8 The designed dimensions and structures for two micromirrors

Spring Type	Side Distance (μm)	Cross-section w×t (μm)	Initial Length L_i (μm)	Final Length L_f (μm)	Parallel Length L_p (μm)	Orthogonal Length L_o (μm)	Air Gap (μm)
Single Rotational Serpentine	300	9×10	21	21	220	19	12
Double Rotational Serpentine	300	11×10	19	19	220	21	12

5.5.4 Measurement of Eigen-Frequency

Table 5.8 shows the designed dimensions for two torsional micromirrors with the same dimensions of length, width and thickness (300μm×240μm×10μm) for the mirror plate but different cross-sections of the rotational serpentine springs. The simulated Eigen frequency spectrums for the two torsional micromirrors symmetrically suspended by the single-loop and double-loop rotational serpentine springs are shown in Figure 5.18. Since the micromirrors in comparison were damaged due to maloperation in other tests, the actual eigen-frequencies of these micromirrors could not be acquired for verification.

However this test has been performed on other similar micromirrors. Due to compliance of the suspensions, the resonant frequency of a torsional micromirror is hard to read accurately from the spectrum meter. And a slight difference may be resulted from different times of test. The more compliant the structure, the more even the frequency response is resulted. Because of an applied electrical bias, the micromirror is subjected to an electrostatic load, which helps stiffen the structure. The curve of frequency responses becomes more tilted when a large voltage is applied on the micromirror and the resonant frequency is then easier to identify. Figure 5.19 shows the frequency responses recorded during tests.

Similar to static performance tests, the measured values of resonant frequency for the proposed micromirrors are higher than those obtained from both analysis and simulation. This difference may be as high as 10%. For example, the predicted resonant frequency

without voltage for the torsional micromirror with a single loop of rotational serpentine is 3.81 kHz, but the corresponding value from tests is 4.22 kHz. The reason for this deviation is not clear. This needs further research to address. Figure 5.20 provides two frequency responses obtained from a torsional micromirror subjected to direct AC excitation and indirect vibration. The frequency response with direct excitation is more legible. The effect of different types of excitation on the frequency response of compliant torsional micromirrors is also needed to further address in the future work.

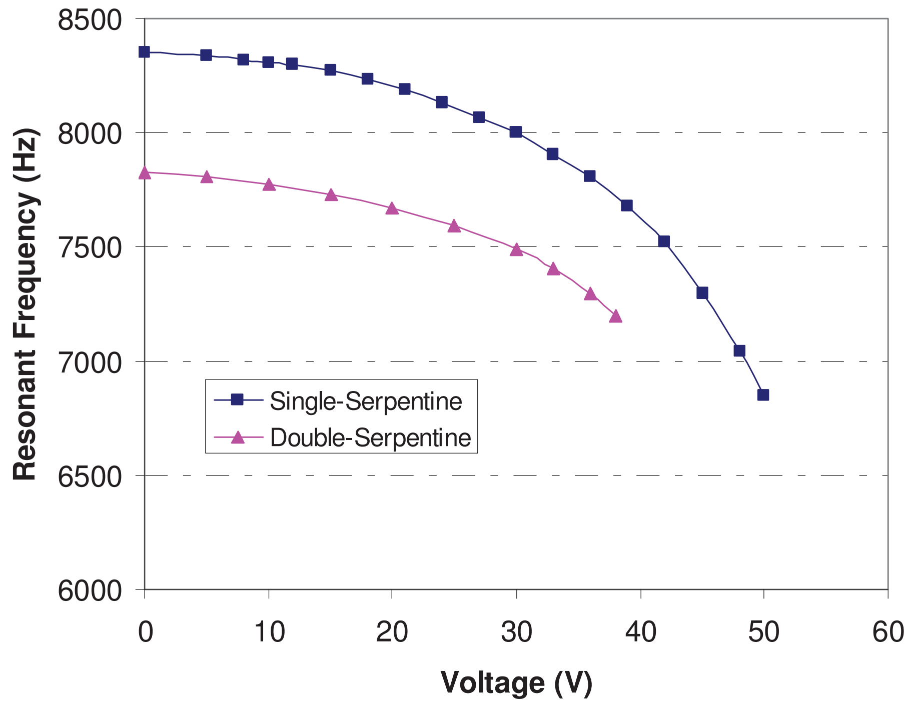

Figure 5.18 The simulated Eigen frequency spectrums for the two torsional micromirrors with the single-loop and the double-loop rotational serpentine springs.

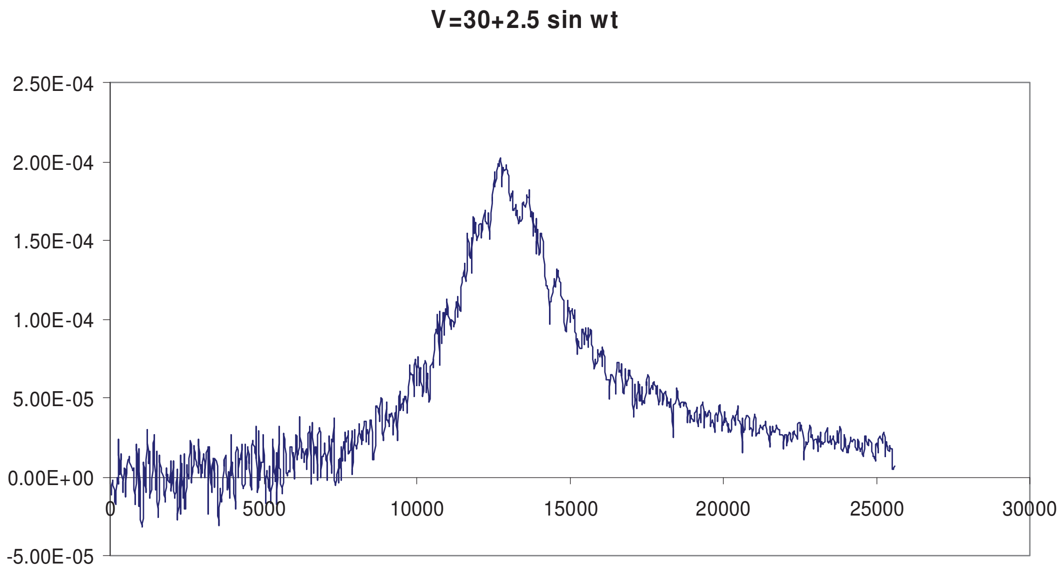

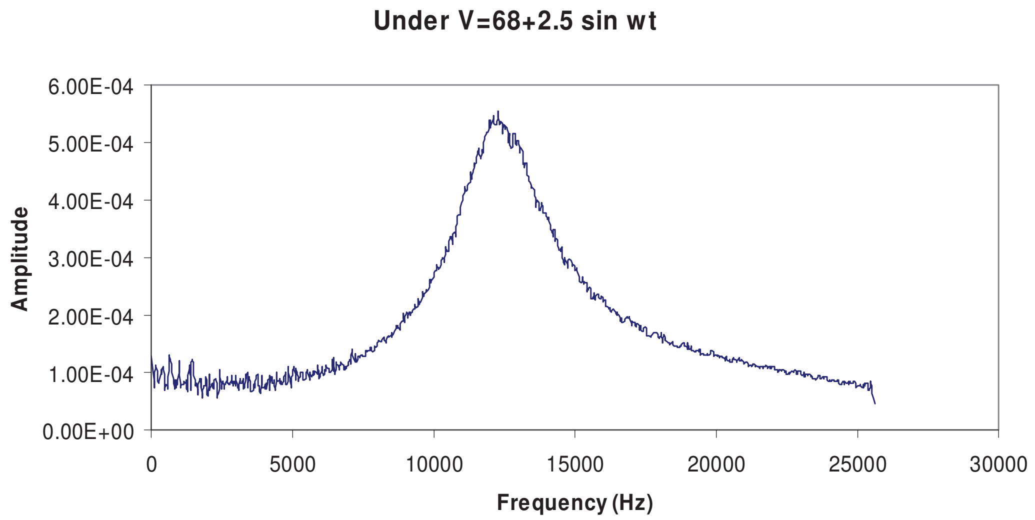

Figure 5.19 The two frequency responses of a torsional micromirror subjected a DC voltage along with a small magnitude of AC sinusoidal voltage.

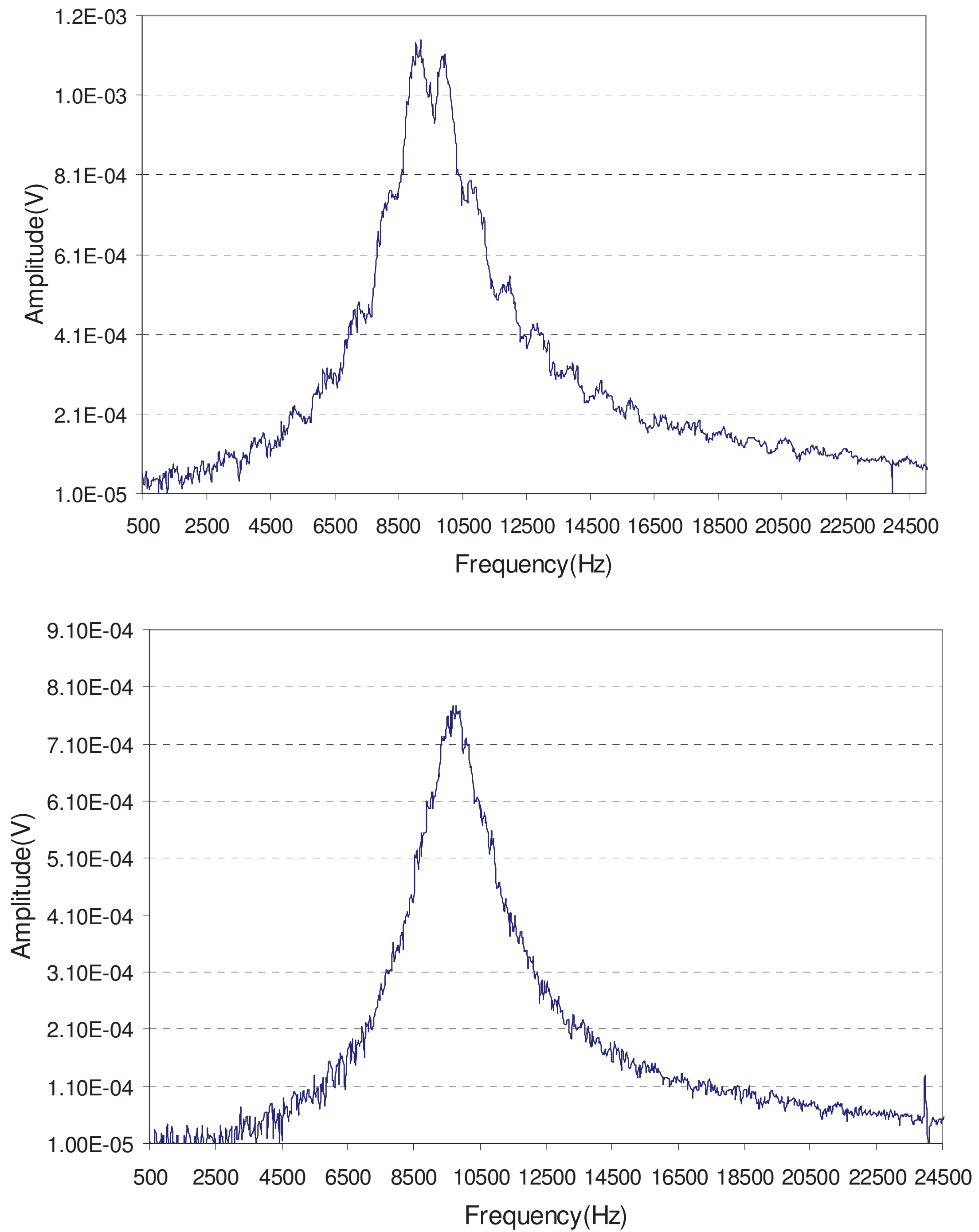

Figure 5.20 The different frequency responses of a torsional micromirror subjected to direct excitation (the bottom) and indirect excitation (the top).

5.6 Summary

The non-contact optical MEMS testing methods are introduced in detail, and typical test set-ups for testing torsional micromirrors are presented and specified. The laser Doppler vibrometer along with electrostatic or piezoelectric excitators is selected for the dynamic tests, while non-contact position sensor based set-ups are used for static performance tests. These include CCD arrays based Spot-On sensor set-up and monolithic photocell based PSD set-up. Mirau objective is introduced for measuring the static performance of torsional micromirrors. Comparison of various interferometric methods is also presented.

However, as found in the tests, the Spot-On CCD sensor based set up is the most preferred method for static performance test due to its simplicity, easy control, and easy data processing. Mirau interferometry is another option for static or dynamic performance tests because of its high capability and accuracy. However post-procesing of the tested results takes more time and some error may happen during data treatment.

Comparison of the results obtained from using analytical methods, FEA simulation and tests was performed. The proposed hybrid analytical method that combines PRBM with linear matrix method is suitable to model and predict mechanical behaviors of the framed microstructures that have compliant beam members. Some effect on dynamic behavior of the compliant micromirrors arising from different test set-ups with direct or indirect excitation was also discussed.

Chapter 6: Conclusions and Extensions

6.1 Conclusions

This thesis discussed the compliant suspensions for proof mass microplatforms or micromirrors in a microstructure based on the presently available surface micromachining technologies. This has led to a conclusion that the planar rotational serpentine springs are one of the suitable types of micro-suspensions for torsional micromirrors as they are relatively rigid to bending but flexible to torsion displacement, which is therefore recommended for the suspensions for low resonant torsional micromirrors. Modeling methodologies for these framed microstructures have been reviewed systematically aiming to predict or analyze the performances of the microstructures, and to approxmate the nonlinearity that may be caused due to the ultra thin beam components in the microstructures or large deformations occur to some beam components in the microstructures. Micro-fabrication tolerance, property drift and irregular micro-frames can all be represented and analyzed and predicted by applying one of these introduced modeling methods. And modeling of micromirrors with compliant torsional suspension and electrostatic actuation has been discussed in depth. The methods for the structural modeling include the linear energy method, the linear matrix method, and the PRBM modeling method. The nonlinear electrostatics along with the pull-in phenomenon is discussed and solved and combined with the structural analysis for static performance. The matrix method is then detailed and extended by formulalizing stiffness matrices with the corresponding PRBM terms for the complex framed microstructures

with or without compliant beam members. Comparison between predictions by these modeling methods and FEM simulations from the same models reveals variations of load-displacement performances even though they are in very good conformity in the linear working range. Less variation results with acceptable deviation can be obtained from using the PRBM hybrid modeling method for nonlinear structural and electrostatic analysis, which demonstrates the great potential of PRBM hydrid method in the analysis and prediction of the framed compliant microstructures.

Testing methodologies for MEMS have been reviewed, in which the preference is given to the optical aided non-contact test mehods. These involve the PSD sensor (CCD arrays or monolithic photocell), low power He-Ne laser, interferometry and Laser Doppler vibrometer and etc for both static and dynamic experiment set ups, in which the CCD arrays PSD sensor based static test set-up and LDV based dynamic set up are more preferred due to the simplicity of the set up, more accuracy in measurement and easy reading. The Mirau interferometry based set up is a competitive option for the static tests, however, there may incur some error when applying the specified post-processing software for the treatment of the fringe patterns obtained and it is time consuming. Nevertheless, Mirau interferometry microscope is the simplest static test set ups and can be recommended for measuring deformations for those MEMS devices that have small flat surfaces or for MEMS surface profile measurement no matter if the testing surfaces are reflective or not. The static curves for the proposed torsional micromirrors obtained from the tests show a stiffener feature than the corresponding simulation models and theoretical models when loading status comes close to nonlinearity. In other words, the

deflections taken from interferometry tests or PSD tests are a little smaller than the calculated and simulated results when the working range is beyond linearity, leading to a conclusion that the stiffened effect always occurs to the micro-structure if loading conditions go beyond its linear range. Moreover, comparisons between the tested results and the results from proposed PRBM modeling methods have demonstrated that acceptable smaller error (around 5~7% as compared to around 8~10% from linear models) can be achieved by applying the hybrid PRBM and linear stiffness matrix method for the proposed framed microstructures that include compliant beam members.

The preference of micromachining processes for the proposed planar compliant microstructures has been given to SOI wafer based MicraGEM process due to its compatibility in fabrication of the microstructures with the desired structural features. This compatibility mainly refers to the desired strength and large thickness for both device layer and the trench etched from the sacrifice layer or the bottom substrate. In addition, the flip-chip bonding technique in the process greatly increases its flexibility in the depth of the trench, which is very important for the microstructures capable of out-of-plane motion and very potential for the 3D microfabrication. The layout design for fabrication has included all related micromachining rules which have been adjusted or tested toward smooth and successful batch production. Packaging of the diced MEMS chips has been focused on how to wire the MEMS devices and how to fix the chip to a holder or a positioner in a test set-up that aims for measurement and verification. Based on research work on this topic, some more conclusions can be elucidated as follows.

- ✓ The electrostatic actuated torsional micromirror with large size mirror plate and compliant suspension, due to its low resonance, easy control and stable static performance as well as flat reflective surface, is suitable for applications such as optical switching, projection display, scanners and etc;
- ✓ The large but narrow space between the two large parallel planes, the upper micromirror and the bottom substrate forms an ideal and easy control actuation for the movable micromirror. The actuation voltage can be small as long as the size of the micromirror is large;
- ✓ The proposed nonsymmetric torsional micromirrors are advantageous to symmetric torsional micromirrors in that the desired drive voltage for the same angular operation is much lower, which is very helpful for the MEMS chips to be compatible with ICs and to be integrated on the same chip with their drive and control circuits, such as the CMOS MEMS.
- ✓ The eigen-frequency of torsional micromirrors varies along with the applied voltage, but the resolution (Q-factor) is not as high as those of high resonant devices. However, because of the adjustable resonance and simple structure and easy fabrication, they are the most suitable design concept for the inertial MEMS devices in this range of sensing or monitoring, such as microaccelerameters, hydrophones, and so on;
- ✓ The planar rotational serpentine spring for a proof mass plate is one of the best suspensions because of its feature of very flexible torsion but very rigid bending resistance.

6.2 Extensions

Research on the torsional micromirrors with electrostatic actuation is one of hot topics in MEMS field due to the great potential for various applications. However, research on compliant torsional micromirrors still needs a long way to go due to the fine structures necessary for the compliance. In a general view this has to be related to such researches as new high strength materials, micro-assembling with other soft materials, and packaging. As such, the following lists the topics or extensions for further study on the topic:

- ✓ Further characterization and verification of the proposed hybrid PRBM method for modeling the framed microstructures that have some compliant beam members;
- ✓ Further study on dynamic performance of the compliant torsional micromirrors in order to provide further theoretical support in development of inertial MEMS;
- ✓ Further verification of performance variations of MEMS due to exposures or experiments or compliant designs by various measurements to provide a base data for reliability research and improvement of MEMS designs;
- ✓ Study on packaging and 3-D micromachining of SOI based processes to lower the drive voltage, to increase the freedom of motion and to extend the life expectancy, etc in order for the real products for industrial applications.

References

1. J. Kilby. Miniaturized Electronic Circuits. US Patent No. 3 138 743, Filed at Feb. 6, 1959, issued at June 1964.
2. O. N. Tufte, P. W. Chapman and D. Long. Silicon Diffused-Element Piezoresistive Diaphragms. *Journal of Applied Physics*. Vol. 33, No. 11, pp. 3322-3327, 1962.
3. Y. Tai and R. Muller. Frictional Study of IC-processed Micromotors. *Sensors and Actuators.* A, A21/A23, pp. 180~183, 1990.
4. http://www.analog.com
5. Status of the MEMS Industry 2009 report. http://www.yole.fr
6. A. Frazier, R. Warrington, and C. Friedrich. The Miniaturization Technologies : Past, Present, and Future. *IEEE Transactions on Industrial Electronics*. Vol. 42, No. 5, 1995.
7. http://en.wikipedia.org/wiki/lab-on-a-chip
8. C. Ho, Y. Tai. Micro-Electro-Mechanical-Systems (MEMS) and Fluid Flows. *Annual Review of Fluid Mechanis*. Vol. 30, pp. 579~612, 1998.
9. K. E. Petersen. Silicon as a Mechanical Material. *IEEE Proceeding*, Vol. 70, No. 5, 1982.
10. H. Helvajian. Microengineering Aerospace Systems. *The Aerospace Press*. California, USA, 1999.
11. M. Waga, E. Mounier, and J.-C. Eloy. Study of MEMS/MOEMS R&D and commercialization trends in Japan and Comparison with Europe. *The 3rd International Conference on Micro Opto Electro Mechanical Systems (Optical MEMS)*, pp. 54-59, 1999.

12. A. J. Jacobs-Cook. MEMS versus MOMS from a Systems Point of View. *Journal of Micromechanics and Microengineering*. Vol. 6, pp. 148-156, 1996.

13. Y. Wu, X. Zeng, Y. Rao, Y. Gong, C. Hou and G. Yang. MOEMS Accelerometer Based on Microfiber Knot Resonator. *IEEE Photonics Technology Letters*. Vol. 21, No. 20, 2009.

14. R. Waters, C. Tally, B. Dick, H. Jazo, M. Fralick, M. Kerber and A. Wang. Design and Analysis of a Novel Electro-Optical MEMS Gyroscope for Navigation Applications. *Proceedings of IEEE Sensors*, pp. 1690-1695, 2010.

15. H. Asanuma, S. Hashimoto, S. Tano, S. Takashima, H. Niitsuma and Y. Shindo. Development of Fiber-Optical Microsensors for Geophysical Use. *The 3rd International Workshop on Scientific Use of Submarine Cables and Related Technologies*. 2003.

16. X. Zhang, X. Ke and Z. Zhang. Research on Micro-Electro-Mechanical-Systems Digital Geophone. *International Conference on Artificial Intelligence and Computational Intelligence*. Vol. 3, pp. 414-417, 2010.

17. H. Miyajima. Medical and Biomedical Application of MEMS and Optical MEMS. *IEEE/LEOS International Conference on Optical MEMS*. pp. 177-178, 2002.

18. J. Lo, E. Kim, M. Gundersen, and L. Marcu. Piezoelectric Optical MEMS Scanning Fluorescence Biosensor. *Proceedings of the SPIE*. Vol. 5692, No. 1, pp. 103-110, 2005.

19. A. Ohta, H. Hsu, A. Jamshidi and M. Wu. Optical MEMS and Nano-Photonics for Diagnostics. *IEEE Conference on Biomedical Circuits and Systems – Intelligent Biomedical Systems*. pp. 345-348, 2008.

20. A. Grayson, R. Shawgo, A. Johnson, N. Flynn, Y. Li, M. Cima, and R. Langer. A BioMEMS Review: MEMS Technology for Physiologically Integrated Devices. *IEEE Proceedings*, Vol. 92, No. 1, pp. 6-21, 2004.

21. B. Guldimann, L. Venancio, K. Wallace, J. Perdigues, Z. Sodnik, B. Furch. Space Instruments Based on MOEMS Technology. *IEEE/LEOS International Conference on Optical MEMS and Nanophotonics*. pp. 126-127, 2008.

22. W. Johnson, R. Phillips. Space Avionics Stellar - Inertial Subsystem. *The 20th Conference on Digital Avionics Systems*, Vol. 2, pp. 8D2.1-8D2.9, 2001.

23. D. Bayat, C. Ataman, B. Guldimann, S. Lani, W. Noel, and N. Rooij. Large Electrostatically and Electromagnetically Actuated Mirror System for Space Applications. *International Conference on Optical MEMS & Nanophotonics*. pp. 193-194, 2010.

24. S. Kim, G. Barbastathis and H. L. Tuller. MEMS for Optical Functionality. *Journal of Electroceramics*. Vol. 12, pp. 133-144, 2004.

25. L. J. Hornbeck. Projection displays and MEMS: Timely convergence for a bright future. *Proceedings of the SPIE*, Vol. 2639, 1995.

26. P. F. Van Kessel, L. J. Hornbeck, R. E. Meier and M. R. Douglass. A MEMS-Based Projection Display. *Proceedings of the IEEE*. Vol. 86, No. 8, pp. 1687-1704, 1998.

27. C. Liao and J. Tsai. The Evolution of MEMS Displays. *IEEE Transactions on Industrial Electronics*. Vol. 56, No. 4, pp. 1057-1065, 2009.

28. R. Apte, F. Sandejas, W. Banyai, D. Bloom. Deformable Grating Light Valves for High Resolution Displays, Technical Digest. *Solid-State Sensor and Actuator Workshop*. pp. 1-6, 1994.

29. R. Dangel, W. Lukosz. Electro-nanomechanically actuated integrated optical interferometric intensity modulators and 22 space switches. *Optics Communications*. Vol. 156, pp. 63-76, 1998.

30. M. Nakada, C. Chong, A. Morosawa, K. Isamoto, T. Suzuki, H. Fujita, and H. Toshiyoshi. Optical coherence tomography by all-optical MEMS fiber endoscope. *IEICE Electronics Express*. Vol. 7, No. 6, pp. 428-433, 2010.

31. D. Hays, A. Zribi, S. Chandrasekaran, S. Goravar, S. Maity, L. R. Douglas, K. Hsu, and A. Banerjee. A Hybrid MEMS-Fiber Optic Tunable Fabry-Perot Filter. *Journal of Microelectromechanical Systems*. Vol. 19, No. 2, 2010.

32. S. Lu, S. Ahir, V. Velasco, B. King, P. Xu, E. Terentjev, and B. Panchapakesan. Photomechanical Actuation of Carbon Nanotubes: Mechanisms and Applications in Micro and Nano-Devices. *Journal of Micro-Nano Mechatronics*. Vol. 5, No. 1, 2009.

33. K. Zandi, B. Wong, J. Zou, R. Kruzelecky, W. Jamroz, Y. Peter. In-Plane Silicon-On-Insulator Optical MEMS Accelerometer Using Waveguide Fabry-Perot Microcavity with Silicon/Air Bragg Mirrors. *Proceedings of the IEEE International Conference on MEMS*. pp. 839-842, 2010.

34. S. Chen, C. Xue, W. Zhang, J. Xiong, B. Zhang, and J. Hu. A new Type of MEMS Two Axis Accelerometer Based on Silicon. *Proceedings of the 3rd IEEE International Conference on Nano/Micro Engineered and Molecular Systems*. pp. 959-964, 2008.

35. L. Guan, J. O. Sin, H. Liu, and Z. Xiong. A fully integrated SOI RF MEMS technology for system-on-a-chip applications. *IEEE Transactions on Electron Devices*. Vol. 53, No. 1, 2006.

36. J. Lo, P. Butte, Q. Fang, S. Chen, T. Papaioanau, E. Kim, M. Gundersen, and L. Marcu. Multiplayed MOEMS Tunable Spectrometer for Fluorescence Lifetime Detection. *IEEE Photonics Technology Letters*. Vol. 22, No. 7, pp. 486-488, 2010.

37. K. Ghose, H. R. Shea. Fabrication and testing of a MEMS based earth sensor. *International Conference on Soild-state Sensors, Actuators and Microsystems*, pp. 327-330, 2009.

38. M. Abdelmoneum, D. Browning, T. Arabi, and W. Khalil. Micro and Nano Electro Mechanical Systems (MEMS/NEMS) for Mobile Computing Systems. *IEEE 70th Vehicular Technology Conference*. pp. 1-4, 2009.

39. B. Donald, C. Levey, C. McGray, I. Paprotny, and D. Rus. An Untethered, Electrostatic, Globably Controllable MEMS Micro-Robot. *Journal of Microelectromechanical Systems*, Vol. 15, No. 1, 2006.

40. H. Ishihara. Overview of International Micro Robot Maze Contest. *IEEE International Symposium on Micro-NanoMechatronics and Human Science*. pp. 303-321, Nagoya, Japan, 2005.

41. L. A. Rocha, E. Cretu, and R. F. Wolffenbuttel. Pull-in Dynamics: Analysis and Modeling of the Transitional Regime. *17th IEEE International Conference on MEMS*. pp. 249-252, 2004.

42. G. Flores, G. Mercado, and J. Pelesko. Dynamics and Touchdown in Electrostatic MEMS. *Proceedings of MEMS, NANO and Smart Systems*. pp. 182-187, 2003.

43. G. Nielson, and G. Barbastathis. Dynamic Pull-in of Parallel-Plate and Torsional Electrostatic MEMS Actuators. *Journal of Microelectromechanical Systems*, Vol. 15, No. 4, pp. 811-821, 2006.

44. E. Garcia, N. Lobontiu, Y. Nam. Mechanics of MEMS: a review of modeling, analysis, and design. *Proc. SPIE*. Vol. 5390, pp. 400-409, 2004.

45. H. Fujita. Two decades of MEMS---from surprise to enterprise. *IEEE 20th International Conference on MEMS*. Hyogo, Japan, 2007.

46. T. Iseki, M. Okumura, T. Sugawara. High-Speed and Wide-Angle Deflection Optical MEMS Scanner Using Piezoelectric Actuation. *IEEJ Transactions on Electrical and Electronic Engineering*. Vol. 5, pp. 361-368, 2010.

47. K. Koh, T. Kobayashi, F. Hsiao, and C. Lee. A 2-D MEMS Scanning Mirror Using Piezoelectric PZT Beam Actuators. *Proceedings of the Eurosensors XXIII Conference*. pp. 1303-1306, 2009.

48. C. Lee, F. Hsiao, T. Kobayashi, K. Koh, P. Ramana, W. Xiang, B. Yang, C. Tan, and D. Pinjala. A 1-V Operated MEMS Variable Optical Attenuator Using Piezoelectric PZT Thin-Film Actuators. *IEEE Journal of Selected Topics in Quantum Electronics.* Vol. 15, No. 5, 2009.

49. S. Mao, H. Wang, Y. Wu, J. Tang, G. Ding. A Latching Bistable Microswitch Using Dual-Beam Electrothermal Actuation. *Proceedings of the 5th IEEE International Conference on Nano/Micro Engineered and Molecular Systems*. pp. 732-735, 2010.

50. W. Zhang, M. Gnerlich, J. Paly, Y. Sun, G. Jing, A. Voloshin, and S. Lucic. A Polymer V-Shaped Electrothermal Actuator Array for Biological Applications. *Journal of Micromechanics and Microengineering*. Vol. 18, pp. 1-8, 2008.

51. K. Jia, S. Pal, and H. Xie. An Electrothermal Tip-Tilt-Piston Micromirror Based on Folded Dual S-Shaped Bimorphs. *Journal of Microelectromechanical Systems.* Vol. 18, No. 5, pp. 1004-1015, 2009.

52. M. Wu. Micromachining for Optical and Optoelectronic Systems. *IEEE Proceedings*. Vol. 85, No. 11, pp. 1833-1856, 1997.

53. J. Bustillo, R. T. Howe, R. S. Muller. Surface Micromachining for Micro-Electro-Mechanical Systems. *IEEE Proceedings*. Vol. 86, pp. 1552-1574, 1998.

54. J. Ristic and M. Shah. Trends in MEMS Technology. *IEEE Conference (WESCON)*. pp. 64-72, 1996.

55. J. Tang, L. Zhang, L. Jiang, L. Xie, Y. Zu, Z. Tian. Three-dimensional Electrochemical Micromachining on Metal and Semiconductor by Confined Etchant Layer Technique (CELT). *2nd IEEE International Conference on Nano/Micro Engineered and Molecular Systems.* pp. 328-332, Bangkok, Thailand, 2007.

56. M. Madou. Fundamentals of Microfabrication. CRC Press LLC, USA, 1997.

57. M. Wu and W. Fang. Design and Fabrication of MEMS Devices Using the Integration of MUMPs, Trench-Refilled Molding, DRIE and Bulk Silicon Etching Processes. *Journal of Micromechanics and Microengineering*. Vol. 15, pp. 535-542, 2005.

58. MEMS Technology Application Center (MCNC). http://www.mcnc.org

59. Silicon Valley Microelectronics Headquarters. http://www.svmi.com

60. G. Celler, S. Cristoloveanu. Frontiers of Silicon-on-Insulator. *Journal of Applied Physics*. Vol. 93, No. 9, pp 4955-4978, 2003.

61. A. Adan, T. Naka, A. Kagisawa, H. Shimizu. SOI as a Mainstream IC Technology. *Proceedings IEEE International SOI Conference*. pp. 9-12, 1998.

62. T. Stanley. The State-of-the-Art in SOI Technology. *IEEE Transactions on Nuclear Science*. Vol. **35**, No. 6, pp. 1346-1349, 1988.

63. M. Alles. Thin-Film SOI Emerges. *IEEE Spectrum*. Vol. 34, No. 6, pp. 37-45, 1997.

64. Q. Tong and U. Gösele. SemiConductor Wafer Bonding: Science and Technology. *Wiley-Interscience*. ISBN 978-0471574811, 1998.

65. J. Colinge. Silicon-on-Insulator Technology: Materials to VLSI. *Springer Verlag*. ISBN 978-0-7923-9150-0, 1991.

66. M. Yoshimi and C. Mazure. Current Status and Future Perspectives of Wafer Bonding SOI Technology. *7th International Conference on Solid-State and Integrated Circuits Technology*. pp. 258-261, 2004.

67. M. Yoshimi, D. Delpra, I. Cayrefourcq, G. Celler, C. Mazure, and B. Aspar. Current Status and Possibilities of Wafer-Bonding-Based SOI Technology in 45nm or below CMOS LSIs. *9th International Conference on Solid-State and Integrated Circuits Technology*. pp. 669-672, 2008.

68. L. Hornbeck. 128×128 deformable mirror devices. *IEEE Transactions on Electron Devices*. Vol. 30, No. 5, pp. 539-545, 1983.

69. R. Bogue. The Fast-Moving World of MEMS Technology. *Assembly Automation*. Vol. 29, No. 4, pp. 313-320, 2009.

70. S. Walsh, H. Mados, D. Narang. Commercializing MEMS: Too Fast or Too Slow. *Proceedings of SPIE*. Vol. 2879, pp. 12-24, 1996.

71. K. Koh, C. Lee, and T. Kobayashi. A Piezoelectric-Driven Three-Dimensional MEMS VOA Using Attenuation Mechanism with Combination of Rotational and Translational Effects. *Journal of Microelectromechanical Systems.* Vol. 19, No. 6, pp. 1370-1379, 2010.

72. Y. Bai, J. Yeow, and B. Wilson. Design, Fabrication and Characterization of a MEMS Micromirror with Sidewall Electrodes. *Journal of Microelectromechanical Systems*. Vol. 19, No. 3, pp. 619-631, 2010.

73. X. Zhang, F. Chau, C. Quan, Y. L. Lam, A. Q. Liu. A Study of Static Characteristics of a Torsional Micromirror. *Sensors and Actuators,* 90, pp 73-81, 2001.

74. R. S. Muller, K. Y. Lau. Surface-Micromachined Microoptical Elements and Systems. *Proceedings IEEE MEMS Workshop*. German, pp.1705-1720, 1998.

75. T.-H. Lin. Implementation and Characterization of a Flexure-Beam Micromechanical Spatial Light Modulator. *Optical Engineering*, Vol. 33, No. 11, pp. 3643-3648, 1994.

76. J. Cecil, D. Vasquez and D. Powell. A Review of Gripping and Manipulatiton Techniques for Micro-Assembly Applications. *International Journal of Production Research*. Vol. 43, No. 4, pp. 819-828, 2005.

77. B. Tamadazte, T. Arnould, S. Dembele, N. Le Fort-Piat, and E. Marchand. Real-Time Vision-Based Microassembly of 3D MEMS. *IEEE/ASME International Conference on Advanced Intelligent Mechatronics*. pp. 34-40, 2009.

78. A. Farahani. Silicon MEMS components: A Fatigue Life Assessment Approach. *Microsystem technologies*. Vol. 11, pp. 129-134, 2005.

79. J. Park, S. Mutlu, Y. Gianchandani. Nano-Scale Abrasion Studies of Materials Used in MEMS Devices and Packages. *ASME Electronic and Photonic Packaging*. Vol. 5, pp. 563-567, 2005.

80. J. Simon, S. Saffer, and C. Kim. A Liquid-Filled Microrelay with a Moving Mercury Microdrop. *Journal of Microelectromechanical Systems*. Vol. 6, No. 3, 1997.

81. H. Zeng, Z. Wan, and A. Feinerman. Tilting Micromirror With a Liquid-Metal Pivot. *Journal of Microelectromechanical Systems*. Vol. 15, No. 6, pp. 1568-1574, 2006.

82. S. Patton, A. Voevodin, R. Vaia, M. Pender, S. Diamanti, and B. Phillips. Nanoparticle Liquids for Surface Modification and Lubrication of MEMS Switch Contacts. *Journal of Microelectromechanical Systems*. Vol. 17, No. 3, 2008.

83. D. Hah, S. Huang, J. Tsai, H. Toshiyoshi, and M. Wu. Low-Voltage, Large-Scan Angle MEMS Analog Micromirror Arrays with Hidden Vertical Comb-Drive Actuators. *Journal of Microelectromechanical Systems*. Vol. 13, No. 2, pp. 279-289, 2004.

84. M. Dokmeci, A. Pareek, S. Bakshi, M. Waelti, C. Fung, K. Heng, and C. Mastrangelo. Two-Axis Single-Crystal Silicon Micromirror Arrays. *Journal of Microelectromechanical Systems*. Vol. 13, No. 6, pp. 1006-1017, 2004.

85. I. Cho and E. Yoon. A Low-Voltage Three-Axis Electromagnetically Actuated Micromirror for Fine Alignment Among Optical Devices. *Journal of Micromechanics and Microengineering*. Vol. 19, No. 8, pp. 1-8, 2009.

86. G. Fedder. Simulation of micro-electro-mechanical systems. PhD Dissertation. University of California at Berkeley, 1994.

87. J. Younse. Mirrors on a Chip. *IEEE Spectrum*. Vol. 30, No. 11, pp. 27-31, 1993.

88. P. Kessel, L. Hornbeck, R. Meier, M. R. Douglass. A MEMS Based Projection Display. *Proceedings IEEE MEMS Workshop*. Vol. 86, No. 8, pp. 1687-1704, 1998.

89. S. Kurth, R. Hahn, C. Kanfmann, K. Kehr, J. Mehner, V. Wollmann, W. Dotzel, T. Gessner. Silicon Mirrors and Micromirror Arrays for Spatial Laser Beam Modulation. *Sensors and Actuators A*. Vol. 66, No. 1~3, pp. 76-82, 1998.

90. L. J. Hornbeck. Deformable-Mirror Spatial Light Modulators. *Proceedings of the SPIE Spatial Light Modulators and Applications III.* Vol. 1150, pp. 86-102, 1989.

91. R. W. Cohn. Link Analysis of a Deformable Mirror Device Based Optical Crossbar Switch. *Optical Engineering*. Vol. 31, pp. 134-140, 1992.

92. K. Petersen. Silicon Torsional Scanning Mirror. *IBM Journal of Research and Development*. Vol. 24, No. 5, pp. 631-637, 1980.

93. H. Toshiyoshi, H. Fujita. Electrostatic Microtorsion Mirrors for an Optical Switch Matrix. *Journal of Microelectromechnical Systems*. Vol. 5, No. 4, pp. 231-237, 1996.

94. L. Hornbeck, J. T. Carlo, M. W. Cowens, P. M. Osterberg, and M. M. DeSmith. Deformable mirror projection display. *Proceedings SID Symposium*. pp. 228-229, 1980.

95. C. Friese and H. Zappe. Deformable Polymer Adaptive Optical Mirrors. *Journal of Microelectromechanical Systems*. Vol.17, No.1, pp. 11-19, 2008.

96. E. H. Conradie and D. F. Moore. Su-8 Thick Photoresist Processing as a Functional Material for MEMS Applications. *Journal of Micromechanics and Microengineering*. Vol. 12, pp. 368-374, 2002.

97. S. He and R. Mrad. Large-Stroke Microelectrostatic Actuators for Vertical Translation of Micromirrors Used in Adaptive Optics. *IEEE Transactions on Industrial Electronics*. Vol. 52, No. 4, pp. 974-983, 2005.

98. J. Simon, S. Saffer, and C.-J. Kim. A Liquid-Filled Micrcorelay with a Moving Mercury Microdrop. *Journal of Microelectromechanical Systems*. vol. 6, No. 3, pp. 208-216, 1997.

99. H. Zeng, Z. Wan, and A. Feinerman. Tilting Micromirror with a Liquid-Metal Pivot. *Journal of Microelectromechanical Systems*. Vol. 15, No. 6, pp. 1568-1575, 2006.

100. H. Zeng, A. Feinerman, Z. Wan, and P. Patel. Piston-Motion Micromirror Based on Electrowetting of Liquid Metals. *Journal of Microelectromechanical Systems.* Vol. 14, No. 2, pp. 285-294, 2005.

101. Z. Wan, A. Feinerman, H. Zeng, and G.Friedman. Electrocapillary Piston Motion and a Prototype of Phase-Manipulating Micromirror. *Journal of Microelectromechanical System.* Vol. 13, No. 4, pp. 620-627, 2004.

102. J. Chiou, C. F. Kuo, Y. Lin, and H. Shieh. A Micromirror with Large Static Rotation and Piston Actuation. *IEEE/LEOS International Conference on Optical MEMS and Their Applications Conference*. pp. 132-133, 2006.

103. S. Todd, H. Xie. An Electrothermomechnical Lumped Element Model of an Electrothermal Bimorph Actuator. *Journal of Microelectromechanical Systems*. Vol. 17, No. 1, pp. 213-225, 2008.

104. Y. Xu, J. Singh, T. Selvaratnam, Nanguang Chen. Two-Axis Gimbal-less Electrothermal Micromirror for Large-Angle Circumferential Scanning. *IEEE Journal of Selected Topics in Quantum Electronics*. Vol. 15, No. 5, pp. 1432-1438, 2009.

105. D. Beasley, M. Bender, J. Crosby, T. Messer, and D. Saylor. Advancements in the Micromirror Array Projector Technology. *Proceedings SPIE*, Vol. 5092, No. 1, pp. 71-82, 2003.

106. D. Beasley, M. Bender, J. Crosby, S. McCall, T. Messer, and D. Saylor. Advancements in the Micromirror Array Projector Technology II. *Proceedings SPIE*. Vol. 5785, No. 1, pp. 72-83, 2005.

107. S. Kim, G. Barbastathis and H. L. Tuller. MEMS for Optical Functionality. *Journal of Electroceramics*. Vol. 12, pp. 133-144, 2004.

108. J. Yeow and S. Abdallah. Novel MEMS L-Switching Matrix Optical Cross-Connect Archtechture: Design and Analysis-Optimal and Staircase-Switching Algorithms. *Journal of Lightwave Technology*. Vol. 23, No. 10, pp. 2877-2892, 2005.

109. Y. Yoon, K. Bae, J. Kim, H. Choi. A Low Voltage Actuated Micromirror with an Extra Vertical Electrode for 90° Rotation. *Journal of Micromechanics and Microengineering*. Vol. 13, pp. 922-926, 2003.

110. J. Huang, A. Liu, Z. Deng, et al. An Approach to the Coupling Effect Between Torsion and Bending for Electrostatic Torsional Micromirrors. *Sensors and Actuators A*. Vol. 115, pp. 159-167, 2004.

111. Z. Xiao, K. Farmer. Experimental Study of Micromachined Electrostatic Torsion Actuators with Full Travel Range. *Sensors and Actuators A*. Vol. 114, pp. 466-472, 2004.

112. V. Milanovic, M. Last and K. Pister. Laterally Actuated Torsional Micromirrors for Large Static Deflection. *IEEE Photonics Technology Letters*. Vol. 15, No. 2, pp. 245-247, 2003.

113. J. You, M. Packirisamy, I. Stiharu. Analysis, Simulation and Testing of a Micromirror with Rotational Serpentine Springs. *Proceedings of 3rd International*

Conference on Intelligent Sensing and Information Processing. Bangalore, India, Dec. 2005.

114. W. Kronast, U. Mescheder, B. Muller, A. Nimo. Development of a Tilt Actuated Micromirror for Applications in Laser Interferometry. *Proceedings of SPIE*. Vol. 7594, San Francisco, California, USA, Jan. 2010.

115. L. Zhou, J. Kahn, and K. Pister. Scanning Micromirrors Fabricated by an SOI/SOI Wafer-Bonding Process. *Journal of Microelectromechanical Systems*. Vol. 15, No.1, pp. 24-32, 2006.

116. J. Kim and L. Lin. Electrostatic scanning micromirrors using localized plastic deformation of silicon. *Journal of Micromechanics and Microengineering*. Vol. 15, pp. 1777-1785, 2005.

117. Y. Eun and J. Kim. Thermally driven torsional micromirrors using pre-bent torsion bar for large static angular displacement. *Journal of Micromechanics and Microengineering*. Vol. 19, 2009.

118. Y. Eun, H. Na, B. Jeong, J. Lee, and J. Kim. Bidirectional electrothermal electromagenetic torsional microactuators for large angular motion at dc mode and high frequency resonance mode operation. *Journal of Micromechanics and Microengineering*. Vol. 19, 2009.

119. D. Kamiya, T. Gozu, and M. Horie. Design and manufacturing of micromechanism elements of 2-DOF micromanipulator. *Microsystem Technologies*. Vol. 1192, pp. 1013-1019, 2005.

120. J. Hsieh, W. Fang. A novel microelectrostatic torsional actuator. *Sensors and Actuators*. Vol. 79, pp. 64-70, 2000.

121. C. Tsou. The design and simulation of a novel out-of-plane micro electrostatic actuator. *Microsystem Technology*. Vol. 12, pp. 723-729, 2006.

122. G. Ananthasuresh and S. Kota. Designing compliant mechanisms. *Mechanical Engineering---Magazine of ASME*. Vol. 117, No. 11, pp. 93-96, 1995.

123. L. Howell. Compliant Mechanisms, 1st edition, *John Wiley & Sons*, New York.

124. M. Wang. Compliant mechanisms for MEMS and flexonics. *IEEE Conference on robotics, automation and Mechatronics*. Chengdu, China, 2008.

125. D. Wilcox, L. Howell. Fully compliant tensural bistable micromechanisms (FTBM). *Journal of Microelectromechanical Systems.* Vol. 14, No. 6, pp. 1223-1235, 2005.

126. M. Baker and L. Howell. On-chip actuation of an in-plane compliant bistable micromechanism. *Journal of Microelectromechanical Systems*. Vol. 11, No. 5, pp. 566-573, 2002.

127. S. Su, H. Yang, and A. Agogino. A resonant accelerometer with two-stage microleverage mechanisms fabricated by SOI-MEMS Technology. *IEEE Sensors Journal*. Vol. 5, No. 6, pp.1214-1223, December 2005.

128. S. Su, H. Yang. Analytical modeling and FEM simulations of single stage microleverage mechanism. *Int. J. of Mechanical Sciences.* Vol. 44, pp. 2217-2238, 2002.

129. S. Chen, M. Culpepper, S. Jordan. Six-axis compliant mechanisms for manipulation of micro-scale fiber optics components. *Proceedings of SPIE*. Vol. 6466, San Jose, CA, USA, 2007.

130. H. Cai, Z. Yang, G. Ding, and H. Wang. Development of a novel MEMS inertial switch with a compliant stationary electrode. *IEEE Sensors Journal*. Vol. 9, No. 7, pp. 801-808, 2009.

131. M. Frecker, G. Ananthasuresh, N. Nishiwaki, N. Kikuchi, and S. Kota. Topological systhesis of compliant mechanisms using multi-criteria optimization. *Journal of Mechanical Design.* Vol. 119, No. 2, pp. 238-245, 1997.

132. S. Kota, J. Joo, Z. Li, S. Rodgers, J. Sniegowski. Design of Compliant Mechanisms: Applications to MEMS. *Analog Integrated Circuits and Signal Processing*. Vol. 29, No. 1-2, pp. 7-15, 2001.

133. J. Joo, S. Kota and N. Kikuchi. Topological synthesis of compliant mechanisms using linear beam elements. *Mechanics of Structures and Machines.* Vol. 28, No. 4, pp. 245-280, 2000.

134. S. Kota. Compliant MEMS: Design methods and applications. *Proceedings of SPIE*. Vol. 4019, 2000.

135. R. Kuharuka, P. Hesketh. Design of fully compliant, in-plane rotary, bistable micromechanisms for MEMS applications. *Sensors and Actuators A*. Vol. 134, pp. 231-238, 2007.

136. C. F. Lin, C. J. Shih. A post-design of topology optimization for mechanical compliant amplifier in MEMS. *Tamkang Journal of Science and Engineering*. Vol. 9, No. 3, pp. 215-222, 2006.

137. F. Jouve, H. Mechkour. Optimization assisted design of compliant mechanisms by the level set method. *12th IFToMM World Congress*. Besancon, June 18-21, 2007.

138. S. Chen, M. Culpepper, S. Jordan. Design of a six-axis micro-scale nanopositioner-μHexFlex. *Precision Engineering.* Vol. 30, No. 3, pp. 314-324, 2006.

139. V. T. Srikar, S. M. Spearing. Mechanical Test Methods for MEMS Devices. *Experimental Mechanics*. Vol. 43, pp. 228-237, 2003.

140. V. T. Srikar and S. M. Spearing. A critical review of microscale mechanical testing methods used in the design of microelectromechanical systems. *Experimental Mechanics*. Vol. 43, pp. 238-247, 2003.

141. A. Kolpekwar and R. D. Blanton. Development of a MEMS Testing Methodology. *IEEE International Test Conference*. Washington, USA, 1997.

142. F. Ericson, J. A. Schweitz. Micromechanical fracture strength of silicon. *Journal of Applied Physics*. Vol. 68, pp. 5840-5844, 1990.

143. W. C. Oliver and G. M. Pharr. An improved technique for determining hardness and elastic modulus using load and displacement sensing indentation experiments. *Journal of Materials Research*. vol. 7, pp. 1564-1583, 1992.

144. T. Ikehara, R. Zwijze, and K. Ikeda. New method for an accurate determination of residual strain in polycrystalline silicon films by analyzing resonant frequencies of micromachined beams. *Journal of Micromechanics and Microengineering*. Vol. 11, pp. 55-60, 2001.

145. T. Yi and C. Kim. Measurement of mechanical properties for MEMS materials. *Measurement Science and Technology*. Vol. 10, No. 8, pp. 706-716, 1999.

146. C. Luo, T. Schneider, R. White. A simple deflection-testing method to determine Poisson's ratio for MEMS applications. *Journal of Micromechanics and Microengineering*. Vol. 13, pp. 129-133, 2003.

147. I. De Wolf. Instrumentation and methodology for MEMS testing, reliability assessment and failure analysis. *24th International Conference on Microelectronics*. Vol. 1, pp. 57-63, 2004.

148. B. Jensen, M. de Boer, N. Masters, F. Bitsie, and D. LaVan. Interferometry of actuated microcantilevers to determine material properties and test structure nonidealities in MEMS. *Journal of Microelecctromechanical Systems*. Vol. 10, No. 3, 2001.

149. J. Conway, J. Osborn, and J. Fowler. Stroboscopic Imaging Interferometer for MEMS Performance Measurement. *Journal of Microelectromechanical Systems*. Vol. 16, No. 3, 2007.

150. M. Hart, R. Conant, K. Lau, and R. Muller. Stroboscopic Interferometer System for Dynamic MEMS Characterization. *Journal of Microelectromechanical Systems*. Vol. 9, No. 4, 2000.

151. W. C. Wang, M. Fauver, J. Ho, E. Seibel, and P. Reinhall. Deformation measurement of MEMS components using Optical interferometry. *Measurement Science and Technology*. Vol. 14, pp. 909-915, 2002.

152. B. Ngoi, K. Venkatakrishnan, B. Tan, N. Noel, Z. Shen, and C. Chin. Two-axis-scanning Laser Doppler Vibrometer for Microstructure. *Optics Communications.* Vol. 182, pp. 175-185, 2000.

153. G. Zhang, Y. Zhong, X. Hong, C. Leng. Microelectromechanical systems motion measurement and modal analysis based on Doppler interferometry. *Journal of Vacuum Science and Technology B: Microelectronics and Nanometer Structures*. Vol. 27, No. 3, pp. 1251-1255, 2009.

154. H. Iwaoka, D. Chino, T. Ikehara, and E. Higurashi. Vibrating sensing system based on optical excitation and detection using optical fiber. *5th International Conference on Networked Sensing Systems*. 2008.

155. T. Miki, K. Ishikawa, H. Mamiya, and Y. Qiang. Large Displacement Electrostatic Micromirror Fabricated Using Solder Flip Chip Bonding. *The 9th Intersociety Conference on Thermal and Thermomechanical Phenomena in Electronic Systems*. Vol. 2, pp. 535-540, 2004.

156. T. Kamiya, K. Takano, T. Satoh, Y. Ishii, H. Nishikawa, S. Seki, M. Sugimoto, S. Okumura, and M. Fukuda. Microbeam Complex at TIARA: Technologies to Meet a Wide Range of Applications. *Nuclear Instruments and Methods in Physics Research*. 2011.

157. G. Barillaro, A. Molfese. Analysis, simulation and relative performances of two kinds of serpentine springs. *Journal of Microelectromechanical Systems*. Vol. 15, pp. 736-746, 2005.

158. H. Xie and G. Fedder. Fabrication, characterization, and analysis of a DRIE CMOS-MEMS gyroscope. *IEEE Sensors Journal*, Vol. 3, pp. 622-631, 2003.

159. T. Masuzawa and H. Tonshoff. CIRO, Three-Dimensional Micromachining by Machine Tool. *CIRP Annals-Manufacturing Technology*. Vol. 46, No. 2, 1997.

160. H. Brussel, J. Peirs, D. Reznaerts, A. Delchambre, G. Reinhart, N. Roth, M. Weck, and E. Zussman. Assembly of Microsystems. *Annals of the CIRP*. Vol. 49, No. 2, 2000.

161. D. Bou, A. Martin. Study on Micro Handling and Assembly Methods and Tools Within the Project ASSEMIC. *IEEE International Conference on Industrial Technology*. Vol. 1, pp. 44-49, 2004.

162. J. Gere and S. Timoshenko. Mechanics of Materials, 3rd edition, *PWS-KENT Publishing Company*, Boston, USA.

163. W. Weaver, J. Gere. Matrix Analysis of Framed Structures, 3rd edition, *Van Nostrand Reinhold*, New York, USA, 1990.

164. J. Doyle. Static and Dynamic Analysis of Structures. *Kluwer Academic Publishers.* The Netherlands, 1991.

165. G. Kovacs. Micromachined Transducers Sourcebook. *McGraw-Hill*, 1st edition, 1998.

166. S. Timoshenko and J. Gere. Mechanics of materials. *Van Nostrand Reinhold Co*., New York, 1972.

167. CMC Microsystems and Micralyne. Introduction to Micragem: A silicon-on-insulator based micromachining process v3.0, 2004.

168. Micralyne website. http://www.micralyne.com

169. J. Huang, A. Liu. An approach to the coupling effect between torsion and bending for electrostatic torsional micromirrors. *Sensors and Actuators A*. Vol. 115, pp. 159-167, 2004.

170. J. Cheng, J. Zhe, X. Wu. Analytical and finite element model pull-in study of rigid and deformable electrostatic microactuators. *Journal of Micromechanics and Microengineering*. Vol. 14, pp. 57-68, 2004.

171. O. Degani, Y. Nemirovsky. Experimental verification of a design methodology for torsion actuators based on a rapid pull-in solver. *Journal of Microelectromechanical Systems*. Vol. 13, pp. 121-129, 2004.

172. J. Zhao and H. Chen. A study on the coupled dynamic characteristics for a torsional micromirror. *Microsystem Technology*. Vol. 11, pp. 1301-1309, 2005.

173. W. Thomson. Theory of Vibration with Applications. *Prentice Hall*. 3rd Edition, 1988.

174. W. Langlois. Isothermal squeeze films. *Quarterly Applied Mathematics*. Vol. 20, No. 2, pp. 131-150, 1962.

175. F. Pan, J. Kubby, E. Peeters, A. Tran and S. Mukherjee. Squeeze film damping effect on the dynamic response of a MEMS torsion mirror. *Journal of Micromechanics and Microengineering*. Vol. 8, pp. 200-208, 1998.

176. M. Changizi and I. Stiharu. Nonlinear versus Linear Deflection Analysis of Microcantilevers. *IEEE ISIE*, July 9-12, 2006, Montreal, Canada.

177. W. Young. Roark's formulas for stress and strain, McGraw-Hill, New York, 1989.

178. J. Hartog. Strength of Materials. *Dover*. New York, 1977.

179. N. Lobontiu. Compliant Mechanisms: Design of Flexure Hinges. *CRC Press*. 2003.

180. S. Timoshenko. Strength of Materials. Part II: Advanced Theory and Problems. *Van Nostrand Reinhold*. New York, 1958.

181. G. Ananthasuresh and L. Howell. Mechanical design of compliant mechanisms A: perspective and prospects. *Journal of Mechanical Design*. Vol. 127, pp. 736-738, 2005.

182. J. You, M. Packrisamy, and I. Stiharu. Static modeling and pull-in analysis of an electrostatic actuator. *IEEE International Symposium on Industrial Electronics*. Vol. 4, pp. 3391-3396, 2006.

183. D. Wilcox and L. Howell. Fully compliant Tensural Bistable Micromechanisms (FTBM). *Journal of Microelectromechanical Systems*. Vol. 14, No. 6, pp. 1223-1235, 2005.

184. J. Zhao, H. Chen, J. Huang, A. Liu. A study of dynamic characteristics and simulation of MEMS torsional micromirrors. *Sensors and Actuators A*. Vol. 120, pp. 199-210, 2005.

185. D. Yan, A. Apsel, and A. Lal. Fabrication and electromechanical characterization of silicon on insulator based electrostatic micro-scanners. *Smart Materials and Structures*. Vol. 14, pp. 775-784, 2005.

186. Y. Cheng, C. Dai, C. Lee. A MEMS micromirror fabricated using CMOS post-process. *Sensors and Actuators A*. Vol. 120, pp. 573-581, 2005.

187. M. Wu, L. Lin, S. Lee, and C. King. Free-space integrated optics realized by surface-micromachining. *International Journal of High Speed Electronic Systems.* Vol. 8, No. 2, pp. 283-297, 1997.

188. J. Parise, L. Howell, and S. Magleby. Ortho-planar linear-motion springs. *Mechanism and Machine Theory*. Vol. 36, No. 11, pp. 1281-1299, 2001.

189. http://www.comsol.com/ and http://www.altasimtechnologies.com/

190. M. Wu, O. Solgaard, and J. Ford. Optical MEMS for Lightwave Communication. *Journal of Lightwave Technology*. Vol. 24, No. 12, 2006.

191. http://www.memscap.com/en_mumps.html

192. http://www2.ensc.sfu.ca/people/faculty/parameswaran/personal/soimumps.pdf

193. H. Xie, Y. Pan, and G. Fedder. A CMOS-MEMS mirror with curled-hinge comb drives. *Journal of Microelectromechanical Systems*. Vol. 12, pp. 450-457, 2003.

194. P. Chu, I. Brener, C. Pu. Design and nonlinear servo control of MEMS mirrors and their performance in a large port-count optical switch. *Journal of Microelectromechanical Systems.* Vol. 14, pp. 261-273, 2005.

195. O. Enge, P. Maiber, U. Jungnickel. Non-linear control of electrically driven micromirrors by means of inverse dynamics. *International Journal of Applied Electromagnetics and Mechanics*. Vol. 13, No. 1, pp. 107-112, 2002.

196. Y. Li. Modeling and Testing of Static and Dynamic Behavior of MEMS Deformable Microstructures with Multiple Electrodes. Master Thesis. Concordia University, 2007.

197. J. Kiihamaki. Fabrication of SOI micromechanical devices. *VTT Information Technology*. Finland, 2005.

198. Bruel & Kjaer S. & V., Skodsborgvej 307, Naerum, 2850, Denmark, http://www.bksv.com.

199. G. Rinaldi. Dynamic Analysis and Validation of Cantilever MEMS Subjected to Electro-Thermo-Mechanical Influences. *PhD Dissertation*. Concordia University, 2006.

200. http://www. newport.com

201. Piezomechanik GmbH. http://www.piezomechanik.com

202. Melles Griot. http://www.mellesgriot.com

203. Hamamatsu. http://www.hamamatsu.com

204. S. Tolansky. Microstructures of surfaces using interferometry. *Edward Arnold*. London, 1968.

205. S. Tolansky. An introduction to interferometry. *Wiliam Clowes and Sons*. London, 1955.

206. Nikon. http://www. microscopyu.com

207. Fringe Processor^{TM}. http://www.fringeprocessor.de